



**Exploring the genetic and transcriptomic regulation  
of stigma development and senescence in bread  
wheat**

**Marina Millán Blázquez**

A thesis submitted to the University of East Anglia for the degree  
of Doctor of Philosophy

John Innes Centre

December 2023

© This copy of the thesis has been supplied on condition that anyone who consults it is understood to recognise that its copyright rests with the author and that use of any information derived therefrom must be in accordance with current UK Copyright Law. In addition, any quotation or extract must include full attribution.



# Abstract

In the absence of pollination, the floral stigma senesces, which leads to an irrevocable loss in the reproductive potential of the flower directly affecting seed set. In self-pollinating crops like wheat (*Triticum aestivum*), the post-anthesis viability of the unpollinated carpel has been overlooked, despite its importance for hybrid seed production systems. The overall aim of this thesis is, therefore, to explore the mechanisms underlying stigma development and senescence in the absence of self-pollination.

To advance our knowledge of stigma development in the absence of pollination, we have created a high-throughput phenotyping approach that combines light microscopy and machine learning to examine stigma growth and senescence. By applying this method, we show that the unpollinated carpel undergoes a well-defined initial growth phase, followed by a peak phase (in which stigma area reaches its maximum), and a final deterioration phase marked by the upregulation of senescence-related genes. We next examine the impact of varying onsets of stigma deterioration on cross-pollination rates under field conditions across two years. Our findings indicate that hybrid seed set remains stable within a 10 to 15-day pollination window, aligning closely with the end of the peak phase of stigma development. Finally, to uncover the genetic mechanisms controlling stigma development, we conduct RNA-sequencing using unpollinated stigmas. This analysis reveals three distinct gene expression waves corresponding to the defined growth, peak, and deterioration phases. Among 66 identified transcription factors expressed predominantly during stigma senescence, the wheat orthologs of Arabidopsis NAC TFs *KIR1* (*KIR1*) and *ORESAR1* (*ORE1*) emerged as potential regulators. Phenotypic characterisation of *kir1* and *ore1* mutants indicated a modest extension of stigma longevity but no significant improvement in seed set under controlled conditions.

In essence, this thesis offers breeders and researchers a new framework for advancing mechanistic insights into female fertility in wheat, thereby laying the groundwork to improve hybrid wheat seed production.

## **Access Condition and Agreement**

Each deposit in UEA Digital Repository is protected by copyright and other intellectual property rights, and duplication or sale of all or part of any of the Data Collections is not permitted, except that material may be duplicated by you for your research use or for educational purposes in electronic or print form. You must obtain permission from the copyright holder, usually the author, for any other use. Exceptions only apply where a deposit may be explicitly provided under a stated licence, such as a Creative Commons licence or Open Government licence.

Electronic or print copies may not be offered, whether for sale or otherwise to anyone, unless explicitly stated under a Creative Commons or Open Government license. Unauthorised reproduction, editing or reformatting for resale purposes is explicitly prohibited (except where approved by the copyright holder themselves) and UEA reserves the right to take immediate 'take down' action on behalf of the copyright and/or rights holder if this Access condition of the UEA Digital Repository is breached. Any material in this database has been supplied on the understanding that it is copyright material and that no quotation from the material may be published without proper acknowledgement.

# Acknowledgements

Firstly, I am extremely grateful to my supervisors, Cristóbal Uauy and Scott Boden, for their invaluable advice, continuous support, and endless enthusiasm. During these four years, I have felt uncertain about many things, but they always took the time to discuss my questions in detail and filled our discussions with such energy that I left every meeting feeling motivated to take on new challenges. Scott, I extend my sincere thanks for sacrificing many family nights to discuss science with us, especially given the UK-Australia time difference. Cristóbal and Scott, you have not only been a great support in my scientific journey but have also gone above and beyond to help me in my overall career development. Thank you for setting a great example of what it means to pursue excellence in science.

I would also like to extend my gratitude to my secondary supervisor, Lars Østergaard, for his insights, kindness, and engaging discussions during our supervisory team meetings. To the rest of my supervisory team: Nick Bird, thank you for providing the NMS lines, offering continuous support throughout my PhD, and help during all my iCASE placements. Your insights into the world of wheat breeding and pre-breeding have been invaluable – thank you! I am grateful to Yann Manes for supplying the CMS lines and for his insightful interactions during meeting and conferences. A heartfelt thank you to my mentor and friend, Azahara Martín. Your guidance helped me to be confident in my results and your curiosity kept me motivated – you are truly an inspiration to me.

I also want to thank every single member of the Uauy Lab. The team spirit is unique to anything I have seen. It has been a blessing working, discussing, and brainstorming with you. Nikolai, James, Pam, Tobin, Andy, Max, Isa, Bernice, Katie, Sophie, and Yuanrong. Thank you all so much.

The John Innes Centre is a wonderful place that brings together people who are fascinated about plant research from all over the world. I am very grateful I could be part of this stimulating and exciting environment. I met many people without their help, this work would not be possible. Many thanks to Marianna for her support in the lab at the beginning of my PhD. Thank you to the whole bioimaging team, especially to Sergio for his help, to Lewis and Damian from the horticultural service for taking good care of my plants, and to Darryl, Chris, and Becca for making the field work as carefree

as possible. I also want to phrase my appreciation to everyone from the Rosalind Franklin Women in Wheat Champions. It has been a great privilege to learn, grow, and work alongside women like you. Special thanks to Diane Saunders for offering us this outstanding platform and the invaluable career development opportunities it brings. I am also thankful to my mentor, Simon Griffiths, for his honesty, support, and advice.

To my sponsors UKRI (UK Research and Innovation), KWS, Syngenta and the John Innes Centre; without their economic support, this project would not have been possible.

Last but not least the biggest love and appreciation to my family and friends who have been with me along the way. To the wonderful members of 90 Portland St (i.e., Chyna, Emma, Franziska, and Sam), to Aura, Anna S., Svenja, Anna B., Marco, Ricardo, Fede, Oscar, Jesús, Saul, Pratik, Giuseppe, Sean, Sonia, and Anna F. Each one of you holds a special place in my heart. To my friends in Spain, Gemma, Pablo, Anne, Julia, Mari Luz, Leti, Blanca y María del Mar. Even after 5 years and many kilometres between us, every visit felt like I never left. Your constant check-ins meant the world to me. To Joaquín Soriano, for helping me become a better friend to myself.

This thesis would never have been possible if it weren't for the unconditional love and support of all my family. Thank you for always being there for me. Papá, Mamá, Gonzalo y Martín, gracias por ser mi faro; y Abuela, gracias por enseñarme que las ganas de aprender nunca desaparecen.

*Cheers to this wonderful journey!*

*Marina*

*December 2023, Norwich*

# Table of contents

<b>Abstract</b> .....	3
<b>Acknowledgements</b> .....	4
<b>Table of contents</b> .....	6
<b>Table of figures</b> .....	10
<b>List of tables</b> .....	13
<b>List of appendices</b> .....	14
<b>List of abbreviations</b> .....	15
<b>1. General introduction</b> .....	16
1.1. Wheat production .....	16
1.2. Hybrid breeding.....	17
1.3. Hybrid wheat .....	19
1.3.1. Male sterility systems in wheat.....	20
1.3.2. Seed production of F <sub>1</sub> hybrid wheat.....	25
1.4. Flowering biology and pollination behaviour of wheat .....	28
1.4.1. The wheat stigma .....	29
1.5. Wheat genomic resources.....	33
1.6. Thesis aims .....	34
<b>2. A scalable phenotyping approach for female floral organ development and senescence in the absence of pollination in wheat</b> .....	36
2.1. Summary .....	36
2.2. Introduction .....	37
2.3. Materials and Methods .....	39
2.3.1. Germplasm .....	39
2.3.2. Glasshouse and field experiments.....	40
2.3.3. Image acquisition and manual annotations .....	42
2.3.4. Development of stigma and ovary CNNs .....	44

2.3.5.	Statistical analyses and data visualisation.....	45
2.3.6.	Stigma transcriptome analysis by RNA-seq .....	46
2.4.	Results .....	48
2.4.1.	Defining quantifiable parameters of late carpel development and senescence.....	48
2.4.2.	Overview of the approach .....	49
2.4.3.	Development and validation of the stigma and ovary convolutional neural networks	51
2.4.4.	Variation in stigma and ovary growth patterns can be studied on fixed carpels	55
2.4.5.	The application of the phenotyping approach provides insight into the developmental behaviour of the unpollinated wheat carpel .....	59
2.5.	Discussion .....	65
2.5.1.	High throughput phenotyping for the quantification of floral traits in unpollinated wheat carpels.....	65
2.5.2.	Considerations on the use of the stigma and ovary adapted CNNs .....	66
2.5.3.	The implementation of the phenotyping approach opens new research paths on the biology of late carpel development .....	67
2.5.4.	First steps towards an integrated developmental scale of the unpollinated wheat flower .....	68
<b>3.</b>	<b>Stigma longevity: not a limiting factor in hybrid wheat seed production .....</b>	<b>70</b>
3.1.	Summary .....	70
3.2.	Introduction .....	71
3.3.	Materials and methods.....	73
3.3.1.	Germplasm .....	73
3.3.2.	Experimental design and sampling .....	74
3.3.3.	Hybridity test.....	78
3.3.4.	Plant phenotyping .....	79
3.3.5.	Statistical analyses .....	80
3.4.	Results .....	82



3.4.1.	Selection and characterisation of carpel development in the female parents	82
3.4.2.	Evaluation of female performance in relation to hybrid seed set and stigma longevity .....	88
3.4.3.	Spatial distribution of hybrid seed set along the inflorescence.....	93
3.5.	Discussion .....	96
3.5.1.	Potential link between carpel size and carpel longevity .....	96
3.5.2.	The challenges of open pollination experiments.....	97
3.5.3.	The duration of stigma receptivity does not represent a major barrier in hybrid production.....	98
<b>4.</b>	<b>Genetic mechanisms regulating stigma development and senescence in the absence of pollination in wheat: insights from transcriptomics and functional characterisation .....</b>	<b>100</b>
4.1.	Summary .....	100
4.2.	Introduction .....	101
4.3.	Material and methods .....	103
4.3.1.	Germplasm .....	103
4.3.2.	Field and controlled environment experiments.....	105
4.3.3.	RNA extraction and sequencing .....	107
4.3.4.	Mapping of raw reads.....	107
4.3.5.	Principal component analysis (PCA) .....	107
4.3.6.	Differential gene expression analysis.....	107
4.3.7.	GO, TF and hormone enrichment analyses.....	109
4.3.8.	Ortholog identification .....	109
4.3.9.	DNA extraction and KASP Marker genotyping .....	109
4.3.10.	Plant phenotyping .....	111
4.3.11.	Statistical analyses .....	115
4.4.	Results .....	116
4.4.1.	Morphology of the unpollinated carpel and its transcriptional landscape	116

4.4.2.	Construction and analysis of a weighted co-expression network .....	118
4.4.3.	Biological significance of gene expression patterns .....	121
4.4.4.	Identifying candidate genes using comparative transcriptomics .....	130
4.4.5.	Functional characterisation of <i>KIR1</i> and <i>ORE1</i> genes in hexaploid wheat	134
4.5.	Discussion .....	145
4.5.1.	The development of the unpollinated stigma is under tight genetic control	145
4.5.2.	Differential expression analysis provides insights into the genetic regulation underlying the growth and peak phases.....	145
4.5.3.	Comparative transcriptomics as a method to identify candidate genes involved in stigma deterioration .....	147
4.5.4.	Lessons from studying <i>kir1</i> and <i>ore1</i> loss of function mutants .....	149
4.6.	Appendices .....	153
<b>5.</b>	<b>General discussion .....</b>	<b>157</b>
5.1.	The longevity of the unpollinated stigma does not represent a major barrier for hybrid seed production .....	157
5.2.	Challenges in assessing stigma receptivity.....	160
5.3.	Future directions in breeding female ideotypes for hybrid seed production..	161
5.3.1.	Ovary expansion.....	161
5.3.2.	Stigma exertion and stigma size .....	162
5.3.3.	Additional strategies.....	162
5.4.	Advancing our understanding of female fertility in wheat.....	163
5.5.	Concluding statement .....	165
	<b>Bibliographical references.....</b>	<b>166</b>
	<b>Appendix A .....</b>	<b>181</b>

## Table of figures

Figure 1.1 Harvested land area per crop type on a global scale, from 1961 to 2021.....	16
Figure 1.2 superior performance of the F1 hybrid compared to its parents.....	17
Figure 1.3 Loss of hybrid vigour in the F <sub>2</sub> generation. ....	18
Figure 1.4 Maize yield measured in bushels per acre in the United States from 1860 until 2000. ....	19
Figure 1.5 Schematic representation of three male sterility systems. ....	25
Figure 1.6 Schematic representation of desired characteristics for male and female wheat parents in comparison to wild type florets (♂) for spike morphology and floret structure.....	27
Figure 1.7 Structure of the wheat spike. ....	29
Figure 1.8 Schematic representation of a carpel at Waddington stage 9.5. ....	30
Figure 1.9 Stigma development and degeneration of male fertile and sterile wheat plants. ....	31
Figure 1.10 Regulatory network of stigma life span in Arabidopsis. ....	32
Figure 2.1 Schematic representations of the field layout.....	41
Figure 2.2 Environmental conditions recorded during 2020 and 2021 field seasons. ....	42
Figure 2.3 Unaccepted and accepted carpel images.....	43
Figure 2.4 Representative stages of late carpel development in the absence of pollination. ....	49
Figure 2.5 Schematic representation of the proposed phenotyping approach for the study of carpel development in the absence of pollination under field conditions.....	51
Figure 2.6 Development and validation of convolutional neural network for stigma and ovary annotation.....	52
Figure 2.7 Validation of convolutional neural network for stigma and ovary annotation. ....	53
Figure 2.8 Effects of the fixative on carpel morphology across time and cultivars.....	56
Figure 2.9 Effects of the fixative on ovary diameter across time and cultivars.....	57
Figure 2.10 Phenotypic quantification of carpel development in three distinct MS cultivars under field conditions.....	60

Figure 2.11 Developmental stigma patterns expressed in percentage from maximum observed stigma area. ....	61
Figure 2.12 Senescence-related transcriptional regulators are up-regulated during the late peak and deterioration phases. ....	64
Figure 2.13 Erroneous stigma area and ovary diameter CNN annotations. ....	67
Figure 3.1 Visual and schematic representation of the field layout in 2020. ....	74
Figure 3.2 Field trial layout of the 2021 hybrid seed production trial before flowering. ....	76
Figure 3.3 Field trial layout of the 2022 hybrid seed production trial before flowering. ....	77
Figure 3.4 Environmental conditions recorded during 2020, 2021 and 2022 field seasons. ....	78
Figure 3.5 Distribution of heterozygous base calls for F <sub>1</sub> and pollen donor seeds. ....	79
Figure 3.6 Diagnostic plots of residual values. ....	80
Figure 3.7 Diagnostic plots of residual values. ....	81
Figure 3.8 Characterisation of stigma traits for the selection of female parents. ....	83
Figure 3.9 Phenotypic diversity observed for stigma development during the 2020 field season. ....	84
Figure 3.10 Phenotypic quantification of carpel development in the female parents across the 2021 and 2022 field seasons. ....	87
Figure 3.11 Relationship between carpel longevity and carpel size. ....	88
Figure 3.12 Temporal dynamics of hybrid seed yields and their hybridity levels. ....	92
Figure 3.13 Bidirectional gradient of carpel development along the spike. ....	93
Figure 3.14 Spatial and temporal distribution of hybrid seed set. ....	95
Figure 3.15 Visual seed set scores for the 2,428 unique combinations. ....	99
Figure 4.1 Hand emasculations of mutant populations. ....	106
Figure 4.2 Workflow employed for conducting differential expression analyses using RNA sequencing data. ....	106
Figure 4.3 Graphical representation of WGCNA module sizes for different soft power thresholds ( $\beta$ ). ....	108
Figure 4.4 Representation of the automated image thresholding process. ....	113
Figure 4.5 The temporal progression of stigma development and degeneration. ....	117

Figure 4.6 Identification of distinct co-expression clusters via WGCNA. ....	119
Figure 4.7 Visualisation of the eigengene network within the developing stigma. ....	120
Figure 4.8 Relationships among gene expression modules and time points of stigma development. ....	121
Figure 4.9 Enriched GO slim terms for biological processes. ....	123
Figure 4.10 Transcription factor families found to be significantly enriched.....	125
Figure 4.11 Stigma specific senescence associated TFs. ....	127
Figure 4.12 Hormone related genes significantly enriched during stigma development. ....	129
Figure 4.13 Differences in the temporal progression of stigma development are genetically controlled. ....	131
Figure 4.14 Proportion of differentially expressed genes (DEGs) shared between different male sterile wheat cultivars. ....	132
Figure 4.15 Differentially expressed senescence associated TFs and auxin biosynthesis related genes during stigma development in 24512, 24522 and BSS1. ....	134
Figure 4.16 Mutations in <i>KIR1</i> and <i>ORE1</i> . ....	136
Figure 4.17 Quantification of stigma size in unpollinated carpels in <i>KIR1</i> and <i>ORE1</i> mutants. ....	138
Figure 4.18 Live-dead staining for monitoring progression of cell death in unpollinated stigmas. ....	140
Figure 4.19 Stigmatic pollen grain germination and seed set to investigate flower receptivity in <i>kir1</i> and <i>ore1</i> mutants.....	141
Figure 4.20 Development of the unpollinated stigma under field conditions for mutant and cv. Cadenza populations and reduced grain set in <i>ORE1</i> and <i>ore1</i> populations. ...	143
Figure 4.21 Flag leaf senescence in <i>KIR1</i> and <i>ORE1</i> mutant and Cadenza populations. ....	144
Figure 4.22 Gene duplication of <i>KIR1</i> in hexaploid wheat.....	152

## List of tables

Table 2.1 Summary of the germplasm used for each experiment described in this study. .....	40
Table 2.2 Summary table on the manual and CNN annotation metrics obtained for stigma area and ovary diameter.....	54
Table 2.3 Summary table of three-way ANOVA on the effect of the fixative on stigma area and ovary diameter across different timepoints.....	58
Table 3.1 Plant scores of pollen donors selected for 2021 and 2022 hybrid seed production field trials. ....	73
Table 3.2 Flowering time (anthesis) of pollen donors in 2021 and 2022. ....	85
Table 3.3 Regression table summarising linear mixed model results.....	90
Table 4.1 Predicted consequences of the selected TILLING mutations in the protein.	104
Table 4.2 KASP primers used for ORE1 and KIR1 TILLING mutants. ....	110
Table 4.3 Components for 100 µL of the primer mix. ....	111
Table 4.4 Reaction components for KASP genotyping. ....	111
Table 4.5 Thermocycling conditions for PCR amplification. ....	111

## List of appendices

Appendix 4.1 ClustalW alignment of KIR1 protein variants 1 and 2 in all three A, B and D homoeologs. ....	153
Appendix 4.2 Analysis of variance for stigma area in <i>ore1</i> and <i>kir1</i> mutant populations at 8, 12, 14 and 16 DAE. ....	154
Appendix 4.3 Analysis of variance for the percentage of green pixels in <i>ore1</i> and <i>kir1</i> mutant populations at 8, 12, 14 and 16 DAE. ....	155
Appendix 4.4 Analysis of variance for the percentage of green pixels between <i>ore1</i> and <i>ORE1</i> and <i>kir1</i> and <i>KIR1</i> mutant populations at 8, 12, 14 and 16 DAE. ....	156
Appendix A Millan-Blanco, M., Hartley, M., Bird, N., Manes, Y., Uauy, C., & Boden, S. A. (2022). A scalable phenotyping approach for female floral organ development and senescence in the absence of pollination in wheat. <i>Development</i> , 149(18), dev200889. ....	181

## List of abbreviations

<b>ANOVA</b>	Analysis of variance
<b>BC</b>	Backcross
<b>BLA</b>	Blue aleurone
<b>CHA</b>	Chemical hybridising agent
<b>CMS</b>	Cytoplasmic male sterility
<b>CNN</b>	Convolutional neural network
<b>DAW9.5</b>	Days after Waddington 9.5
<b>DEG</b>	Differentially expressed gene
<b>DSC</b>	Dice similarity coefficient
<b>EMS</b>	Ethyl methanesulfonate
<b>FDA</b>	Fluorescein diacetate
<b>FDR</b>	False-discovery rate
<b>HSD</b>	Turkey's honestly significant difference
<b>KASP</b>	Kompetitive allele specific PCR
<b>ML</b>	Machine learning
<b>MS</b>	Male sterile
<b>NMS</b>	Nuclear male sterility
<b>PCA</b>	Principal component analysis
<b>PCD</b>	Programmed cell death
<b>PI</b>	Propidium iodide
<b>QTL</b>	Quantitative trait loci
<b>RCBD</b>	Randomised complete block design
<b>RGB</b>	Red, green, and blue
<b>RIN</b>	RNA integrity number
<b>RNA-Seq</b>	RNA Sequencing
<b>SNP</b>	Single nucleotide polymorphism
<b>TF</b>	Transcription factor
<b>TILLING</b>	Targeting induced local lesions in genomes
<b>TPM</b>	Transcript per million
<b>WGCNA</b>	Weighted gene co-expression network analysis
<b>WT</b>	Wild type



# 1. General introduction

## 1.1. Wheat production

Wheat (*Triticum aestivum*) stands as one of the most important crops globally playing a critical role in human nutrition, food security and economic growth. It is farmed on more land area than any other food crop (Figure 1.1; FAO., 2022) and its widespread cultivation is attributed primarily to its high environmental adaptation. It contributes 20% of the daily caloric intake and provides more protein than all forms of meat combined, thereby serving as the primary protein source for the world population (Poutanen et al., 2022).

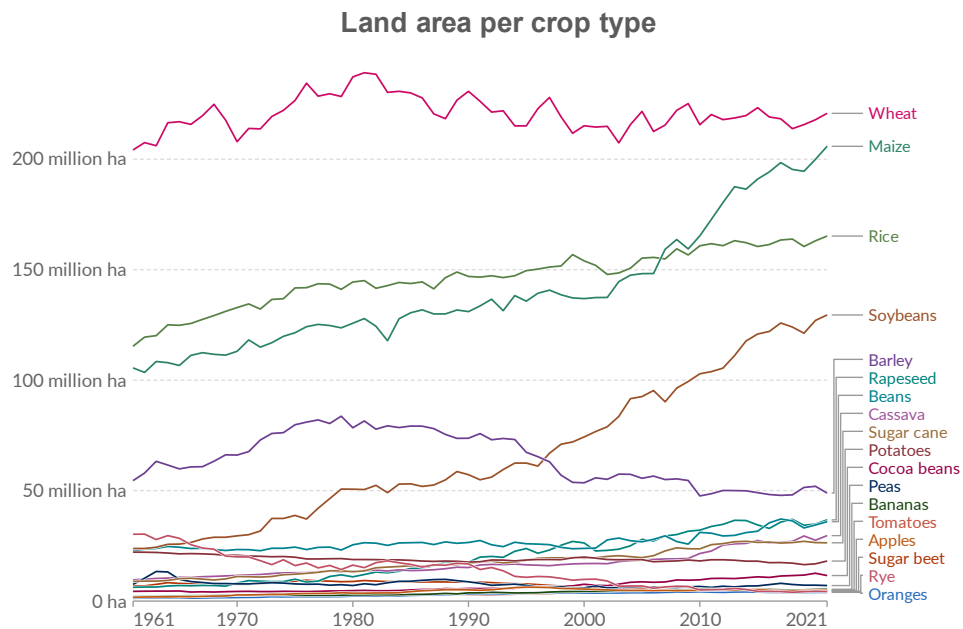


**Figure 1.1 Harvested land area per crop type on a global scale, from 1961 to 2021.**

Data published and retrieved from Food and Agriculture Organization of the United Nations on June 12, 2023. Data visualisation from OurWorldInData: [Land area per crop type, World, 1961 to 2021 \(ourworldindata.org\)](https://ourworldindata.org/land-area-per-crop-type).

However, global wheat production faces threats from climate change, which is anticipated to bring about challenges such as heat and drought stress, along with the emergence of new pests and diseases compromising food security (Tester & Langridge, 2010). Furthermore, the adverse impacts of climate change are expected to be particularly severe in countries across the global south that are already grappling with

food security issues. For instance, wheat yields are projected to decline by 2050 by 15% and 16% in African and Southern Asian countries, respectively (Pequeno et al., 2021).

In response to climate change challenges, there is a continually growing societal demand for sustainability, quality, and safety in agricultural production, including wheat (Paux et al., 2022). These demands include reducing land use, minimising the use of fertilisers and pesticides due to increasing costs and their negative impact on the environment when misapplied, and promoting the development of climate-resilient cultivars. These challenges can be addressed through various approaches, ranging from integrated pest management, more efficient selection using conventional breeding and genomic selection approaches through to the adoption of innovative technologies such as the exploitation of heterosis (Beddington, 2010; Whitford et al., 2013).

## 1.2. Hybrid breeding

In hybrid breeding, two genetically distinct lines are crossbred to produce an offspring, known as an F<sub>1</sub> hybrid. Typically, this F<sub>1</sub> hybrid demonstrates superior phenotypic performance in comparison to its parents, a phenomenon referred to as heterosis or hybrid vigour (Figure 1.2).

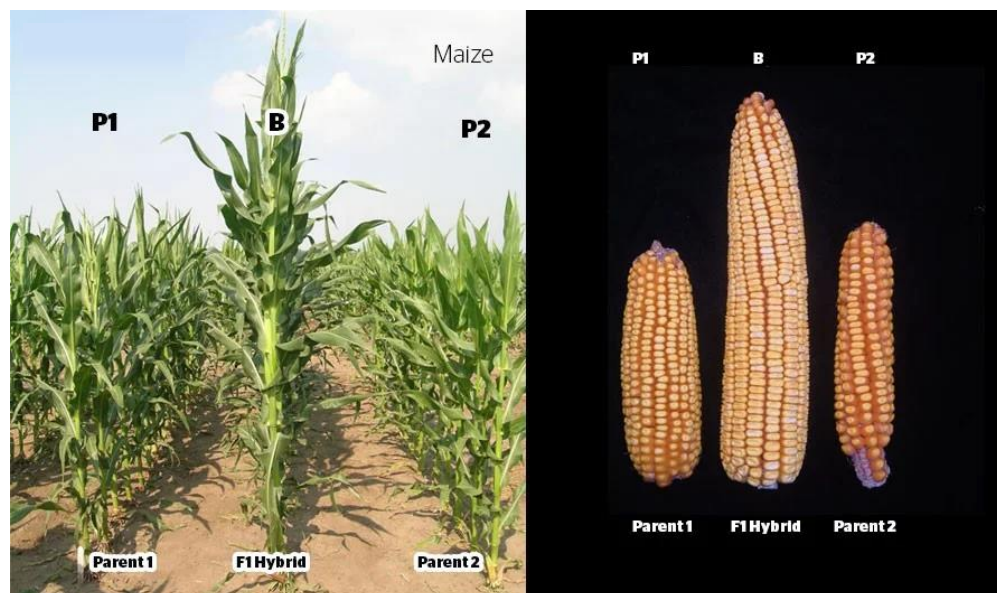


**Figure 1.2 superior performance of the F1 hybrid compared to its parents.**

Figure obtained from [Hybrid seed production in Maize - AgriHunt - A Hunt for Agricultural Knowledge](#)

Efficient exploitation of heterosis, or hybrid vigour, relies on the separation of lines into genetically distinct groups, termed heterotic pools. By strategically organising lines into heterotic pools, breeders can capitalise on the complementary genetic traits present in the distinct parental lines, thereby maximising the potential for hybrid vigour in subsequent generations. One of the keys lies in the genetic divergence or distance between the parents within these pools. However, the main advantage of  $F_1$  hybrids comes with a limitation – the sustained expression of heterosis is confined to the  $F_1$  generation. Subsequent generations resulting from self-pollination or uncontrolled cross-pollination, exhibit significant phenotypic variability among individuals due to genetic segregation of traits (Figure 1.3). This lack of uniformity and potential loss of favourable traits seen in the  $F_1$  hybrid make  $F_2$  seeds less predictable and less desirable for commercial or agricultural purposes. Nonetheless, from a commercial standpoint, this duality represents an added benefit of hybrid breeding systems as it prevents the use of ‘farm-saved’ seed, an increasingly common and concerning practice for breeding companies as it reduces return from investment into new varieties (Longin et al., 2012).

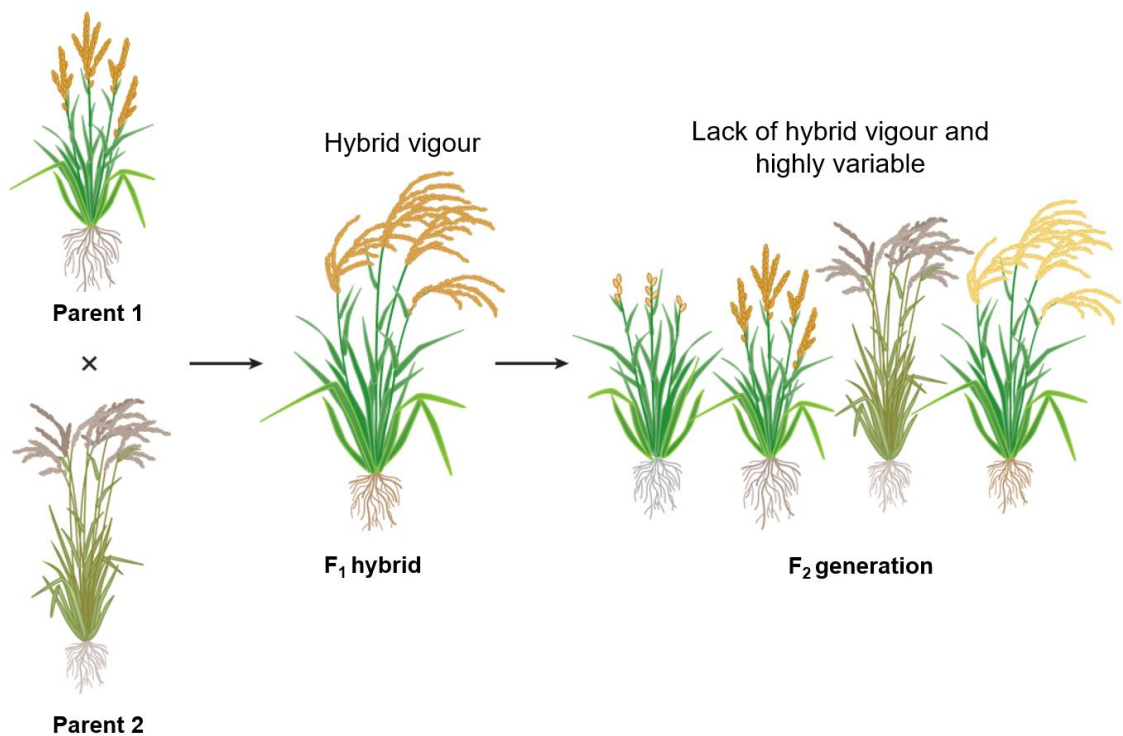


**Figure 1.3 Loss of hybrid vigour in the  $F_2$  generation.**

$F_2$  generation shows significant variation resulting from the shuffling of genetic information and may produce less yield than the  $F_1$  hybrid due to the lack of hybrid vigour. First arrow indicates the cross between Parent 1 and Parent 2, while the second arrow denotes either self-pollination or uncontrolled cross-pollination. Figure adapted from Underwood & Mercier (2022).

Despite the challenges associated with  $F_2$  seeds, hybrid breeding, together with advances in agronomic practices and improved inbred lines has played a crucial role in increasing crop yields and improving the overall productivity of agriculture (Figure 1.4; Kingsbury, 2011). It is widely used in the production of many allogamous (cross-fertilising) crops, including maize (*Zea mays*), sunflower (*Helianthus annuus*), sorghum (*Sorghum bicolor*), as well as numerous vegetable species including tomato (*Solanum lycopersicum*) or kale (*Brassica oleracea*), to name a few.

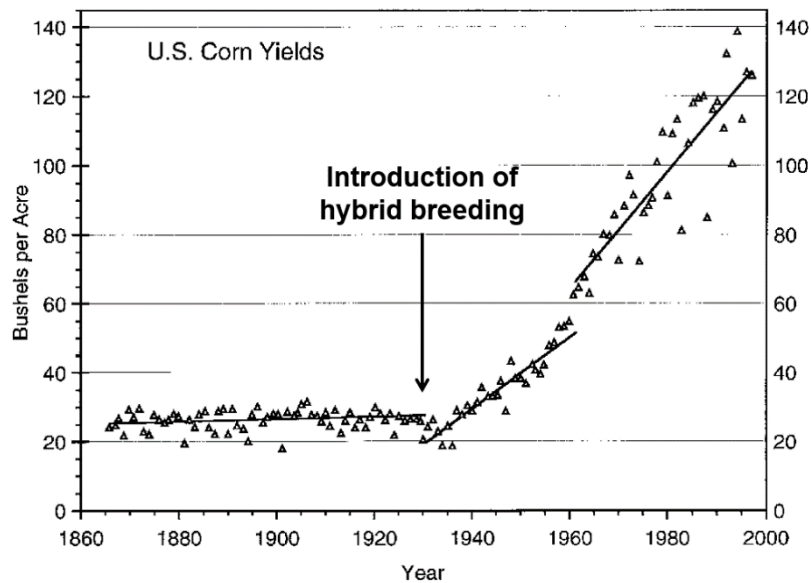


**Figure 1.4** Maize yield measured in bushels per acre in the United States from 1860 until 2000.

Maize yields experienced a sudden increase after the introduction of maize hybrids in the 1930s. Graph adapted from Crow (1998).

### 1.3. Hybrid wheat

Hybrid breeding in self-pollinating or autogamous crops, like wheat, presents considerable technical challenges. In these species, hybrid seed production depends on the unnatural procedure of cross-fertilisation, for which the species are inherently ill-adapted. Wheat, for instance, exhibits natural outcrossing rates estimated to be less than 1% (Hucl, 1996). To facilitate hybrid seed production, obligate outcrossing is essential. Consequently, the discovery of male sterility systems in wheat during the 1960s played a crucial role in achieving outcrossing, as it provided the means for commercial-scale production of hybrid wheat seed by preventing unwanted self-pollination of the female parent.

The exploitation of heterosis in wheat has been proposed as an alternative for addressing future challenges in food supply (Longin et al., 2013; Longin & Reif, 2014). The use of heterosis in wheat promises benefits such as average yield advantages of 3.5-15% over commercial inbred parents, higher biotic and abiotic stress resistance, better fertiliser-use efficiency, or an enhanced yield stability, especially in fluctuating environments (Longin et al., 2013). However, despite the recognised advantages of hybrids and the decades of research invested into hybrid wheat breeding programmes, hybrids account for less than 1% of the total wheat growing area (Longin et al., 2012). The success of hybrid wheat in the market has been hindered significantly by several factors: (1) the lack of reliable male sterility systems; (2) the absence of cost-effective hybrid seed production systems, mainly due to the low cross-pollination rates; (3) the inexistence of established heterotic groups exhibiting high heterosis when crossed; and (4) the current level of yield heterosis which is perceived by breeders to be too low compared to conventional line breeding to justify higher seed production costs estimated to be two to three times as expensive (Akel et al., 2019; Selva et al., 2020; Whitford et al., 2013). Although hybrid breeding in wheat is presently not cost-efficient, the potential to minimise many of these costs through recent technological advances, such as wheat genomics and targeted modification of plant phenotypes, does exist. Genomic selection, for instance, is being instrumental in enhancing heterotic gains in hybrid wheat by ensuring larger yields compared to line-bred varieties (Longin et al., 2015). Moreover, this approach help minimise the time and costs associated with phenotyping and the breeding cycle, which typically spans around ten years in conventional selection methods. As a result, these advancements, along with other developments discussed in section 1.5, have reignited renewed interest and investments from both the public and private sectors (Selva et al., 2020).

### 1.3.1. Male sterility systems in wheat

Establishing a robust pollination control system is a prerequisite for successful hybrid breeding to avoid self-fertilisation. The most effective way to avoid self-pollination and promote cross-pollination in hermaphrodite flowers is through male sterility. Plant male sterility is characterised by the absence of functional anthers, pollen, or male gametes. Male sterility can be technically achieved through two primary approaches: genetic systems, which encompass cytoplasmic male sterility and nuclear male sterility, and non-genetic methods, such as chemical hybridisation and hand emasculation. For both

methods, incomplete sterility is a major risk as it may lead to self-fertilisation of the female parent, compromising the purity of the F<sub>1</sub> hybrid seed production. It is crucial, therefore, to ensure a precise sterilisation process to maintain the purity of hybrid seeds. The following section delineates the main male sterility methods developed for commercial hybrid wheat production as they can produce large populations of male sterile plants. Other approaches exist and are reviewed in Gupta et al., 2019. The female lines used in this thesis were derived from cytoplasmic male sterility and nuclear male sterility techniques and were provided by industrial partners.

#### 1.3.1.1. *Cytoplasmic male sterility*

Cytoplasmic male sterility (CMS) is controlled by hereditary factors within the cytoplasm and, primarily arises from rearrangements of mitochondrial DNA, leading to the formation of chimeric genes that prevent the production of viable pollen (Hanson & Bentolila, 2004). These genetic alterations disrupt normal mitochondrial function and hamper the communication between cytoplasmic and nuclear genes (Hanson & Bentolila, 2004). Clues regarding how CMS-associated genes induce male sterility have emerged across various systems and are extensively reviewed by Chen & Liu (2014). CMS is inherited maternally through the cytoplasmic genome. However, for practical application in grain crops where the seed is required as the end product, a reliable fertility restoration mechanism is essential. Male sterility can be reversed by nuclear-encoded restorer-of-fertility (*Rf*) genes. Although the mechanisms underlying restoration are probably as diverse as the mechanisms by which mitochondrial mutations cause CMS, *Rf* proteins are typically transported to the mitochondria, where they affect mRNA processing of CMS-associated gene products and prevent their accumulation (Bohra et al., 2016). However, the limited availability of effective *Rf* genes has been a major limiting factor for the application of CMS to hybrid seed production in wheat (Whitford et al., 2013).

Various CMS systems have been developed in wheat by backcrossing the wheat nuclear genome into the cytoplasm of a related species like *Triticum timopheevii* (Chen & Wehling, 2003) or *Hordeum chilense* (Martín et al., 2008). This system involves three lines: the male sterile CMS line (with sterile cytoplasm and recessive nuclear restorer genes), the male parent with backcrossed restorer genes for fertility restoration in the F<sub>1</sub> hybrid progeny, and a fully fertile maintainer line with identical genotype as the CMS line but with a fertile cytoplasm to produce more male sterile progeny (Figure 1.5;

Whitford et al., 2013). For F<sub>1</sub> production, the CMS female is pollinated with a genetically distinct male line containing one or more *Rf* genes to produce fully fertile F<sub>1</sub> seed (heterozygous for dominant restorer genes). Despite its utility, the CMS system is complex and expensive, requiring extensive backcrossing to introduce cytoplasm and restorer genes into desired lines. This process may result in promising material lagging behind new conventional varieties during the development phase (Edwards, 2001). This presents a significant drawback, especially considering that conventional pure-line breeding consistently boosts yield by an average of 0.9% per annum (Ray et al., 2013). Consequently, any delay in germplasm development for hybrid breeding will diminish the relative yield advantage of hybrids over pure-line cultivars.

#### 1.3.1.2. Nuclear male sterility

Unlike CMS, nuclear male sterility (NMS) is characterised by mutations or alteration in the nuclear DNA of plants hindering the production of viable pollen. In wheat, at least, five nuclear genes for male sterility have been identified (*ms1-5*; Srivastava, & Kumar, 2014). Fertility can be readily restored by crossing a wheat line carrying the deletion or mutation/modification in a homozygous state with any normal wheat. The resulting hybrids are fertile since the deletion, or the mutation/modification is present in a heterozygous state. The majority of wheat varieties will act as fertility restorers; thus, it is only necessary to breed special female parents. The maintenance of a male sterile parent involves using a heterozygous male fertile population that is segregating for the fertility trait. However, it is important to highlight that besides being male sterile, NMS lines do not typically manifest other apparent phenotypes. This raises the concern of distinguishing male sterile plants from their male fertile siblings and therefore requires a strategy to remove the male fertile plants. One effective solution to this problem is to ensure that the male-sterile mutant locus is closely linked to a visible marker, such as height or grain colour (Bing-Hua & Jing-Yang, 1986). For instance, the BLue Aleurone (BLA) system, recently developed by Darvey et al., (2020), introduces the Blue aleurone (Ba) seed colour marker from chromosome 4E of *Agropyron elongatum* (Figure 1.5). Briefly, in this system, the male parent (isogenic to the female) carries a monosomic alien chromosome with a dominant male fertility restorer gene from *Triticum boeoticum*, and the *BLA* gene from *Agropyron elongatum*. When expressed, the *BLA* gene offers a distinct blue coloration to the fertile progeny facilitating the physical separation of the progeny seeds based on the colour. In theory, white seeds remain male sterile due to the deletion of the *ms1* gene and lack of the alien chromosome. These

white seeds can then be used as female parents in subsequent hybrid wheat production, while the harvested blue seeds are used as male or maintainer lines. However, challenges related to genomic stability occasionally lead to mis-division of the alien chromosome (1-2% of the time), resulting in white male fertile seeds (Figure 1.5). Additionally, other issues, such as the purity of male sterile seeds, have prevented the commercial exploitation of NMS for hybrid wheat production (Gupta et al., 2019).

#### *1.3.1.3. Chemical hybridising agents*

Plants can also be sterilised by spraying chemical hybridising agents (CHAs), which act as gametocides, preventing the development of viable pollen when applied at specific growth stages in the field (Figure 1.5; Kempe & Gils, 2011). The use of CHA eliminates the need for techniques to maintain parental lines or restore fertility in hybrids, making it a simpler alternative compared to CMS or NMS. CHAs also remove the requirement to select female parents with specific characteristics for maintenance, enabling the production and evaluation of numerous parental combinations. Croisor® 100 (active component: 100 g/L sintofen, Asur Plant Breeding) is the primary CHA currently used by Sateen Union for commercial hybrids in Europe. Despite being the prevailing method for hybrid production in Europe, the adoption of CHAs has been limited due to concerns about phytotoxicity (potential induction of female sterility based on the applied dosage), incomplete induction of male sterility, susceptibility to environmental conditions (e.g., rain, wind, and heat), and a restricted range of suitable genotypes as some combinations of CHAs and genotypes exhibit lower levels of sterility (Easterly et al., 2019; Whitford et al., 2013).





### **Figure 1.5 Schematic representation of three male sterility systems.**

From left to right, cytoplasmic male sterility (CMS), nuclear male sterility (NMS), and chemical hybridising agents (CHA). In CMS-based system, individuals inherit CMS or native (N) cytoplasm as well as nuclear-encoded restorer loci (*Rf*, *rf*). Blue Aleurone (BLA) system is used as an example of an NMS-based system. It is based on a deletion on chromosome 4BS (i.e., *ms1* mutant allele). Fertility can be restored in the homozygous male sterile mutant through the action of an alien chromosome (Bla-chromosome). Seeds containing the Bla-chromosome are identifiable by blue aleurone. The Bla-chromosome is poorly transmitted, resulting in 75% white-seeded progeny (i.e., no Bla-chromosome). The problem of the mis-division is also represented. The production of fully fertile white seeds poses a problem in hybrid seed production, while fully sterile blue seeds have a limited impact on breeding and seed production. In CHA-based systems, the mother line is produced by applying a gametocide and planted in alternating strips with the untreated male pollinator. CMS and CHA diagrams are adapted from Whitford et al., 2013 and Kempe & Gils, 2011, respectively.

#### 1.3.2. Seed production of F<sub>1</sub> hybrid wheat

Irrespective of the method used to achieve a male sterile line, the low levels of seed set in these male sterile lines (when exposed to open pollination) remains the major bottleneck for the commercial success of hybrid wheat, as it increases the cost of seed production (Gupta et al., 2019). This constraint arises from the inherent autogamous nature of the crop which has evolved an anatomy and behaviour of the floral organs during the pollination period which limits cross-pollination (further discussed in section 1.3.2.3). This is further confounded by environmental factors such as the necessity of wind for pollen transport and, consequently, cross pollination (De Vries, 1971; Whitford et al., 2013).

##### *1.3.2.1. Hybrid production fields*

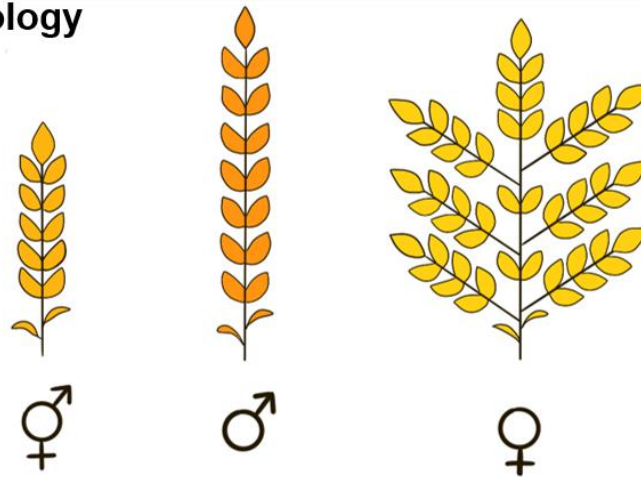
To overcome these limitations, various strategies have been explored, including the optimisation of pollen dispersal in hybrid seed production systems. This optimisation is crucial for the commercial viability of the system, not only as a prerequisite for obtaining hybrid seed from the female line but also to minimise the spatial footprint occupied by the male genotype, which does not contribute to the harvested hybrid seed (Edwards, 2001; Gupta et al., 2019). Currently, hybrid seed production fields, such as those of the industrial partners, are organised with alternating strips of female and male parents. One approach involves adjusting the widths and ratios of the male sterile and pollinator strips in the hybrid wheat seed production field (Edwards, 2001). This can range between male / female width ratios of 4 m / 4 m, 6 m / 4 m and 6 m / 6 m (Leahy,

2008). Another strategy is the use of ‘blend hybrids’. In this method, the commercial hybrid seed consists of a blend of seeds sourced from a field containing a minor percentage of male parents (5-20%) and a majority of male sterile parents which will act as females (80-95%). The small percentage of male parents is sufficient to provide enough pollen for the larger population of females. Moreover, by allowing pollen to travel a very short distance, this ‘blend hybrids’ seed production field maximises the chances of successful cross-pollination (Gupta et al., 2019).

#### *1.3.2.2. Suitability of male and female floral structures for cross-pollination*

Despite the use of various production methods, the associated costs remain excessively high and often prohibitive. Hence, there is a pressing need for innovative approaches to further optimise hybrid production. Acknowledging this, it is also well accepted that an efficient hybrid wheat breeding programme requires the redesign of the floral biology and architecture (Selva et al., 2020). This redesign aims to maximise cross-pollination and seed set by creating populations with optimal characteristics for plants performing the male and female role. In an ideal hybrid system, the male ideotype features well-spaced spikelets, long-extruding anthers producing large quantities of pollen which has good dispersal (e.g., aerodynamic, light) and survives well under different environmental conditions. Optimising pollen shedding attributes could lead to a reduction in the number of male plants required, consequently increasing hybrid seed production per surface area and lowering associated costs (Figure 1.6). Conversely, the female ideotype would showcase an extruded stigma with a high density of long stigmatic hairs, increasing the likelihood of pollen interception. It would also possess an extended pollen receptive period, supernumerary carpels within the floret and a more open floret structure to facilitate stigma extrusion and the access of airborne pollen (Figure 1.6).

## Spike morphology



## Floret structure



**Figure 1.6 Schematic representation of desired characteristics for male and female wheat parents in comparison to wild type florets (♀) for spike morphology and floret structure.**

An ideal male spike would feature numerous spaced spikelets. A branched female spike enhances the carpel count per unit of area. Regarding floret structure, the male parent would exhibit optimal pollen shedding characteristics, including increased filament length and anther size as well as greater, and a higher pollen count. Conversely, the female parent would possess good pollen-receptive qualities, such as an increased density of stigmatic hairs or supernumerary carpels, along with an expanded floret aperture facilitated by larger lodicules. Figure modified from Selva et al. (2020).

### 1.3.2.3. *Relative flowering dates of male and female parents*

In addition, the synchronisation or ‘nick’ of flowering times between the female and male plants is essential for the optimisation of seed set in production fields (Pickett, 1993). Nonetheless, the selection of genetically dissimilar parents for the purpose of achieving heterosis often results in broader flowering times. In the case of wheat, the challenge of varying flowering times between the genetically distinct male sterile line and the pollinator is exacerbated by the short life span of released pollen grains (0.5-3 hours; D'Souza, 1970) and the brief duration of stigma receptivity (up to 7 days in

moderate temperature and humidity; Imrie, 1966). Strategies like staggered planting, burning, or mowing male plants, and adjusting fertilizer rates differentially have been implemented to ensure synchronisation between male and female plants (Edwards, 2001). However, these methods are characterised by erratic outcomes, further contributing to the increase in production costs for hybrid seeds. Prolonging the flowering period for both male and female plants could expand the possibilities for potential crosses, allowing for a more diverse range of hybrids. This extension would facilitate the incorporation of a wider array of genetic resources (e.g., regional landraces or local varieties) into hybrid breeding programmes (Schneider et al., 2021). This inclusivity is especially significant in mitigating the challenge posed by the homogeneity of European germplasm (Cseh et al., 2021), where wheat breeding has traditionally relied on a very limited pool of elite genotypes, thereby restricting the potential for heterotic gains. While substantial efforts have historically focused on improving the out-crossing ability of the male parent, there has been a lack of attention to the female parent. Hence, reassessing the role of the female parent is crucial not only for enhancing hybrid seed production efficiency but also fostering a broader range of hybrids and, consequently, realising the full benefits of hybrid wheat breeding (Selva et al., 2020). This PhD thesis is dedicated to unravelling the underlying biology of wheat female fertility traits, specifically focusing on stigma longevity and receptivity to pollen.

#### **1.4. Flowering biology and pollination behaviour of wheat**

The wheat inflorescence or spike (Figure 1.7) is arranged on a number of reproductive branches named spikelets which are comprised of two outer glumes and a composite of two to five fertile florets that have the potential to set seeds (De Vries, 1971). In addition, each floret consists of the lemma and palea. Between them are the reproductive organs, including three stamens and a single carpel composed of an ovary bearing a twin-branched feathery stigma. Additionally, there are two small lodicules at the base of the floret that are involved in floret opening at anthesis (flowering), exposing both male and female reproductive organs for pollination. Flowering usually begins in the central third of the spike and continues towards the top and the bottom, normally progressing more rapidly upwards. Likewise, within the spikelet the primary floret flowers first followed by the second, third and subsequent florets in an alternating

direction (De Vries, 1971). As a consequence, the flowering period of a single spike extends for a duration of two to six days.

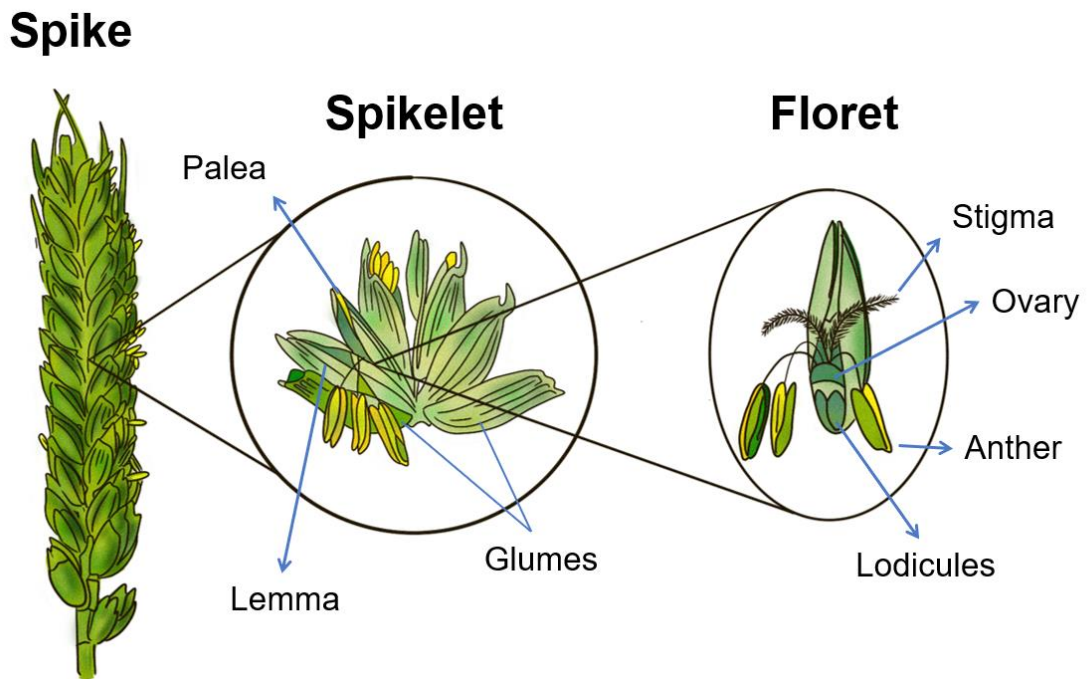


**Figure 1.7 Structure of the wheat spike.**

#### 1.4.1. The wheat stigma

The angiosperm stigma has been functionally defined as the part of the pistil or style that receives pollen. Additionally, the receptive surface of this female reproductive organ provides the right conditions for the compatible pollen grain to germinate offering entry points for the growing pollen tube and guidance to the stylar channel (Edlund et al., 2004). Thus, the viability or receptivity of the stigma, understood as the capacity of the stigma to support pollen germination, is key for effective pollination and seed set. Alterations in any of these events may seriously disrupt, or potentially enhance, seed production. However, our mechanistic understanding of stigma biology in wheat remains limited.

At the stage of maturity (Waddington growth stage 9.5; Waddington et al., 1983), the wheat pistil consists of an ovary bearing two short (3-4 mm) stylodia branches (through which the pollen tubes grow to reach the ovule) that form a dense cluster of secondary stigma branches, which curve outwards when flowering occurs (Figure 1.8). These delicate stigmatic branches are made of four rows of elongated papilla cells with reflexed tips that provide convenient resting places for the pollen grain (Figure 1.8;

Percival, 1921). ‘Dry’ at the time of pollination (Heslop-Harrison & Shivanna, 1977), the receptive surface of the grass stigma is covered with a thin mucilaginous layer overlaid with a proteinaceous pellicle (Heslop-Harrison & Heslop-Harrison, 1980), which actively promotes compatible pollen adhesion, hydration and eventually the breaching of the discontinuous cuticle (Heslop-Harrison, 2000). In tobacco (*Nicotiana tabacum*), for example, the elimination of the stigmatic secretory zone, involved in producing the exudates, results in female sterility (Goldman et al., 1994). In Brassica, the use of acetone to remove the waxy layer and proteinaceous stigma pellicle disrupts the ability of the viable papilla cells to capture the pollen grain (Heizmann et al., 2000). These outcomes demonstrate the crucial role that the receptive zone of the floral stigma plays during the pollination process.

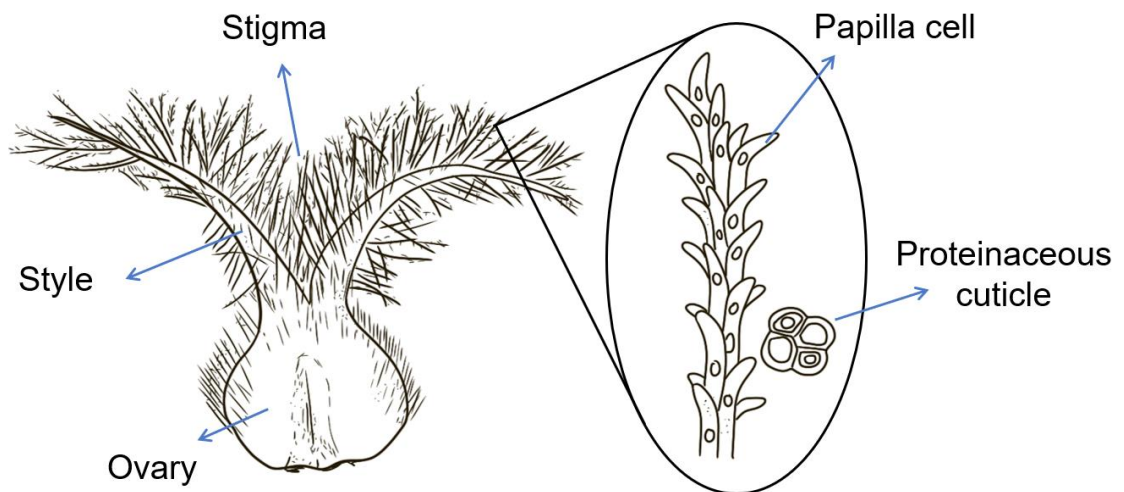


**Figure 1.8 Schematic representation of a carpel at Waddington stage 9.5.**

In wheat, previous work on stigma receptivity (measured as the percentage of seed set after cross-pollination) suggests that stigmas are receptive from anthesis holding their ability to produce seeds for around 6 to 13 days (De Vries, 1971). Imrie (1966) additionally demonstrated that stigmatic receptivity is gradually lost over time, a process that is accelerated by high temperatures. In fact, the big plasticity reported in the stigma receptive period has been attributed mainly to the influence of climatological conditions after flowering and leading to pollination. However, none or very little attention, has been given to the genetic differences between the studied genotypes (De Vries, 1971). Therefore, further investigations are needed to shed light on the genetic contribution to the already documented phenotypic variation in the duration of stigma receptivity in wheat.

#### 1.4.1.1. Developmental programme of unpollinated stigmas

A more comprehensive and integrated knowledge of the maturation and senescence process of the stigma is still lacking in wheat, principally due to the passive role that has been given to this floral organ in self-pollinating crops. To date, all the published scales and scoring methodologies describing floral morphogenesis in wheat end once pollination takes place (upper part of Figure 1.9; Waddington et al., 1983; Zadoks et al., 1974). After successful pollination, a series of developmental events sets in, leading to longitudinal growth of the ovary and a rapid degeneration of the stigma (Z71, Z73 and Z77 in Figure 1.9). Nonetheless, the senescence of the stigma can also be triggered in the absence of pollination. It is a tightly regulated process that can range from mere hours to several weeks depending on the species (Carbonell-Bejerano et al., 2010; Gao et al., 2018; Šimášková et al., 2022; Williams, 1965).

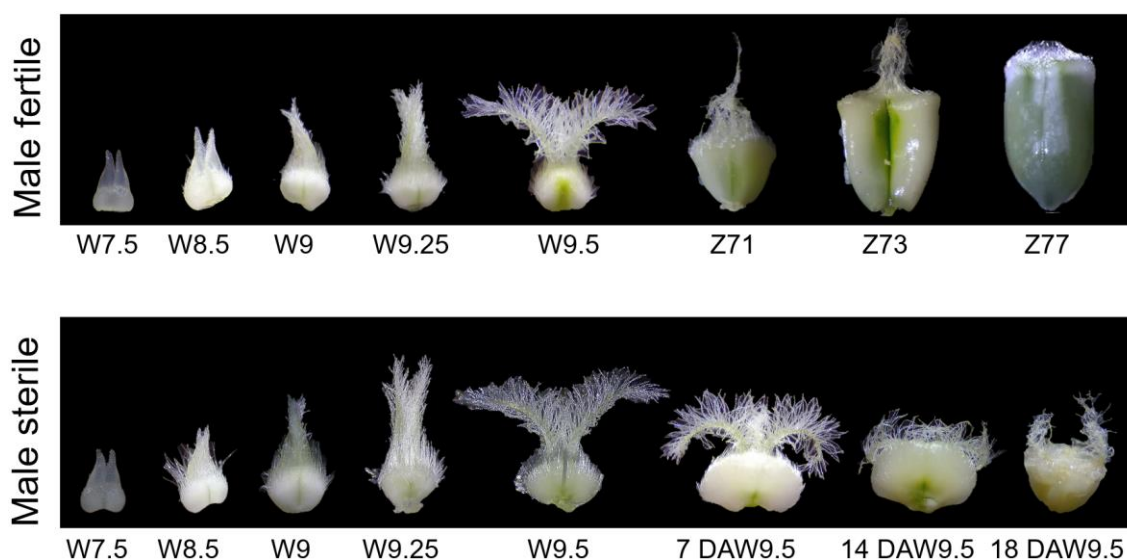


**Figure 1.9 Stigma development and degeneration of male fertile and sterile wheat plants.**

In the upper row a quantitative scale is provided based on previously published scales (W: Waddington; Z: Zadoks). In contrast, no scale has quantitatively nor qualitatively described the progression of changes the stigma experiences in the absence of pollination. DAW9.5: Days After Waddington 9.5. Images not to scale.

This idea is supported by a study in *Arabidopsis* (*Arabidopsis thaliana*) which demonstrated that the functional life span of the unpollinated, and viable, stigma is partly terminated by the execution of a highly regulated programmed cell death (PCD) process (Figure 1.10; Gao et al., 2018). Two NAC transcription factors, *KIRAI* (*KIR1*, *ANAC074*) and *ORESARAI* (*ORE1*, *ANAC092*), were identified to promote the



expression of PCD-associated genes, leading to the abortion of stigma functions. However, the observed increment in the stigma life span of *ore1kir1* mutants was only accompanied by a minor extension of the seed set rate (Gao et al., 2018), which suggests that suppressing PCD is not sufficient to maintain full papilla functionality and that additional processes must be involved in controlling the duration of floral receptivity.

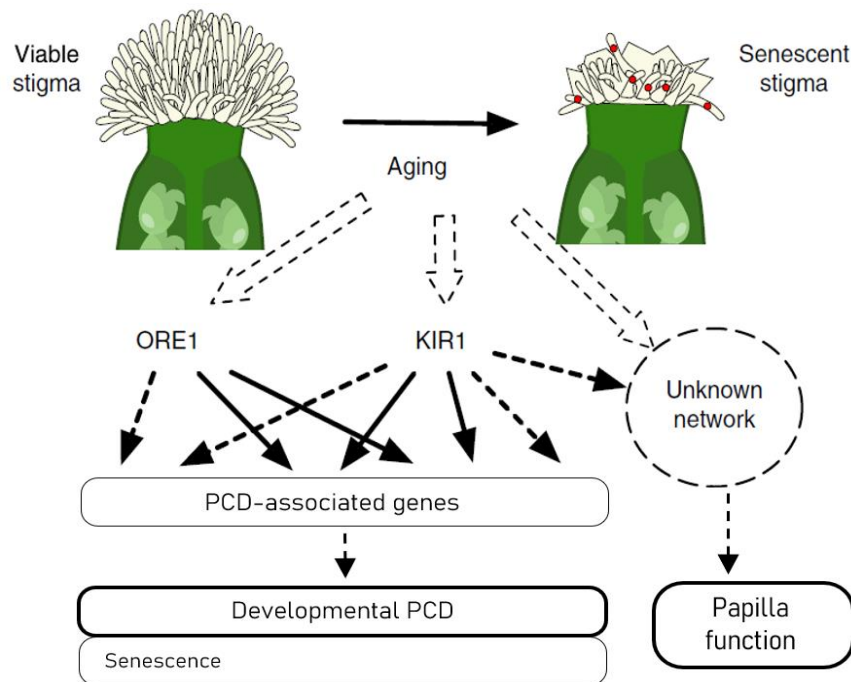


**Figure 1.10 Regulatory network of stigma life span in Arabidopsis.**

During stigma senescence the NAC TFs ORE1 and KIR1 activate downstream genes to promote PCD. Concurrently, KIR1, ORE1 and additional TFs end stigma function through an unknown network. Image modified from Gao et al., (2018).

Identifying the genetic factors controlling the mechanisms of stigma receptivity and senescence in wheat could offer new opportunities for breeders seeking to extend the receptivity of stigma to pollen. The quest to decipher genetic and physiological processes involved in the development of the unpollinated stigma benefits from the diverse range of genetic and bioinformatics tools now available for wheat (Adamski et al., 2020). Additionally, the implementation of innovative phenotyping approaches, such as machine learning, further facilitates the rapid and accurate study of plant traits in large-scale breeding experiments (Pound et al., 2017). The use of deep learning techniques for image-based plant phenotyping is further discussed in Chapter 2.

## 1.5. Wheat genomic resources

Around 9,000 years ago, hexaploid bread wheat originated from the hybridisation of emmer wheat, a domesticated tetraploid progenitor (genome AABB), and *Aegilops tauschii*, the diploid donor of the D subgenome (Levy & Feldman, 2022). This hybridisation resulted in each gene typically existing as three copies (A, B, and D), each comprising seven chromosomes. Known as homoeologous genes, these closely related copies display an average sequence similarity of 96-98% across their coding regions and generally maintain a highly conserved gene structure. The large (16 Gbp) and highly (>85%) repetitive nature of the wheat genome has historically imposed limitations on genomic resources until recent advances in sequencing technologies and bioinformatics tools. These advancements have significantly expanded the resources available for genomic analysis in wheat (reviewed in Adamski et al., 2022). The resources most relevant to this thesis are detailed below.

The most widely used assembly of hexaploid wheat, called RefSeq v1.0, is a chromosome-level genome assembly annotated with high and low confidence gene models that resulted in the RefSeq v1.1 gene model set (Appels et al., 2018). Recently, in 2021, an improved reference genome assembly (RefSeq v2.1) was released (Zhu et al., 2021). This update was accompanied by a new annotation (RefSeq v1.2) that incorporated a small set of novel genes and microRNAs alongside an increment in the annotation of transposable elements (Zhu et al., 2021). The integration of the RefSeq v1.0 assembly and RefSeq v1.1 gene models into the open-access genome browser Ensembl Plants (<https://plants.ensembl.org>) additionally provided a fast and accurate way for the identification of putative wheat orthologs of a particular gene (Bolser et al., 2015; Howe et al., 2020). Simultaneously, the decreasing cost of next generation sequencing tools has fuelled a significant surge in the generation and publication of wheat RNA-Seq data. Expression browsers, such as the expVIP database ([www.wheat-expression.com](http://www.wheat-expression.com); Borrill, Ramirez-Gonzalez, & Uauy, 2016), aim to aggregate and collectively analyse this expanding pool of public datasets. Currently, expVIP integrates expression data from 36 studies comprising 1,016 RNA-Seq datasets aligned to the RefSeq v1.1 transcriptome reference. These datasets span a diverse array of tissues, developmental stages, cultivars, and environmental conditions, which facilitates the examination and comparison of gene expression profiles. This type of analysis can be extremely helpful, especially when ranking candidate genes for further investigation. After identification of a candidate gene, several resources can now be used in wheat to

aid the functional characterisation and validation. One relevant tool for this PhD is the exome-sequenced TILLING (Targeting Induced Local Lesions in Genomes) mutant population, featuring 1,200 hexaploid (*cv.* Cadenza) EMS mutagenised lines (Krasileva et al., 2017). Exome capture followed by Illumina sequencing was conducted on these lines. Further comparison to RefSeqv1.1 gene models allowed for the detection of EMS-induced mutations and *in silico* prediction of their effects. This powerful resource enables the swift identification of novel mutations in a gene of interest. Alongside induced variation approaches like TILLING and genome editing, exploring natural variation resources, such as the pangenome, wild wheat relatives, and bi-parental populations, provides additional avenues for functional genomics in wheat. The resources outlined in this section represent just a glimpse of the remarkable expansion in tools for conducting genomic analyses in wheat, primarily propelled by recent advancements in available reference sequences (Adamski et al., 2020).

## 1.6. Thesis aims

The overall aim of this thesis is to explore the mechanisms underlying stigma development and senescence in the absence of self-pollination. Specifically, this thesis will address the following questions:

1. Is there a defined developmental programme for wheat stigmas in the absence of pollination? And if so, is there phenotypic variation for this trait? To answer these questions, Chapter 2 introduces the implementation of a scalable phenotyping method to investigate the development of the unpollinated stigma, focusing on its phenotypic diversity under field conditions.
2. It is widely accepted that the short duration of stigma receptivity continues to be a limiting factor for the efficiency of hybrid seed production, however, is this the case? To understand the extent of this limitation, Chapter 3 investigates the time span during which cross-fertilisation and seed set can occur among different male sterile cultivars under field conditions.
3. Finally, building on the genetic regulation documented for stigma senescence in *Arabidopsis*, we asked: Are the mechanisms governing the deterioration of the unpollinated wheat stigma similarly controlled by a set of endogenous biological processes? If so, what are these processes, and is it possible to manipulate them genetically? Chapter 4 explores the genetic regulation of stigma development

and survival using transcriptomics to unveil molecular insights, followed by the functional characterisation of candidate genes *KIR1* and *ORE1*.

This thesis seeks to offer breeders and researchers a new framework for advancing mechanistic insights into female fertility in wheat, thereby laying the groundwork to improve hybrid wheat seed production.

## **2. A scalable phenotyping approach for female floral organ development and senescence in the absence of pollination in wheat**

All results described in this chapter are part of the following publication (Appendix A): Millan-Blaquez, M., Hartley, M., Bird, N., Manes, Y., Uauy, C., & Boden, S. A. (2022). A scalable phenotyping approach for female floral organ development and senescence in the absence of pollination in wheat. *Development*, 149(18), dev200889.

### **2.1. Summary**

In the absence of pollination, female reproductive organs senesce leading to an irrevocable loss in the reproductive potential of the flower, directly affecting seed set. In self-pollinating crops like wheat (*Triticum aestivum*), the post-anthesis viability of the unpollinated carpel has been overlooked, despite its importance for hybrid seed production systems. To advance our knowledge of carpel development in the absence of pollination, we created a relatively high-throughput phenotyping approach to quantify stigma and ovary morphology. We demonstrate the suitability of the approach, which is based on light microscopy imaging and machine learning, for the detailed study of floral organ traits in field grown plants using both fresh and fixed samples. We also show that the unpollinated carpel undergoes a well-defined initial growth phase, followed by a peak phase (in which stigma area reaches its maximum and the radial expansion of the ovary slows), and a final deterioration phase. These developmental dynamics were largely consistent across years and could be used to classify male sterile cultivars. This phenotyping approach provides a new tool for examining carpel development which we hope will help advance research into female fertility in wheat.

## 2.2. Introduction

The fertilisation of the pistil by a pollen grain is a vital event in the life cycle of a flowering plant as it contributes to the reproductive fitness of a species. In grasses, the pistil (or carpel) typically consists of an ovary bearing two styles densely covered by a feathery and dry-type stigma (Heslop-Harrison & Shivanna, 1977; Walker, 1906). The stigmatic tissue plays a key role in successful fertilisation as it facilitates the interception and hydration of the pollen grain and mediates pollen tube growth into the stylodia branches towards the ovary containing the ovule (Edlund et al., 2004; Heslop-Harrison, 1979). After successful fertilisation, the ovary undergoes growth and differentiation to develop into a grain. Under favourable growing conditions, the duration of carpel receptivity (or functionality) does not present a serious limitation to seed formation in self-pollinating species, such as wheat (*Triticum aestivum*) or rice (*Oryza sativa*). However, environmental stresses such as heat and drought (Fábián et al., 2019; Mitchell & Petolino, 1988; Onyemaobi et al., 2017) or the absence of viable pollen (e.g., male sterile cultivars used in hybrid breeding (Kempe & Gils, 2011)) can affect normal seed set.

Female floral organs have developed a series of survival mechanisms to secure seed set in the absence of self-pollination by increasing the likelihood of receiving pollen from neighbouring male fertile plants. Indeed, this process (directly or indirectly) has been harnessed by breeders to produce hybrid seeds in crops like maize (*Zea mays*), rice, barley (*Hordeum vulgare*), and wheat. In maize, one of the survival strategies described to increase pollen capture is silk (i.e., stigma) emergence and elongation from the husk (Bassetti & Westgate, 1993), while in wheat, the radial expansion of the unfertilised ovary pushes the floret open facilitating the access to airborne pollen, a phenomenon known as the ‘second opening’ (Molnár-Láng et al., 1980; Okada et al., 2017). However, if pollination still does not occur after a specific time, which varies between species (Ashman & Schoen, 1994; Primack, 1985), a series of developmental processes leads to the senescence of the floral organs and the irreversible loss of reproductive potential (Carbonell-Bejerano et al., 2010). For example, in several plants, the loss of papilla integrity has been regarded as one of the primary symptoms indicating the end of the floral receptive period and stigma senescence which is often manifested by the shrunken appearance of the stigma (Gao et al., 2018; González et al., 1995; Okada et al., 2017). These senescence processes are coordinated by transcription factors, including

*KIRAI (KIRI)* and *ORESARAI (OREI)* in *Arabidopsis* (Gao et al., 2018). Similarly, the unfertilised ovary undergoes a series of morphological changes that converges in the lignification of the epidermal cells and eventual collapse of the ovary walls (Carbonell-Bejerano et al., 2010; Okada et al., 2017). In many of these studies, the phenotypic characterisation of these processes is time-consuming and labour intensive and is, therefore, usually performed only under controlled growing conditions and on a small number of plants. These phenotyping approaches, although extremely informative, are often not conducive for translation into breeding targets where the screening of large germplasm sets is required.

In recent years, high-throughput phenotyping technologies have provided new opportunities to phenotype a diverse range of plant species at various scales, ranging from cellular to tissue and organ levels (Furbank & Tester, 2011; Pieruschka & Schurr, 2019). For instance, machine learning based algorithms, like neural networks, have become an essential tool for reliably extracting morphological information and providing visual quantitative parameters of microscopy images. These approaches can be used in large-scale experiments, like those of crop breeding programmes, and provide a way to quantify the morphological changes of the developing carpel in the absence of pollination.

To advance our knowledge of carpel development in the absence of pollination, we developed a phenotyping approach for the quantification of stigma area and ovary diameter of field grown plants by combining light microscopy and machine learning. We focused on bread wheat carpels due to the current need to improve outcrossing rates in hybrid breeding programmes (Selva et al., 2020) and the lack of knowledge on the dynamics of stigma and ovary development among male sterile (MS) wheat cultivars under production conditions in the field. We applied our phenotyping approach to three MS cultivars during two consecutive field seasons to gain insights into genetic and environmental variation for these two floral traits and show that it is scalable to produce practical advances in breeding programmes.

## 2.3. Materials and Methods

### 2.3.1. Germplasm

We used both spring and winter male sterile hexaploid wheat (*Triticum aestivum*) cultivars derived from commercial inbred lines. Cytoplasmic and nuclear male sterility (CMS and NMS) systems were used for the generation of the male sterile cultivars. BSS1 and GSS2 correspond to winter CMS cultivars while the winter cultivars 24511, 24512, 24516 and 24522, and the spring cultivars Jetstream, Alderon, BLA1, Mairra, Cadenza, Chamsin and BLA2 are NMS cultivars. All NMS and CMS cultivars were provided by KWS Ltd (Thriplow, UK) and Syngenta (Whittlesford, UK), respectively. Lines have been codified due to their commercial nature.

We used MS cultivar 24516 as an example to illustrate the developmental dynamics of the unpollinated wheat stigma and ovary in Figure 2.4. To train the convolutional neural network (CNN) for the quantification of carpel traits we used a random sample of plants extracted from a set of the seven spring NMS cultivars. The selection criteria for the generation of the training set, however, were based on diversity of carpel images rather than on a per cultivar-based criteria.

We used four winter male sterile cultivars (24511, 24516, BSS1, GSS2) to characterise the effects of the fixative on stigma area and ovary diameter during the 2020 field season. Finally, for the multi-year field experiment performed to investigate the developmental patterns of the unpollinated carpel, we grew three winter male sterile cultivars (BSS1, 24512 and 24522) during two consecutive years. We selected these three cultivars as they represent a large part of the variation observed for carpel development in the absence of pollination from an original pool of 31 MS cultivars phenotyped in 2020 under field conditions (data not shown). Table 2.1 provides a summary of all cultivars used in the experiments.



**Table 2.1 Summary of the germplasm used for each experiment described in this study.**

<b>Experiment</b>	<b>Output</b>	<b>Germplasm used</b>	<b>Growth</b>
Representative stigma and ovary growth patterns	Figure 2.4	24516	Field
Training set for the development of stigma and ovary CNNs	Trained CNNs	Jetstream, Alderon, BLA1, Mairra, Cadenza, Chamsin, BLA2	Glasshouse
Effect of fixative on stigma area and ovary diameter	Figure 2.8 and Figure 2.9	24511, 24516, BSS1, GSS2	Field
Multi-year field experiment	Figure 2.10	BSS1, 24512, 24522	Field
Stigma transcriptome	Figure 2.12B	24512	Field
Mock example provided to run "Stigma_area_script.R"	Appendix A	24524, GSS2	Field

### 2.3.2. Glasshouse and field experiments

For the development of the stigma and ovary CNNs we grew between 10 to 20 plants per MS cultivar (Jetstream, Alderon, BLA1, Mairra, Cadenza, Chamsin and BLA2) in the glasshouse in 1 L pots under long day conditions (16 h light: 8 h dark) and hand dissected carpels from either the first, second or third tiller at various timepoints representative of the different carpel morphologies. We stored a random selection of the dissected carpels in a fixative solution of 95% ethanol and absolute acetic acid (75% v/v) and kept them at 4 °C until image acquisition (approx. a month after fixation). The cultivars selected are representative of carpel morphology diversity in wheat germplasm.

For the carpel development time course experiments, we grew plants at John Innes Centre Church Farm (Bawburgh, UK; 52°37'50.7" N 1°10'39.7" E) in a randomised complete block design with two replicates (1 m plots) per MS cultivar in 2020, and three replicates in 2021 (Figure 2.1). Number of replicates were chosen according to traditional use in field experiments and seed availability. To avoid unwanted cross-pollination, sterile rye barriers were grown surrounding the male sterile plots. To record environmental data, we placed data loggers (EasyLog USB, Lascar Electronics) next to the experimental plots at 50 cm height. Average temperature and relative humidity were measured every hour during the duration of the experiment (Figure 2.2).

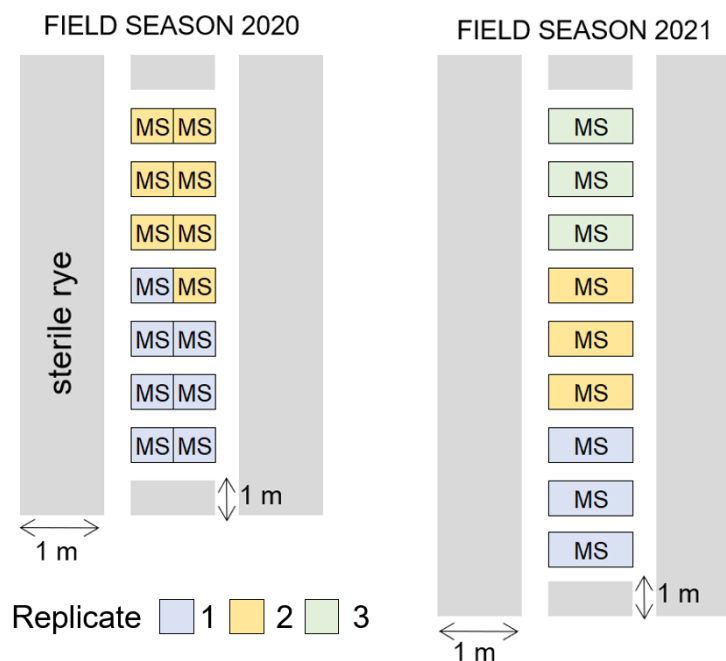


**Figure 2.1 Schematic representations of the field layout.**

Male sterile (MS) cultivars were grown surrounded by a continuous stripe of sterile rye that was used as pollen barrier. Plots were replicated twice in 2020 (N = 2) and 3 times in 2021 (N = 3).

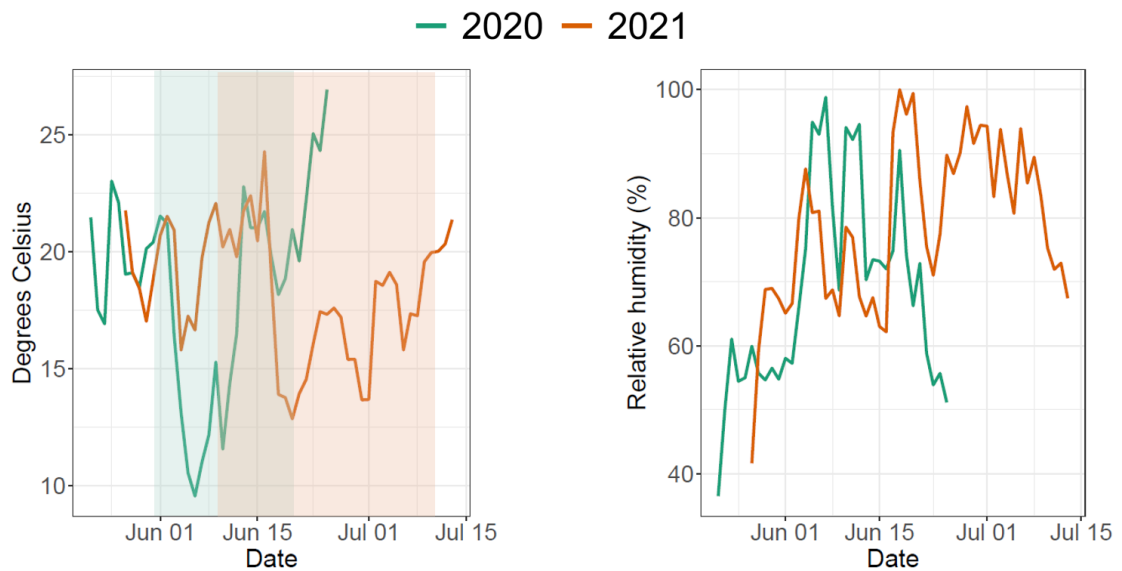


**Figure 2.2 Environmental conditions recorded during 2020 and 2021 field seasons.**

Left panel illustrates mean daily temperatures in degrees Celsius recorded during both field experiments (2020: green line; 2021: orange line). Shaded rectangles indicate the beginning and end of 2020 and 2021 time courses. Right panel shows the water vapor contained in the air expressed in percentage of relative humidity.

In both field seasons, we tagged main spikes when carpels in the outer florets (florete 1 and 2) of central spikelets reached Waddington stage 9.5 (W9.5; Waddington et al., 1983). This is shortly after full ear emergence (Zadoks' growth stage 59; Zadoks et al., 1974). At the time of sampling, we cut individual tillers between the uppermost and penultimate internode and transported them in water to the laboratory for carpel dissection. We harvested four to seven carpels from the outer florets of central spikelets from two spikes per plot and timepoint. These timepoints were W9.5 and 3, 7, 13 and 18 days after W9.5 (DAW9.5), with the only exception that the 2021-time course was extended for 9 more days (i.e., 27 DAW9.5) in cases where the carpel was not completely senesced at 18 DAW9.5. Due to the limited availability of spikes tagged at W9.5, sample size for the extended timepoints varied from 2 to 6 spikes per timepoint. Carpels that needed fixation were placed in 2 mL Eppendorf tubes containing fresh fixative solution, as described above.

### 2.3.3. Image acquisition and manual annotations

To generate the training set we used two different stereo microscopes equipped with an integrated camera for image capture (ZEISS Stemi 305 with a 1.2 Megapixel integrated

colour camera; Leica MZ16 coupled with a Leica CLS100x white light source and a Leica DFC420 5 Megapixel colour camera). For the downstream experiments using the adapted CNNs we only used the ZEISS Stemi 305 since it is easier to operate and to transport to the field. Depending on the size of the carpel, we used different magnifications (from 1x to 4x) to ensure that the complete carpel was captured in the image (Figure 2.3). We adapted illumination and time of exposure to each image to ensure high contrast between the carpel and the black background. To maintain the feathery structure of the stigma in fixed samples, we imaged the carpels submerged in a 70% ethanol solution using a Petri dish (one carpel per image). Images were saved as RGB jpeg files.

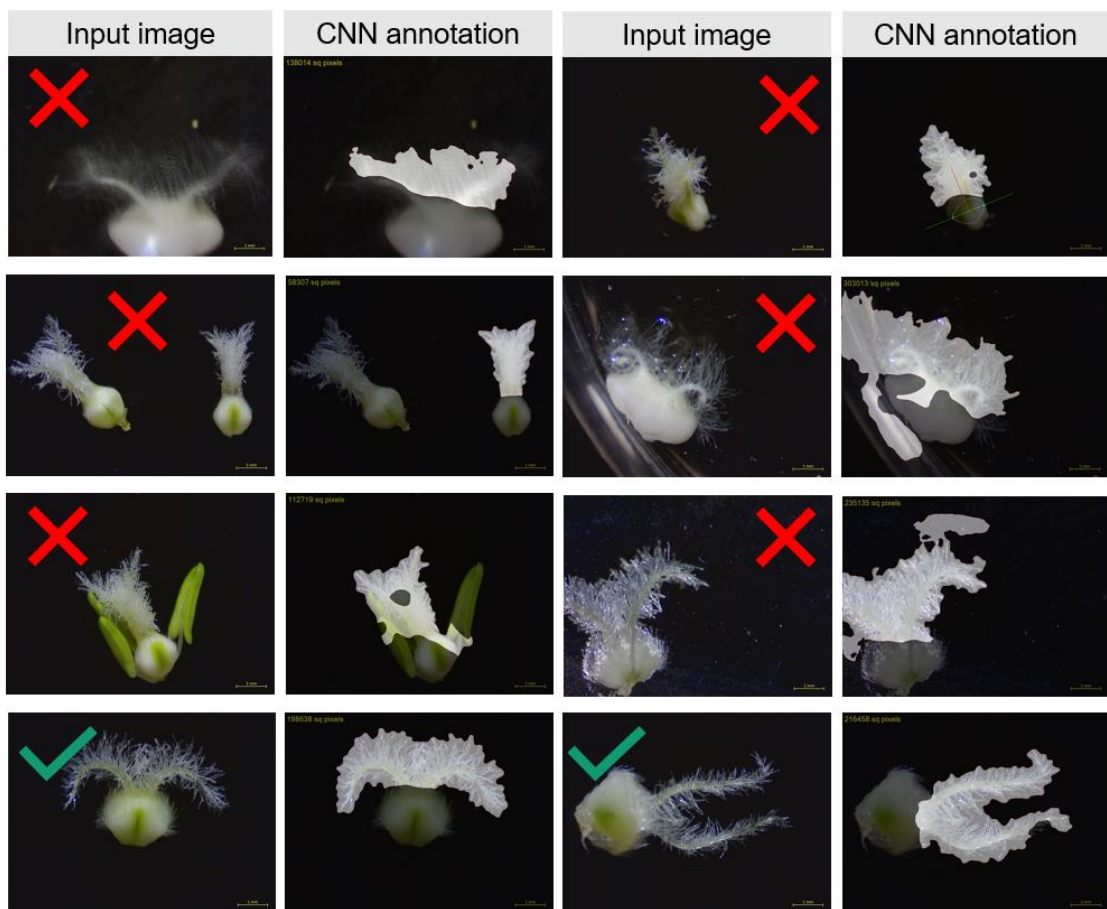


**Figure 2.3 Unaccepted and accepted carpel images.**

Representation of images (jpeg format) unlikely to be correctly annotated by either the stigma CNN or ovary CNN (red crosses, e.g., blurry, or out of focus images, lifted carpels, presence of other objects, etc.) and example of images the stigma and ovary CNNs expect and would be able to annotate accurately (green ticks).

To evaluate the effect of the fixative on carpel morphology traits, we first imaged the carpels as non-fixed samples, and we then placed them in the fixative solution (as described previously) for image acquisition at a later time. For manual annotations of stigma and ovary perimeters, we analysed the resulting images using open-source image processing package Fiji.

#### 2.3.4. Development of stigma and ovary CNNs

To carry out automated image annotation and measurement, we trained a CNN using the U-Net design which can be easily adapted to new tasks with only few annotated images (Falk et al., 2019). The network was implemented in the PyTorch framework (Paszke et al., 2019), using the dtoolAI library (Hartley & Olsson, 2020). The networks were trained on carpel jpeg images with manual annotations of the stigma perimeter ( $n = 86$  images) and ovary perimeters ( $n = 121$  images). These 207 images were randomly selected from a total of 1601 dissected carpels. The Dice coefficient (Dice, 1945) was used as a loss function, and weight updates were applied using the Adam optimizer (Kingma & Ba, 2014).

The trained stigma network predicted a mask corresponding to the stigma location for each RGB input image. The stigma mask was used to calculate the stigma area directly by extracting the number of pixels. The trained ovary network predicted two masks for each RGB input image, one corresponding to the ovary location and the other to the stigma location. To determine the ovary diameter, the following algorithm was applied:

1. Determine the centroid of the predicted stigma mask.
2. Determine the centroid of the predicted ovary mask.
3. Take the perpendicular to the line drawn through the centroids.
4. Determine the two points where this line crosses the border of the predicted ovary mask.
5. Measure the length of this line, converting to physical units from the original input image scale.

We converted pixels (CNN output) to stigma area ( $\text{mm}^2$ ), and ovary diameter (mm) according to the scale bar used in each image. Implementation scripts and training data

are available at [https://github.com/Uauy-Lab/ML-carpel\\_traits](https://github.com/Uauy-Lab/ML-carpel_traits) and [https://opendata.earlham.ac.uk/wheat/under\\_license/toronto/Millan-Blanquez\\_et\\_al\\_2022\\_machine-learning-carpel-traits/](https://opendata.earlham.ac.uk/wheat/under_license/toronto/Millan-Blanquez_et_al_2022_machine-learning-carpel-traits/), respectively.

### 2.3.5. Statistical analyses and data visualisation

#### 2.3.5.1. *Evaluation of CNN performance*

To evaluate differences in stigma area and ovary diameter between the manual and CNN annotations, we selected a random set of 60 microscopy images that were not used to train the networks (30 images of fixed carpels and 30 of non-fixed carpels). We divided the images into three different developmental stages based on the appearance of the carpel to account for all the possible carpel morphologies the algorithm could be exposed to. Stage 1 represents a young carpel (stigma and ovary still developing), stage 2 represents a fully developed carpel (widely spread stigma and enlarged ovary), and stage 3 includes visibly deteriorated carpels. We performed one-way analysis of variance (ANOVA) for each trait and sampling method, including “floral age” as the single factor (Table 2.2). To measure the spatial overlap between the manual and CNN annotation, we calculated Dice similarity coefficients on the same set of images.

#### 2.3.5.2. *Carpel development time courses*

For the quantification of stigma area and ovary diameter of fixed and non-fixed samples, a total of 666 and 634 images were annotated by the stigma CNN and ovary CNN, respectively, and used for subsequent analyses. We conducted three-way ANOVAs (fixative, timepoint, cultivar) to test the effect of the fixative on stigma area and ovary diameter and their interaction with floral age (timepoint) and cultivar (Table 2.3). We include in the model block and spike information as random effects to account for the nested nature of the experimental design. Tukey’s multiple comparison method was used to adjust for multiple comparisons.

To generate the patterns describing stigma and ovary development for MS cultivars 24512, 24522 and BSS1, 294 and 520 images were annotated by the stigma and ovary CNNs, in 2020 and 2021, respectively, and used for downstream analyses. Next, we filtered out outliers following the interquartile range criterion and used loess smooth lines with a span value of 0.9 (i.e., width of the moving window when smoothing the data) and a 95% confidence interval. To have an estimate of the amount of growth the

plants achieved during the different field seasons we calculated cumulative degree days using 0 °C as base temperature (according to (Miller et al., 2001) and average daily temperatures as follows:

$$\text{Cumulative degree days} = \sum_{i=0}^j (\text{mean Temp}) - \text{Base Temp}$$

*i*: beginning of the temporal window considered (e.g., W9.5 date)

*j*: end of the temporal window considered (e.g., sampling date at 7 days after W9.5)

Codes to model carpel and ovary development were conducted in RStudio Version 4.0.3 and are available at: [https://github.com/Uauy-Lab/ML-carpel\\_traits](https://github.com/Uauy-Lab/ML-carpel_traits). Image data used for the statistical analyses (i.e., one-way and three-way ANOVAs provided in Table 2.2 and 2.3, respectively) also available at:

[https://opendata.earlham.ac.uk/wheat/under\\_license/toronto/Millan-Blanquez\\_etal\\_2022\\_machine-learning-carpel-traits/](https://opendata.earlham.ac.uk/wheat/under_license/toronto/Millan-Blanquez_etal_2022_machine-learning-carpel-traits/). Detailed step-by-step instructions are provided in Appendix A.

### 2.3.6. Stigma transcriptome analysis by RNA-seq

During the 2021 field season, we used MS cultivar 24512 to investigate the expression patterns of senescence-related genes in the stigmatic tissues. We collected stigma samples at four developmental timepoints spanning the proposed growth, peak and deterioration phases (3, 7, 13 and 18 DAW9.5). We sampled plants between 11:00-15:00 and dissected five to eight stigmas (size dependent) from the primary and secondary florets of the central four spikelets. We stored stigmas in DNA/RNA Shield solution (ZYMO Research Cat. R1100-50) at -20 °C. The stigma samples include both the stigma and style as these structures are intimately linked in wheat.

We extracted RNA from three independent biological replicates. RNA was extracted using TRIzol/Chloroform (TRI Reagent® (Sigma-Aldrich); Chloroform, >= 99.8% (Fisher Scientific)) and purified using the RNA Clean and Concentrator kit (ZYMO-Research, Cat. R1013) as specified in <https://dx.doi.org/10.17504/protocols.io.36wgq7kj3vk5/v1>. RNA quantity and quality were assessed by spectrophotometric analysis (NanoDrop™ One/OneC; Thermo) and by agarose gel electrophoresis. Total RNA samples with a quality value greater than an

RNA integrity number (RIN) of 6 were used for Illumina HiSeq 150-bp paired-end sequencing (Novogene).

RNA-seq data were pseudoaligned to the wheat RefSeqv1.1 transcriptome (Appels et al., 2018) using kallisto (Bray et al., 2016). We filtered for genes expressed on average  $> 0.5$  transcripts per million (TPM) in at least one of the timepoints to exclude low expressed genes (consistent with Ramírez-González et al., 2018). TPM values were normalised across the four timepoints for each gene.



## 2.4. Results

### 2.4.1. Defining quantifiable parameters of late carpel development and senescence

To investigate the development of wheat carpels in the absence of pollination and determine parameters that correlate with key phases of its life cycle, we used nuclear and cytoplasmic male sterile plants. We imaged the unpollinated carpels of field-grown plants starting from Waddington stage 9.5 (W9.5, normally shortly after ear emergence; Figure 2.4A) which corresponds with the most advanced developmental stage for an unpollinated carpel; W9.5 is only shortly before when male-fertile plants would reach anthesis (at W10) and release viable pollen on the receptive stigma surface. At W9.5, stigma branches are well elongated and spread outwards to generate the plumose architecture, while the unfertilised ovary shows a round shape (Figure 2.4A). In subsequent timepoints after W9.5, the unfertilised ovary will gradually expand horizontally leading to the “second opening” of the floret (as previously described by Molnár-Láng et al., 1980; Okada et al., 2017). During this period of ovary growth, stigma branches continue growing and quickly curve away from each other, increasing the stigma surface area and contributing to the extrusion of unpollinated stigma outside the floret and thus, to the capture of airborne pollen. Towards the end of the time course, papilla cells of the stigma hairs start to lose turgor and become atrophied as the stigma degenerates (Figure 2.4A, red arrowheads). Finally, the onset of stigma degeneration is followed by a slight and gradual decline in ovary radial size, causing the floret to close again (Molnár-Láng et al., 1980).

To quantify the observed morphological changes in these parameters, we imaged unpollinated carpels and manually delineated the area covered by the stigma hairs and the diameter of the ovary using Fiji (Figure 2.4B). We distinguished a developmental pattern for stigma area characterised by an initial bell curve shape followed by a gradual reduction in area indicative of tissue deterioration. The ovary diameter gradually increased and reached a plateau with little changes in the diameter thereafter (Figure 2.4C). More importantly, these patterns appear to be quite consistent across different cultivars and replicates (see Results below). Together, these findings suggest that stigma area and ovary diameter are promising parameters to quantitatively track the life cycle of the unpollinated carpel.

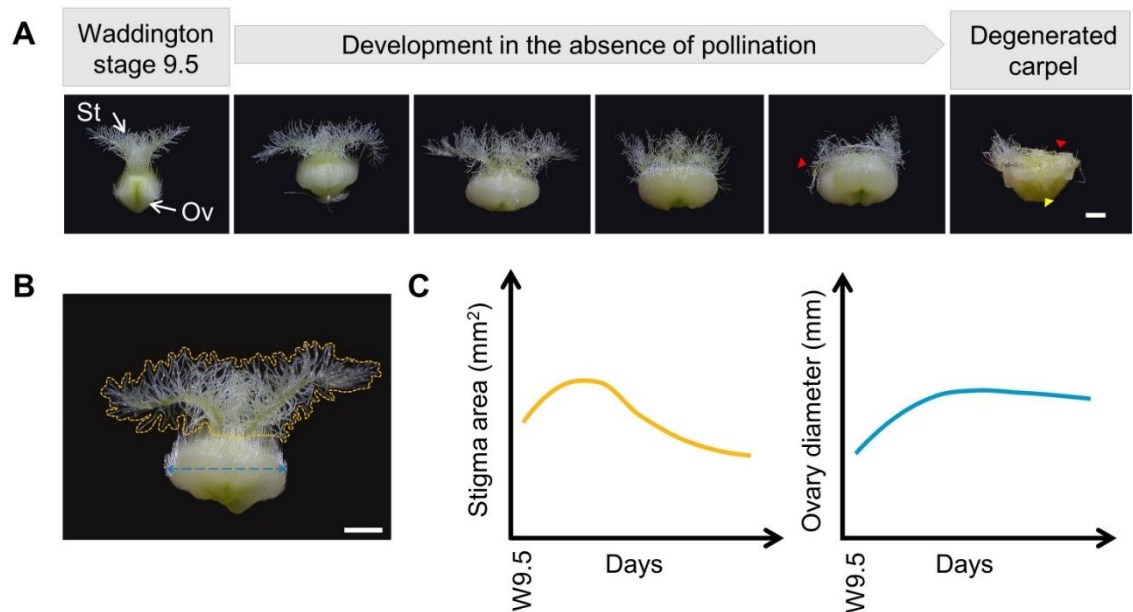


**Figure 2.4 Representative stages of late carpel development in the absence of pollination.**

(A) Morphological changes observed in the stigma (St) and ovary (Ov) from Waddington stage 9.5 (approx. ear emergence) until complete degeneration of the carpel (from left to right). Arrowheads indicate regions of the stigma (red) and ovary (yellow) where symptoms of cell degeneration are visible. (B) Diagram illustrating the morphological traits of interest: the yellow line delimits the area covered by the stigmatic hairs, the blue line depicts the diameter of the ovary. (C) Representative growth trends observed for the stigma hair area (yellow) and ovary diameter (blue) in the absence of pollination for field grown plants. For the regression curves we have used a single exemplar male sterile cultivar ( $n = 10\text{-}30$  carpels sampled from a total of 6 plants per timepoint. Total of 8 timepoints). In A and B, scale bar = 1 mm.

#### 2.4.2. Overview of the approach

The rapid and accurate phenotyping of large numbers of field-grown plants represents a challenge for plant researchers. Here, to accelerate research into female floral traits, we propose a phenotyping approach that can be implemented in the screening of large populations, such as those of pre-breeding programmes (Figure 2.5). This approach provides a visualization and quantification toolbox for morphometric information of stigma area and ovary diameter. A summary of each step is provided below, and detailed descriptions can be found in the Materials and Methods section.

##### 2.4.2.1. *Experimental design, sample collection and image acquisition*

As our main aim was to study carpels in the absence of pollination, the first step is to prevent cross-pollination of MS plants in the field. To achieve this, different strategies can be used. For example, in this study we grew sterile rye surrounding the experimental plots to create an effective pollen barrier from surrounding fertile plants (Figure 2.5A and 2.1). When anthers from the outer florets of the central spikelets are

turning yellow and stigmatic branches are starting to spread outwards (W9.5), we tag spikes to indicate the beginning of the time course. Depending on the location and scale of the experiment, logistical issues such as transport and preservation methods also need to be considered at the time of sampling. For sample collection, we carefully dissect wheat carpels from central spikelets in the field, which can be performed by eye as they are relatively large (Figure 2.5B). Alternatively, we cut individual tillers between the uppermost and penultimate internode and transport them in water to the laboratory for carpel dissection. Once dissected, we store the carpels in 95% ethanol and acetic acid (75% v/v) for image acquisition at a later timepoint, or fresh (non-fixed) specimens are imaged directly if tillers have been transported to the laboratory. We use a stereo microscope with an integrated camera to acquire the two-dimensional RGB image of the carpel against a black background (Figure 2.5C). We use different magnifications and fields of view to help capture the best representative plane of the carpel (Figure 2.3). In the case of the fixed samples, we place carpels in a Petri dish with 70% ethanol to preserve the feathery appearance of the stigma. Only one image per sampled carpel is required for subsequent steps.

#### *2.4.2.2. Annotation of microscopy images and quantification of carpel traits*

To process and perform quantitative analyses of the microscopy images, we trained a machine learning (ML)-based algorithm to automatically and rapidly annotate and measure stigma area and ovary diameter (Figure 2.5D). The trained networks return a set of annotated images alongside their shape descriptors, together with a csv file containing the measurements of the analysed images in an output folder (see Appendix A for a step-by-step guide on how to use the trained networks). This step requires some manual curation whereby the user inspects, detects, and corrects annotation errors, or removes corrupted images (Figure 2.5E).

#### *2.4.2.3. Data modelling and knowledge transfer*

We developed code to model growth dynamics of stigma area and ovary diameter (Figure 2.5F). The open-access customizable R scripts (see Appendix A) can produce a range of outputs to compare genotypes, environmental conditions, or specific developmental stages, thereby helping to generate new hypotheses. Additionally, the exploitation of the knowledge generated could be key in the progress towards

establishing successful hybrid breeding programmes as the selection of MS cultivars will be now based on novel phenotypic information.

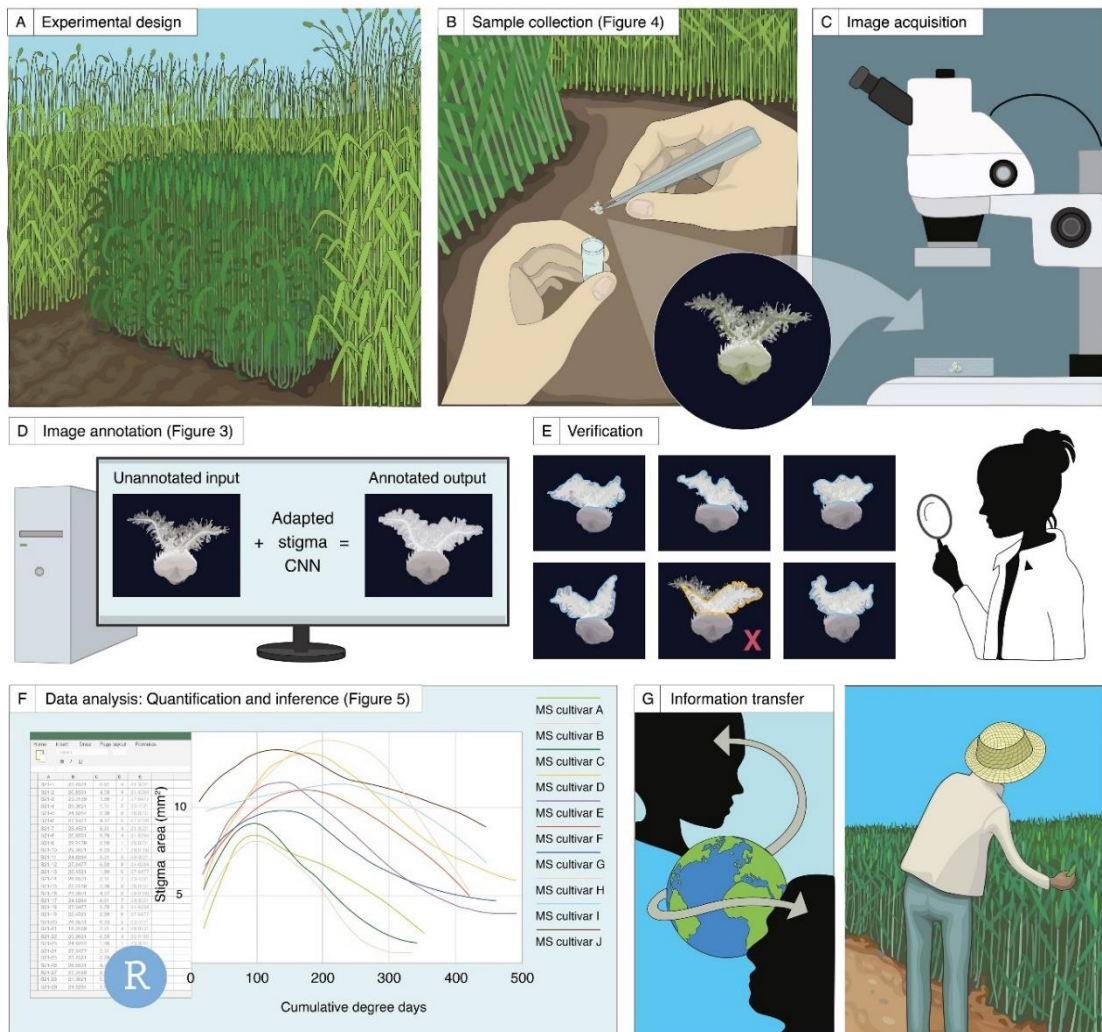


**Figure 2.5 Schematic representation of the proposed phenotyping approach for the study of carpel development in the absence of pollination under field conditions.**

(A-C) Experimental design, sample collection and image acquisition. (D-E) Annotation of microscopy images and quantification of the stigma area (as an example, D) and verification of the CNN outputs (E). (F) and (G) illustrates the applicability of the phenotyping approach to enhance our understanding of the post-anthesis behaviour of unpollinated carpels.

### 2.4.3. Development and validation of the stigma and ovary convolutional neural networks

Our aim was to develop an automated phenotyping method to detect and annotate the perimeter covered by the stigma hairs and the ovary to determine stigma area and ovary diameter across the life cycle of wheat carpels. To carry out automated image annotation and measurement, we trained a convolutional neural network (CNN) on a set

of representative carpel images with manual annotations of the stigma perimeter ( $n = 86$  images) and ovary perimeter ( $n = 121$  images) using the UNet design (Figure 2.6A; Falk et al., 2019). The training dataset spanned a random sample of seven genotypes, ranging from early carpel development (W9.5 and earlier) to fully degenerated carpels (Figure 2.4A), and included both fixed and non-fixed carpels. After successfully training the networks, we obtained an adapted stigma CNN able to quantify the area covered by stigmatic hairs and an adapted ovary CNN that, after some post-processing of the network output, quantifies the diameter of the ovary (Figure 2.6B).

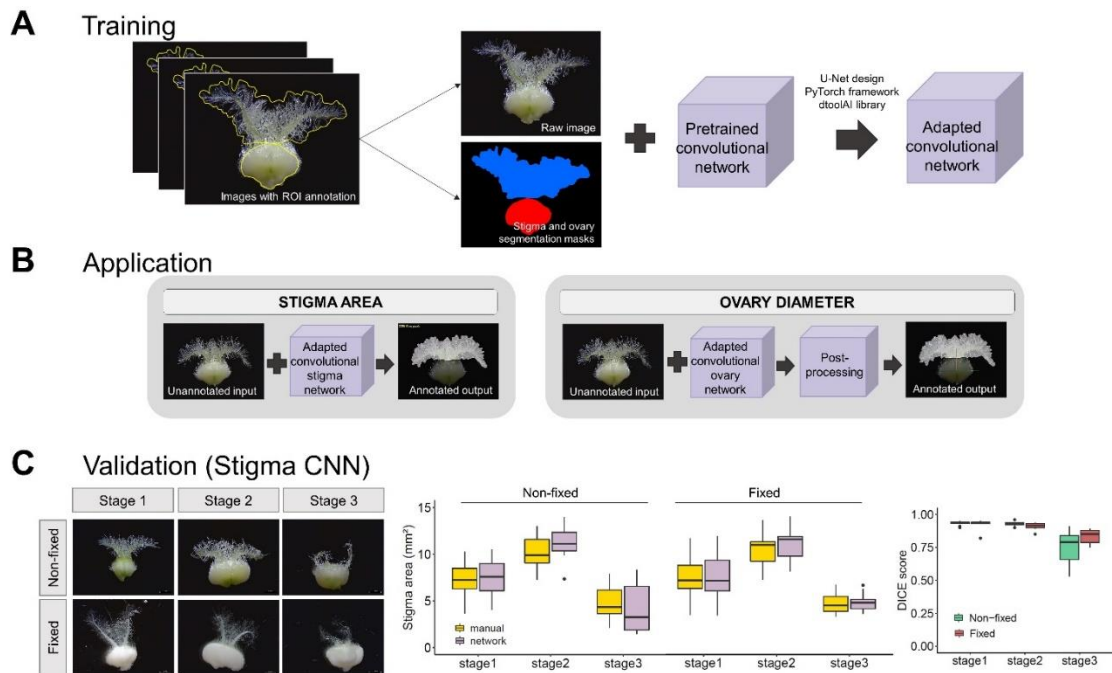


**Figure 2.6 Development and validation of convolutional neural network for stigma and ovary annotation.**

(A) Pipeline for the development of the stigma and ovary networks. (B) Application of the adapted network for stigma area annotation to new data. (C) Cross-validation of ground-truth measurements and network values extracted from 60 randomly chosen images divided into six classes according to floral age (stage) and sampling method. First box plot shows the distribution of the stigma areas in  $\text{mm}^2$  per cross-validation class ( $n = 10$  images per stage  $\times$  method combination) determined by manual (yellow) and network (grey) annotation. There were no significant differences for any of the six classes (stage  $\times$  sampling method combination). Second box plot indicates DICE scores of stigma area in non-fixed (green) and fixed (red) samples. A DICE score of 0 indicates no spatial overlap between the two sets of annotation results, 1 indicates complete overlap. The box plots show the middle 50% of the data with the median represented by the horizontal line. Whiskers represent datapoints within 1.5 times the interquartile range with outliers highlighted as individual points.

To evaluate the performance of the resulting adapted CNNs we applied the network to an unseen set of 60 microscope images without manual annotations (Figure 2.6C). Subsequently, we manually annotated this new dataset using Fiji to provide a ground truth reference with which to compare to the CNN annotated outputs. We divided the cross-validation process according to the developmental stage of the carpels, sampling method (fixed or non-fixed), and the tissue of interest (Figure 2.6C and 2.7 for ovary CNN validation). We observed a high overlap in stigma areas and ovary diameters of fixed and non-fixed samples between the manual and automated annotations across all three developmental stages. There were no significant differences between the manual and automated annotations, apart from ovary diameter of the non-fixed samples at stage 3 ( $P = 0.03$ , one-way ANOVA with Tukey's post hoc test; Table 2.2). Additionally, we calculated the Dice Similarity Coefficient (DSC) for each group of images which allowed quantitative evaluation of the performance of the adapted networks (Figure 2.6C and 2.7). Overall, we found very uniform DSC values between the ground-truth and CNN annotation across floral traits, sampling methods and developmental stages (with the exception of the stigma CNN at the last developmental stage) with DSC mean averages of 0.89 and 0.95 for the stigma and ovary CNN, respectively. Together, these results show that our machine learning approach quantifies key parameters of the carpel life cycle in wheat in agreement with the more time-consuming manual measurements.

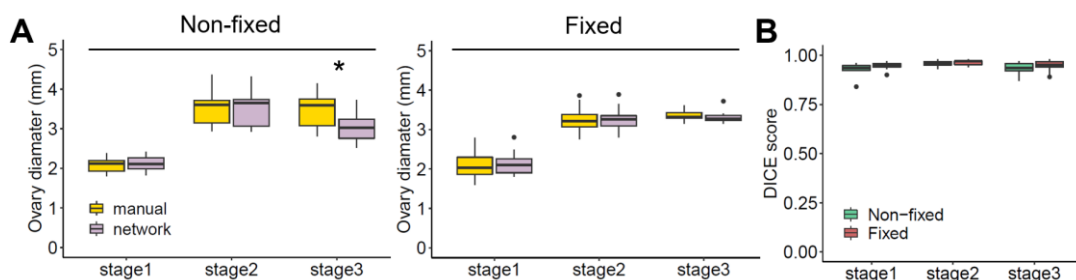


**Figure 2.7 Validation of convolutional neural network for stigma and ovary annotation.**

(A) Cross-validation of ground-truth measurements and network values extracted from 60 randomly chosen images divided into six classes according to floral age and sampling method. Distribution of the ovary diameter in mm per cross-validation class ( $n = 7-10$ ), determined by manual (yellow) and automated (violet) annotation. (B) Box plots showing Dice similarity coefficient of ovary diameter in non-fixed (green;  $n = 10$ ) and fixed (red;  $n = 10$ ) samples (0 indicates no spatial overlap between the two sets of annotation results, 1 indicates complete overlap). Box plots show the middle 50% of the data with the median represented by the horizontal line. Whisker represents datapoint within 1.5 times the interquartile range with outliers highlighted as individual

**Table 2.2 Summary table on the manual and CNN annotation metrics obtained for stigma area and ovary diameter.**

<i>Stigma area (mm<sup>2</sup>)</i>									
	<b>Stage-1</b>			<b>Stage-2</b>			<b>Stage-3</b>		
	Manual annot.	CNN annot.	ANOVA <i>P value</i>	Manual annot.	CNN annot.	ANOVA <i>P value</i>	Manual annot.	CNN annot.	ANOVA <i>P value</i>
<b>Non-fixed carpels</b>	7.27 ± 0.648	7.54 ± 0.648	0.7741	10.23 ± 0.648	11.16 ± 0.648	0.3118	4.75 ± 0.648	4.19 ± 0.648	0.5488
<b>Fixed carpels</b>	7.54 ± 0.605	7.6 ± 0.605	0.9358	10.54 ± 0.605	11.1 ± 0.605	0.514	4.73 ± 0.605	4.84 ± 0.605	0.9005
<i>Ovary diameter (mm)</i>									
	<b>Stage-1</b>			<b>Stage-2</b>			<b>Stage-3</b>		
	Manual annot.	CNN annot.	ANOVA <i>P value</i>	Manual annot.	CNN annot.	ANOVA <i>P value</i>	Manual annot.	CNN annot.	ANOVA <i>P value</i>
<b>Non-fixed carpels</b>	2.09 ± 0.122	2.12 ± 0.122	0.8556	3.58 ± 0.129	3.59 ± 0.129	0.9769	3.48 ± 0.137	3.04 ± 0.137	0.0298
<b>Fixed carpels</b>	2.1 ± 0.0975	2.15 ± 0.0975	0.7473	3.27 ± 0.1027	3.27 ± 0.1027	0.9966	3.36 ± 0.1165	3.33 ± 0.1165	0.8659

Note: Estimated marginal means ± standard errors are given for each type of annotation. P values indicate statistical significance of the pairwise comparison in one-way ANOVA.

#### 2.4.4. Variation in stigma and ovary growth patterns can be studied on fixed carpels

Chemical fixation is commonly used to prevent tissue autolysis and degradation, while preserving morphology and cellular details for subsequent macro or microscopic evaluations. Fixatives, however, can lead to changes in volume and shape of the treated specimens due to cell shrinkage or swelling. Thus, artefacts of the technique could potentially lead to erroneous conclusions when measuring morphological traits of fixed samples.

To assess the effect of the fixative solution (ethanol and acetic acid) on stigma area and ovary diameter, we used four MS cultivars and sampled carpels at five timepoints over an 18-days period. Analysis of variance (three-way ANOVA) indicated that the fixative significantly reduces stigma area ( $P < 0.001$ ), whereas ovary diameter remained unchanged after applying the fixative ( $P = 0.25$ ; Figure 2.8A-C and 2.9). For stigma area, the fixative x timepoint interaction was borderline non-significant ( $P = 0.09$ ; Table 2.3) suggesting that the response to the fixative might change with floral age. By analysing individual timepoints, we observed that at 3 and 7 days after W9.5, at the peak of the stigma area, there are no-significant differences between fixed and non-fixed samples, whereas at 0, 13 ( $P < 0.05$ ) and 18 days after W9.5 ( $P < 0.001$ ; Figure 2.8A) the fixed samples show a reduced stigma area. Importantly, the absence of a significant fixative x cultivar interaction ( $P > 0.52$ ) suggests that all four cultivars react to the fixative in a similar manner (Figure 2.8D). Taken together, we see that fixing the carpels in ethanol and acetic acid reduces stigma area although the developmental dynamics of stigma area are conserved in the four cultivars across the 18 days (Figure 2.8D). We therefore conclude that the use of ethanol and acetic acid fixative allows us to accurately capture the growth dynamics of stigma area and ovary diameter and investigate phenotypic variation among diverse genotypes. Nonetheless, caution must be taken to compare absolute stigma areas across development given the significant reduction at early and late timepoints.



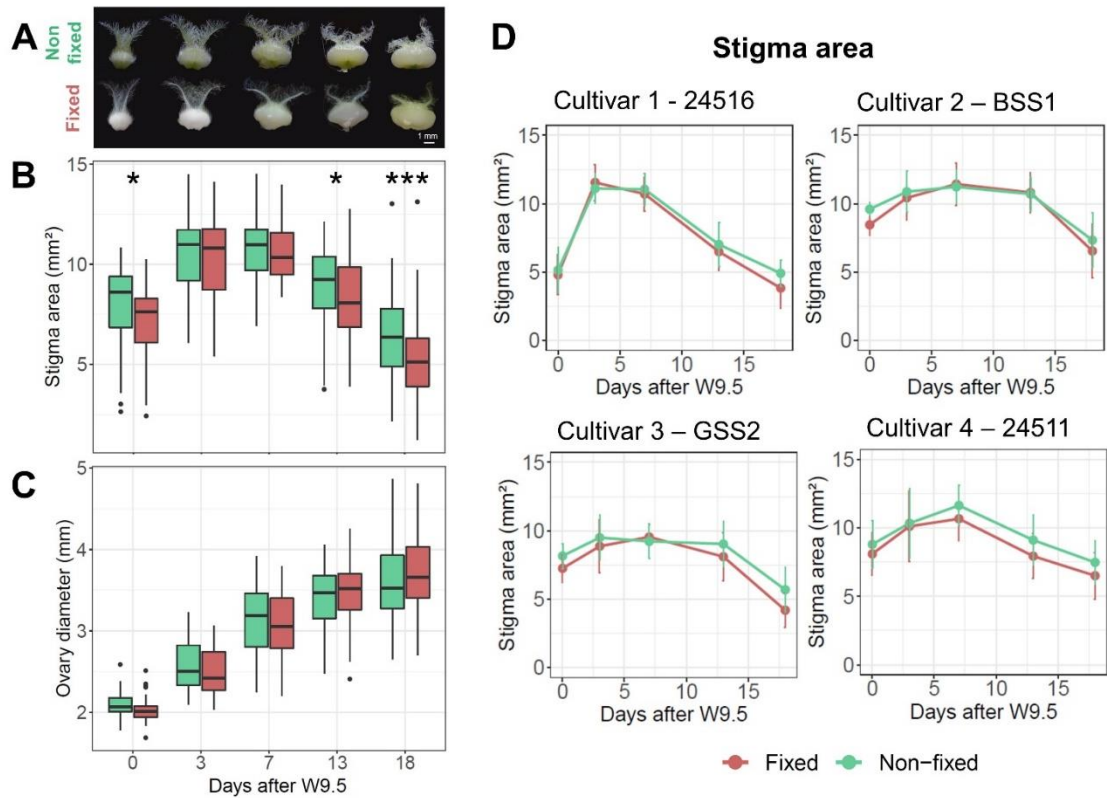


**Figure 2.8 Effects of the fixative on carpel morphology across time and cultivars.**

(A) Representative images of carpels before (non-fixed) and after (fixed) applying the fixative. (B-C) Box plots showing the comparison between non-fixed (green) and fixed (red) samples for stigma area (B) and ovary diameter (C) at different sampling points. Data are the average of the four cultivars shown in panel D which comprise 10-20 carpels from a total of 4 plants per timepoint and cultivar. \*  $P < 0.05$ ; \*\*\*  $P < 0.001$ . The box plots show the middle 50% of the data with the median represented by the horizontal line. Whiskers represent datapoint within 1.5 times the interquartile range with outliers highlighted as individual. (D) Developmental dynamics of stigma area of four male sterile cultivars, comparing non-fixed (green) and fixed (red) carpel samples (between 10-20 carpels from a total of 4 plants per timepoint). Error bar denotes the standard error of the mean.

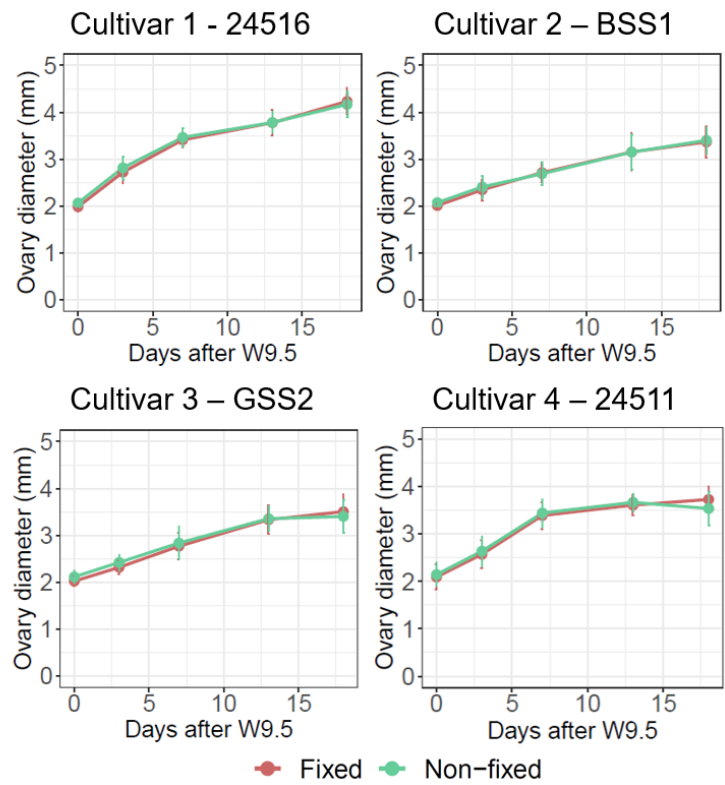


**Figure 2.9 Effects of the fixative on ovary diameter across time and cultivars.**

Stigma area development dynamics of four MS cultivars comparing non-fixed (green) and fixed (red) carpel samples (between 10-20 carpels from 4 plants per timepoint). Error bar denotes the standard error.

**Table 2.3 Summary table of three-way ANOVA on the effect of the fixative on stigma area and ovary diameter across different timepoints.**

<b>ANOVA <i>P</i> value</b>				
	Fixative	Fixative x Timepoint	Fixative x Cultivar	Fixative x Timepoint x Cultivar
<b>Stigma area</b>	6.39E-06	0.08956	0.52333	0.781
<b>Ovary diameter</b>	0.24692	0.08693	0.96446	0.98034
<b>0 DAW9.5</b>				
	Fixed	Non-fixed	Fixative effect (%)	<i>P</i> value
<b>Stigma area (mm<sup>2</sup>)</b>	7.15 ± 0.265	7.92 ± 0.265	-9.72	0.0292
<b>Ovary diameter (mm)</b>	2.01 ± 0.0468	2.09 ± 0.0468	-3.83	0.2299
<b>3 DAW9.5</b>				
	Fixed	Non-fixed	Fixative effect (%)	<i>P</i> value
<b>Stigma area (mm<sup>2</sup>)</b>	10.24 ± 0.179	10.46 ± 0.178	-1.91	0.3855
<b>Ovary diameter (mm)</b>	2.49 ± 0.0324	2.57 ± 0.0324	-3.11	0.058
<b>7 DAW9.5</b>				
	Fixed	Non-fixed	Fixative effect (%)	<i>P</i> value
<b>Stigma area (mm<sup>2</sup>)</b>	10.58 ± 0.242	10.78 ± 0.219	-1.85	0.5164
<b>Ovary diameter (mm)</b>	3.06 ± 0.0431	3.09 ± 0.0396	-0.97	0.479
<b>13 DAW9.5</b>				
	Fixed	Non-fixed	Fixative effect (%)	<i>P</i> value
<b>Stigma area (mm<sup>2</sup>)</b>	8.34 ± 0.180	8.97 ± 0.18	-7.02	0.0132
<b>Ovary diameter (mm)</b>	3.47 ± 0.0328	3.49 ± 0.0418	-0.57	0.677
<b>18 DAW9.5</b>				
	Fixed	Non-fixed	Fixative effect (%)	<i>P</i> value
<b>Stigma area (mm<sup>2</sup>)</b>	5.27 ± 0.178	6.35 ± 0.178	-17	<0.0001
<b>Ovary diameter (mm)</b>	3.71 ± 0.0328	3.63 ± 0.0339	2.2	0.0662

Note: *P* values shown for the different timepoints indicate the *P* values for the pairwise comparisons. Estimated marginal means  $\pm$  standard errors are also given for each treatment (fixed or non-fixed).

#### 2.4.5. The application of the phenotyping approach provides insight into the developmental behaviour of the unpollinated wheat carpel

Having established the method to quantitatively measure the progression of carpel development in the absence of pollination, we next sought to employ this approach to gain insights into genetic and environmental variation for these two floral traits. To accomplish this, we applied our phenotyping approach to three MS cultivars grown during two consecutive field seasons (2020 and 2021) where we performed a developmental time course ranging from W9.5 until the carpel had visually deteriorated. We selected MS cultivars BSS1, 24522 and 24512 as they captured large part of the variation observed in a broader panel phenotyped in 2020 (data not shown). To accommodate for season-specific differences in temperature between the two seasons (Figure 2.2), we incorporated daily temperatures in our model to normalise developmental stages by cumulative degree days.

We found that all three MS cultivars exhibit contrasting developmental patterns for stigma area and ovary diameter and that these differences among cultivars are largely maintained across field seasons (Figure 2.10A and B). The phenotypic differences, particularly in stigma area, are observed in both the growth (positive slope) and deterioration (negative slope) phases of carpel development, which inevitably impacts on the overall duration of the life cycle. For instance, we can distinguish the fast development of carpels from cultivar 24522 from the slow progression of carpels from cultivar BSS1 (Figure 2.10A). Despite these differences, all three patterns seem to underline a common developmental trend for the dynamics of stigma and ovary traits that is characterised by: (1) an initial growth phase, (2) followed by a peak phase in which stigma reaches its maximum and the radial expansion of the ovary slows down, and (3) a final deterioration phase. This conceptual framework for quantifying and classifying the development of the unpollinated carpel is presented in Figure 2.10C and D. The results obtained from breaking down late carpel development into more descriptive phases are detailed below.

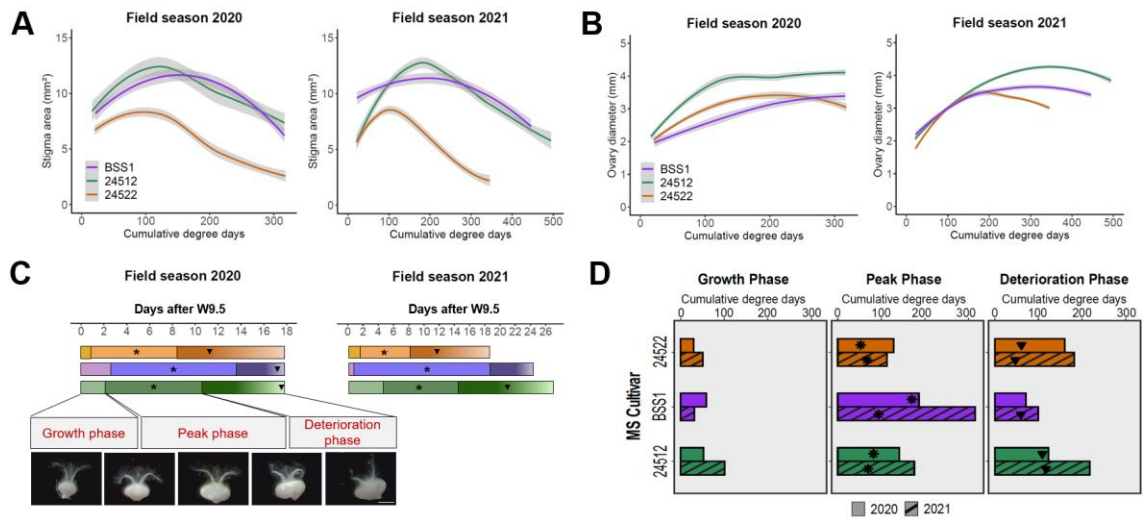


**Figure 2.10 Phenotypic quantification of carpel development in three distinct MS cultivars under field conditions.**

(A) Temporal trends of stigma area (mm<sup>2</sup>) in 2020 and 2021. (B) Temporal trends of ovary diameter (mm) for 2020 and 2021 field seasons. (C) Growth, peak and deterioration phases represented in days after W9.5 for 24522 (orange), BSS1 (purple) and 24512 (green) (temporal units are directly comparable to cumulative degree days in panel A). Representative images illustrating carpel appearance at the beginning and end of each phase (3<sup>rd</sup> picture represent carpel with 100% stigma area). (D) Bar charts show the duration (in degree days) of each of the phases across cultivars and field seasons. The end of the deterioration phase is marked by the last sampling point. In A and B, polynomial regression models at a 95% confidence interval (Loess smooth line) are shown. Grey shading represents standard error. Five carpels from 4 and 6 plants were sampled at each timepoint in 2020 and 2021, respectively. Scale bar in C = 2 mm. C and D, (\*) indicates maximum stigma area; (▼) indicates a 40% drop in stigma area with respect to the maximum area. Before plotting, outliers were filtered out following the interquartile range criterion.

#### 2.4.5.1. Growth phase

Stigma and ovaries experience rapid and exponential growth during the first phase. The growth phase is underway at W9.5 (around ear emergence) and extends for 1 to 4 days until the stigma is well developed and potentially receptive for pollination. The end of the phase coincides with a developmental stage parallel to W10 (anthesis) in male-fertile plants. We found that for all three cultivars the end of this phase could be described by the stigma showing an area of approximately 85% of its maximum size. The criteria for us to select the 85% cut-off as the end of the growth phase was based on 85% being the percentage that was present in all three cultivars across both field seasons and happened shortly after W9.5, thus mimicking anthesis (Figure 2.11).

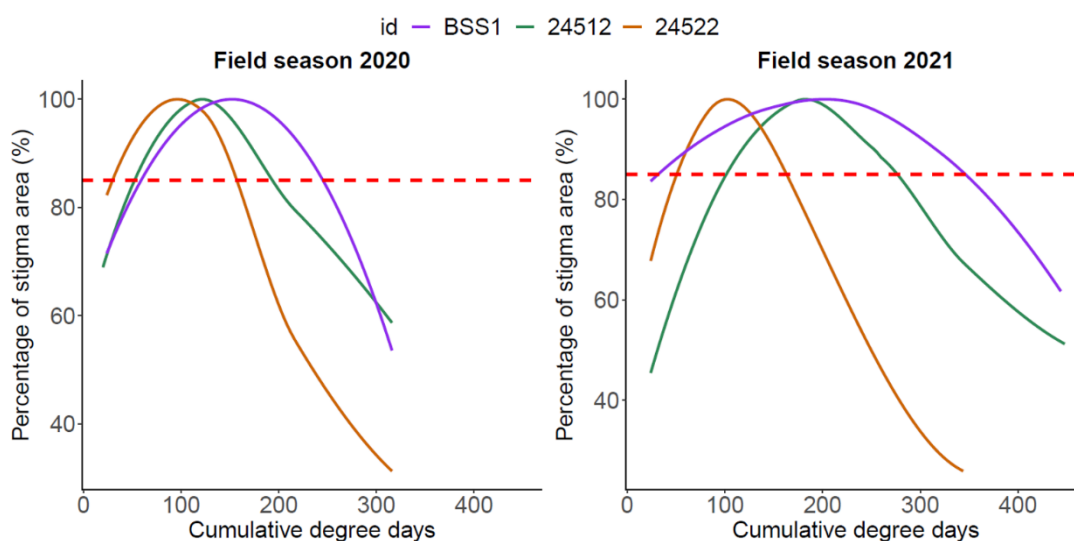


**Figure 2.11 Developmental stigma patterns expressed in percentage from maximum observed stigma area.**

Red dashed line indicates 85% benchmark for the selection of the boundaries of the peak phase with the growth and deterioration phases.

#### 2.4.5.2. Peak phase

This second phase is denoted by the stigmatic tissue reaching its maximum size (asterisks in Figure 2.10C) at around 5 to 10 days after W9.5 (depending on the cultivar and year). After reaching this peak, a gradual and irreversible decline in stigma area is accompanied by a notable arrest of the ovary radial expansion. To mirror the behaviour of stigma area at the beginning of this phase, we selected a 15% drop in stigma area to mark the end of the peak phase. Using this classification, we observed that this phase

extends until 8 to 14 days after W9.5 in 2020, and 8 to 18 days in 2021 (Figure 2.10C). Considering previous studies on female receptivity in wheat where hybrid seed set was maintained from 2 to 13 days (De Vries, 1971; Kirby, 2002; Pickett, 1993), we hypothesise that the peak phase of wheat stigma development coincides with the maximum reproductive potential of the carpel under free pollination conditions. Nonetheless, further analyses of pollen germination and seed setting rates during each of the three phases are needed to prove this hypothesis. Ideally these experiments would be conducted both under free-pollinating conditions (i.e., field trials mimicking hybrid production blocks) and using controlled hand-pollinations, as results will most likely differ between experiments since other aspects of the female flower (e.g., opening angle of glumes) play a part in the reproductive potential of the floret (Selva et al., 2020).

#### 2.4.5.3. *Deterioration phase*

During this phase, symptoms of stigma deterioration start to become obvious, where clusters of stigma hairs are collapsing in response to a loss in turgor pressure (inverted triangles in Figure 2.10C indicate a 40% drop in stigma area). The collapse of the remaining stigma hairs continues for several days resulting in a completely deteriorated stigma at 18 and 27 days after W9.5 in 2020 and 2021, respectively (Figure 2.10C and D). By the end of this phase the ovary walls also show an irregular surface due to tissue deterioration. Based on these observations, we speculate that the onset of this phase marks the irrevocable loss of the reproductive potential of the floret.

Dissecting carpel development into growth, peak and deterioration phases allowed us to assign the cultivars BSS1, 24512 and 24522 into slow, moderate, and fast developing carpels, respectively, according to when they reach the beginning of the deterioration phase. For example, cultivar BSS1 reached the onset of the deterioration phase at 14 and 18 days after W9.5 in 2020 and 2021, respectively. This was approximately 4 days after cultivar 24512 and between 6 to 10 days after cultivar 24522 in 2020 and 2021, respectively (Figure 2.10C). The developmental pattern classification also allows comparisons across field seasons, where the relative ranking of cultivars was well conserved between years. Although we adjusted for cumulative degree days, the colder and damper weather conditions of 2021 (Figure 2.2) were reflected in an extension in the duration of most phases in some, but not all cultivars (Figure 2.10D). For example, duration of the three phases was largely unaffected in cultivar 24522, whereas in cultivar BSS1, the duration of the peak phase in 2021 (315 degree days) was almost

twice that of the previous year (186 degree days). These initial analyses suggest that while the developmental dynamics of stigma area and ovary diameter are largely consistent across years there are cultivars in which the duration of the developmental phases could be sensitive to other environmental changes that remain to be tested.

To provide further support for the proposed stages of the stigma life cycle, we investigated the expression of genes encoding senescence-related transcriptional regulators that we expect to be up-regulated during the late peak and deterioration phases. Stigmas were sampled across the different phases of development using field-grown MS cultivar 24512, and the extracted RNA from these samples were used for an RNA-sequencing transcriptome experiment<sup>1</sup>. We focused on the expression of wheat homologues of the *KIR1* and *ORE1* transcription factors (TF; Figure 2.12A), shown previously to promote stigma senescence in Arabidopsis (Gao et al., 2018), and the 36 top-ranked TFs proposed to coordinate leaf senescence in wheat (Borrill et al., 2019), which included genes belonging to the GRAS, HSF, and RWP-RK TF families. All six *KIR1* and *ORE1* wheat homoeologs were expressed, and 28 of the 36 TFs associated with leaf senescence were also expressed in stigma, suggesting a large overlap between leaf and stigma senescence processes (Figure 2.12B). Of the 34 TFs expressed in the stigma, we identified distinct waves of expression in their transcript profiles across the four sampling time points. While eight TFs had highest expression in the growth and early peak phase, over 70% of the expressed senescence-related TFs (including wheat *KIR1* and *ORE1*) were upregulated towards the end of the peak phase (10 genes) or at the deterioration phase (15 genes; Figure 2.12B). These results highlight that the proposed phases of late carpel development, determined using microscopy, associate with expected transcriptional changes based on the biological processes that occur during these later stages (Figure 2.12B).

---

<sup>1</sup> This section was added to address peer reviewers' comments during publication process. For further details and additional experiments related to the investigation of the transcriptional landscape of the unpollinated stigma, please refer to Chapter 4.



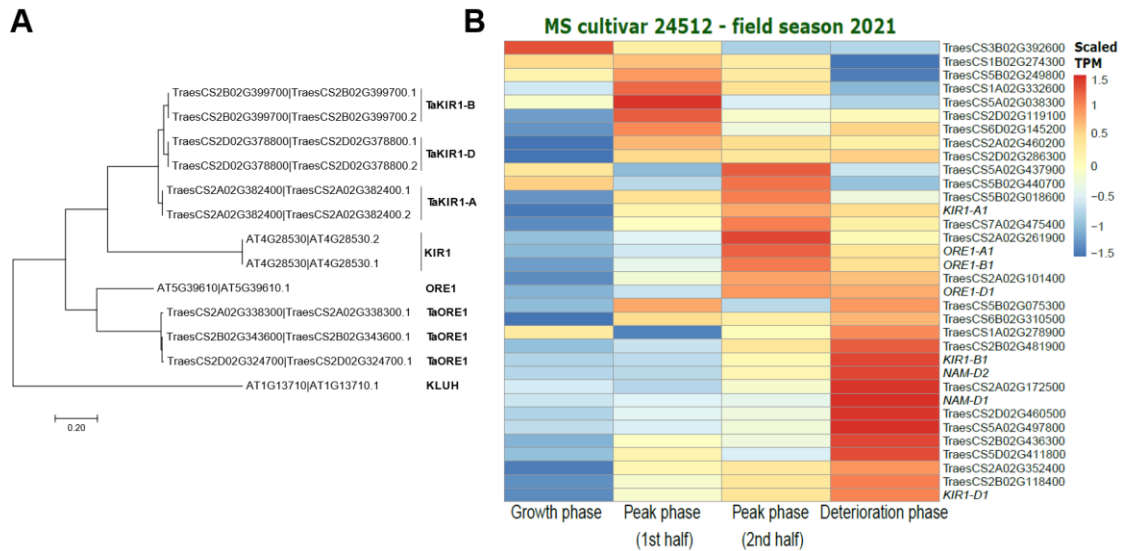


**Figure 2.12 Senescence-related transcriptional regulators are up-regulated during the late peak and deterioration phases.**

(A) Peptide sequences used to construct a rooted neighbor-joining tree of both splice variants of KIR1 (AT4G28530), ORE1 (AT5G39610) and its orthologs in wheat. To root the tree, KLUH (AT1G13710) was used as outgroup. (B) Heatmap illustrating the relative expression of KIR1, ORE1 and genes associated with leaf senescence (Borrill et al., 2019) in stigma samples from MS cultivar 24512. Samples were collected in the growth, peak (1st and 2nd half) and deterioration phase during the 2021 field season. Expression levels are normalised within each gene across the four timepoints and rows are sorted according to the similarity of expression and waves of expression in each phase of stigma development.

## 2.5. Discussion

### 2.5.1. High throughput phenotyping for the quantification of floral traits in unpollinated wheat carpels

Our understanding of floral developmental processes has been assisted by the establishment of scales that describe changes in the shape, size and surface features of floral organs leading up to anthesis (Smyth et al., 1990; Waddington et al., 1983). These scales often divide a continuous developmental process into defined stages, which are characterised by landmark events, such as the appearance of stigmatic branches. These scales have facilitated the interpretation of genetic studies and have contributed towards our understanding of the mechanisms that underlie the transitions leading to a given landmark event. During post-pollination stages, the focus shifts towards the developing fruit. Previous work, however, has also illustrated the importance of the quantitative monitoring of morphological changes associated with late carpel development (i.e., in the absence of pollination), such as silk elongation in maize (Bassetti & Westgate, 1993) or ovary radial expansion in wheat (Okada et al., 2017), as they represent survival mechanisms to ensure seed set by cross-pollination. So far, the few studies investigating the progression of the unpollinated female carpel after anthesis have focused in giving detailed descriptions of flowers from one or two different genotypes grown in controlled environmental conditions. These types of meticulous approaches are arduous and expensive not only to implement in large scale experiments but also to execute under field conditions, where equipment is often limited. Consequently, studies investigating detailed phenotypes in the field are lacking.

To enhance our understanding of the biological processes that occur in unpollinated carpel under breeding-relevant conditions, we created a machine learning-based approach to phenotype field-grown MS wheat cultivars. Given the sequence of morphological changes we observed in the unpollinated wheat carpel (Figure 2.4A), we next quantified changes in stigma area and ovary diameter to describe carpel development. Our findings are two-fold: (1) we demonstrate the suitability of our approach for the detailed study of floral organ traits in field screenings, and (2) we show that the unpollinated carpel undergoes a well-defined pattern of growth and senescence characterised by gradual changes in stigma and ovary sizes (Figure 2.10A and B). Based on these findings, we propose developmental phases that are relative to the maximum

stigma area and ovary size (Figure 2.4C; Figure 2.10C) with which to build the foundations of future research of floral organ development and senescence in the absence of pollination.

### 2.5.2. Considerations on the use of the stigma and ovary adapted CNNs

The quantification of stigma area and ovary diameter cannot be easily determined from surface observations of wheat spikes and requires the dissection and microscopy of individual carpels. The manual annotation and quantification of microscopy images is cumbersome and often delays scientific discoveries. Deep learning-based approaches, such as Convolutional Neural Networks (CNNs), have emerged as a solution to perform image quantification in an automated, rapid, and less biased manner, lifting the burden of image analysis from researchers. In this work we developed two CNNs (both publicly available at [https://github.com/Uauy-Lab/ML-carpel\\_traits](https://github.com/Uauy-Lab/ML-carpel_traits)) that enable non-machine-learning experts to quantify stigma area and ovary diameter on their local computer in a matter of hours (Figure 2.6). Evaluation metrics on the performance of the adapted networks (Figure 2.6C and Table 2.2) demonstrate their capability to satisfactorily measure both floral traits by condensing each RGB image to a single value (i.e., pixels). Measurements between manual and CNN annotation were largely indistinguishable (Table 2.2), with the network being less capable at later stages (Figure 2.6C). We believe one of the reasons for the poorer performance could be due to the difficulty in distinguishing the stigma and ovary from each other when the stigma is severely deteriorated and resting on top of the ovary (Figure 2.13). Also, it is worth noting that the ovary CNN relies on the performance of the stigma CNN to correctly predict the diameter of the ovary (see Materials and Methods for the detailed description of the algorithm), such that a bad prediction of the stigma area will likely affect ovary annotation. Poor quality images (i.e., out of focus, poor resolution images) and certain carpel orientations (Figure 2.3) also hinder the identification of the ovary and/or stigma, impairing the normal performance of the CNNs. In the case of blurry images, using post-processing tools (e.g., Photoshop or other image sharpening techniques) to adjust the sharpness of the image might help reduce the likelihood of incorrect annotations. However, there will still be certain cases where there is not an immediate reason for the failure of the CNN. We suggest, therefore, including an additional output verification step (Figure 2.5E) to identify potential errors before continuing with the downstream analyses.

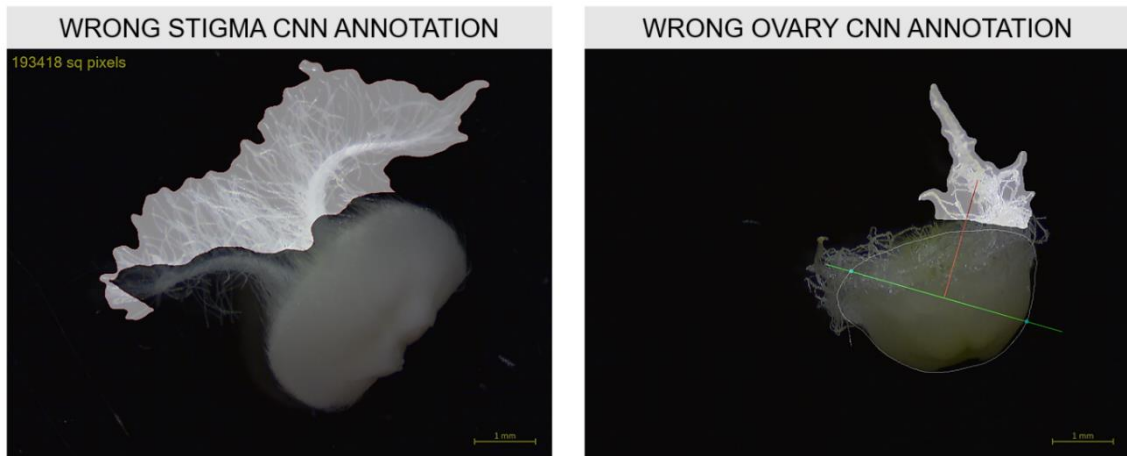


**Figure 2.13 Erroneous stigma area and ovary diameter CNN annotations.**

Examples of bright field images of carpels wrongly annotated by the stigma (left) and ovary (right) CNNs.

### 2.5.3. The implementation of the phenotyping approach opens new research paths on the biology of late carpel development

To gain a more comprehensive overview of the developmental dynamics of the unpollinated carpel, we used our phenotyping approach (Figure 2.5) to examine the sequential progression of changes in stigma and ovary morphology in three MS cultivars over two field seasons (Figure 2.10). Across cultivars and seasons, we were able to identify an initial stigma and ovary growth phase, followed by a peak phase describing carpel developmental maturity, and a subsequent deterioration phase characterised by the eventual collapse of the female reproductive tissues and expression of multiple senescence-associated genes (Figure 2.10C and E). Equivalent patterns for the post-anthesis development of the unpollinated stigma have also been reported in maize, peas (*Pisum sativum*) and Arabidopsis (Bassetti & Westgate, 1993; Carbonell-Bejerano et al., 2010; Vercher et al., 1984), suggesting a conserved developmental programme that ensues in the absence of pollination.

Despite the conserved overall patterns, we identified differences in the duration of the growth, peak and deterioration phases in the three wheat MS cultivars used here. Gene expression studies of unpollinated carpels and stigma in Arabidopsis and maize (Carbonell-Bejerano et al., 2010; Gao et al., 2018; Šimášková et al., 2022) have demonstrated that the lifespans of these floral structures are controlled by transcription factors that regulate developmental programmed cell death in these tissues. Here, we also identified distinct waves of expression of genes encoding senescence-associated TFs across late stigma development in a single wheat MS cultivar. Our results, along

with previous evidence from *Arabidopsis* and maize, raise the prospect that the phenotypic variation observed between the three wheat MS cultivars could be due to differential gene expression patterns across cultivars that alter the onset of stigma senescence (Figure 2.10B and C). Thus, new transcriptomic studies investigating the developmental transitions observed among the different field-grown cultivars would contribute to our understanding of the mechanisms governing these phases. We also observed that MS cultivars 24512 and 24522 had largely equivalent peak phase durations across years, whereas the duration of the peak phase in the CMS cultivar BSS1 varied almost two-fold between field seasons (Figure 2.10D). This suggests that, despite accounting for temperature in our analyses (by using cumulative degree days), the duration of the stigma peak phase is sensitive to additional environmental factors. The response to these additional environmental factors could depend on the genotype, sterility system used, and/or the developmental phase in which the environmental stimuli are encountered. Consistent with this, several studies in wheat have attributed differential seed set rates of out-crossing MS plants (i.e., an indicator for the duration of stigma receptivity) to environmental factors such as temperature, relative humidity, and soil water availability (De Vries, 1971; Fábíán et al., 2019; Imrie, 1966). Therefore, additional studies under field and controlled environment conditions will shed light on the causalities for the variation observed in ovary and stigma development across field seasons. Our phenotyping approach now improves the accessibility of the wheat carpel to detailed phenotypic analyses of the size of populations that are used in breeding programmes. This facilitates the identification of mutations that underpin genetic variation in carpel development contributing to understand gene function on a genome-wide scale. All in all, we provide a framework in which to conduct these new studies targeting diverse environments and genotypes, facilitating future hypothesis generation not only in wheat but also in other cereal crops.

#### 2.5.4. First steps towards an integrated developmental scale of the unpollinated wheat flower

The ultimate role of the carpel is the production of a viable seed. Thus, increasing the functional lifespan of carpels and stigmas (i.e., floral receptivity) are desirable agronomic traits that have the potential to increase the effective pollination period and seed set (Williams, 1965). Yet, detailed evaluations of carpel and stigma development and how they relate to female floral receptivity and seed set are still lacking, even more

so in cereals. It is reasonable to think that the functional lifespan of stigma receptivity would coincide with stigma cell integrity, as illustrated in early studies of kiwifruit (*Actinidia deliciosa*) and maize (Basseti & Westgate, 1993; González et al., 1995). According to these studies we could, for example, speculate that (a) seed set rates will be higher if pollination occurs during the peak phase compared to the deterioration phase, or (b) that cultivars with a prolonged peak phase (such as BSS1) will be receptive to pollination for longer than cultivars with a shorter peak phase (such as 24512 or 24522; Figure 2.10C). However, as recently demonstrated in Arabidopsis, a delay in stigma senescence caused by the disruption of two programmed cell death-promoting transcription factors was only accompanied by a minor extension in floral receptivity, suggesting that additional processes must be involved in controlling the duration of floral receptivity, for instance, ovule viability (Gao et al., 2018). New studies, therefore, need to be conducted to help investigate stigma receptivity under defined phases of carpel development to help clarify the relationship between stigma morphology and viability, pollen germination, and seed set. Additionally, such information will allow a greater understanding of how genetic and environmental factors affect various aspects of the stigma life cycle (e.g., loss of stigma receptivity, onset of stigma cell death). The next steps towards understanding the cross-pollination process in the field will also require integrating the changes in carpel morphology with those of the overall spike. For instance, as reviewed by Selva et al., 2020, certain wheat spike architectures, like the openness of the floret, facilitate airborne pollen access which would additionally contribute to increasing out-crossing rates in hybrid production.

Our approach for phenotyping carpel development provides a new tool for examining a fertility trait that is poorly understood and hitherto time-consuming to analyse. Together with recent advances in genetic resources (Krasileva et al., 2017; Wingen et al., 2014) and genome sequence data (Appels et al., 2018; Walkowiak et al., 2020), this approach provides a new opportunity to unlock genetic variation for stigma and ovary traits that associate with floret fertility, which is vital given that improved fertilisation will help address the increasing demands to enhance global food production.

## **3. Stigma longevity: not a limiting factor in hybrid wheat seed production**

### **3.1. Summary**

One of the major challenges in achieving successful hybrid wheat production lies in the low outcrossing rates of the maternal parent. This is often attributed to suboptimal synchronisation of male and female flowering as delayed pollination can result in reproductive failure due to deterioration of the female stigma. To test this accepted dogma, we examined the seed set capacity of a subset of six male sterile (MS) cultivars, each varying in the onset of stigma deterioration. To mimic a hybrid seed production scenario, MS cultivars were grown during two consecutive field seasons, and open pollination was allowed up to 15 days after flowering of the female parent. To ensure good pollen availability throughout the time course, a blend of seven male fertile cultivars with varying flowering times was used. Detailed analysis of the temporal and spatial distribution of hybrid seed set along the MS spike across the six MS cultivars showed that grain production remained remarkably stable during the pollination window tested. These findings suggest sustained receptivity to pollen across all tested MS cultivars throughout the entire time course. We therefore conclude that stigma longevity does not represent a limiting factor in hybrid wheat seed production and that breeding efforts should prioritise the study of other female traits, such as enhanced access to airborne pollen.

## 3.2. Introduction

The production of hybrid seed as part of an economically viable system relies on successful pollination between a male donor and a female or male sterile (MS) plant. Synchronous pollen shed and stigma receptivity is therefore essential to achieve efficient hybrid seed production. However, the autogamous flowers of wheat and other crops, which form floral organs with short life spans, favour self-pollination, limiting the opportunity for the out-crossing required for hybrid seed production. As a result, desirable traits for efficient hybrid seed production include an extended pollen shedding window and prolonged stigma receptivity (Selva et al., 2020; Whitford et al., 2013).

The discovery of male sterility systems (see Chapter 1 section 1.3.1) in the 1960s sparked interest in studying the biology of the wheat stigma. De Vries (1971) summarised the existing literature showing that stigma receptivity lasted between 6 and 13 days depending on the experimental conditions and the methods used for calculating receptivity relative to initiation of flowering. However, the only data dealing with performance of male sterile plants under open pollination conditions are those reported by Zeven (1968). Zeven determined that the greatest receptivity of male sterile plants relocated for 24 hours to a field of flowering plants happened on the third (1.47 grains per spikelet) and fourth (1.28 grains per spikelet) day after the start of flowering. Thereafter, the receptivity decreased quickly, and on the seventh day practically no more seeds were set. Notably, apart from these studies, there has been limited research dedicated to exploring the influence of female floral traits on hybrid seed set, with most research focused on enhancing pollen-donating qualities (Selva et al., 2020). This underscores the need for a more comprehensive investigation into the role of stigma receptivity in hybrid seed production.

In Chapter 2, we showed that the unpollinated carpel undergoes a well-defined developmental programme that can be used to classify MS cultivars according to the onset and progression of stigma deterioration. We therefore hypothesised that MS cultivars with extended stigma longevity can significantly improve the chances of successful pollen germination, fertilisation, and seed set. The aim of this chapter is to test this hypothesis by better understanding how the dynamics of stigma development can influence the performance of the female plant in a hybrid production scenario. To achieve this, we selected six MS cultivars showing distinct patterns of stigma



development and investigated their contribution to hybrid seed set when open cross-pollination takes place at multiple days after Waddington 9.5 (DAW9.5).

### 3.3. Materials and methods

#### 3.3.1. Germplasm

A total of 29 winter male sterile (MS) hexaploid wheat (*Triticum aestivum*) cultivars derived from commercial inbred lines were initially screened in 2020. Cytoplasmic and nuclear male sterility (CMS and NMS, respectively) systems were used for the generation of the male sterile cultivars. BSS1, BSS2, GSS1 and GSS2 correspond to CMS cultivars provided by Syngenta (Whittlesford, UK) while the remaining are NMS cultivars provided by KWS (Thriplow, UK). PCA and hierarchical clustering analysis was used to select six MS cultivars (24485, 24512, 24526, 24522, BSS1 and GSS1) for further field analyses in 2021 and 2022 field seasons.

For the crossing plots, I used a mixture of pollen donors including seven different male fertile cultivars provided by KWS-UK (i.e., Nirvana, Elysee, Piko, Poros, Creator, Quartz and Stava). The selection of these pollen donors was based on visual anther extrusion scores greater than 1.5 (0 = no anthers extruded; 3 = maximum anther extrusion) and distinct flowering times to ensure good pollen availability throughout the time courses (Table 3.1). To avoid unwanted cross-pollination, sterile rye barriers were grown surrounding the male sterile and crossing plots (e.g., Figure 3.1).

**Table 3.1 Plant scores of pollen donors selected for 2021 and 2022 hybrid seed production field trials.**

Data obtained from KWS based on a 2020 field trial. AEX: anther extrusion (0 = no anthers extruded; 3 = maximum anther extrusion); EE: ear emergence.

<b>Pollen donor</b>	<b>AEX</b>	<b>EE</b>	<b>Height (cm)</b>
Nirvana	2.26	24/05/2020	70
Elysee	2.93	27/05/2020	100
Quartz	2.4	29/05/2020	56
Stava	1.68	03/06/2020	95
Creator	2.78	03/06/2020	64
Poros	2.33	04/06/2020	109
Piko	-	-	-

Note: No data was available for Piko based on the KWS 2020 field trial. Piko was selected for its excellent male floral traits (e.g., anther extrusion, height; Boeven et al., 2018). It also shows late ear emergence compared to most of pollen donors used in UK pollination trials.

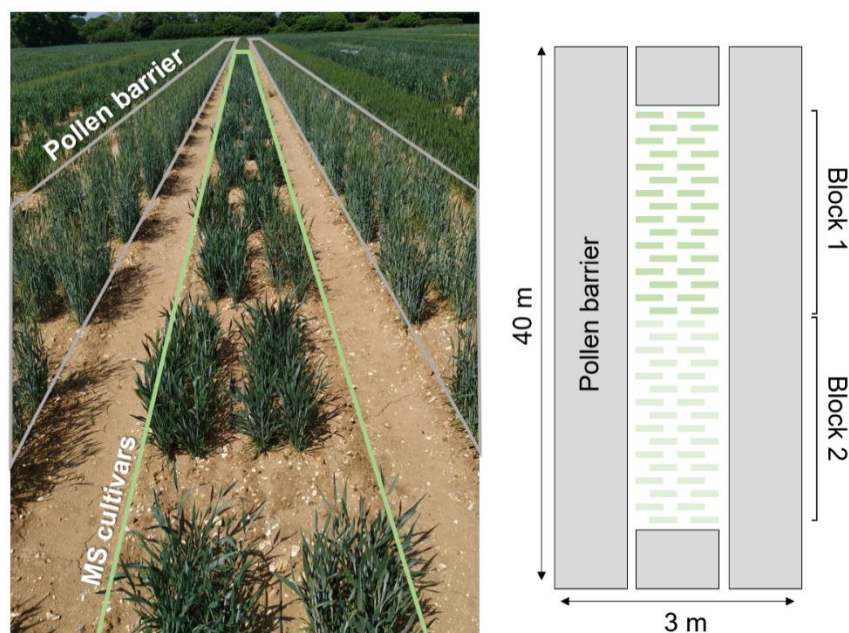


**Figure 3.1 Visual and schematic representation of the field layout in 2020.**

MS cultivars (in green) were grown surrounded by a continuous sowing of sterile rye that was used as pollen barrier. Plots were replicated twice in 2020 ( $n = 29$  per block). This layout aligns with experiments focused on characterising the development of unpollinated carpels and was replicated in both 2021 and 2022.

### 3.3.2. Experimental design and sampling

Field experiments were conducted during the 2019/2020, 2020/2021 and 2021/2022 growing seasons at John Innes Centre Church Farm (Bawburgh, UK;  $52^{\circ}37'50.7''$  N  $1^{\circ}10'39.7''$  E). Plants were grown in a randomised complete block design (RCBD) with two replicates ( $1 \text{ m}^2$  plots) per MS cultivar in 2020 (Figure 3.1), and three replicates in 2021 and 2022 for carpel development time course. Hybrid production plots were also grown in RCBD with three replicates in 2021 and 2022 (Figure 3.2 and 3.3).

Meteorological data were obtained from data loggers (EasyLog USB, Lascar Electronics; and Tinytag Plus 2) placed next to the experimental plots at 50 cm height. Temperature and relative humidity were measured every hour during the duration of the experiments (Figure 3.4).

#### 2.5.4.1. *Carpel development time course*

For the carpel development time course experiments, I followed the experimental approach described in Chapter 2. Briefly, main spikes were tagged when carpels in florets 1 and 2 of central spikelets reached Waddington stage 9.5 (W9.5). At the time of sampling, I cut individual tillers (two tillers per plot and time point) and transported them in water to the laboratory for carpel dissection. On average, five carpels from

central spikelets (floret 1 and 2) were stored in freshly made 95% ethanol and absolute acetic acid (75% v/v) fixative solution and kept at 4°C until image acquisition.

#### 2.5.4.2. *Open pollination time course*

To control the timing of pollen flow between neighbouring male and MS plants, male and MS plants were separated by isolation walls (1.5 m height protection fleece, LBS Horticulture, Lancashire, UK) in 2021 and pollination bags in 2022 (catalogue No. 2D.4-1W, PBS International, Scarborough, UK), which covered the MS plants before ear emergence (Figure 3.2 and 3.3). At the time of pollination, I removed the walls or bags (depending on the year) allowing cross-pollination to take place from that point onwards. In 2021, the hybrid seed set time course spanned four time points (from 0 to 15 DAW9.5), and six time points (from 0 to 13 DAW9.5) in 2022. Notably, these time points exhibited slight variations among MS cultivars due to divergent phenology, with BSS1 and GSS1 reaching W9.5 later and 24522 reaching W9.5 earlier compared to other MS cultivars.

To determine the level of unwanted cross pollination and level of sterility of MS plants, I included negative control plots in which isolation measures (walls or bags) remained in place throughout the experiment. In 2022, I introduced positive control plots, allowing unrestricted pollen flow (i.e., no bags). It is worth noting that the positive control plots essentially represent the first time point of cross-pollination since, in both cases, pollination was feasible from W9.5 onwards. Each crossing plot consisted of two rows of MS plants flanked by two rows of male fertile plants on either side with 0.17 m spacing between rows (inset in Figure 3.2). To maximise pollen flow, crossing plots were sown downwind of the main wind direction. At full plant maturity, I hand-harvested between five and ten main spikes per hybrid production plot and 50 spikes from control plots for subsequent hybrid seed set assessments.

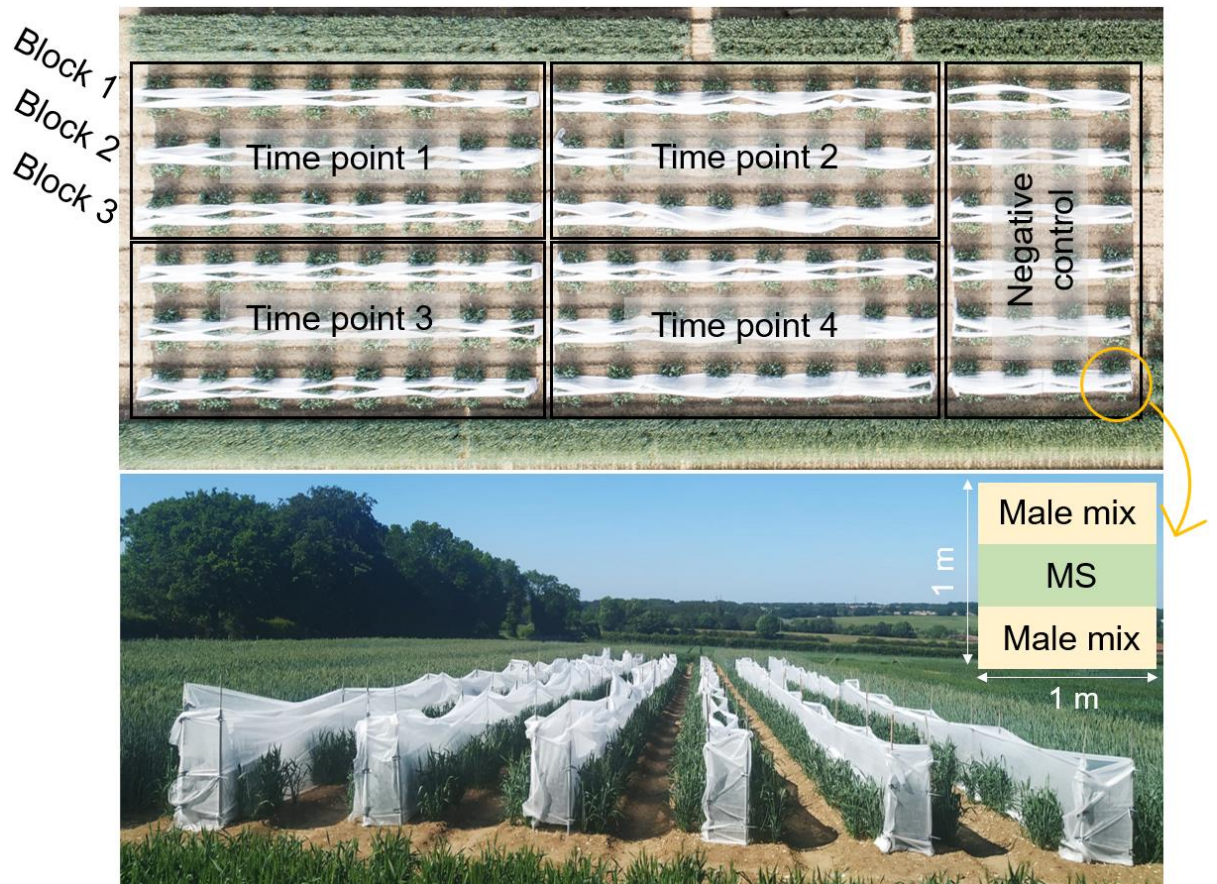


**Figure 3.2** Field trial layout of the 2021 hybrid seed production trial before flowering.

Isolation walls encircle the MS plots, blocking pollen flow from adjacent male fertile plants. Note that the setup required the complete removal of these walls for each block.



**Figure 3.3 Field trial layout of the 2022 hybrid seed production trial before flowering.**

Pollination bags covering the MS plots, blocking pollen flow from adjacent male fertile plants. Note that some bags were already removed at time point 1 and 2 as this setup, contrary to 2021, allowed for the individual removal of bags.

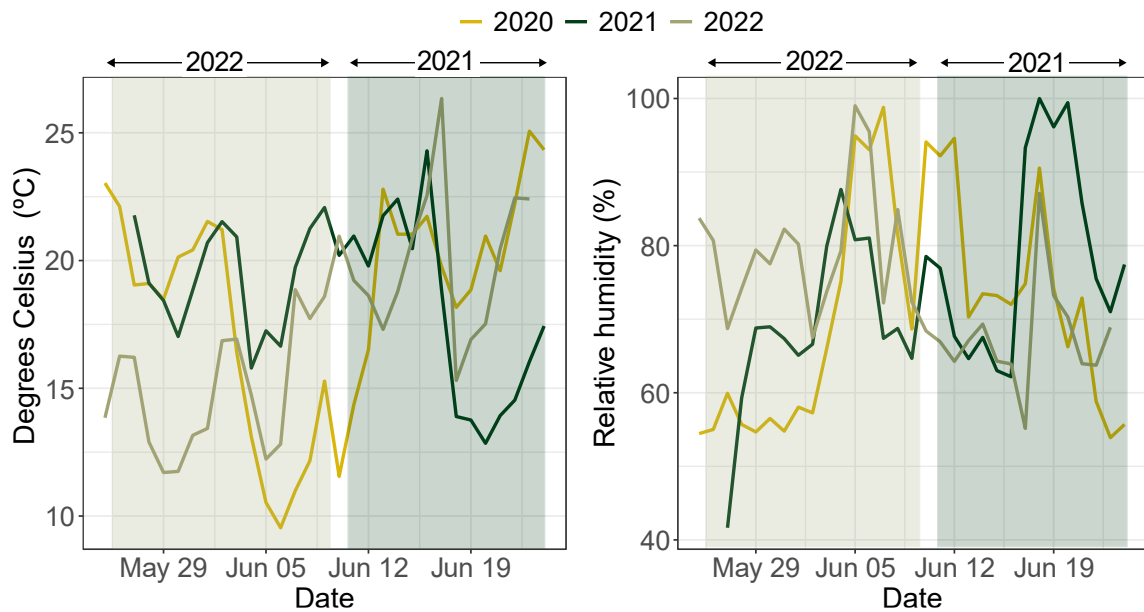


**Figure 3.4 Environmental conditions recorded during 2020, 2021 and 2022 field seasons.**

Left panel illustrates mean daily temperatures in degrees Celsius recorded during the field experiments. Shaded rectangles indicate the beginning and end of 2021 and 2022 time courses (i.e., pollination windows). Right panel shows the water vapor contained in the air expressed in percentage of relative humidity.

### 3.3.3. Hybridity test

A set of 93 F<sub>1</sub> seeds were randomly sampled from the 2021 and 2022 field trials for each MS cultivar to undergo hybridity testing. Additionally, 40 seeds from each of the pollen donors were included in the analysis (except for Poros, for which 32 seeds were tested). KWS conducted DNA extraction and genotyping, employing a panel of 23 identity single nucleotide polymorphisms (SNP) markers. The analysis revealed a distinct separation in the distribution of heterozygous base calls between the pollen donors (self-pollinated seeds) and F<sub>1</sub> seeds (Figure 3.5). Specifically, out of the 272 seeds tested in the pollen donors, only four exhibited one or more heterozygous calls (1.47%) indicating that seeds resulting from self-pollination are highly homozygous (i.e., number of heterozygous base calls = 0). The established cutoff for determining identity status of the seed was set at four or more heterozygous base calls.

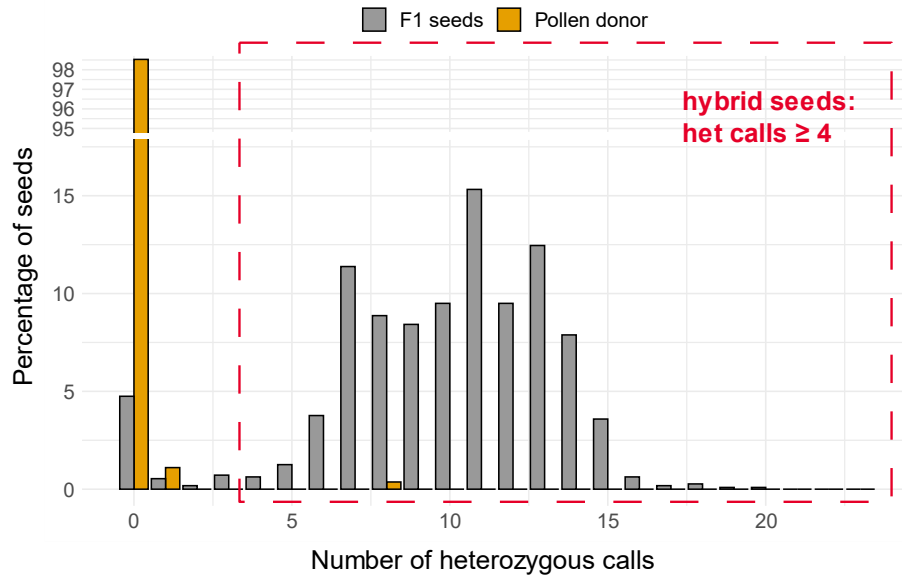


**Figure 3.5 Distribution of heterozygous base calls for F<sub>1</sub> and pollen donor seeds.**

Bar plot illustrates where the number of heterozygous base calls are concentrated for F<sub>1</sub> seeds (grey) and pollen donor seeds (orange). Y-axis represents the percentage of seeds showing heterozygous base calls (from 0 markers showing heterozygous base calls to all 23 markers being heterozygous). Note the gap in numbering of Y-axis.

### 3.3.4. Plant phenotyping

The following traits were assessed in this study:

#### 3.3.4.1. *Stigma area and ovary diameter measurements*

Image acquisition and annotation and quantification of carpel traits was performed as described in Chapter 2, section 2.3.3. The phases of stigma development were calculated based on the  $\pm 15\%$  of the maximum stigma area measured (also outlined in Chapter 2, section 2.4.5).

#### 3.3.4.2. *Hybrid seed set assessment*

To study seed set of the MS cultivars in a hybrid seed production setting, I manually counted the number of seeds and number of spikelets per spike. I assigned seeds to either apical, central, or basal sections based on their relative position along the spike. The apical section was defined as the top-most quarter of spikelets, the central section included spikelets from the central half of the spike, and the basal section consisted of the bottom-most quarter of spikelets. Additionally, I threshed spikes from the control plots and used seed counters (Seed Counter R-25 Plus and R-60 Plus, DATA Detection



Technologies Ltd.) to determine seed number. In control plots, I calculated the grain number per spikelet by considering the average spikelet number per spike and the respective grain number per MS cultivar.

### 3.3.5. Statistical analyses

To evaluate the effect of pollination time on grain per spikelet, I used a linear mixed model using a restricted maximum likelihood (REML) method from the R package lme4 v1.1.34 (Bates et al., 2015):

$$\text{Grain number per spikelet} \sim \text{pollination time} * \text{MS cultivar} + \text{year} + (1/\text{year}:\text{rack}) + (1/\text{year}:\text{rack}:\text{plot})$$

To account for variation between biological replicates I treated plot information as random effects. Diagnostic plots were generated to assess the goodness of fit of the model to the data (Figure 3.6). R package lmerTest v3.1-3 (Kuznetsova et al., 2017) was used to calculate *P* values.

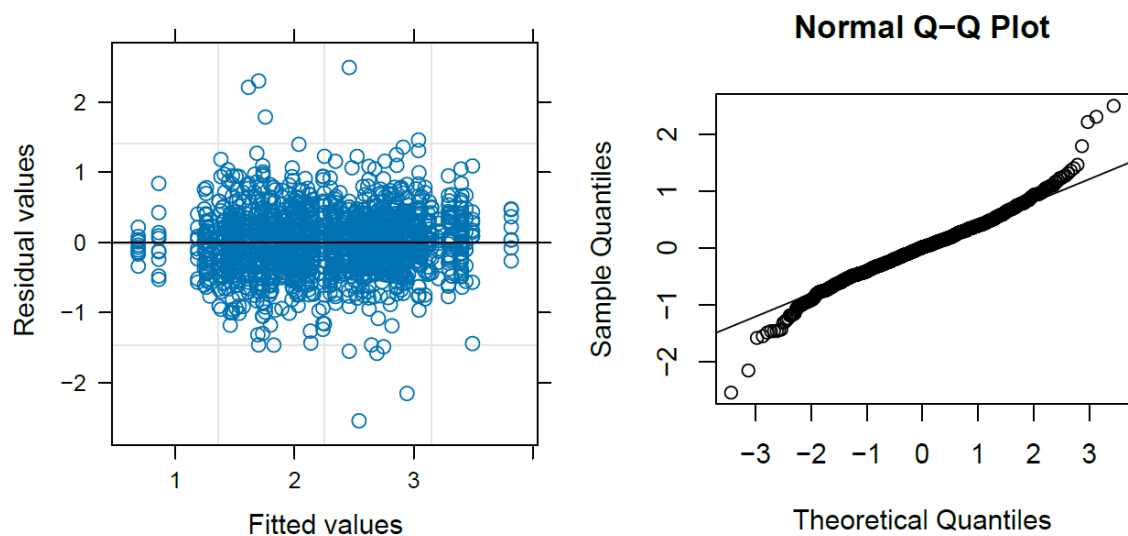


**Figure 3.6 Diagnostic plots of residual values.**

Scatter plot on the left shows the variance of the Pearson's residuals is constant with a fairly uniform distribution of the residuals indicative of a well fitted model. On the right, the quantile plot does not raise significant concerns around normality of the residuals.

The linear mixed model used to analyse the effect of pollination time on grain per spikelet per spike section is as follows:

$$\text{Grain number per spikelet section} \sim \text{section} * \text{pollination time} * \text{MS cultivar} + \text{year} + (1/\text{year}:\text{rack}) + (1/\text{year}:\text{rack}:\text{plot})$$

Diagnostic plots are shown in Figure 3.7.

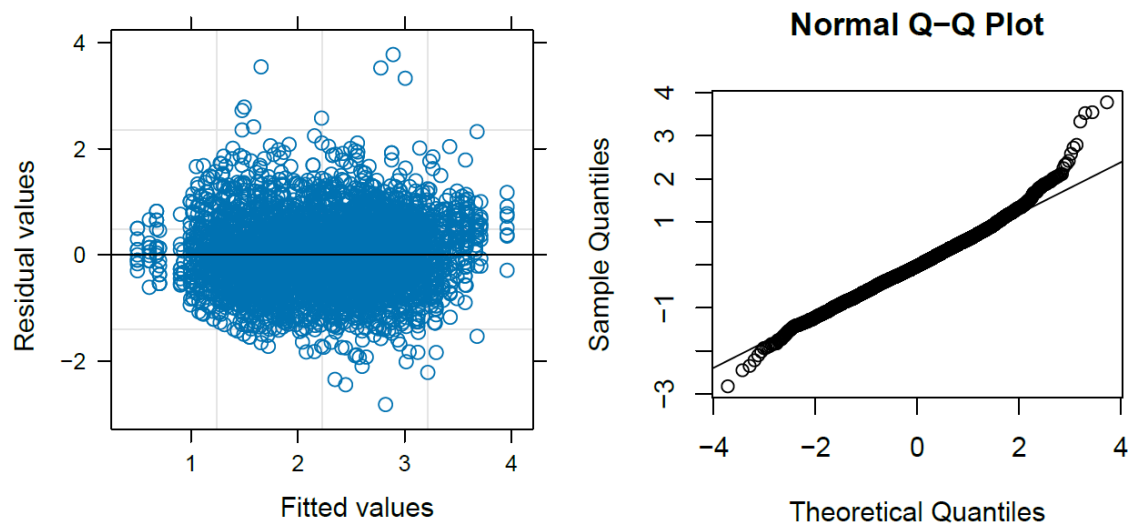


**Figure 3.7** Diagnostic plots of residual values.

Scatter plot on the left shows the variance of the Pearson's residuals is constant with a fairly uniform distribution of the residuals indicative of a well fitted model. On the right, the quantile plot does not raise significant concerns around normality of the residuals.

To calculate the slopes for each combination of section and MS cultivar I used the “lm” function from the inbuilt R package stats v4.3.0 to fit the following linear model:

$$\text{Grain number per spikelet}_{ij} \sim \text{pollination time} + \text{year}$$

In grain number per spikelet,  $ij$  refers to a particular spike section ( $i$ ) and MS cultivar ( $j$ ) combination.

## 3.4. Results

### 3.4.1. Selection and characterisation of carpel development in the female parents

To understand how the longevity of the stigma in the female parent influences hybrid seed set under field conditions, I first evaluated the patterns of stigma development in the absence of pollination in 29 MS cultivars derived from commercial inbred lines (provided by Syngenta and KWS) during the 2020 field season (Figure 3.8). I tracked the progression of stigmatic growth and deterioration at different timepoints, starting shortly after ear emergence at Waddington 9.5 (W9.5), and continuing at 3, 7, 13 and 18 days after W9.5 (DAW9.5). Hierarchical clustering (Figure 3.8A) and principal component analysis (PCA; Figure 3.8B) facilitated the identification of six distinct groups characterising diverse developmental patterns (see Figure 3.9). Interestingly, PC1 seemed to explain the variation observed in the rate of stigma deterioration. For example, MS cultivars in groups 1, 2 and 3 showed slower progression of stigma deterioration (right section of PCA plot; Figure 3.8B and 3.9), while groups 5 and 6 represented the most prevalent developmental profile, including 20 of the tested MS cultivars (69%). Conversely, group 4, comprising cultivars 24500, 24522, and 24524, displayed a more premature stigmatic deterioration (left section of PCA plot; Figure 3.8B and 3.9).

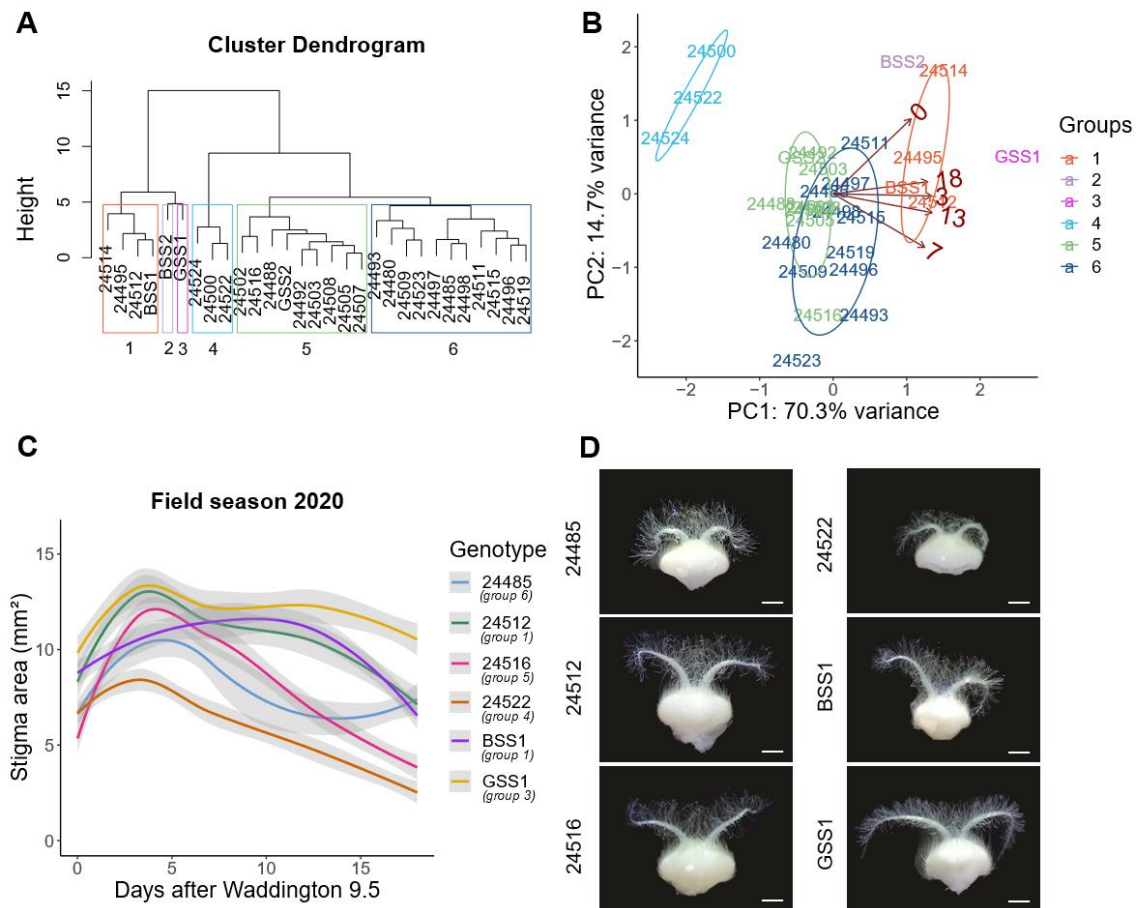


**Figure 3.8 Characterisation of stigma traits for the selection of female parents.**

(A) Hierarchical clustering analysis to visualise the relationships between the 29 MS cultivars based on stigma area at 0, 3, 7, 13 and 18 DAW9.5. Coloured boxes define six distinct phenotypic groups labelled from 1 to 6. (B) Principal component analysis (PCA) of stigma area. MS cultivars are colour coded according to groups defined in (A). (C) Developmental pattern of stigma area ( $\text{mm}^2$ ) for the selected MS cultivars (24485, 24512, 24516, 24522, BSS1 and GSS1) during the 2020 field season. Polynomial regression models at a 95% confidence interval (Loess smooth line) are shown. Grey shading represents the standard error of the mean (s.e.m). Five carpels from each of four plants were sampled at each timepoint. Note the colour scheme has been altered in relation to panels A and B. (D) Representative images of unpollinated carpels at 7 DAW9.5. Carpels are fixed in 95% ethanol and absolute acetic acid (75% v/v). Scale bar = 1 mm.

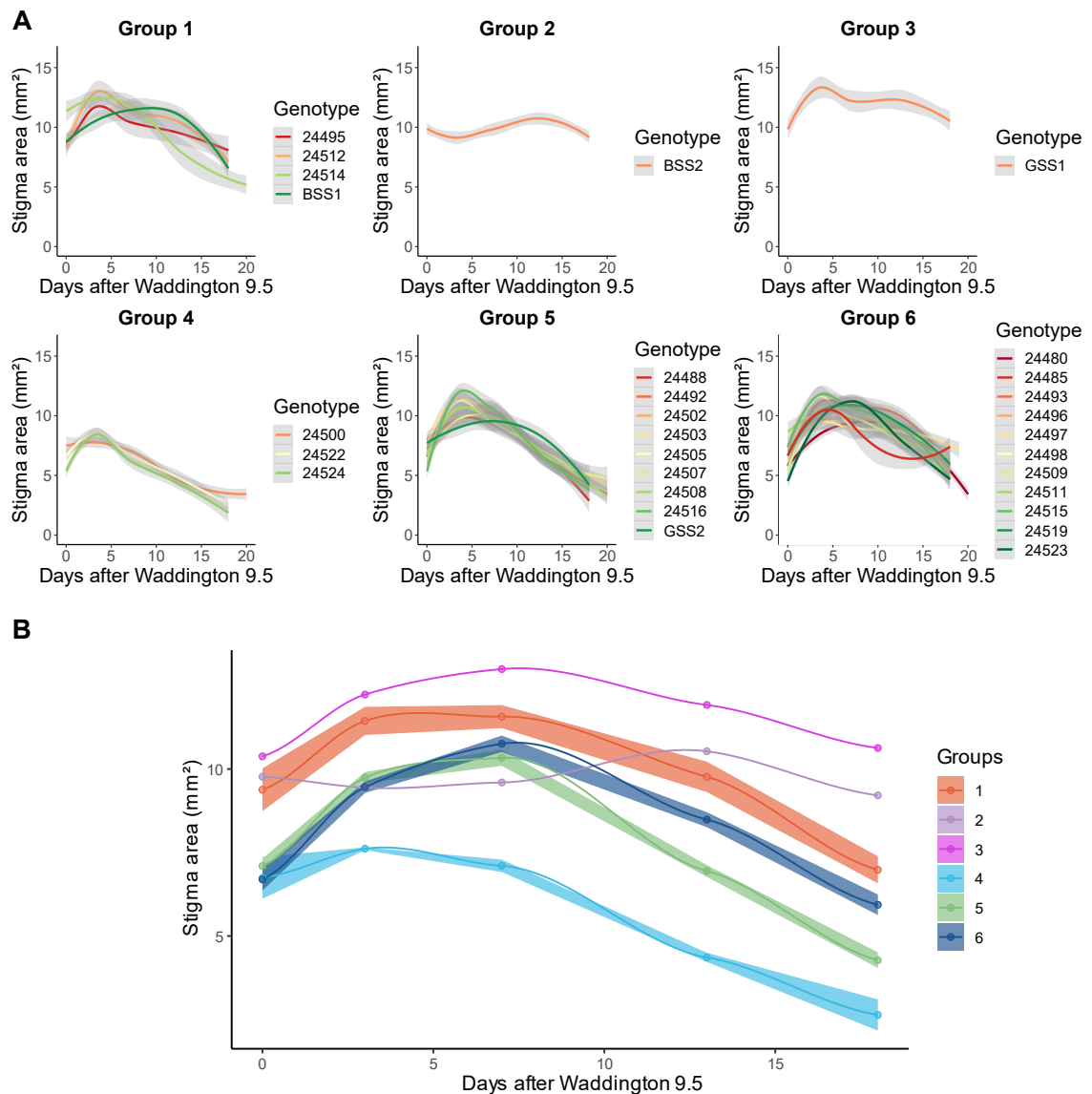


**Figure 3.9 Phenotypic diversity observed for stigma development during the 2020 field season.**

(A) Each plot represents a distinct group based on clustering analysis (see Figure 3.8A). Polynomial regression models are shown for stigma area. Grey shading represents the standard error of the mean (s.e.m). Five carpels from each of four plants were sampled at each timepoint. (B) Ribbon plot illustrates how stigma area (mm<sup>2</sup>) varies over the range of the six distinct groups. The width of each ribbon represents s.e.m.

For each group, I chose a single MS cultivar to represent the observed variation, except for BSS2 in group 2, which was excluded due to its unusual growth and deterioration pattern (Figure 3.9). Additionally, from group 1, I selected two MS cultivars, namely 24512 and BSS1. These six cultivars collectively represent a substantial portion of the variability observed in stigma area throughout development (Figure 3.8C). Interestingly, these cultivars not only exhibited differences in the rate of deterioration, as exemplified

by BSS1 and 24485, but also showed differences in stigma size, highlighted by a 5.5 mm<sup>2</sup> contrast at 7 DAW9.5 between GSS1 and 24522 (Figure 3.8D). These differences in stigma size might have important implications for the efficiency of hybrid seed production as they influence the level of stigma extrusion from the floret, thereby facilitating pollen capture (Tadlock, 2015; Tan et al., 2023). To ensure constant pollen flow throughout the hybrid seed production trials, I chose seven male fertile cultivars with good anther extrusion phenotypes and distinct flowering times. These cultivars were combined into a pollen donor mixture for use in the 2021 and 2022 field seasons (see Materials and Methods, section 3.3.2). In 2021 and 2022, the pollination window spanned a period of 13 days. Notably, Nirvana was the earliest among the male cultivars to begin flowering, while the last cultivar to flower varied between the two years (Table 3.2). In some instances, male flowering initiated prior to the MS cultivar reached W9.5 stage, as observed with BSS1 and GSS1. In other cases, MS cultivars such as 24522 reached W9.5 before the earliest male cultivar, Nirvana, entered the anthesis phase. As a consequence, the effective pollination window differed among the MS cultivars.

**Table 3.2 Flowering time (anthesis) of pollen donors in 2021 and 2022.**

Flowering time was assessed in test plots without mix cultivation. Note that not all the pollen donors were grown separately in each of the two seasons.

<b>Pollen donor</b>	<b>Anthesis (2021)</b>	<b>Anthesis (2022)</b>
Nirvana	11/06/2021	26/05/2022
Elysee	15/06/2021	05/06/2022
Quartz	-	02/06/2022
Stava	-	07/06/2022
Creator	-	08/06/2022
Poros	22/06/2021	-
Piko	24/06/2021	03/06/2022

To comprehensively assess the carpel longevity of the selected MS cultivars during the 2021 and 2022 hybrid seed production trials, I replicated the phenotypic screenings carried out in 2020 to validate variations in stigma traits (Figure 3.10). During the 2021 and 2022 field seasons, alongside the evaluation of stigma traits, we also quantified the diameter of the unfertilised ovary, considering its potential role in floret opening and pollen capture (Okada et al., 2017). To facilitate the analysis of stigma development, I applied the methodology detailed in Chapter 2 for the quantification of the growth, peak, and deterioration phases (Figure 3.10A and B). Based on the onset of stigma

deterioration, I identified three groups. Among the MS cultivars, 24522 was the earliest to enter the deterioration phase, occurring around 9 DAW9.5. Meanwhile, the stigmas of the MS cultivars 24516 and 24485 started to deteriorate around 12 DAW9.5. In contrast, GSS1, BSS1, and 24512 reached the deterioration phase roughly at 14 DAW9.5. Notably, BSS1 exhibited substantial variability across field seasons, with a 5-day difference in reaching the onset of the deterioration phase (at 19 DAW9.5 in 2021 and at 13 DAW9.5 in 2022), consistent with findings in Chapter 2, section 2.4.4. Regarding stigma size, GSS1 and 24512 displayed the largest stigmas, reaching maximum sizes of 13.5 mm<sup>2</sup> in 2021 and 12.3 mm<sup>2</sup> in 2022. An intermediate group, consisting of 24516, BSS1, and 24485, exhibited maximum sizes around 11 mm<sup>2</sup>. In contrast, 24522 had the smallest stigma, with a maximum size of 9 mm<sup>2</sup>. Interestingly, we find that smaller stigmas reached their maximum size earlier than intermediate and larger stigmas, resulting in an overall 3-day difference in peak stigma area between the smallest and largest stigmas. Furthermore, I observed that 24522 consistently exhibited the smallest stigma size in both years, while growth patterns in the remaining cultivars exhibited some variation over the two years with 2022 showing less variability between MS cultivars than in 2021. In relation to ovary size, I observed two distinct groups: the first comprises MS cultivars GSS1, 24512, and 24516, which formed wider ovaries that reached a maximum estimated diameter of 4.16 and 4.22 mm in 2021 and 2022, respectively. The second group exhibited narrower ovaries, with maximum widths of 3.56 and 3.57 mm in 2021 and 2022 (

Figure 3.10C and D). As seen for stigma size, this latter group reached its maximum size, on average, 3 to 6 days earlier than the MS cultivars with broader ovaries, suggesting a potential correlation between carpel size and longevity. Additional analyses uncovered a positive correlation between carpel longevity and both stigma size ( $R = 0.6$ ) and ovary diameter ( $R = 0.23$ ; Figure 3.11). This result implies that larger carpels are associated with increased longevity leading to delayed carpel deterioration. However, the latter correlation was weaker and not statistically significant, indicating that a larger sample size could better address the hypothesis regarding the potential association between carpel size and longevity.

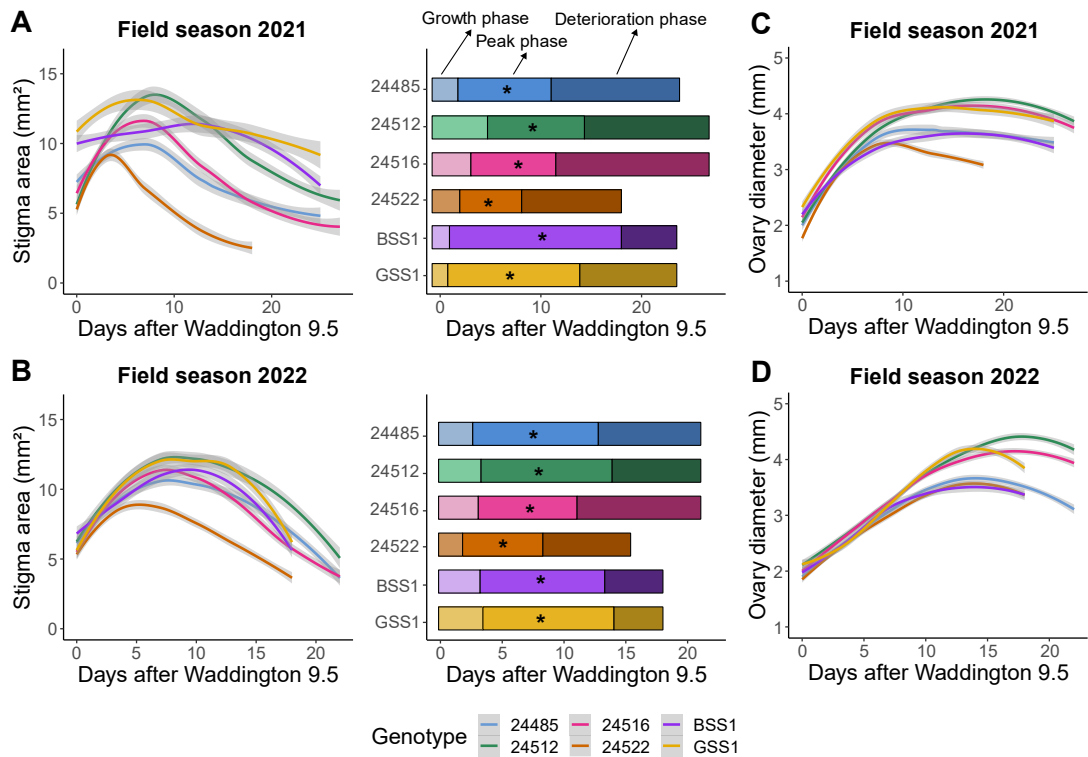


**Figure 3.10 Phenotypic quantification of carpel development in the female parents across the 2021 and 2022 field seasons.**

(A, B) Developmental patterns of stigma area ( $\text{mm}^2$ ) and bar charts illustrating the growth, peak and deterioration phases represented in days after Waddington 9.5. The end of the deterioration phase is marked by the last sampling point and asterisks indicate maximum stigma area. (C, D) Developmental patterns of ovary diameter (mm). As for Figure 3.8C, polynomial regression models are shown for stigma area and ovary diameter. Five carpels from each of six plants were sampled at each timepoint.



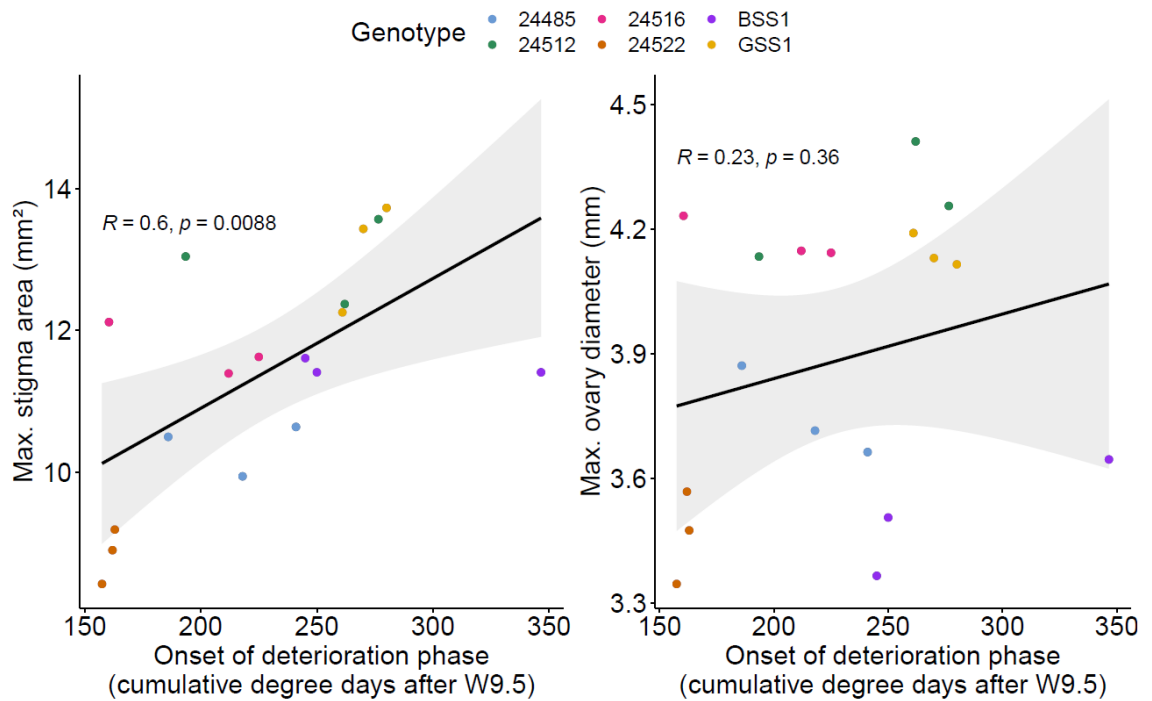


**Figure 3.11 Relationship between carpel longevity and carpel size.**

Scatter plots display the relationship between the onset of deterioration phase and maximum stigma size (left) and maximum ovary diameter (right) for all six MS cultivars selected. The onset of the deterioration phase is measured in cumulative degree days after W9.5 to accommodate variation in temperatures between field seasons 2020, 2021 and 2022 ( $n = 3$ ). Regression lines are shown along with Pearson correlation coefficients and significance levels. Grey shaded area represents confidence intervals for the regression lines.

### 3.4.2. Evaluation of female performance in relation to hybrid seed set and stigma longevity

Following the assessment of stigma and ovary traits, I tested hybrid seed set performance of the six MS cultivars selected by allowing cross-pollination to happen during multiple time windows starting after Waddington 9.5 up to 10 to 15 DAW9.5 (Figure 3.12A). To control the time of pollination, I used pollen proof barriers to prevent pollen flow between pollen donors and MS cultivars (Figure 3.2 and 3.3). Cross-pollination was subsequently allowed upon removing the barriers, leading to progressively shorter pollination windows as the barriers were removed during the pollen-shedding period.

In a broad overview, I observed substantial variation in hybrid seed set between 2021 and 2022, with a mean difference of one grain per spikelet greater in 2022 than in 2021 ( $0.94 \pm 0.114$ ;  $P$  value  $< 0.0001$ ). Given pollen dispersal is influenced by variations in

humidity during the day, it is possible that the lower seed set in 2021 was caused by increased humidity brought on by precipitation for a significant portion of the time course (Figure 3.4; Vogler et al., 2010). On average, hybrid seed set exhibited a slow yet statistically significant decline over time after W9.5, characterised by a negative rate of  $-0.05 \pm 0.02$  grains per spikelet  $\text{DAW9.5}^{-1}$  ( $P$  value = 0.007; Table 3.3). However, the presence of a significant “pollination date x MS cultivar” interaction term indicated that the time of pollination had a non-uniform effect on seed set across the different MS cultivars. Specifically, MS cultivar 24522 was the only cultivar influenced by the timing of pollination, displaying a significant decline in hybrid seed set (linear slope =  $-0.06 \pm 0.03$  grains per spikelet  $\text{DAW9.5}^{-1}$ ;  $P$  value = 0.033; Table 3.3). Conversely, for the remaining MS cultivars, the rate at which seed set varied did not significantly differ from zero (Table 3.3). Overall, our findings provide limited evidence to support the hypothesis that the duration of stigma receptivity or the longevity of the female parent has a substantial impact on hybrid seed set in a free pollination experiment spanning ten to 15 DAW9.5.

**Table 3.3 Regression table summarising linear mixed model results.**

Fixed effect coefficients along with their standard errors (in parenthesis) and P values are given for each relationship between the dependent variable (grain number per spikelet) and the independent variables. Key model fit statistics are also provided: Log Likelihood, Akaike Information Criterion (AIC), and Bayesian Information Criterion (BIC). \*p<0.05; \*\*p<0.01; \*\*\*p<0.001.

	<b>Dependent variable:</b>
	<b>Grain number per spikelet</b>
<i>Pollination date</i>	-0.054** (-0.02)
<i>MS 24512</i>	-0.451* (-0.19)
<i>MS 24516</i>	-0.164 (-0.192)
<i>MS 24522</i>	0.161 (-0.208)
<i>MS BSS1</i>	-0.485** (-0.169)
<i>MS GSS1</i>	-0.112 (-0.17)
<i>Year</i>	0.935*** (-0.114)
<i>Pollination date x MS 24512</i>	0.031 (-0.026)
<i>Pollination date x MS 24516</i>	-0.038 (-0.026)
<i>Pollination date x MS 24522</i>	-0.056* (-0.026)
<i>Pollination date x MS BSS1</i>	0.035 (-0.026)
<i>Pollination date x MS GSS1</i>	0.019 (-0.026)
<i>Constant</i>	-1888.106*** (-230.121)
<i>Observations</i>	1684
<i>Log Likelihood</i>	-1283.977
<i>Akaike Inf. Crit.</i>	2599.953
<i>Bayesian Inf. Crit.</i>	2686.816

The maintenance of seed set across the complete sampling time course raised concerns about the hybridity of the seeds, especially in light of the well-known challenges associated with achieving complete sterility in male sterility systems, particularly within the “BLue Aleurone (BLA)” system (Darvey et al., 2020; Chapter 1 section 1.3.1.2), which was used to develop MS cultivars 24485, 24512, 24516 and 24522. This concern was supported by the identification of seeds in our negative controls, where pollination barriers remained in place throughout the experiment (i.e., preventing any cross-pollination), indicating that all harvested seeds resulted from self-pollination. Notably, MS cultivars 24522 and 24485 appeared to be more significantly affected by residual

fertility (Figure 3.12A). To better understand how this might impact the interpretation of our results, I selected a random sample of the harvested F<sub>1</sub> seeds from the test plots in 2021 and 2022 for hybridity assessment (Figure 3.12B and C). While BLA-derived MS cultivars displayed the highest percentage of self-pollinated (i.e., homozygous) seeds, all hybridity levels significantly exceeded the 85% threshold previously used by Schneider et al. (2021) to classify seed set data as high-quality (hybrid) data. Thus, we can conclude that hybrid seed production, and therefore, flower receptivity, remained uniform across the various pollination windows tested, with the sole exception being a slight reduction in hybrid seed set observed in MS cultivar 24522, which is likely attributed to its premature stigma deterioration (Figure 3.10). This ability of MS cultivars to sustain seed set performance for more than 10 DAW9.5 is further exemplified by the positive controls implemented in 2022, where no pollen barriers were used and seed set levels closely mirrored those of plants pollinated at 10 DAW9.5 and after (Figure 3.12A).

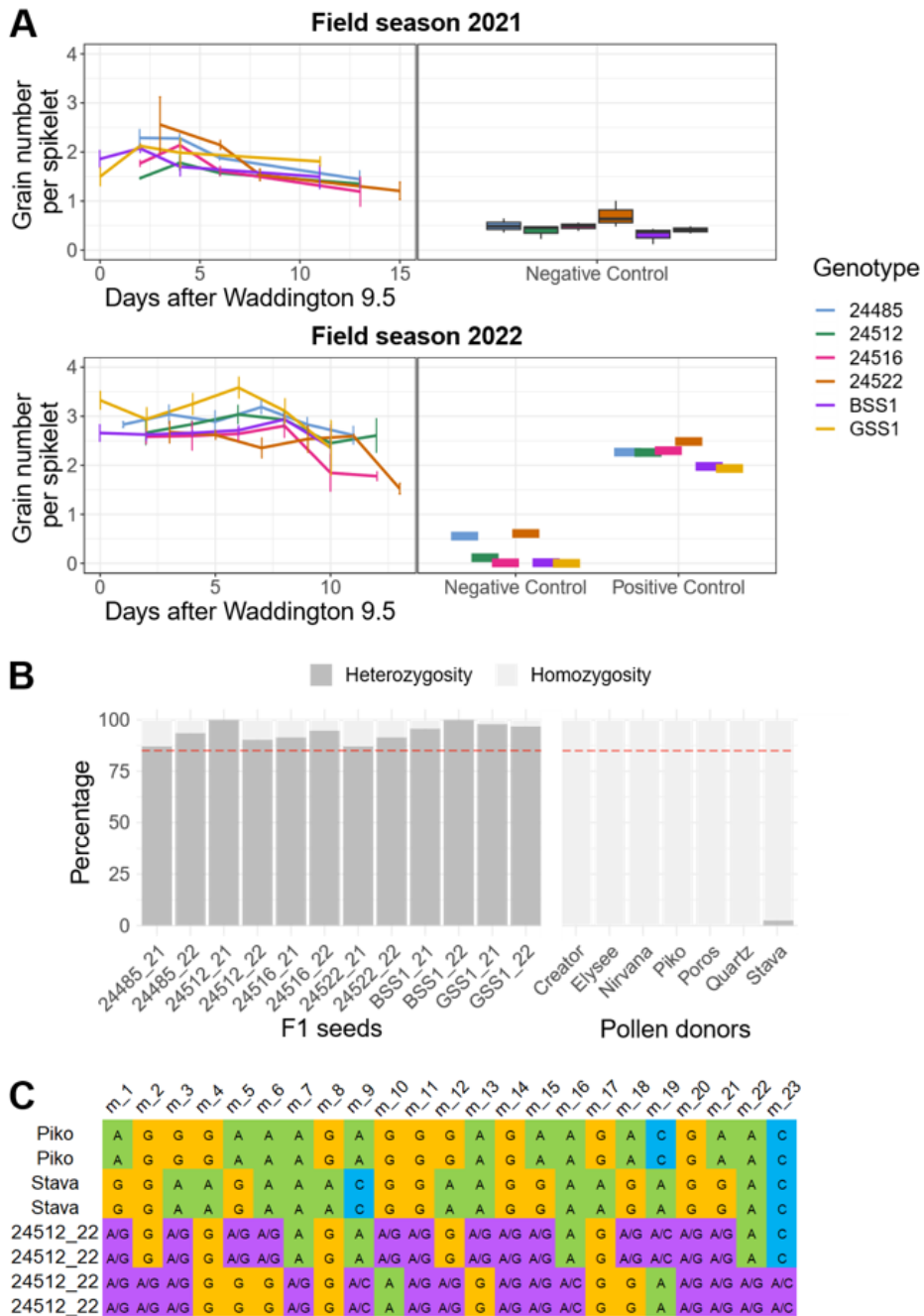


**Figure 3.12 Temporal dynamics of hybrid seed yields and their hybridity levels.**

(A) Line graphs illustrate the effect of pollination time on seed set (grain number per spikelet) for the different MS cultivars. Error bars denote the s.e.m. for each pollination window. In 2021 and 2022, four and six pollination windows were examined, respectively. Between five and ten spikes were sampled in each replication ( $n = 3$ ). Negative and positive controls are depicted as box plots. In 2021, box plots display the middle 50% of the data with the median indicated by a horizontal line. Whiskers represent datapoints within 1.5 times the interquartile range ( $n = 3$ ). In 2022, box-like plots show single data points for negative and positive controls ( $n = 1$ ). (B) Bar plots show, in dark grey, the percentage of seeds with four or more heterozygotic base calls (i.e., hybrid seeds) and, in light grey, percentage of seeds with less than four heterozygotic base calls (i.e., self-pollinated seeds). The left section represents F<sub>1</sub> seeds harvested from different MS cultivars in 2021 (\_21) and 2022 (\_22). Right section represents seeds used as pollen donors.

Dashed red line shows 85% threshold. (C) Schematic representation of the genotyping data. Each column corresponds to one of the 23 single nucleotide polymorphism markers (m<sub>i</sub>), and rows represent individual seeds. Heterozygotic base calls are colour-coded in purple.

### 3.4.3. Spatial distribution of hybrid seed set along the inflorescence

In this study, I focused exclusively on the developmental dynamics of carpels situated within central spikelets. However, it is well-known that maturation of the wheat florets (anthesis) begins in the middle of the spike and progresses bidirectionally towards the top and bottom of the spike, resulting in a spike completing anthesis over a 2 to 6 day period (Lukac et al., 2012; Percival, 1921; Waines & Hegde, 2003). This asynchronous pattern is mirrored in stigma development, with stigma from florets of central spikelets being more advanced than those at the apical and basal sections (Figure 3.13).

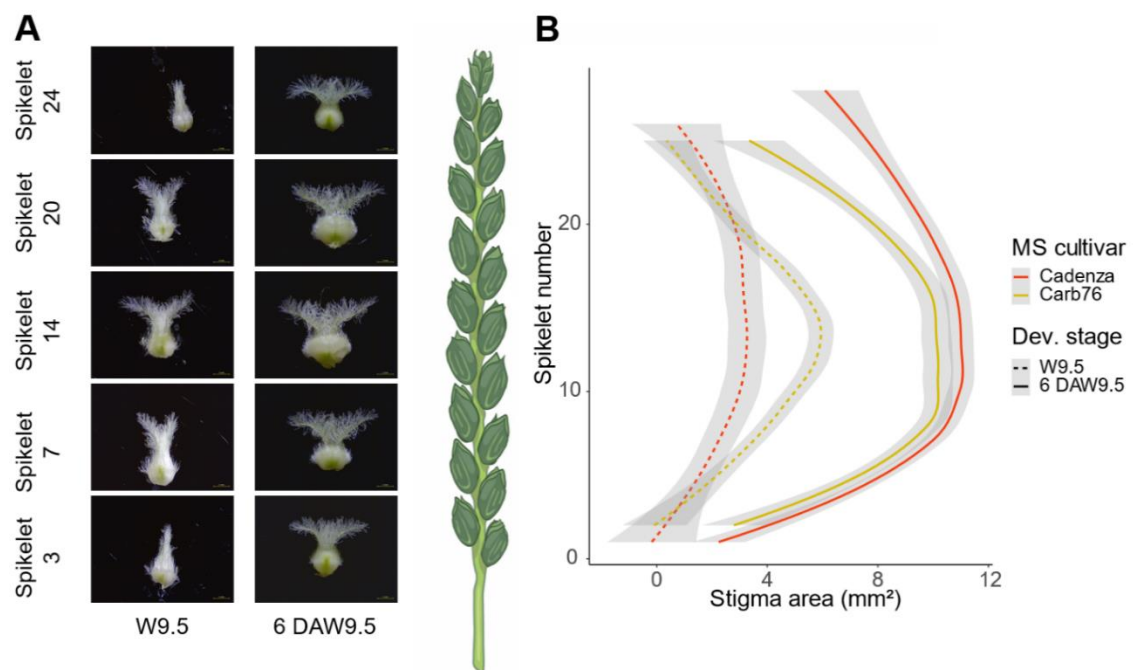


**Figure 3.13 Bidirectional gradient of carpel development along the spike.**

(A) Representative images of carpels of MS cultivar Cadenza at Waddington 9.5 (W9.5) and at 6 days after W9.5 (DAW9.5). (B) Dynamics of stigma development along the spike for MS spring cultivars Cadenza and Carb76 under glasshouse conditions ( $n = 3$ ). Polynomial regression models are shown for stigma area of florets 1 and 2.

To gain deeper insights into how these developmental gradients might have influenced both the temporal and spatial distribution of hybrid seed set, I dissected spikes into three sections: apical (top 25% spikelets), central (50%) and basal (bottom 25%; Figure 3.14A). By analysing the contribution of the different sections to hybrid seed production, I observed that grain number per spikelet was unevenly distributed along

the spike, with central spikelets producing 0.5 and 0.4 grains per spikelet more than their apical and basal counterparts ( $P$  value  $< 0.0001$ ). Spatial distribution of hybrid seeds therefore mimicked that of selfed seeds, where central spikelets produce the most grains (Philipp et al., 2018). Moreover, I found that the temporal dynamics of grain number per spikelet differed between sections, and these dynamics were further influenced by the MS cultivar tested. To illustrate these complex interactions, we calculated the linear slopes for the temporal progression of grain number per spikelet within each section and MS cultivar combination while accounting for the variability observed across years (Figure 3.14B; see Materials and Methods section 3.3.5 for full models). Overall, we saw that hybrid seed production in apical and basal sections followed very similar trends, with slopes close to zero (Figure 3.14B). This means that the number of grains formed in these apical and basal spikelets was consistently maintained over the sampled time, and hence, flowers were receptive to pollen across the complete time course. Notably, basal spikelets seemed to decrease at a slightly slower rate than apical spikelets, aligning with the progression of flowering (De Vries, 1971), although the difference is minimal (linear slope apical section =  $-0.03 \pm 0.02$ ; linear slope basal section =  $-0.02 \pm 0.02$ ). In contrast, central sections showed a more rapid decrease in hybrid seed set (linear slope:  $-0.07 \pm 0.02$ ), suggesting a significant decline at later pollination dates, likely explained by the gradual loss of flower receptivity as stigmas age. However, the lack of available pollen beyond these later dates did not allow for the extension of the time course to further investigate these trends. As anticipated by previous results (Table 3.3), not all MS cultivars behave similarly over time. For example, the reduction in hybrid seed set in MS cultivar 24522 can be attributed to a collective drop in all three sections as slopes are very similar to each other (linear slope apical section =  $-0.08 \pm 0.02$ ; central section =  $-0.12 \pm 0.02$ ; basal section =  $-0.07 \pm 0.02$ ). Additionally, I note that some MS cultivars showed a decline in seed set in the central section, while spikelets in apical and basal sections continued to perform equally well during the time course, as exemplified by 24516 and 24485. Finally, BSS1, GSS1 and 24512 displayed consistent seed set across all three sections, which aligns with a prolonged stigma lifespan (Figure 3.10A). In summary, we observe that hybrid seed production remains relatively stable in the apical and basal sections of the spike, whereas central spikelets exhibit a more rapid decline, likely due to their more advanced stigma developmental age. However, it is important to emphasise that these differences are minimal and the ability of the MS cultivars to

equally sustain seed set performance over the sampled period is not significantly affected.

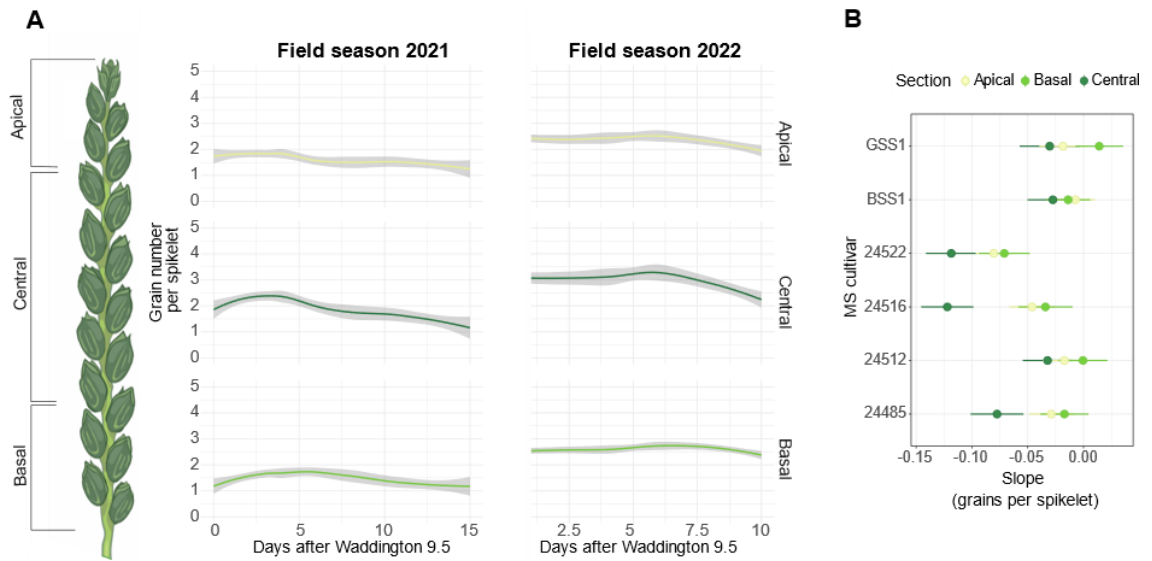


**Figure 3.14 Spatial and temporal distribution of hybrid seed set.**

(A) Average association between hybrid seed set (grain number per spikelet) and the time of pollination per each section of the spike (i.e., apical, central, and basal) in 2021 and 2022. Polynomial regression models are shown. (B) Forest plot illustrates the progression of hybrid seed set (slope) for each section and MS cultivar. Horizontal lines represent the 95% confidence intervals.



## 3.5. Discussion

Extending the duration of stigma receptivity in the female or male sterile (MS) parent has been commonly suggested as an important breeding target for improved hybrid seed production (De Vries, 1971; Selva et al., 2020). However, a noticeable knowledge gap exists in the literature, with very limited studies investigating the life cycle of the unpollinated stigma and its contribution to hybrid seed production. This chapter addresses this void by investigating how the longevity of the wheat stigma in a MS parent influences out-crossing under field conditions when plants are exposed to free pollination.

### 3.5.1. Potential link between carpel size and carpel longevity

An aim of this chapter was to identify MS cultivars with varying stigma longevities through detailed phenotypic characterisation of carpel development in the absence of pollination (Figure 3.8 and 3.10). From the subset of MS cultivars selected, we found that the majority entered the phase of stigma deterioration between 12 and 14 DAW9.5; with the sole exception of 24522, which initiated stigma deterioration as early as 9 DAW9.5 (Figure 3.8A and B). These MS cultivars also showed differences in the magnitude of carpel growth. Interestingly, larger stigmas and wider ovaries were mostly linked to MS cultivars featuring delayed carpel deterioration, such as 24512 and GSS1. On the contrary, those with more premature deterioration, like 24522 and 24485, displayed smaller carpels.

These initial observations prompted questions about a potential association between carpel size and longevity, which was partially substantiated by additional correlation analyses (Figure 3.11). While it is premature to speculate on the biological implications of these findings, the suggested association between carpel size and the longevity of the reproductive organ aligns with a characteristic of the "selfing syndrome". This syndrome, consequence of the shift from cross to self-fertilisation mating system, often involves substantial morphological changes, such as the reduction in flower size and life span (Lesaffre & Billiard, 2020). Following this logic, it is reasonable to hypothesise that the selection of larger carpels – already a target for improved pollen access due to larger stigmatic area and wider ovary (El Hanafi et al., 2020; Okada et al., 2017) – may also lead to indirect selection of longer carpel longevities.

### 3.5.2. The challenges of open pollination experiments

The scarcity of studies investigating a role of stigma receptivity on cross-pollination and hybrid seed production can be attributed to the myriad of challenges inherent in conducting such experiments in the field. Cross-pollination is very dependent on the climatic conditions prevailing at the time of anthesis, which makes certain geographical areas unsuitable for pollination (Keydel et al., 1979). For instance, the range and quantity of pollen dispersal is influenced greatly by the direction and speed of the wind (downwind vs crosswind), sunlight, temperature, precipitation levels, and relative humidity during anthesis (De Vries, 1971; Pickett, 1993). Interestingly, this phenomenon aligns with the “pollination Moran effect” hypothesis in population ecology, which predicts that weather conditions affect wind-pollination efficiencies and can result in bumper crops (Koenig, 2002). Together, this information provides context for the significant increase in average hybrid seed yield observed in 2022 compared to the preceding year, when lower temperatures and higher precipitation was reported (Figure 3.4 and 3.12). Such notable fluctuations in hybrid seed yield across field seasons are not unique and have been documented in other studies, where environmental factors contribute up to 65% of the total variation in hybrid seed yield (Schneider et al., 2021). Another challenge stems from the limited availability of late flowering pollinators. This constraint made it impractical to study hybrid seed set performance of female parents during the deterioration phase as fresh pollen became unavailable beyond the 10 to 15 DAW9.5 pollination window (Figure 3.12). Alternatively, different sowing dates could be used to alleviate this limitation, allowing for a more extended study period. While no significant differences in height were noted between the MS plant and the pollinators, it is relevant to highlight that cross-pollination is improved when the pollinator is taller than the MS cultivar, as it is easier for the pollen to travel to the female flower (Würschum et al., 2018). Finally, additional challenges impacting the interpretation of open pollination studies are associated with the female parent. As previously mentioned, residual male fertility represents a recurrent issue in wheat male sterility systems (Kempe & Gils, 2011), inevitably resulting in some degree of selfed seed contamination within the test material, which in this case, was minimal (Figure 3.5 and 3.12B). Some other aspects that have not been considered and could significantly influence the success of cross-pollination and hybrid seed set are related to variability in pollen accessibility among MS cultivars influenced by relative plant height and the openness of the floret, both affecting optimal pollen

receptive abilities of the female parent (Selva et al., 2020). Stigma receptivity has generally been measured by seed set on the male sterile, however, it is important to acknowledge that seed set is influenced by factors beyond stigmatic receptivity or longevity. Alternative methods, discussed in Chapter 5 (section 5.2), could be employed to exclusively study the pollen germination capacities of the wheat stigma.

### 3.5.3. The duration of stigma receptivity does not represent a major barrier in hybrid production

Despite all the challenges presented by open pollination experiments, we found a remarkable consistency in the patterns of hybrid seed set across MS cultivars and field seasons (Figure 3.12). Surprisingly, there was no substantial reduction in hybrid seed set during the 10 to 15 day pollination time course, suggesting sustained stigma receptivity up to 10 DAW9.5. Due to the lack of viable pollen at later time points, it was not possible to extend the time course to study the reproductive potential of the stigma during the deterioration phase; therefore, this hypothesis remains untested. Additionally, we showed that the overall absence of reduced hybrid seed set is partially masked by asynchronous nature of stigma development along the spike (Figure 3.13 and 3.14), with central spikelets displaying a slightly greater drop in seed set compared to younger spikelets in apical and basal regions of the spike. Despite the biological relevance of understanding the dynamics of hybrid seed set during the latest stages of stigma development, from an agronomic standpoint, it is of minor significance. In commercial hybrid programmes, anthesis (i.e., pollen release) mostly occurs within a 10-day window, ranging from five days before ear emergence of the female parent (approximately W9.5) to five days after ear emergence (Schneider et al., 2021; Figure 3.15). If we take this timeframe into account, we can conclude that stigma receptivity does not represent a major barrier in hybrid seed production, as female parents are able to sustain similar levels of seed set up to 10 DAW9.5. Thus, future breeding efforts aimed at improving cross-pollination efficiencies should focus on other desired qualities of the female parent, such as ovary and stigma size and floret openness.

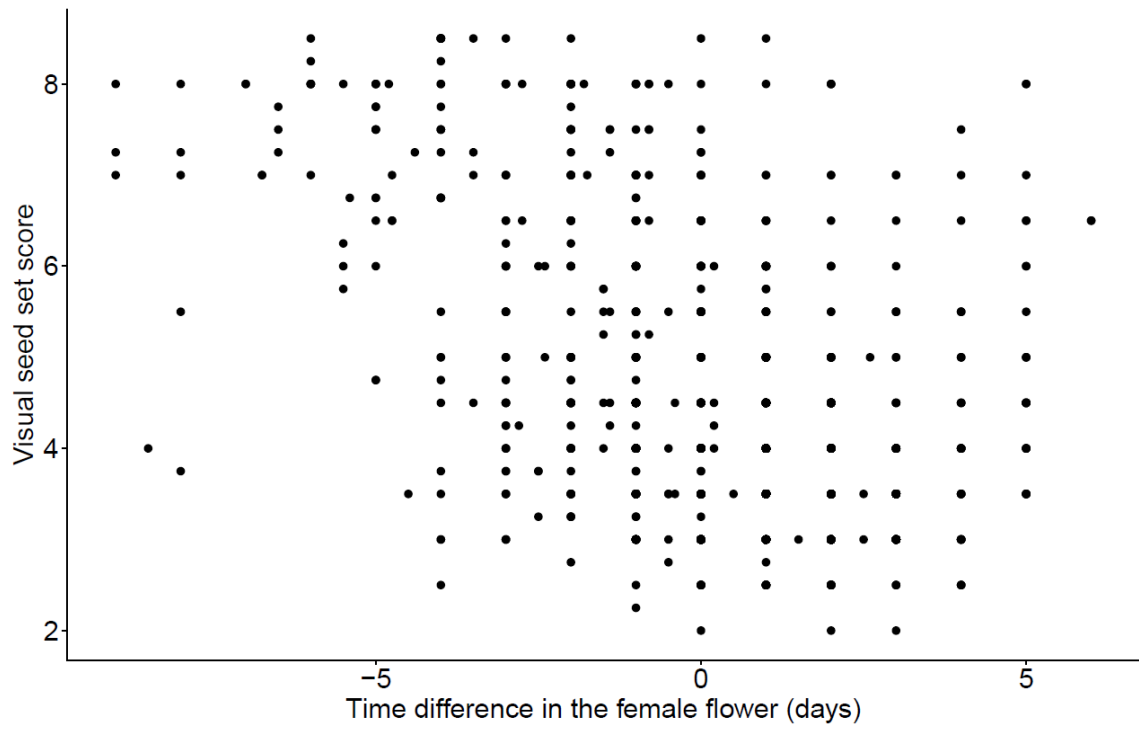


**Figure 3.15 Visual seed set scores for the 2,428 unique combinations.**

Visual seed set scores range from 1 (seed set similar to a fully fertile spike) to 9 (no seed set). X-axis indicates difference in flowering dates between the female parent and pollen donor. Negative values represent hybrid combinations where anthesis of the pollen donor started “n” days before full ear emergence of the female; 0 indicates that pollination coincides with ear emergence of the female parent; and positive values indicate pollination started “n” days after full ear emergence of the female.

## **4. Genetic mechanisms regulating stigma development and senescence in the absence of pollination in wheat: insights from transcriptomics and functional characterisation**

### **4.1. Summary**

In the absence of pollination, a deliberate developmental programme terminates stigmatic receptivity in ageing flowers limiting the time span in which pollination, fertilisation, and seed set can occur. In this chapter, I performed RNA-Seq on unpollinated stigmas of male sterile cultivars to investigate the genetic mechanisms that potentially influence stigma development from its early phases of stigmatic growth (Waddington stage 9) to its complete deterioration at 18 days after Waddington Stage 9.5. Our data revealed three major waves of gene expression coinciding with the previously defined phases of stigma development: growth, peak and deterioration. These phases, additionally, are characterised by the presence of many wheat genes that have been associated with key aspects of cellular growth, signal transduction and cell death in wheat and in other species. A more in-depth comparative transcriptomics examination of the transcription factors (TF) expressed during the deterioration phase resulted in a specific set of 66 TFs predominantly expressed in senescent stigmatic tissues. Among these, the wheat orthologs of the Arabidopsis NAC TFs *KIRAI* (*KIR1*) and *ORESARAI* (*ORE1*), stood out as candidate transcriptional regulators of stigma senescence. Phenotypic characterisation of loss of function *kir1* and *ore1* wheat mutants, under controlled environmental conditions, revealed a two-days extension of stigma longevity in *ore1* mutants accompanied by an increase of stigma receptivity to pollen in *ore1* and *kir1* mutants. However, the moderate extension of stigma longevity in the mutants was not accompanied by higher seed set at later time points, indicating that additional processes might participate in the control of female fertility. These phenotypic differences were not replicated under field conditions, highlighting the importance of additional field-based experiments.

## 4.2. Introduction

As previously described in Chapters 1 and 2, stigma development in the absence of pollination represents a complex process that includes cell growth and proliferation, stigma maturation, and the induction and execution of senescence once stigmas have reached a specific age. In wheat, this well-defined developmental pattern is consistently replicated across genotypes and field seasons (Chapter 2) and resembles that of the unpollinated stigmas of maize, peas, and *Arabidopsis* (Bassetti & Westgate, 1993; Carbonell-Bejerano et al., 2010; Vercher et al., 1984). Collectively, this implies an active control of the trait.

Additional studies in maize and *Arabidopsis* (Carbonell-Bejerano et al., 2010; Gao et al., 2018; Šimášková et al., 2022) have shown that viability of the unpollinated stigma is indeed terminated by a deliberated developmental programme that activates transcription factor (TF) cascades leading to the cessation of stigma vital functions. Many of the senescence-associated genes found to be differently expressed during the latest stages of stigma development are also central regulators of leaf and petal senescence (Shahri & Tahir, 2014) drawing interesting parallelism between both processes at a transcriptional level. For example, among the family of NAC TFs, expression of *ORESARAI* (*ORE1*, *ANAC092*) has been shown to be concurrently upregulated with leaf and stigma aging in *Arabidopsis* (Balazadeh et al., 2010; Gao et al., 2018; Kim et al., 2014; Kim et al., 2009). These studies showed that *ore1* dominant loss-of-function mutants lead to delays in loss of chlorophyll content in aged leaves and a remarkable extension of stigma life span in the absence of pollination with a moderate extension of seed set in aged flowers. However, its wheat orthologs were not found to be expressed differentially during a 23-day leaf senescence time course (Borrill et al., 2019), highlighting the likelihood that many of the genes influencing senescence might not be evolutionarily conserved between the two species. A second NAC TF identified to positively regulate age-dependent senescence in unpollinated stigmas was the previously uncharacterised *KIRAI* (*KIR1*, *ANAC074*). *KIR1* was discovered to be a potent activator of programmed cell death processes, and its inducible overexpression in the stigma results in the early senescence of the organ, subsequently leading to a loss of reproductive potential. Conversely, its knockout mutants exhibited a notable extension of the fertility window by four days in maize flowers and one day in *Arabidopsis* flowers (Gao et al., 2018; Šimášková et al., 2022). To date, only these two genes, *ORE1*

and *KIR1*, have been described to regulate stigma senescence in the absence of pollination in *Arabidopsis* and maize, and to our knowledge, no such experiments have been performed in male sterile (MS) cultivars of wheat. Therefore, a deeper understanding of the network of transcription factors controlling this process is essential to fully grasp the potential of altering the onset of stigma senescence in wheat.

To investigate the genetic mechanisms that potentially influence the mid to late development of the unpollinated stigma in wheat, I carried out transcriptome profiling of different MS cultivars. In addition, I used comparative transcriptomics to aid the identification of a small set of differentially regulated genes that represent interesting candidates for downstream analyses. Finally, I performed functional validation of the prime regulators of stigma senescence, *KIR1* and *ORE1*, by generating loss of function mutants in hexaploid wheat.

## 4.3. Material and methods

### 4.3.1. Germplasm

I used the winter NMS (nuclear male sterile) hexaploid wheat cultivars 24485, 24512 and 24522 and the CMS (cytoplasmic male sterile) cultivar BSS1 for RNA sequencing experiments. CMS and NMS cultivars were provided by Syngenta (Whittlesford, UK) and KWS (Thriplow, UK), respectively. I selected cultivar 24485 as a representative cultivar to describe the transcriptomic landscape of the developing stigma in the absence of pollination under field conditions. Additionally, I selected cultivars 24512, 24522 and BSS1 for RNA sequencing based on the contrasting carpel development profiles they showed during consecutive field seasons in 2020 and 2021 (Chapter 2, Figure 2.10).

For the validation of *KIR1* (*TraesCS2A02G382400*, *TraesCS2B02G399700*, *TraesCS2D02G378800*) and *ORE1* (*TraesCS2A02G338300*, *TraesCS2B02G343600*, *TraesCS2D02G324700*) as regulators of age-induced senescence in wheat stigmas, I selected eight mutant lines from the Cadenza TILLING population (C1797, C1928, C0217, C0100, C0127, C1441, C1588, C0113; <https://www.seedstor.ac.uk/>) with either nonsense or missense mutations (Table 4.1 and Figure 4.15). As illustrated in Figure 4.15C (results section), I crossed mutant lines to obtain triple homozygous mutant populations for *KIR1* and *ORE1*. For each of the crosses, heterozygous seeds were left to self-pollinate to generate F<sub>1</sub>S<sub>1</sub>, F<sub>2</sub>S<sub>1</sub> or BC<sub>1</sub>S<sub>1</sub> (backcross 1) homozygous populations. BC<sub>1</sub>S<sub>1</sub> triple homozygous mutants (*ORE1-A1B1D1*, *ore1-alb1d1*, *KIR1-A1B1D1*, *kir1-alb1d1.1*) were finally selected for phenotypic evaluation.



**Table 4.1 Predicted consequences of the selected TILLING mutations in the protein.**

Data obtained from Ensembl Plants based on Krasileva et al., 2017.

<b>Gene name</b>	<b>Gene ID</b>	<b>Line</b>	<b>Transcript variant</b>	<b>Consequence type</b>	<b>Position in protein</b>	<b>Amino acid substitution</b>
<i><b>ORE1-B1</b></i>	<i>TraesCS2B02G343600</i>	C1588	1	stop gained	56/355	W/*
<i><b>ORE1-A1</b></i>	<i>TraesCS2A02G338300</i>	C1441	1	stop gained	57/354	W/*
<i><b>ORE1-D1</b></i>	<i>TraesCS2D02G324700</i>	C0113	1	stop gained	8/353	Q/*
<i><b>KIR1-A1</b></i>	<i>TraesCS2A02G382400</i>	C1797	1	stop gained	177/310	W/*
			2	stop gained	148/281	W/*
<i><b>KIR1-B1</b></i>	<i>TraesCS2B02G399700</i>	C1928	1	stop gained	53/307	W/*
			2	stop gained	53/278	W/*
		C0217	1	stop gained	171/315	W/*
			2	intron variant	-	-
<i><b>KIR1-D1</b></i>	<i>TraesCS2D02G378800</i>	C0100	1	missense variant	59/315	A/T
			2	missense variant	59/278	A/T
		C0127	1	missense variant	84/315	R/H
			2	missense variant	84/278	R/H

### 4.3.2. Field and controlled environment experiments

For the RNA sequencing experiments, plants were grown at John Innes Centre Church Farm (Bawburgh, UK; 52°37'50.7"N 1°10'39.7"E) in a randomised complete block design (RCBD) with two replicates (1 m<sup>2</sup> plots) per MS cultivar in 2020, and three replicates in 2021 field season (Chapter 2, Figure 2.1). To avoid unwanted cross-pollination, sterile rye barriers were grown surrounding the MS plots. The time course in 2020 started at W9, while in 2021 the first sampling point was 3 DAW9.5. In both time courses, visual stigma deterioration marked the last sampling point (18 DAW9.5).

In both field seasons, I tagged main spikes when carpels in the outer florets (floret 1 and 2) of central spikelets reached W9.5 (Waddington et al., 1983), shortly after full ear emergence (Zadoks' growth stage 59; Zadoks et al., 1974). Additionally, in 2020, W9 samples were collected a few days before W9.5, mostly coinciding with Zadoks' growth stage 51 (i.e., first spikelets visible above flag leaf). At the time of sampling, I cut two tillers between the uppermost and penultimate internode per plot (n per time point in 2020 = 4; in 2021 = 6) and transported them in water to the laboratory for stigma dissection. For each spike, I dissected five to eight stigmas (size dependent) from the primary and secondary florets of the central four spikelets and immediately stored them in DNA/RNA Shield solution (ZYMO Research Cat. R1100-50) and kept them at -20 °C to maintain nucleic acid integrity. All stigma dissections were carried out between 1100 and 1500 h and within 90 minutes after trimming the tiller. Note that stigma samples include both the stigma and style, as these structures are intimately linked in wheat. In 2020, an extra step prior to sample fixation in DNA/RNA Shield was added for image acquisition of dissected carpels under a stereomicroscope (ZEISS Stemi 305 with a 1.2 Megapixel integrated colour camera).

For the phenotypic characterisation of *KIR1* and *ORE1*, I grew mutant (*kir1*, *ore1*) and wild-type (*KIR1*, *ORE1*) BC<sub>1</sub>S<sub>1</sub> plants in 1 L pots in a controlled environment room (CER) at 20 °C (day) and 16 °C (night) with a 16-hour photoperiod and 70% humidity. For each plant, I emasculated the first and second spike when carpels in the outer florets of central spikelets reached W9.5 (Figure 4.1A). To accelerate the emasculation process, all inner florets as well as apical and basal spikelets were removed and only the outer florets of eight central spikelets remained (Figure 4.1B). Spikes were then tagged and bagged to avoid cross-pollination. BC<sub>1</sub>S<sub>1</sub> mutant seeds (including single mutant *kir1-al*) and the parental line Cadenza were sown in February 2023 at the John Innes

Centre Church Farm for field evaluations in a RCBD with three replicates (plots). Following the same approach, I hand emasculated eight main spikes per plot.



**Figure 4.1 Hand emasculations of mutant populations.**

(A) Developmental stage at which carpels were emasculated. Scale bar = 1 mm. (B) Spike appearance after emasculatation.

Sections 4.3.3 to 4.3.8 outline the workflow used for transcriptomic analyses, with a visual summary provided in Figure 4.2.

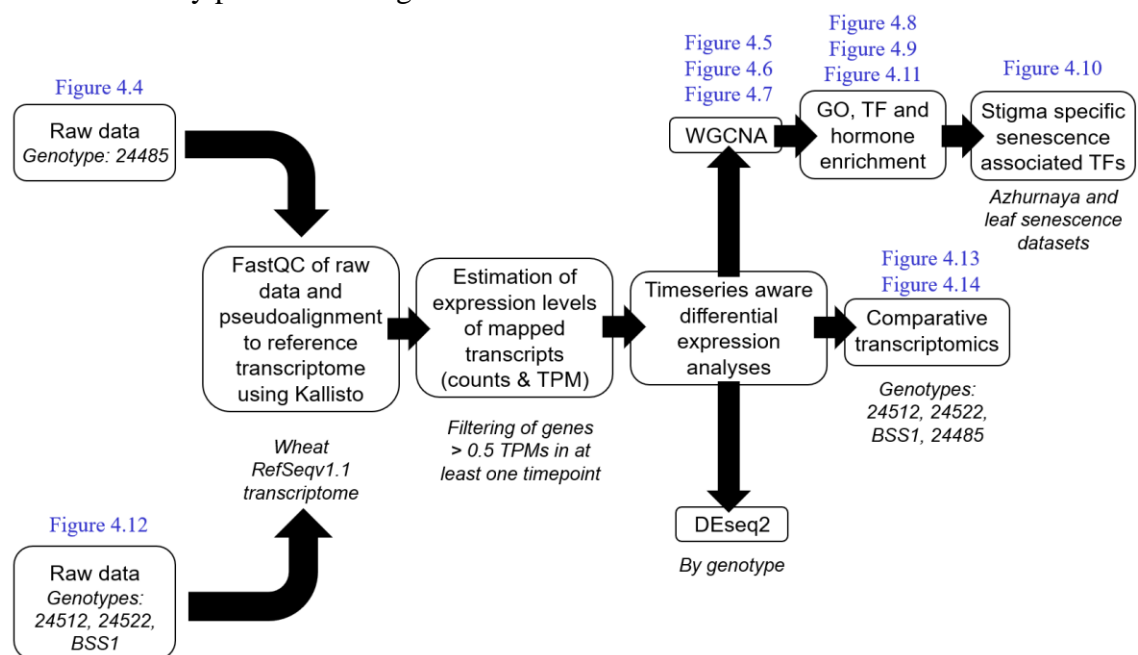


**Figure 4.2 Workflow employed for conducting differential expression analyses using RNA sequencing data.**

### 4.3.3. RNA extraction and sequencing

RNA extraction and sequencing was performed as described in Chapter 2, section 2.3.6. The 18 DAW9.5 samples in MS line 24522 had severely deteriorated stigmas, and none of the replicates yielded high-quality RNA; these samples were therefore excluded from further analyses.

### 4.3.4. Mapping of raw reads

Mapping of raw reads was carried out as described in Chapter 2, section 2.3.6.

### 4.3.5. Principal component analysis (PCA)

PCA was used to determine whether the samples exhibit more variation between the different time points than between biological replicates of the same time point. To remove potential differences in sequencing depths in the different RNA libraries, I used the `varianceStabilizingTransformation` function from the R package DESeq2 (Love et al., 2014) to normalise count data. I used `plotPCA` function to visualise the segregation of the samples based on the top two principal components.

### 4.3.6. Differential gene expression analysis

#### 4.3.6.1. *Weighted gene co-expression network analysis (WGCNA)*

To identify genes with similar expression patterns I used R package WGCNA v1.69 (Langfelder & Horvath, 2008, 2012) for hierarchical clustering of normalised gene counts. For the construction of the network, I used the function `pickSoftThreshold` to calculate the soft power threshold ( $\beta$ ) as the first value that crosses a scale-free topology fit index of 0.9. However, the 0.9 threshold was not reached indicating there might be strong expression changes between the different time points. Following the guidelines of the WGCNA manual

(<https://horvath.genetics.ucla.edu/html/CoexpressionNetwork/Rpackages/WGCNA/>), I selected two soft thresholds according to the number of samples within the dataset ( $\beta = 8$  for signed hybrid networks) and the highest reasonable power for signed hybrid networks ( $\beta = 15$ ). For block-wise network construction and module detection, I used the following parameters: `maxBlockSize = 10,000` genes, `power = 8` and `15`, `NetworkType = "signed hybrid"`, `TOMType = "unsigned"`, `minModuleSize = 30` genes,

corType = “bicor”, maxPOutliers = 0.1, mergeCutHeight = 0.25, detectCutHeight = 0.995 and deepSplit = 2. The network constructed using  $\beta = 8$  detected 42 modules with two modules containing over 18,000 genes each, 19 modules with less than 100 genes per module and 13,331 genes that were unassigned (i.e., not differentially expressed; ME = 0; Figure 4.3A). Conversely, when constructing the network with  $\beta = 15$ , I identified 29 modules, two of which comprise approximately 12,000 genes, while only six contain fewer than 100 genes per module (Figure 4.3B). For  $\beta = 15$ , a total of 28,751 genes remained unassigned, aligning with supplementary analysis conducted using the R package ImpulseDE2 (Fischer et al., 2018), which identified 23,128 genes with *P.adj* values above a 0.05 threshold (i.e., not differentially expressed). Due to a more uniform distribution of genes into modules in the network constructed using  $\beta = 15$  and the similarities with additional ImpulseDE2 differential expression analysis, I opted to proceed with a soft power threshold of 15.

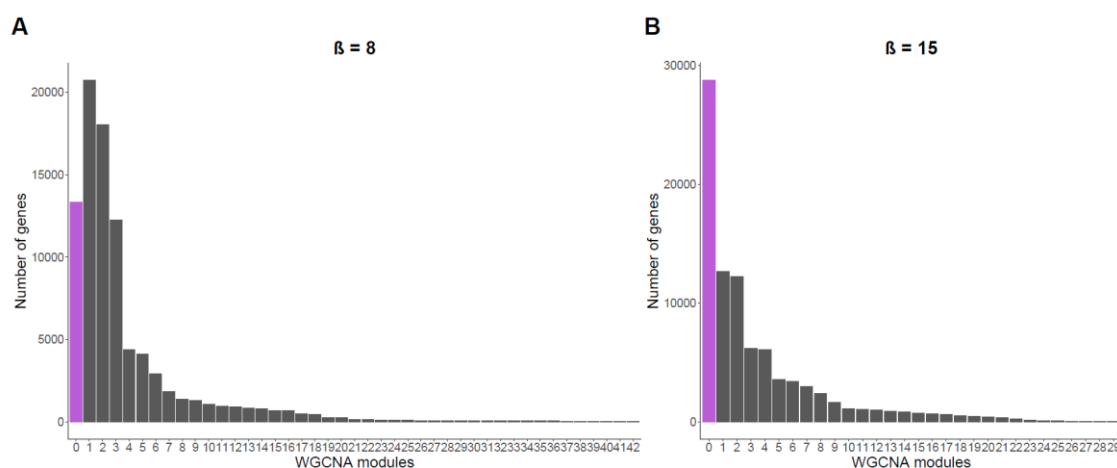


**Figure 4.3 Graphical representation of WGCNA module sizes for different soft power thresholds ( $\beta$ ).**

(A) Number of genes identified per module for the co-expression network constructed with  $\beta = 8$  and (B)  $\beta = 15$ . Purple bar represents number of genes in module 0 (i.e., unassigned, or not differentially expressed genes).

#### 4.3.6.2. DESeq2

Normalisation of counts and differential expression analyses for MS 24512, 24522 and BSS1 were performed using the R package DESeq2 v1.28.1 (Love et al 2014). For the detection of DEGs I followed the guidelines for time-series experiments as described in: <https://bioconductor.org/packages/devel/bioc/vignettes/DESeq2/inst/doc/DESeq2.html#>

time-series-experiments and selected those genes with log<sub>2</sub>fold change > |1| and *P* value < 0.05 for subsequent analyses.

#### 4.3.7. GO, TF and hormone enrichment analyses

For GO enrichment analysis, I used the wheat ontologies deposited in the Grassroots Data Repository ([Index of /under license/toronto/Ramirez-Gonzalez et al 2018-06025-Transcriptome-Landscape/data/TablesForExploration/ on public \(earlham.ac.uk\)](https://www.earlham.ac.uk/~ramirez-gonzalez/)). Gene names were converted from RefSeq version 1.0 gene annotation to RefSeq version 1.1 using the conversion file downloaded from [Index of /download/iwgsc/IWGSC RefSeq Annotations/v1.1 \(inra.fr\)](https://www.inra.fr/~iwgsc/). I used the R package GOseq v1.44.0 (Young et al., 2010) to detect over or underrepresented GO categories in the different modules of gene expression. Adjustment for false discovery rate was included using Benjamini-Hochberg adjustment. Significantly overrepresented GO slim terms ("slim\_IWGSC+Stress") are shown in Figure 4.9. Fisher's exact test (fisher.test from R package stats v3.6.2) was used to calculate the enrichment of TF families and hormone-related genes (data obtained from Evans, Arunkumar, & Borrill, 2022; Jones et al., 2022. respectively).

#### 4.3.8. Ortholog identification

The rice (*Oryza sativa ssp. Japonica*) and Arabidopsis (*Arabidopsis thaliana*) orthologs of the wheat genes were identified using BioMart in Ensembl Plants (Kersey et al., 2018). *ORE1* orthologs were previously identified in Borrill et al., 2019.

#### 4.3.9. DNA extraction and KASP Marker genotyping

I extracted DNA from young leaf tissue following the protocol for "Wheat DNA extraction in 96-well plates" available at <https://www.wheat-training.com/>. I used pre-designed KASP markers from EnsemblPlants (Ramirez-Gonzalez et al., 2015) to track the presence or absence of *KIR1* and *ORE1* mutations in segregating populations (Table 4.2). Sequences for fluorescent dyes (FAM: GAAGGTGACCAAGTTCATGCT; and HEX: GAAGGTCTGGAGTCAACGGATT) were added to 5' end of the mutant (Mut) and WT sequences, respectively. Primer mix, PCR components and thermocycler conditions are outlined in Table 4.3, Table 4.4 and, Table 4.5. For all KASP reactions, 2.5 µL of the reaction mix (Table 4.4) was loaded onto 384-well plates. After conducting KASP reactions, PHERAstar microplate reader (BMC Labtech, UK) was

used to analyse the plates. KlusterCaller software (LGC Biosearch Technologies) was then used to classify samples into wild-type, mutant, or heterozygote by quantification of HEX and FAM fluorescence levels.

**Table 4.2 KASP primers used for *ORE1* and *KIR1* TILLING mutants.**

Note that primers to amplify wildtype (WT) and mutant (Mut) allele do not include the HEX or FAM sequences, respectively. The common (Com) does not include any additional sequence.

Gene	Primer	Sequence (5' - 3')
<i>ORE1-A1</i>	C1441_WT	aacaagtgcgagccctgg
<i>ORE1-A1</i>	C1441_Mut	aacaagtgcgagccctga
<i>ORE1-A1</i>	C1441_Com	gggttctatcgtatggatcacac
<i>ORE1-B1</i>	C1588_WT	ctcaacaagtgcgagccctg
<i>ORE1-B1</i>	C1588_Mut	ctcaacaagtgcgagcccta
<i>ORE1-B1</i>	C1588_Com	gggttctatcgtatggatcacat
<i>ORE1-D1</i>	C0113_WT	caggtccatggcgtgctg
<i>ORE1-D1</i>	C0113_Mut	caggtccatggcgtgcta
<i>ORE1-D1</i>	C0113_Com	aaaaggaagtgatggagcaca
<i>KIR1-A1</i>	C1797_WT	aacaccctgcagagcacc
<i>KIR1-A1</i>	C1797_Mut	aacaccctgcagagcact
<i>KIR1-A1</i>	C1797_Com	cggcgtttctaattgatctggat
<i>KIR1-B1</i>	C1928_WT	ggactcaccaggaagctcc
<i>KIR1-B1</i>	C1928_Mut	ggactcaccaggaagctct
<i>KIR1-B1</i>	C1928_Com	ggactcaccaggaagctct
<i>KIR1-D1.1</i>	C0217_WT	ccagattagcaacgccgacc
<i>KIR1-D1.1</i>	C0217_Mut	ccagattagcaacgccgact
<i>KIR1-D1.1</i>	C0217_Com	ccactcttcgggtagctcc
<i>KIR1-D1</i>	C0100_WT	ggcgagcgaagacgtgg
<i>KIR1-D1</i>	C0100_Mut	ggcgagcgaagacgtga
<i>KIR1-D1</i>	C0100_Com	cggtcctgaagctgaagaa
<i>KIR1-D1</i>	C0127_WT	gtagccggctcttggtggcgc
<i>KIR1-D1</i>	C0127_Mut	gtagccggctcttggtggcgt
<i>KIR1-D1</i>	C0127_Com	cttcagggaccgcaagtatg

**Table 4.3 Components for 100  $\mu$ L of the primer mix.**

Component	Volume ( $\mu$ L)
WT Primer (100 $\mu$ M)	12
Mut Primer (100 $\mu$ M)	12
Common Primer (100 $\mu$ M)	40
dH <sub>2</sub> O	36

**Table 4.4 Reaction components for KASP genotyping.**

Component	1X ( $\mu$ L)
KASP Reagent or PACE reagent	2.5
Primer mix	0.056
DNA (diluted 1:10)	2

**Table 4.5 Thermocycling conditions for PCR amplification.**

Step	Temperature	Time
Hot-start Taq activation	94 °C	15 min
Touchdown (x10 cycles)	94 °C	20 s
	65°C (Decreasing 0.8 °C per cycle to reach 57°C)	60 s
Amplification (x30-35 cycles)	94 °C	20 s
	57 °C	60 s
Hold	10 °C	-

#### 4.3.10. Plant phenotyping

I carried out the following phenotypic assays to characterise *KIR1* and *ORE1* BC<sub>1</sub>S<sub>1</sub> mutant and wild-type populations. I performed stigma area measurements and pollen germination assays using carpels dissected from primary tillers. Meanwhile, secondary tillers were used to evaluate the progression of cell death and assess seed set. In all these assays, I ensured the use of at least three biological replicates, each derived from distinct plants. Additionally, for each emasculated spike, I subsampled two to four carpels from floret one (i.e., outermost floret).



#### *4.3.10.1. Stigma area and hair length measurements*

At the time of sampling, I dissected carpels from four floret 1 positions from the primary tiller of the plant and imaged under a stereomicroscope (ZEISS Stemi 305 with a 1.2 Megapixel integrated colour camera). Stigma area annotation and quantification was performed as described in Chapter 2. Stigmatic hair length was measured manually using the Fiji distribution of ImageJ (Schindelin et al., 2012). Hair length was estimated for each stigma using average of 10 independent measurements. For the statistical analyses, the average hair length or stigma area of each individual spike was used.

#### *4.3.10.2. Progression of cell death measurements*

##### *4.3.10.2.1. Live/dead dual staining of papilla cells*

On the day of sampling, a stock solution of 2 mg of fluorescein diacetate (FDA, catalogue No. F1303, Invitrogen) dissolved in 1 mL acetone was diluted in sterile water to a 5 µg/mL working solution. Additionally, a 10 µg/mL stock solution of propidium iodide (PI, catalogue No. P4864-10ML, Sigma) dissolved in water was further diluted to 5 µg/mL for the working solution. FDA stock solution was kept at – 20 °C and PI stock solution at 4 °C in black coloured eppendorf tubes. A dual FDA/PI working solution was prepared by mixing 500 µL of FDA and PI working solutions in a final volume of 1 mL. After very careful dissection (i.e., without touching the stigmatic tissue), entire carpels were placed in black Eppendorf tubes containing freshly prepared FDA-PI mix and left for 10 minutes at room temperature. Next, carpels were thoroughly washed in sterile water and mounted on 76 mm x 26 mm single cavity slides (cavity depth = 0.2 mm, Academy Microscope Slides). Ovaries were dissected out using a scalpel. A drop of sterile water was added before covering the stigma with a cover slip (22 x 22 mm, thickness 1.5).

##### *4.3.10.2.2. Image acquisition*

For image acquisition, the Leica SP8X confocal microscope was used with 10x immersion objective (0.4 NA). The Argon laser was used at 20 % power to excite FDA at a 488 nm wavelength in bidirectional mode while, the white light laser (WLL) was used at 70 % power to excite PI at 470-670 nm also in bidirectional mode. FDA signal was detected between 518 and 550 nm with a laser intensity of 0.4 % and PI signal was

detected between 560 and 630 nm and laser intensity of 1.8 %. In some cases, laser intensity was adjusted to obtain similarly strong signal as observed for most samples.

Optical sectioning (Z-stacks) and tile scanning was used to generate high resolution images of entire stigmas. To obtain the images, multi-dimensional acquisition mode was used with laser speed 400, line accumulation of 1 (pixel dwell time of 600 ns) and pinhole size of 1 AU. Image format 1024x1024 pixels. Maximum intensity projection of stitched images was obtained for each stigma.

#### 4.3.10.2.3. Calculation of live to dead cells ratio

To quantify the ratio of live to dead cells, I used the Yen algorithm (function `filters.threshold_yen()` from `scikit-image` package; Van der Walt et al., 2014) for automated image thresholding. The implementation of this algorithm resulted in cut-off thresholds for both PI and FDA images (Figure 4.4). Pixels with intensities below the threshold were classified as background. For each image, the ratio of live to dead cells was calculated by dividing the number of FDA foreground pixels by the number of PI foreground pixels. In the later stages of stigma development, I encountered images with weaker signals, which raised the potential for inaccuracies in live to dead cell ratios as papilla cells are completely disintegrated. To address this issue, only images with a total foreground pixel count above 30,000 were used in the quantification process. Images with less than 30,000 foreground pixels were regarded as fully senesced stigmas (i.e., 100% red pixels and 0% green pixels). The script used for automated image thresholding was developed by Dr. Sergio López (BioImaging Platform, JIC).

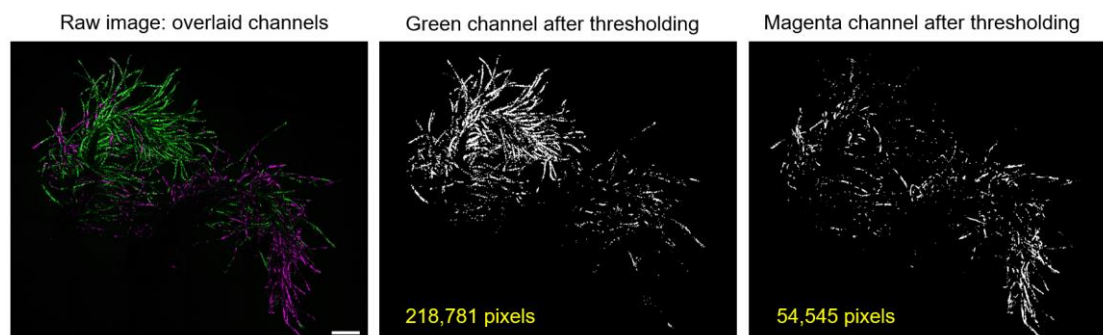


**Figure 4.4 Representation of the automated image thresholding process.**

The first image shows the combination of both FDA (green) and PI (magenta) channels. The black and white images show the detected foreground pixels (in white) after automated thresholding of raw FDA and PI images. Number of pixels for each image is also indicated. Scale bar = 500  $\mu\text{m}$ .

#### 4.3.10.3. *Stigmatic germination of pollen grains*

##### 4.3.10.3.1. Hand pollinations

Pollen from mature Cadenza WT anthers was used to pollinate the stigmas of mutant and wild-type plants. Generally, two to three anthers were used to pollinate emasculated spikes. Pollinations were carried out in the morning between 9 and 11.30 am.

##### 4.3.10.3.2. Carpel dissections and fixation

Carpels were dissected 4.5 h after pollination to allow sufficient time for pollen tube emergence. Samples were stored in a fixative solution of 95% ethanol and absolute acetic acid (75% v/v) and kept at 4 °C until sample preparation for fluorescence microscopy.

##### 4.3.10.3.3. Aniline blue staining of pollinated stigmas

On the day of sampling, a stock solution of 1% aniline blue (catalogue No. 415049, Sigma-Aldrich) dissolved in 1x PBS buffer (pH=7) was diluted in a 0.1 M K<sub>3</sub>PO<sub>4</sub> solution to a final concentration of 0.1%. Fixed samples were washed three times for 5 minutes in sterile water and transferred to 0.1% aniline blue solution and kept overnight at 4 °C. Without washing the samples, the ovaries were dissected and removed, and the remaining stigmatic tissue was left to dry at 45 °C in a hot plate for a few minutes until most of the aniline blue solution was evaporated. I covered the hot plate with an opaque lid to avoid exposure to light. Finally, I used Vectashield (catalogue No. H-1000-1, 2BSCIENTIFIC LTD) as an antifade mounting media to preserve fluorescence.

##### 4.3.10.3.4. Image acquisition

For image acquisition, the Zeiss Axio Zoom V16 II stereo microscope was used with a 1.5x objective. I used a monochrome camera for fluorescence imaging and the X-Cite Xylis lamp as fluorescence light source to excite aniline blue. Aniline blue signal was detected with “49 DAPI” filter cube between 415 and 455 nm while autofluorescence of pollen grains was detected with a “38 HE GFP” filter cube between 500 and 550 nm. For each image, auto exposure was used to find a suitable exposure time and laser intensity corrected. In addition, multidimensional acquisition mode was used to create a composite of the entire stigma from a series of smaller overlapping images. After

acquisition, images were stitched together (tile overlap > 20%) and shading was corrected using a reference.

#### 4.3.10.4. *Seed set*

After hand pollinations, developing grains were left to develop until full maturity of the plant when they were harvested and manually counted.

#### 4.3.10.5. *Flag leaf senescence*

I used SPAD-502 chlorophyll meter (Konica Minolta) to measure chlorophyll content in the flag leaf at 13, 24, 33 and 38 days after anthesis. For each time point, I scored eight main tillers per plot and measure chlorophyll levels at three distinct positions along the length of the flag (uppermost) leaf.

#### 4.3.11. Statistical analyses

Appropriate statistical tests were used for all data analyses, with detailed descriptions provided in the results section. All statistical analyses were conducted using Rstudio (v4.3.0).

## 4.4. Results

### 4.4.1. Morphology of the unpollinated carpel and its transcriptional landscape

To investigate the molecular regulation of stigma senescence in the absence of pollination in wheat, I used transcriptome sequencing of unpollinated stigma-styles at seven successive stages of stigma development: Waddington 9 (W9), W9.5 (heading) and 3, 7, 11, 14 and 18 days after W9.5 (DAW9.5). Measurements of the area covered by the stigmatic hairs described the initiation and progression of the senescence process across the sampled time period for the male sterile cultivar 24485 (Figure 4.5). As described in Chapter 2, section 2.4.5, we distinguished an initial growth phase in W9 and W9.5 samples, a subsequent peak phase where the stigma reaches its maximum size spanning from 3 to 11 DAW9.5, and a final deterioration phase with the gradual collapse of stigma hairs in 14 and 18 DAW9.5.

Conducting transcriptomic studies on field samples resulted challenging due to the necessary dissection of tissues and limited access to liquid nitrogen. To address this, I developed a protocol optimised for extracting high-quality RNA from wheat stigmas stored in DNA/RNA shield, serving as a practical alternative to liquid nitrogen. This protocol involves a two-step process, beginning with TRIzol/Chloroform phase separation and followed by purification of the aqueous phase using the RNA Clean and Concentrator kit (ZYMO-Research). Notably, the inclusion of in-tube DNase treatment during purification renders this protocol suitable for tissues with high carbohydrate content, such as wheat stigma, as it prevents DNA co-precipitation with carbohydrates, which can otherwise interfere with on-column purification steps. This protocol has been successfully tested on various plant tissues, including maize and wheat pollen, and floral meristems in wheat and is publicly available at protocols.io (<https://dx.doi.org/10.17504/protocols.io.36wgg7kj3vk5/v1>).

The RNA extracted from three replicates of each of the seven time points was sequenced using an Illumina NextSeq instrument (Novogene, UK). For each sample, an average of 43 million paired-end reads were obtained (sequencing length of 150 bp), of which 78.8% aligned to the RefSeqv1.1 transcriptome annotation (Appels et al., 2018; Figure 4.5B). I found that 89,263 unique high (HC) and low confidence (LC) genes (58,123 and 31,140 genes, respectively) were expressed (transcripts per million (TPM)

> 0.5) in at least one time point during the time course from a total of 107,891 HC and 161,537 LC gene models (Appels et al., 2018). To assess global gene expression changes, I followed a multidimensional scaling approach that showed a clear separation of the seven time points and a temporal trajectory in which each time point seamlessly transitioned into the next (Principal Component Analysis, PCA; Figure 4.5C). Grouping of the samples indicated data quality issues for one of the 7 DAW9.5 samples which was subsequently removed from downstream analyses (data including 7 DAW9.5 #1 stigma sample is not shown in Figure 4.5). Examination of the scatterplot of data points after removal of the outlier did not reveal any unexpected patterns (Figure 4.5C).

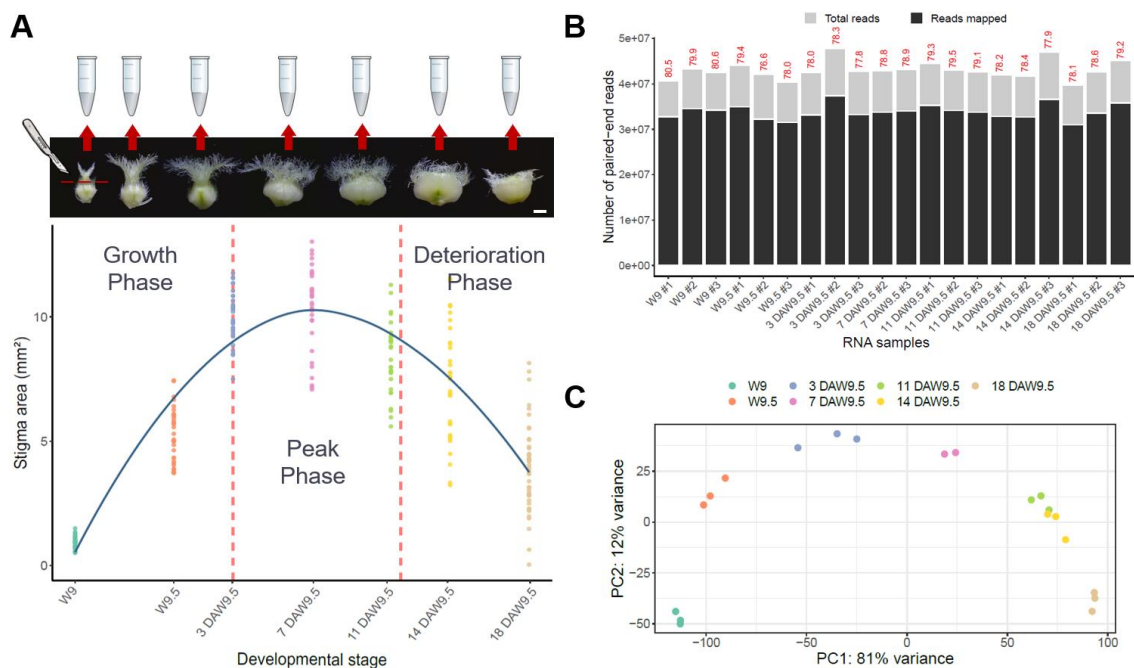


**Figure 4.5 The temporal progression of stigma development and degeneration.**

(A) Developmental pattern of stigma area (mm<sup>2</sup>) for male sterile (MS) cultivar 24485 in the 2020 field season. Dots represent individual stigmas collected for each time point (DAW9.5: Days After Waddington 9.5). Polynomial regression model at a 90% confidence interval (Loess smooth line) is also shown in blue. Red dashed lines separate the three phases of stigma development based on the 85% cut-off of stigma area (see Chapter 2, section 2.4.5, for details): left section illustrates the growth phase; middle section corresponds to peak phase; and right section shows the time points within the deterioration phase. Representative images of carpels during the time course are shown. Scale bar = 1mm. (B) Total reads and pseudoaligned reads per sample. In red, percentage of reads pseudoaligned. (C) Principal component analysis (PCA) plot based on variance-stabilised transformed (vst) counts per sample.

#### 4.4.2. Construction and analysis of a weighted co-expression network

The gradual morphological changes observed in the unpollinated stigma, alongside the temporal progression found within the sequenced samples, suggest that temporal changes in gene expression underly the transition between the phases of stigma development (i.e., growth, peak and deterioration phase).

To test this hypothesis, I used the weighted gene co-expression network analysis (WGCNA) R package (Langfelder & Horvath, 2008, 2012) to develop a co-expression gene network to group genes with comparable expression patterns. To address the lack of scale-free topology fit of the data, I selected the power of  $\beta = 15$  as the best soft threshold to yield reasonable metrics for a signed hybrid network (i.e., scale-free topology fit index  $>0.8$  and mean connectivity in the hundreds). This choice of soft threshold proved to be optimal to accentuate strong gene-to-gene correlations and penalise weaker correlations. Based on this analysis, 60,512 (HC genes = 46,272) of the 89,263 expressed genes (67.8 % of expressed genes) could be assigned to 29 modules, with each displaying unique differential expression along the time course. The remaining 28,751 genes (32.2 % of expressed genes) did not fit well into any of the defined co-expression modules mainly due to low expression or low variability across the developmental stages and therefore were regarded as not differentially expressed. Module size ranged from 32 to 12,641 genes. The expression patterns of all genes within a single module were summarised into a module eigengene (ME: representative gene of the module) and are shown as line graphs by plotting ME values in relation to the stages of stigma development (Figure 4.6).

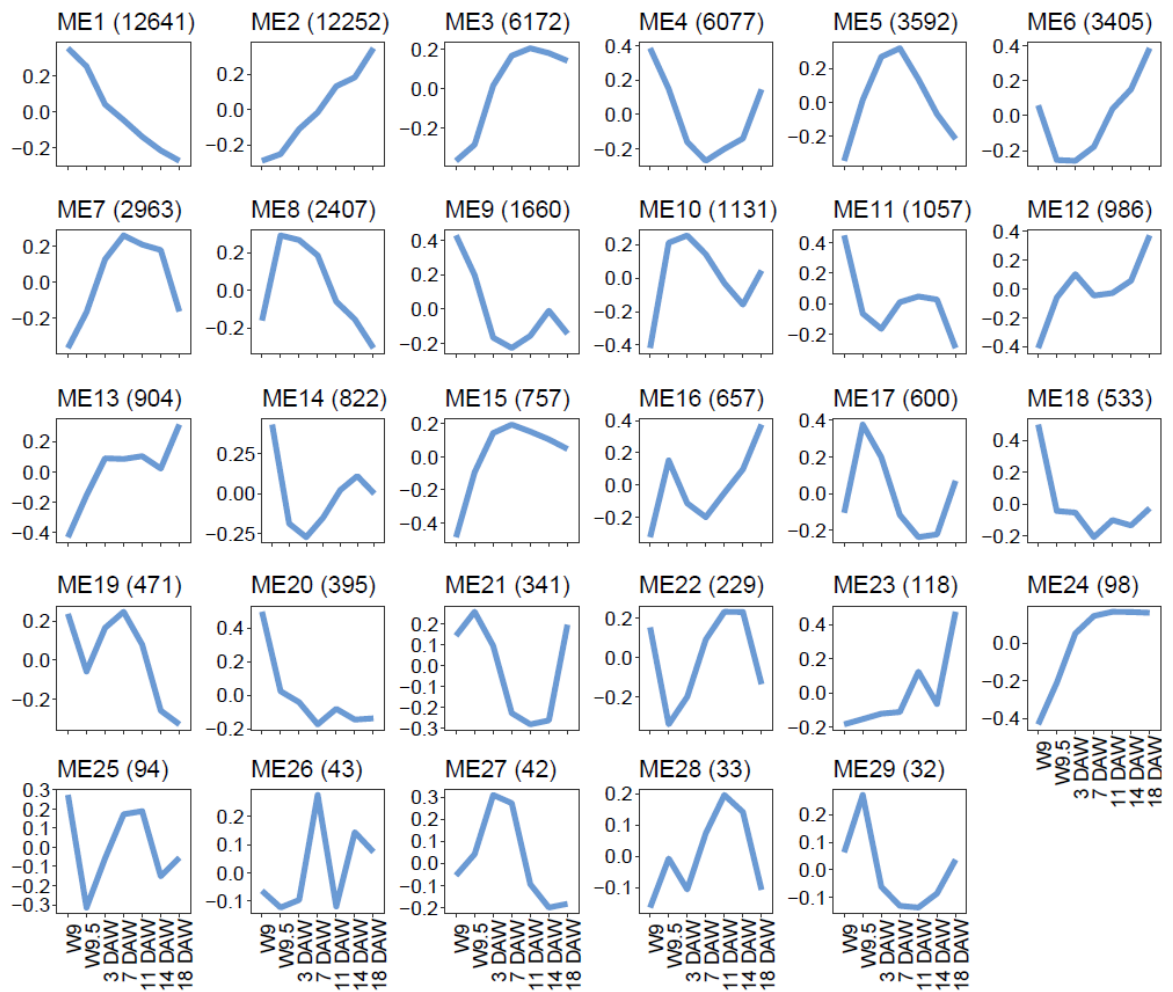


**Figure 4.6 Identification of distinct co-expression clusters via WGCNA.**

Each plot shows the gene expression profile of a module eigengene (ME). Y-axis corresponds to eigengene values and X-axis to the different time points (DAW: Days After Waddington 9.5). Gene number per ME is shown between parentheses.

Although each ME exhibited a unique pattern of gene expression, I could detect instances in which several MEs shared similar transcriptional trends, as seen with ME18 and ME20 or ME4, ME9 and ME14. These commonalities between MEs suggest that genes within these MEs could be involved in related biological processes. To quantify module similarity, I used hierarchical clustering (Figure 4.7A) and eigengene adjacency (Figure 4.7B) to reveal three major meta-modules (i.e., groups of highly related eigengenes with a correlation of at least 0.5). Specifically, ME11, ME14, ME1, ME4, ME9, ME18, ME20, ME19, ME22 and ME25 constitute one meta-module, with elevated gene expression during the early stages of the time course (growth phase meta-module in Figure 4.7A). Another significant meta-module comprises ME27, ME8, ME5, ME10, ME29, ME17, and ME21, showing a prominent spike in gene expression



between W9.5 and 3 DAW9.5 (peak phase meta-module in Figure 4.7A). Finally, the third meta-module (ME6, ME7, ME15, ME3, ME24, ME16, ME12, ME13, ME2 and ME23) shows upregulation of gene expression towards the end of the life cycle (deterioration phase meta-module in Figure 4.7A). ME26 and ME28 were excluded from the deterioration meta-module due to their fluctuating expression pattern and the limited number of genes they contain (Figure 4.6).

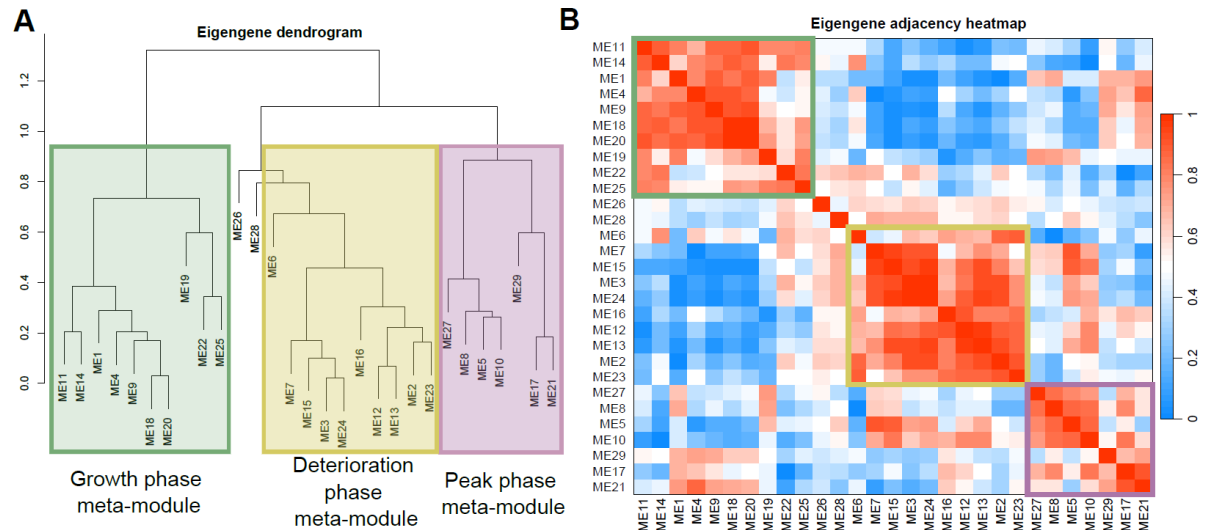


**Figure 4.7 Visualisation of the eigengene network within the developing stigma.**

(A) Hierarchical clustering dendrogram of the eigengenes. Boxes illustrate the classification of the different MEs into three distinct meta-modules associated to the growth (in green), peak (in purple) and deterioration (in yellow) phase. (B) Heatmap shows eigengene adjacency measured as  $(1 + \text{cor}(\text{Eigengene}_i, \text{Eigengene}_j))/2$ . Meta-modules are highlighted in green, yellow, and purple as in panel A.

In addition to our preliminary observations, I conducted a correlation analysis using the 29 MEs and the seven distinct time points (Figure 4.8) to identify modules of gene expression showcasing the strongest associations with the different stages of stigma development. As anticipated, genes within the growth phase meta-module are most highly expressed at W9, which hints at their potential involvement in the developmental progression of growing stigma. Genes grouped within the peak phase meta-module show high expression at W9.5 and at 3 DAW9.5 extending, in some cases, to 7 DAW9.5, while upregulation of gene expression at later stages of development (7 DAW9.5 onwards) is positively correlated with the deterioration phase meta-module. Thus, in support of my hypothesis, I found evidence for profound transcriptional shifts (42.9% of the annotated HC genes differentially expressed) that occur during the development of the unpollinated stigma (Figure 4.7), which align significantly with the physiological phases of stigma growth, peak and deterioration (Figure 4.8).

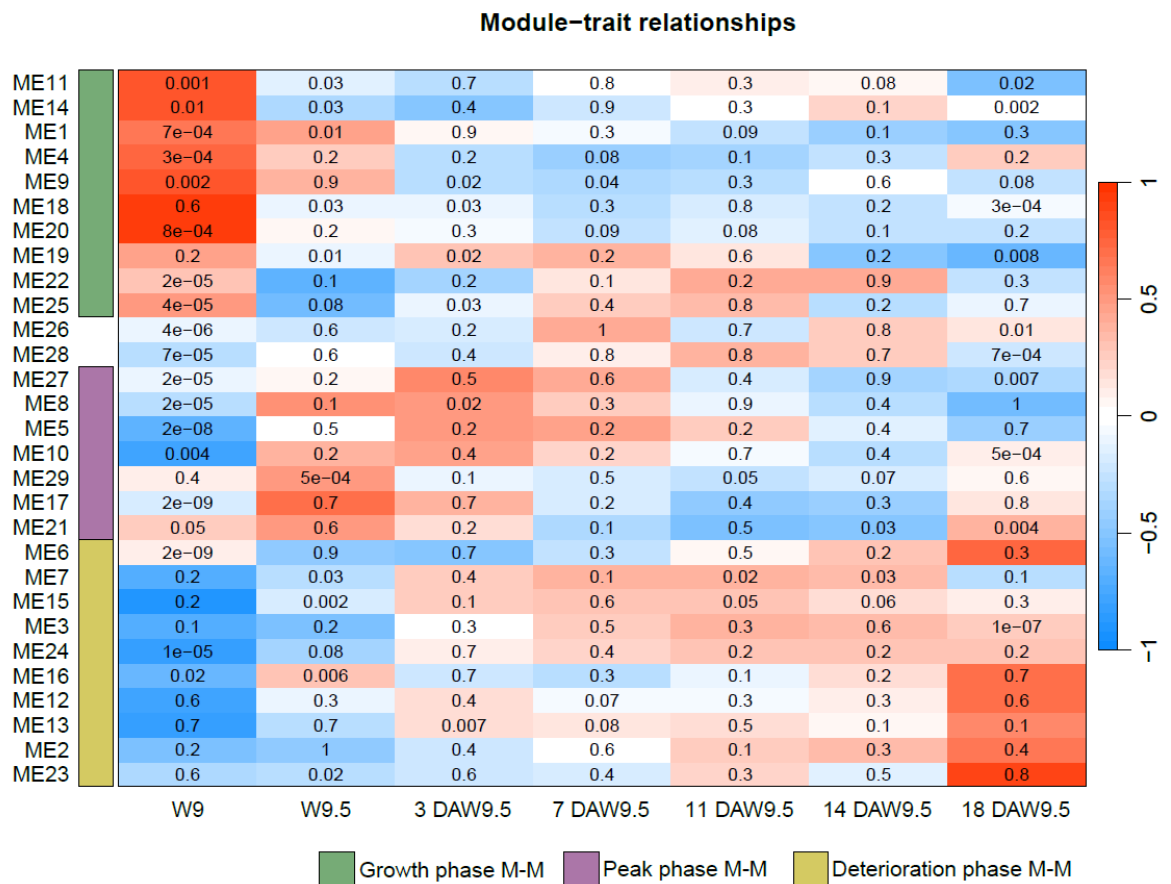


**Figure 4.8 Relationships among gene expression modules and time points of stigma development.**

Each row represents a module and each column a time point. Cells in the heatmap contain the false discovery rate (FDR) adjusted  $P$  value ( $P_{adj}$ ) of the corresponding correlation represented by a red-blue scale. The coloured bars on the left-hand side identify the meta-modules (M-M) associated with developmental stages, as determined by hierarchical clustering and eigengene adjacency map in Figure 4.7.

#### 4.4.3. Biological significance of gene expression patterns

##### 4.4.3.1. *Gene ontology enrichment*

To validate the preliminary observations linking groups of co-expression modules to the different phases of stigma development, I performed a gene ontology (GO) enrichment analysis using differentially expressed genes (DEGs) assigned to the 29 MEs. I found that this temporal divide between the different meta-modules associated to either the growth, peak or deterioration phase was also reflected in different GO term enrichments in these groups of DEGs (Figure 4.9).

Some of the most enriched GO terms among DEGs in the growth phase meta-module are related to biological processes such as cell cycle (GO:0007049), cell differentiation (GO:0030154), anatomical structure morphogenesis (GO:0009653) or flower development (GO:0009908). Among the genes annotated to be involved in cell cycle, cell differentiation and anatomical structure morphogenesis, I found several genes from the TCP TF family such as *TaTCP17*, *PCF1*, *TCP5*, *PCF8*, or *TCP21* with different roles in promoting cell proliferation and differentiation (Martín-Trillo & Cubas, 2010). Under the flower development GO term, I detected the MADS-box TFs *SEPI*, *AGL6*, *API*, and *AP2L5* primarily in ME1 and ME19 along with other genes associated to auxin signalling and GA biosynthesis such as *GA20ox4*. On the other hand, DEGs present in the peak phase meta-module are significantly enriched for carbohydrate and lipid metabolism (GO:0005975; GO:0006629), energy-associated processes (GO:0006091) and various responses to exogenous and endogenous stimulus terms (Figure 4.9). In relation to these GO terms, I find, for instance, the genes *PG37*, *PG61*, *PG68* and *PG69* that belong to a family of hydrolases (polygalacturonases) with important functions in pectin degradation and fruit ripening and previously identified in rice and wheat mature stigmas (Li et al., 2007; Robinson et al., 2023; Zhang et al., 2019). For example, this meta-module also included the putative wheat ortholog of *AtCIPK26*, a protein kinase involved in calcium binding and transport as well as ROS production, processes essential in pollen hydration by the stigma and pollen tube growth (Kimura et al., 2013; Liu et al., 2021; Mähls et al., 2013; McInnis et al., 2006). Unexpectedly, floral reproduction related GO terms (i.e., GO:0000003, GO:0009856, GO:0009875) were not enriched in the peak phase meta-module and instead they were significantly overrepresented in modules within the growth and deterioration phase meta-modules, suggesting that different aspects of these processes are being regulated differentially around the beginning and end of the peak phase. Finally, within the deterioration phase meta-module, the most enriched GO terms are predominantly associated with catabolic processes and cell death (GO:0009056, GO:0008219), defence against various stresses and cell communication (GO:0007154), and transport (GO:0006810). Some genes within these categories include the wheat orthologs of *OsPAO*, which is involved in chlorophyll degradation (Tang et al., 2011), the senescence related gene, *CAT3* (Du et al., 2008), *OsMAPK6*, *OsMPK1* and *OsSIPK* that are associated with wounding and stress responses (Lee et al., 2008; Yoo et al., 2014), and different class III peroxidases, such as *TaPRX*, an antioxidant enzyme involved in the protection against ROS damage (Su et al., 2020).

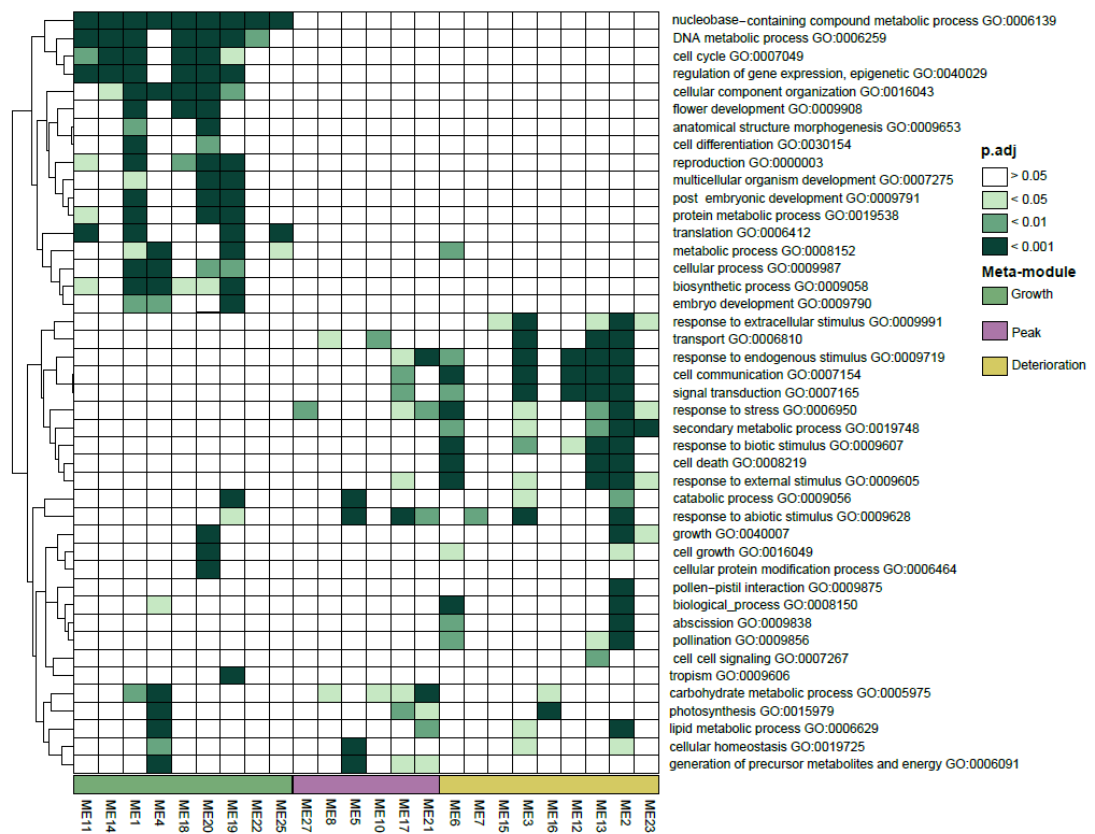


**Figure 4.9 Enriched GO slim terms for biological processes.**

Heatmap of selected GO slim terms that are significantly enriched in at least one ME. Fisher’s Exact Test was used to determine significant enrichments. MEs with no GO enrichment ( $P_{adj} > 0.05$ ) are not shown (ME9, ME24, ME26, ME28 and ME29). The coloured bars on the bottom identify the meta-modules associated with the different developmental stages, as determined by hierarchical clustering and eigengene adjacency map in Figure 4.7.

#### 4.4.3.2. Transcription factor enrichment

Transcription factors play a pivotal role in orchestrating gene expression patterns and regulating various biological processes. In the context of the wheat stigma, understanding the contribution of TFs to key developmental stages may offer valuable insights into the underlying regulatory networks coordinating the observed transcriptional changes (Figure 4.6). I identified 3,190 out of 6,128 annotated TFs (Evans et al., 2022) that were expressed ( $>0.5$  TPM) during the time course, from which 2,683 TFs (43.8 % of the annotated TFs) were differentially expressed across the stages analysed here (i.e., assigned to one of the 29 MEs). I then classified the genes into TF families for enrichment analysis (Figure 4.10) and found seven TF families (Alfin-like, B3 and B3-ARF, C3H, DDT, HB-HD-ZIP, TCP, Trihelix and TUB) that showed significant enrichment in downregulated genes within the growth phase modules ME1,

ME11 and ME4. Members of these families perform crucial roles in various aspects related to organ development and hormone signalling (Wils & Kaufmann, 2017). For instance, within the B3 family, *NGA1*, *NGA2*, and *NGA3* play essential roles in apical gynoecium formation (Ballester et al., 2021; Gaillochet et al., 2018). The TF families HSF, LOB, MADS-MIKC and NF-X1 are significantly overrepresented in ME27, ME8, ME5 and ME17 (peak phase meta-module). Finally, I found significant enrichment in the deterioration phase modules ME2, ME3, ME6 and ME13 for the senescence-associated TFs AP2/ERF-ERF, NAC, MYB, and WRKY TFs, among others (Figure 4.10). These are TF families that have been widely characterised to play a role in promoting programmed organ senescence in plants with well-established members like the NAC TFs *ANAC092 (ORE1)* and *ANAC074 (KIR1)* whose role in regulating the expression of programmed cell-death associated genes is known to influence stigma longevity in *Arabidopsis* (Gao et al., 2018). Other core transcriptional activators of leaf and floral senescence found to be expressed in the unpollinated wheat stigma are *ANAC2 (ATAF1)*, *ANAC029 (NAP)*, *ANAC047 (SHYG)* or the AP2/ERF-ERF member *RAP2* (Garapati et al., 2015; Licausi, 2011; Shaikhali et al., 2008; Van Durme et al., 2023). These findings indicate that particular TF families trigger temporal changes in gene expression, broadly classified into an initial growth phase that transitions via an intermediate peak phase to a later deterioration or senescence phase.

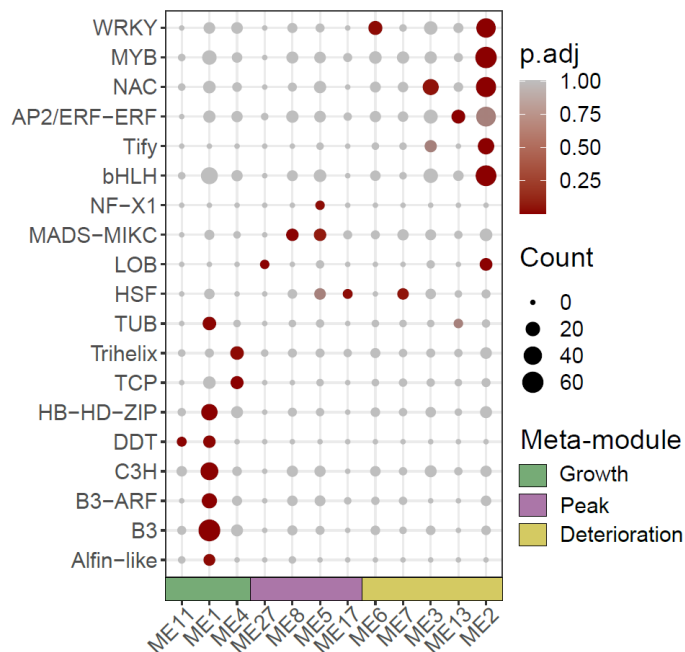


**Figure 4.10 Transcription factor families found to be significantly enriched.**

Circle size corresponds to the number of TF genes per TF family and module. Circle colour represents the P adjusted (P.adj) value of the enrichment analysis. The TF family with a P.adj value < 0.05 was considered as significantly overrepresented (dark red). Fisher's Exact Test was used to determine significant enrichments. The coloured bars on the bottom identify the meta-modules associated with the different developmental stages. Modules with no significant TF enrichment are not shown.

#### 4.4.3.2.1. Identification of stigma specific senescence associated TF genes

Given the relevance of the AP2/ERF-ERF, NAC, WRKY, and MYB TFs as hub genes in senescence-related pathways (Bengoa Luoni et al., 2019; Yoshida, 2003), I sought to investigate their potential involvement in specifically regulating the onset of stigma deterioration in wheat. To do so, I studied the expression patterns of these genes by comparing my transcriptome data to those of two publicly available datasets: (1) a developmental time course entailing various tissues and time points in the spring wheat *cv.* Azhurnaya (Ramírez-González et al., 2018), and (2) a 23 day senescence-specific time course (from 3 until 26 days after anthesis) using flag leaves from the spring wheat *cv.* Bobwhite 26 (Borrill et al., 2019). To narrow down the number of analysed genes, I decided to focus my analysis on the co-expression modules that included *ORE1* or *KIR1* genes, as it is likely that other TFs relevant to the senescence process are clustered together. In addition to the modules hosting the wheat orthologs of *ORE1* and *KIR1* (i.e., ME2 and ME3), I included the deterioration phase modules ME13 and ME6 as they were also significantly enriched for genes involved in cell death processes

(GO:0008219 in Figure 4.9) and for the senescence associated TFs AP2/ERF-ERF and WRKY (Figure 4.10). Of the initial 352 senescence associated TF genes identified to be expressed in the selected modules, I found 126 genes to be more expressed predominantly in stigma tissues relative to other tissues across the Azhurnaya and leaf senescence datasets (green boxes in Figure 4.11). Out of the 126 TFs, I found that 58 exhibited consistent expression patterns across their homoeolog copies (i.e., A, B and D gene copies assigned to the deterioration phase meta-module). These TFs displayed upregulation towards the end of the stigma life cycle as described by the modules correlated with the deterioration phase. This consistent and synchronised gene expression pattern strongly suggests that these TFs play an active and coordinated role in the regulation of senescence processes specifically and uniquely within the stigmatic tissue. Additionally, I found that nine of those genes have all three homoeolog copies present within the set of 126 genes investigated. These include the orthologs from *Arabidopsis* *ORE1*, *KIR1*, *ERF-1*, *MYB116*, *DREB26*, *RAP2.2* and the orthologs from *rice* (*Oryza sativa* ssp. *japonica*) *ONAC080*, *WR3* and *WRKY11* (Figure 4.11). As mentioned before, the NAC TFs *ORE1* and *KIR1* have been shown to function as regulators of stigma senescence (Gao et al., 2018; Šimášková et al., 2022), whereas the other genes are involved in different aspects of stress responses and leaf and flower senescence (Hickman et al., 2013; Krishnaswamy et al., 2011; Lee et al., 2008; Xie et al., 2019). The comparison between these independent datasets suggests that these 126 genes may have a specific function in senescing stigmatic tissues, and therefore, may be less likely to induce pleiotropic effects when altering their expression in mutant lines.

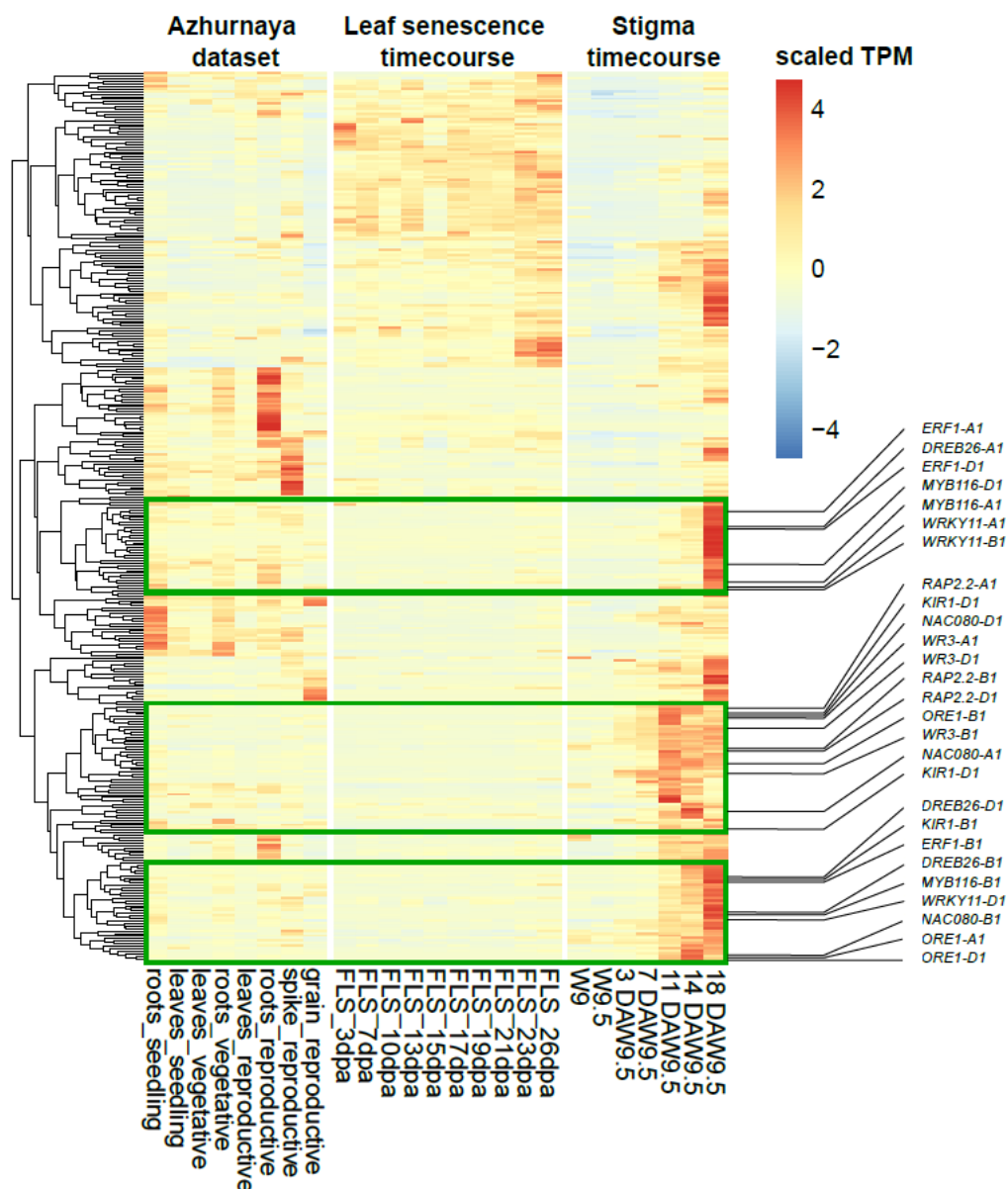


**Figure 4.11 Stigma specific senescence associated TFs.**

Heatmap illustrating the expression patterns of 352 senescence associated TF genes (AP2/ERF-ERF, NAC, WRKY, and MYB) using independent RNA-Seq experiments. Left part of the heatmap shows Azhurnaya spring wheat data summarised into “high level” tissues (i.e., root, leaves spike and grain) and “high level” plant age (i.e., seedling, vegetative and reproductive stage). Central section shows expression data from the flag leaf senescence (FLS) time course in Bobwhite spring wheat at ten different time points after anthesis (dpa: days post anthesis). Expression data for the stigma specific time course are shown on the right part of the heatmap. Expression levels are normalised within each gene across all samples and rows and sorted according to the similarity of expression. Genes predominantly expressed in stigma tissue are highlighted by green boxes. Genes with all three genome copies falling within the green boxes are labelled.



#### 4.4.3.3. *Hormone pathway enrichment*

The onset and progression of senescence in leaves, flowers and fruits is regulated by a complex network of TFs that are strongly associated with changes in phytohormone levels (Bengoa Luoni et al., 2019; Forlani et al., 2019; Jibrán et al., 2013; Ma et al., 2018). Generally, ethylene, ABA, jasmonate, and its derivatives (e.g., salicylic acid, brassinosteroids) promote senescence, while cytokinins, auxins, and gibberellins delay the onset of organ death. In agreement with this association, I observed changes in gene expression in the TF family AP2/ERF-ERF (APETALA2/Ethylene Responsive Factor) in modules associated with the senescence stages and TF family B3-ARF (B3-Auxin Responsive Factor) in early developmental stages. Understanding this intricate interplay between TFs and phytohormones could be a key in unravelling the mechanisms behind the regulation of stigma senescence in wheat.

I identified 1,072 hormone associated genes that are expressed (> 0.5 TPM) during the developmental time course, from which 926 genes (86.4%) were expressed differentially across the different developmental stages (i.e., assigned to one of the 29 MEs). I used the classification of genes into the hormonal processes of biosynthesis, transport, signalling, and catabolism provided by Jones et al., (2022) for enrichment analysis (Figure 4.12A). Auxin signalling was detected as the only hormonal process to be significantly enriched among the downregulated DEGs in the growth and peak phase meta-modules (ME1 and ME8), pointing to a decrease in auxin transport and homeostasis during stigma senescence (Mueller-Roeber & Balazadeh, 2014; Šimášková et al., 2022). Interestingly, however, I did detect an enrichment of auxin biosynthesis during these stages, with auxin production being shown previously to delay senescence (Mueller-Roeber & Balazadeh, 2014). Genes involved in auxin synthesis, such as *YUCCA7* and *TAR*, exhibited significant upregulation at 18 DAW9.5 (Figure 4.12B). Although the presence of active auxin in the senescent stigma remains uncertain, there is a possibility that it may be conjugated and inactivated by enzymes like *GH3.3*, whose closest wheat ortholog (*TraesCS2B02G210600*) reaches its expression peak at 18 DAW9.5 (in ME16). Unexpectedly, no other hormone related process was significantly enriched in the dataset, possibly due to the limited hormone-related gene information currently available for wheat (total of 1,709 hormone-related genes identified).

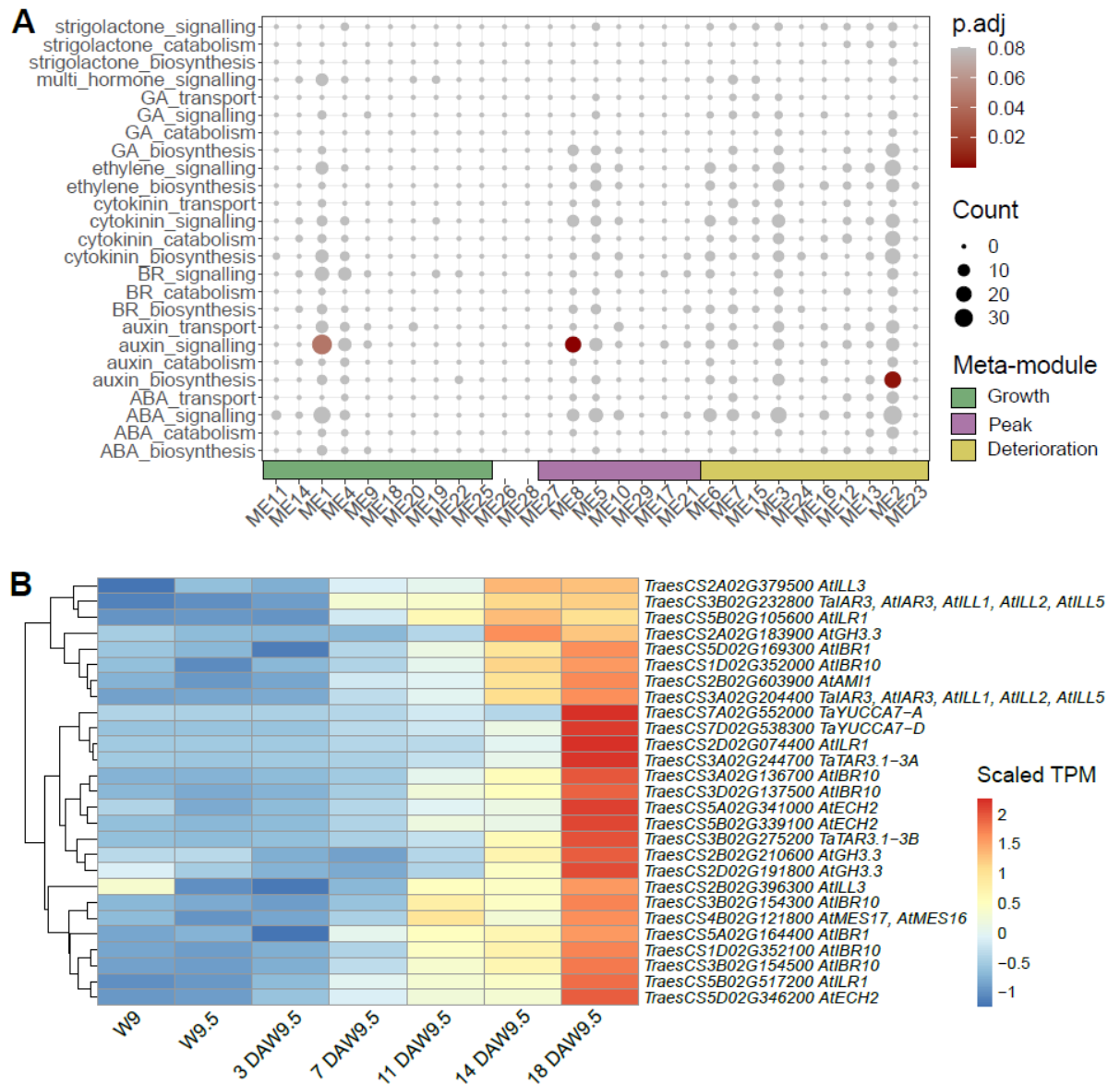


**Figure 4.12 Hormone related genes significantly enriched during stigma development.**

(A) Circle size corresponds to the number of hormone genes per hormonal process and module. Circle colour represents the  $P$  adjusted value of the enrichment analysis. Hormone processes with a  $P.adj$  value  $< 0.05$  were considered as significantly overrepresented (dark and lighter red). Fisher's Exact Test was used to determine significant enrichments. The coloured bars on the bottom identify the meta-modules associated with the different developmental stages. (B) Heatmap of expression data for auxin biosynthesis related genes in ME2 and putative wheat orthologs of *GH3.3* across the time course. Expression levels are normalised within each gene across all samples and rows are sorted according to the similarity of expression.

#### 4.4.4. Identifying candidate genes using comparative transcriptomics

In Chapter 2, we established that the development of unpollinated stigmas exhibits a highly conserved pattern in field conditions, even though variations exist in the duration of the growth, peak, and deterioration phases among diverse MS cultivars. This observation raised the prospect that beneath the phenotypic diversity across distinct cultivars, there might be a fundamental conservation of functional processes happening at slightly different times during development. To investigate this hypothesis further, I performed additional RNA-sequencing analyses in three MS cultivars that consistently showed distinct patterns of stigma development (BSS1, 24512 and 24522 in Figure 4.13A and Chapter 2, section 2.4.5, for more details). I extracted RNA from stigma samples of field grown plants at 3, 7, 13 and 18 DAW9.5 to capture the potential transcriptional changes underlying the transition from the peak to deterioration phase. For MS 24522, it was not possible to extract good quality RNA of 18 DAW9.5 samples due to advanced deterioration of the stigmatic tissue. After aligning the reads, following the same approach as described for cultivar 24485 (section 4.4.1), I found that BSS1, 24522, and 24512 had 76,790, 73,765, and 79,386 distinct genes (HC and LC) expressed, respectively, with an average abundance of  $> 0.5$  TPM in at least one time point. To identify the main sources of variability within the samples, I performed PCA on normalised count data and found that more than half of the variation (63 %) across samples is solely explained by the first principal component (PC1) or time variable (Figure 4.13B). The second largest source of variation in gene expression is captured by PC2, which is associated with the genotype. Furthermore, aligning with the phenotypic aspect of the stigma, the clustering of the 13 DAW9.5 samples from the MS cultivar 24522 with those from 18 DAW9.5 shows how 24522 stigmas are, transcriptionally, in a more advanced stage of senescence compared to BSS1 and 24512 at the same time point (13 DAW9.5). However, it is worth noting that the levels of gene expression of 24522 at 7 DAW9.5 are consistent with the other two cultivars at the same developmental stage. This suggests the existence of an active transcriptional process taking place between 7 and 13 DAW9.5 in 24522 mirroring the significant decrease in stigma area. Collectively, these results imply strongly that the differences observed in the onset of stigma senescence between the MS cultivars are indeed reflected by differential gene expression.

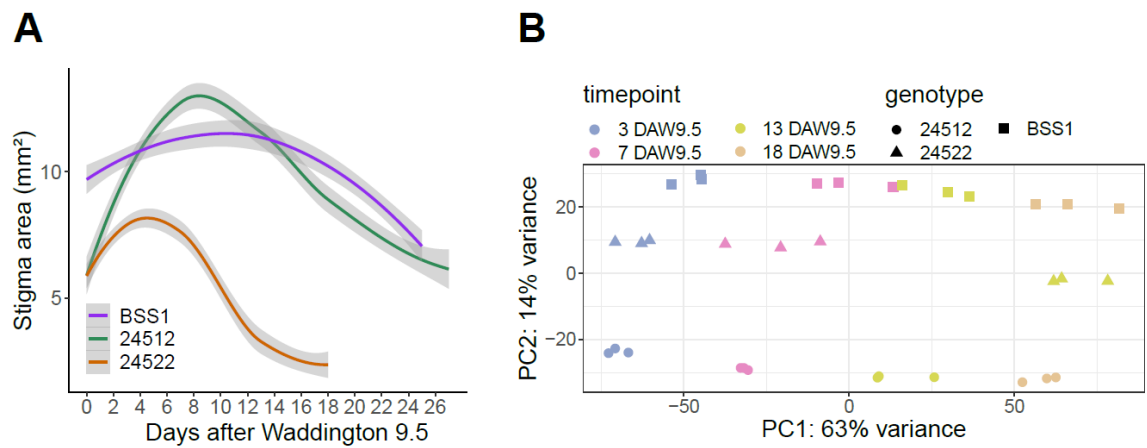


**Figure 4.13 Differences in the temporal progression of stigma development are genetically controlled.**

(A) Developmental pattern of stigma area (mm<sup>2</sup>) for MS cultivars 24512, 24522 and BSS1 in the 2021 field season. Polynomial regression models at a 95% confidence interval (Loess smooth line) are shown. Grey shading represents the standard error of the mean (s.e.m). Five carpels from six plants were sampled at each timepoint. (B) PCA plot based on variance-stabilised transformed (vst) counts per sample. Note that stigma samples used to plot trends in panel A were not used for RNA-Seq. RNA-Seq samples were collected from other plants within the same plot and field season as samples in panel A.

#### 4.4.4.1. *Stigma senescence associated genes*

To further explore the genes that might be underlying the transcriptional changes triggering the onset of stigma senescence in wheat, I used the R package DESeq2 (Love et al., 2014) to identify genes differentially expressed ( $\log_2$ fold change  $> |1|$  and  $P$  value  $< 0.05$ ) throughout the different time series for 24512, 24522 and BSS1. Pairwise comparisons of DEGs between the different MS cultivars (BSS1, 24512, 24522 and 24485; Figure 4.14A) detected 10,830 core genes (16% of the total DEGs) that are shared by all cultivars. Among these, 81.5% belonged to the group of genes associated with the peak (14.9 %) and deterioration (66.5 %) phases (Figure 4.14B), consistent with the time points collected for this second RNA-seq analysis (3 DAW9.5 – or beginning of peak phase – onwards).

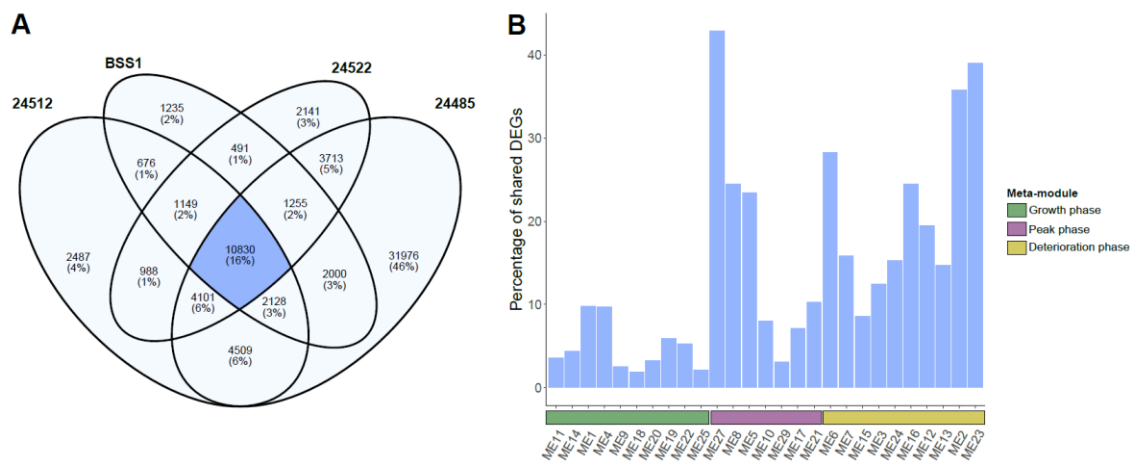


**Figure 4.14 Proportion of differentially expressed genes (DEGs) shared between different male sterile wheat cultivars.**

(A) Venn diagram displaying the number of DEGs shared between 24512, BSS1, 24522 ( $\log_2$ fold change  $> |1|$  and P value  $< 0.05$ ) and 24485 for all developmental stages. (B) Bar plot showing the distribution of the 10,830 DEGs shared by all male sterile cultivars (highlighted in blue in panel A) across the different co-expression modules grouped into growth, peak and deterioration phase meta-modules. No shared genes were found in ME26 and ME28 (not shown).

In the analysis, I also discovered that among the 10,830 shared DEGs, a subset of 769 genes (7.1% of the shared DEGs) were annotated as TFs. By focusing on the senescence-associated TF (SATF) families, namely AP2/ERF-ERF, NAC, WRKY, and MYB, I identified 223 DEGs that were expressed by each of the MS cultivars, and of those, 165 were associated with the previously defined senescence related modules ME6, ME2, ME3, and ME13 (section 4.4.2). Plotting of the data provided compelling evidence for the conservation of their expression profiles, mostly mirroring those observed in 24485, with upregulation at 13 and 18 DAW9.5. In fact, many of the 126 genes encoding TFs that were expressed predominantly in senescing stigmas of MS 24485 were also conserved across the other three cultivars (SS in Figure 4.14 and green boxes in Figure 4.11). From the original set of nine candidate genes identified in Figure 4.11 with all three homoeologs up-regulated, only *ORE1*, *KIR1*, *ERF-1*, *MYB116* and *WRKY11* showed strong upregulation at 13 and 18 DAW9.5, while *DREB26* and *RAP2.2* were not found in the set of differentially expressed core genes (Figure 4.14A), and *WR3* was upregulated at earlier stages (3 and 7 DAW9.5). In light of this, I propose that *ERF-1*, *MYB116*, *WRKY11*, and *ONAC080*, as well as the already known regulators of stigma senescence, *KIR1* and *ORE1*, represent good candidate genes for further

investigation as potential regulators of stigma senescence in wheat, independent of cultivar.

Moreover, I wanted to investigate whether the upregulation of auxin biosynthesis genes during stigma deterioration is a developmental response shared by other cultivars. From the set of genes identified in Figure 4.12B, 45.8% of genes (11) were found to be differentially expressed and shared between the cultivars (Figure 4.14), possibly indicating a common response to aging in unpollinated wheat stigmas. It is premature, however, to speculate on the biological relevance of these findings, and further studies recording auxin levels and functional characterisation of these genes will be needed.

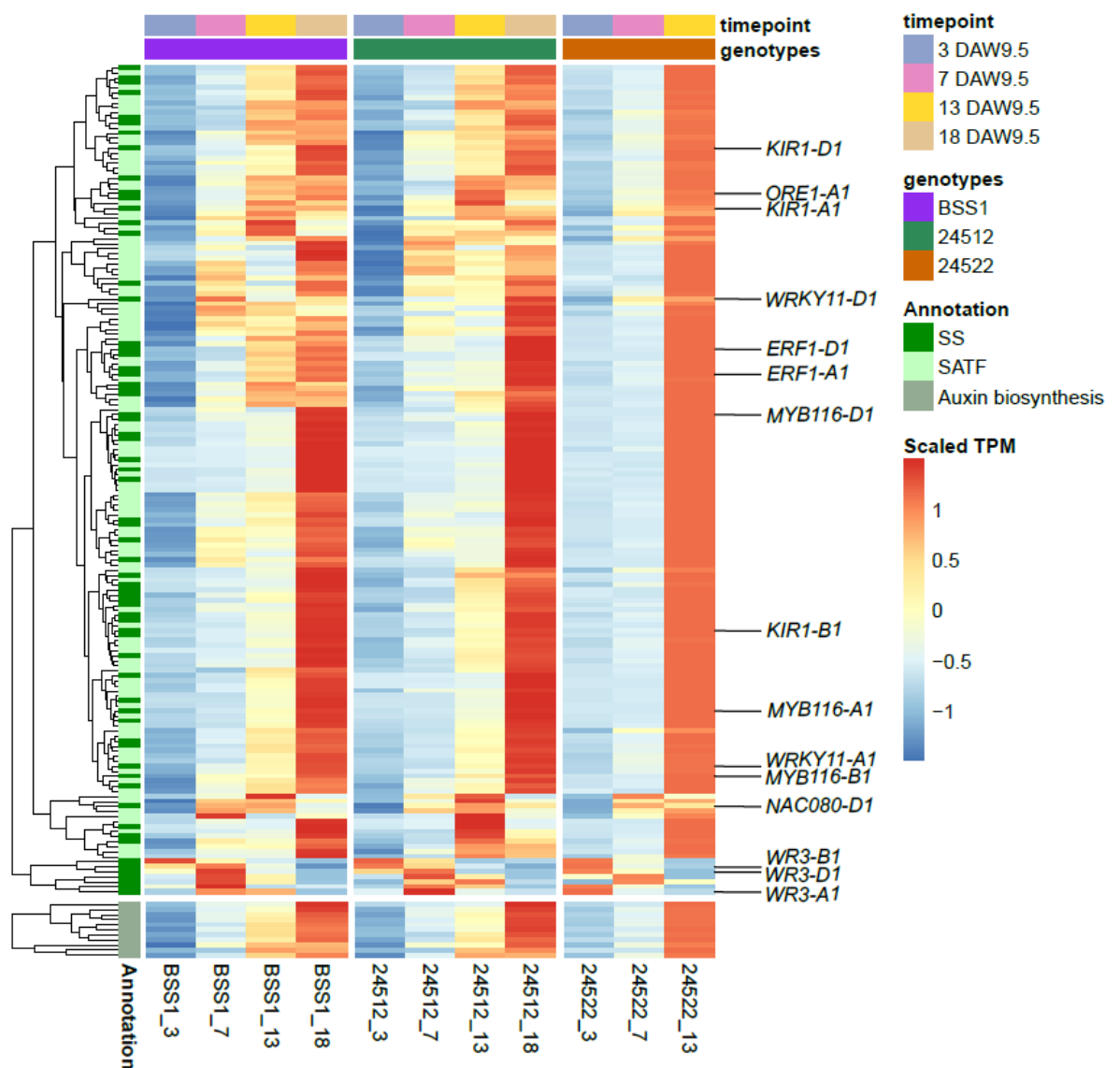


**Figure 4.15 Differentially expressed senescence associated TFs and auxin biosynthesis related genes during stigma development in 24512, 24522 and BSS1.**

Heatmap of normalised TPMs (transcripts per million) of differentially expressed genes (log<sub>2</sub>fold change > |1| and *P* value < 0.05) at 3, 7, 13 and 18 DAW9.5. SS refers to the stigma specific genes identified in Fig. 7 and SAFT refers to senescence associated TFs. Candidate genes are also shown. Normalisation of TPM values was performed by genotype.

**4.4.5. Functional characterisation of *KIR1* and *ORE1* genes in hexaploid wheat**

To gain deeper insights into the molecular mechanisms determining stigma longevity, I investigated the effects of manipulating *KIR1* and *ORE1* on senescence processes.

*4.4.5.1. Selection and generation of mutant populations*

Based on data from previous work on stigma senescence in Arabidopsis (Gao et al., 2018), I selected wheat orthologs for *KIR1* (*TraesCS2A02G382400*, *TraesCS2B02G399700*, *TraesCS2D02G378800*) and *ORE1* (*TraesCS2A02G338300*, *TraesCS2B02G343600*, *TraesCS2D02G324700*) for phenotypic characterisation in bread wheat. The relevance of these two genes as candidate TFs that positively regulate age-dependent senescence in wheat was later supported by the transcriptomic analyses described in section 4.4.3.2.1.

To test the hypothesis that *KIR1* and *ORE1* act as regulators of stigma senescence in wheat, I selected TILLING (Targeting Induced Local Lesions in Genomes) mutations in hexaploid wheat (*cv.* Cadenza; Uauy et al., 2009; Krasileva et al., 2017) that disrupt the function of the encoded proteins. I generated triple *KIR1-A1/B1/D1* and *ORE1-A1/B1/D1* knockout mutants by crossing single mutants to overcome the potential redundancy between homoeologs across the three genomes (Borrill et al., 2015). I identified mutations leading to premature stop codons in all three homoeologs of *KIR1* and *ORE1* located in different positions across the NAC domain (grey shading in Figure 4.15A). These mutations are all expected to abolish the function of the protein as they would lack all or partial sections of the DNA-binding domain. For *KIR-D1*, the identified premature stop codon mutation affects transcript variant 1 exclusively (*KIR1-D1.1*), which was later found to not be highly expressed during development and senescence of the stigmatic tissue (Figure 4.15B). Conversely, the three-exon model,

akin to variant 2, was more prevalent and exhibited higher expression levels across all three subgenomes (Figure 4.15B). In this case, I selected two additional TILLING lines for *KIR1-D1* affecting both transcript variants (C0100 and C0127, Figure 4.15A) with missense mutations located between the NAC subdomains II and IV (Appendix 4.1) generating deleterious SIFT (Sorting Intolerant From Tolerant; Ng and Henikoff, 2003) scores (SIFT = 0). I first crossed the single mutants to generate double mutant populations for both *KIR1* and *ORE1* that were then self-pollinated to produce an F<sub>1</sub> S<sub>1</sub> population. I then selected double mutants that were inter-crossed between each other to subsequently create triple mutant F<sub>2</sub> S<sub>1</sub> populations (Figure 4.15C). The resulting offspring were then screened for triple mutants and backcrossed to wild-type cv. Cadenza to generate a final BC<sub>1</sub> S<sub>1</sub> generation that was multiplied (BC<sub>1</sub> S<sub>2</sub>) and phenotyped under control environment and field conditions.

Acknowledging the potential of the missense mutations in *KIR1-D1.2* to impair protein function, I opted to focus on the mutant harbouring all three stop codon mutations for our subsequent phenotypic analysis, as the triple knockout mutant population (*KIR1-abldl.1*) was more advanced in the crossing scheme compared to the mutant populations containing the missense alleles. Nonetheless, future experiments should also include mutants, like C0100 and C0127, targeting *KIR1-D1.2*, to fully characterise the consequences of eliminating *KIR1* function.



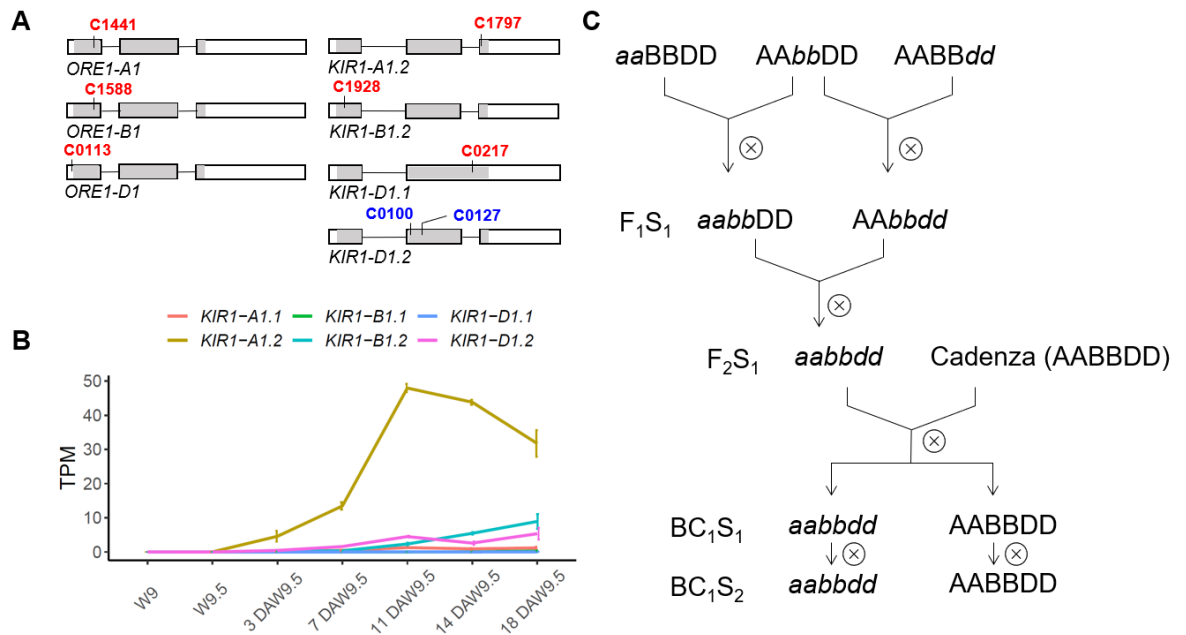


**Figure 4.16 Mutations in *KIR1* and *ORE1*.**

(A) Selected stop (red) and missense (blue) mutations. Grey shading illustrates the NAC domain of the protein. (B) Expression profile for transcript variants of *KIR1*. Data obtained from stigma development time course (section 4.4.1). Values are the average TPM (transcripts per million)  $\pm$  s.e.m. of three biological replicates. (C) Design of crossing scheme. Circled crosses indicate self-pollination.

#### 4.4.5.2. Characterisation of mutants under controlled environment

To determine the duration of the stigma life span and receptivity to viable pollen of the *kir1* and *ore1* triple mutants, I conducted a time course analysis of the stigma life cycle under controlled environments at different time points during late stages of stigma development (8, 12, 14 and 16 days after emasculature (DAE)). I first measured the progression of stigma senescence in the absence of pollination by quantifying stigma area (Figure 4.17) and the rate of cell death (Figure 4.18).

##### 4.4.5.2.1. Stigma size reduction

By taking the reduction in stigma area as an initial estimation of tissue deterioration, I found that stigmas in mutant plants (i.e., *kir1* and *ore1*) shrunk significantly two days later than their wild-type counterparts (i.e., at 14 DAE in *kir1* and at 16 DAE in *ore1* when compared to the first time point at 8 DAE, Figure 4.17B and Appendix 4.2).

Despite the overall size reduction found in all genotypes, stigmas from mutant lines also

shrunk less between 8 and 16 DAE than sibling lines with wild type alleles, with a mean difference of 3.8 mm<sup>2</sup> in *ore1* (vs 4.9 mm<sup>2</sup> in *ORE1*) and 5.4 mm<sup>2</sup> in *kir1* (vs 7.6 mm<sup>2</sup> in *KIR1*). The *ore1* mutants consistently exhibited stigmatic hairs that were significantly shorter (Figure 4.17C and D) than the wild-type *ORE1* stigmas (mean difference 0.34 mm,  $P = 0.0006$ ), indicating stigma hair elongation is disrupted in wheat in the absence of *ORE1* function. However, it is worth noting that not all *ore1* stigmas measured showed the short hair length phenotype and, in some cases, this variability was found within a single spike (Figure 4.17C and D), which could indicate incomplete penetrance of the phenotype under the environmental conditions used during the experiment (see Materials and Methods, section 4.3.2, for details). Although similar phenotypes have been recorded in rice stigmas of the *osmads3* and type-B *rr* (response regulators) mutants (Worthen et al., 2019; Yamaguchi et al., 2006), this observation represents the first documented instance of aberrant stigma phenotype in wheat, and it could hold significant interest for future research, especially in the context of developing female sterile parental lines for hybrid crop production.

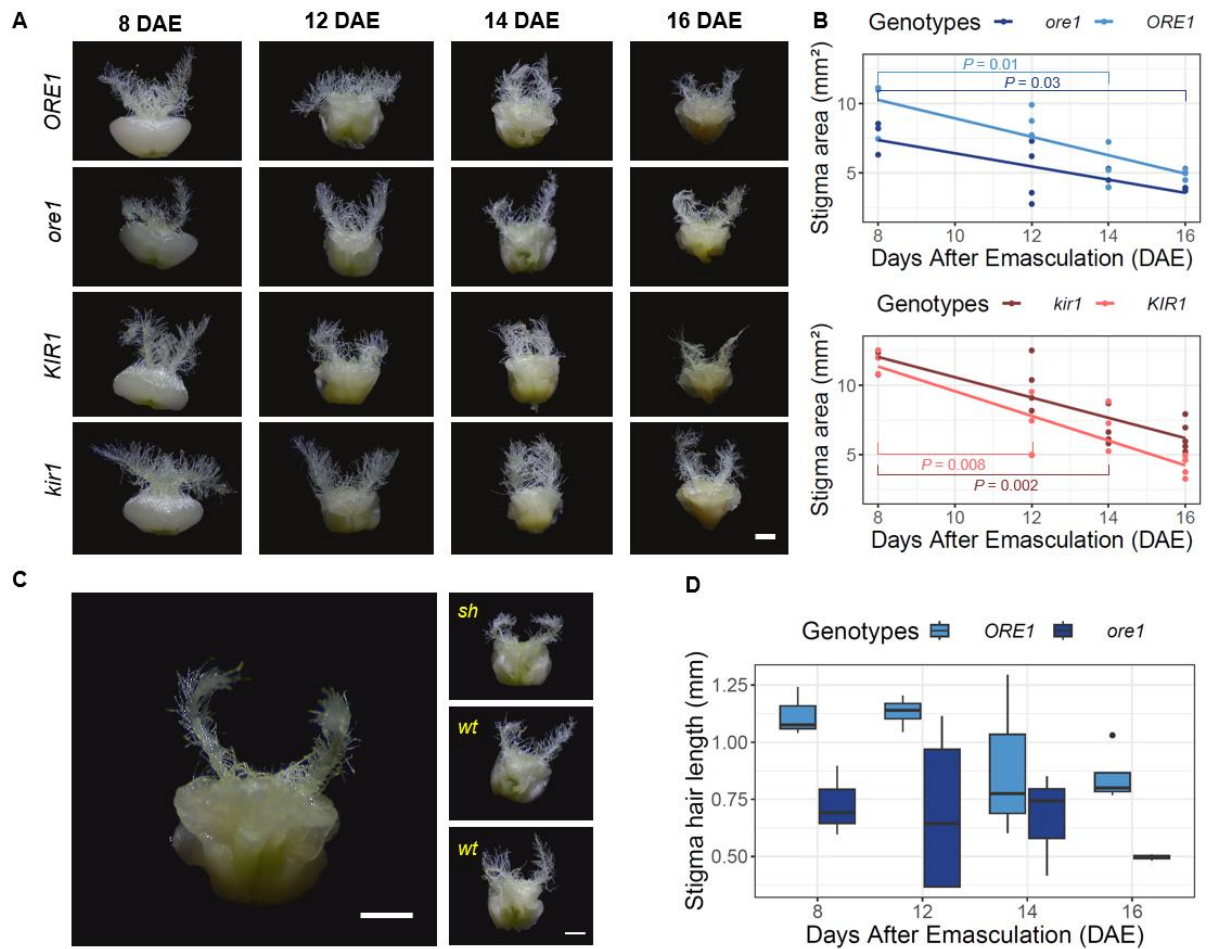


**Figure 4.17 Quantification of stigma size in unpollinated carpels in *KIR1* and *ORE1* mutants.**

(A) Representative images of four stages of carpel development after emasculation in BC<sub>1</sub>S<sub>2</sub> wildtype (*ORE1*, *KIR1*) and mutant (*ore1*, *kir1*) plants. (B) Graphs show linear regression models for stigma area (mm<sup>2</sup>). Each dot represents mean area of stigmas analysed per spike ( $n = 4$ ).  $P$  values (Tukey's test) obtained from two-way ANOVA are also shown for the first significant difference with respect to 8 DAE. (C) On the left-hand side, *ore1* mutant carpel with short stigmatic hairs phenotype. On the right, three carpels collected from an individual *ore1* spike showing wild-type stigmas (*wt*) and short stigmas (*sh*). (D) Box plot showing the comparison between *ORE1* and *ore1* stigma hair lengths. The box plots show the middle 50% of the data with the median represented by the horizontal line. Whiskers represent datapoints within 1.5 times the interquartile range with outliers highlighted as individual points ( $n = 4$ ). Scale bars: 1 mm.

#### 4.4.5.2.2. Progression of stigmatic cell death

To further analyse the role of *KIR1* and *ORE1* in inducing cell death within aging stigmas, I used a combination of fluorescein diacetate (FDA) and propidium iodide (PI) staining to investigate cell viability as described by Gao et al., (2018). This analysis involved determining the proportion of stigmatic tissue that was stained by either FDA (live tissues; green pixels) or PI (dead tissue; magenta pixels) at different developmental stages to characterise the progression of cell death within each genotype (Figure 4.18A, see Material and Methods for detailed explanation). Despite the wide variability observed between samples, I found that papilla cell death was generally visible at 12 DAE, with dead tissue comprising around 50 % of the stigma in some cases (Figure 4.18B). Cell death spread gradually from the edges of the stigma towards the central region through the formation of small clusters of senescing cells, as illustrated in Figure 4.18A (stigma 14 DAE), which is supported by results from Gao et al., (2018). For most of the genotypes, the collapse of the entire stigma (% green pixels ~ 0) was recorded at 14 DAE, with the exception of *ore1* mutants that persistently showed good levels of stigma viability at 12 and 14 DAE with total tissue degeneration only happening at 16 DAE. These results demonstrate that loss of ORE1 function is sufficient to delay stigma cell death in wheat. However, in contrast to our initial hypothesis, the progression of cell death remained unaltered after disrupting protein function in *kir1* mutants (*KIR1* vs. *kir1*, assessed via two-way ANOVA accounting for time; *P* value = 0.1; Appendix 4.4), suggesting that KIR1 function alone is insufficient to regulate stigma longevity.

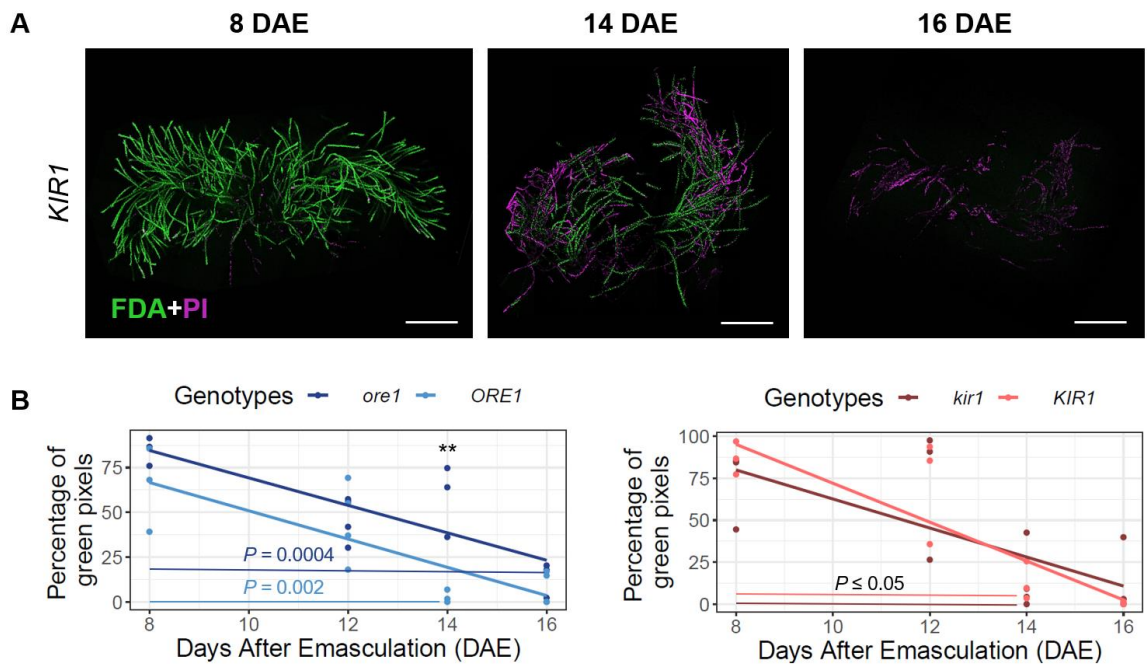


**Figure 4.18 Live-dead staining for monitoring progression of cell death in unpollinated stigmas.**

(A) Maximum intensity projection of confocal images of stained stigmas at 8, 14 and 16 days after emasculation (DAE). In green, FDA stains the cytoplasm of viable cells; in magenta, PI stains nuclei of dead cells. Scale bar: 1 mm. (B) Linear regression models for the percentage of green pixels. Each dot represents mean percentage of green pixels for the total of stigmas analysed per spike ( $n = 2$ ). Statistical differences were calculated using two-way ANOVA with P values obtained by Tukey's test (Appendix 4.2 and 4.3). For each genotype, the first significant difference with respect to 8 DAE is shown. Black asterisks indicate the only significant pairwise comparison between wild-types and mutants (\*\*P value < 0.01).

#### 4.4.5.2.3. Stigma receptivity

To explore the relationship between stigma deterioration and receptivity loss (i.e., ability of the stigma to support pollen germination), I hand-pollinated stigmas at 8, 12, 14 and 16 DAE with *cv.* Cadenza mature pollen grains and subsequently scored pollen tube emergence and seed production (Figure 4.19). To visualise pollen tube growth on the stigma, I used aniline blue as a stain specific for callose, which is formed during the process of pollen tube elongation (Edlund et al., 2004). Pollen germination was successful in virtually all stigmas pollinated at 8 DAE (Figure 4.19B). At 12 DAE, pollen germination decreased rapidly in the wild-type *ORE1* stigmas with only one out of the six pollinated stigmas (16.7%) presenting signs of pollen germination, while receptivity at 14 DAE was completely lost (Figure 4.19B). Conversely, 60 and 33% of the stigmas in *ore1* exhibited receptivity at 12 and 14 DAE, respectively. In addition, *kir1* mutants also showed an extension of stigma receptivity with 100% of the pollinated

stigmas showing pollen germination at 12 DAE, as opposed to 50% in *KIR1* wild-type stigmas. Seed set, on the other hand, was only observed at 8 DAE, and not all pollinated carpels developed into grains (Figure 4.19C). These results indicate that pollen tube migration towards the micropyle along with ovary and ovule viability are important processes involved in the control of female fertility, in addition to stigma functionality, and they should be considered in future studies.

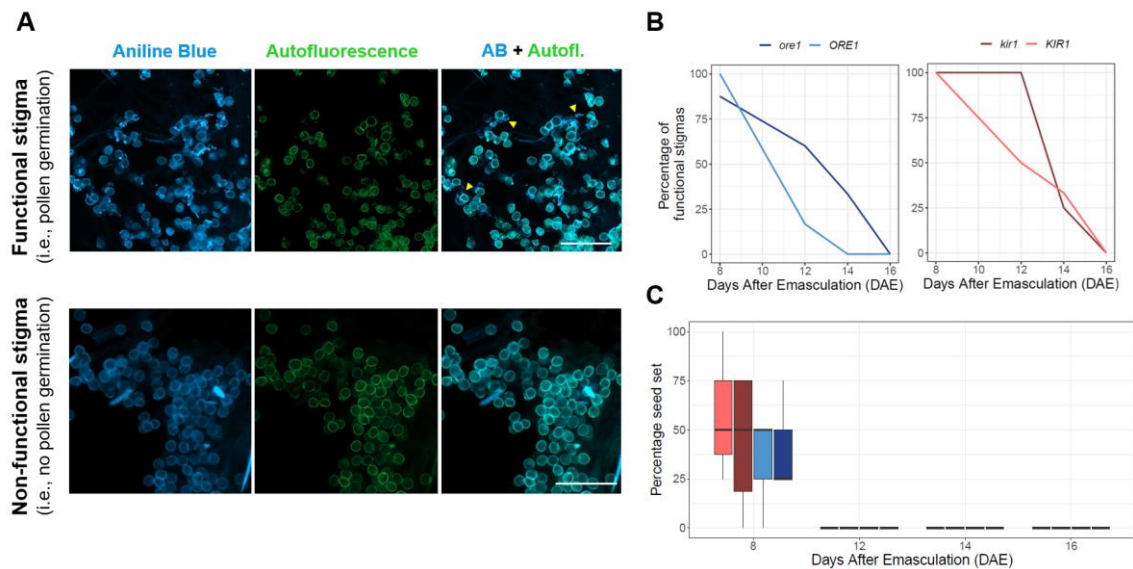


**Figure 4.19 Stigmatic pollen grain germination and seed set to investigate flower receptivity in *kir1* and *ore1* mutants.**

(A) Representative images of cv. Cadenza pollen grains on wheat stigmas. Pollen tubes are stained with aniline blue (yellow arrowhead), and to facilitate visualisation of pollen tubes, autofluorescence of pollen grains is also shown in green. Scale bars: 250 μm. (B) Line graph with the distribution (in %) of receptive stigmas per genotype and time point ( $n \geq 6$ ). (C) Box plot showing percentage of pollinated carpels setting seeds per genotype and time point. Box plots show the middle 50% of the data with the median represented by the horizontal line. Whiskers represent datapoints within 1.5 times the interquartile range.

#### 4.4.5.3. Characterisation of mutants under field conditions

To test the performance of *kir1* and *ore1* mutant plants in a large-scale production set up, I grew plants in a field trial at the John Innes Centre Church Farm (2022-2023). In addition to the triple *kir1* (i.e., *kir1-a1b1d1*) mutant, I also grew single *kir1-a1* mutants as *KIR1-A1* expression is substantially higher than the two homoeologs on the B and D genomes (Figure 4.15B). In fact, according to Ramírez-González et al., 2018, the presence of A, B or D dominant triads is not a rare feature in the stigma and ovary compared to any other tissues in wheat. The unbalanced transcription of the triad could

point towards *KIR1-A1* having a more important role in regulating downstream changes in gene expression and a mutant phenotype could manifest in single *kir1-a1* plants. Wild-type *cv.* Cadenza plants were included in the experiment as controls.

#### 4.4.5.3.1. Morphology of the unpollinated stigma

To avoid self-pollination, I hand-emasculated eight main spikes per plot at ear emergence (Zadoks' growth stage 59; Zadoks et al., 1974) and assessed the physical appearance of the unpollinated stigma at 2, 4, 6, 10 and 14 DAE (Figure 4.20A). I found no obvious differences in the progression of stigma senescence between wild-type *cv.* Cadenza, *KIR1*, *kir1-a1* and *kir1* (representative images at 6 and 10 DAE are shown in Figure 4.20A) with stigmas generally starting to show visible symptoms of stigma deterioration and shrinkage at 10 DAE. Following our previous findings under controlled conditions, *ore1* carpels showed very short or no stigmatic tissue. Unexpectedly, I also observed the same phenotype in the wild-type sister plants, raising questions about a potential mistake during the genotyping process that was later confirmed by erroneous calling of the genotypes. Due to the severe stigma phenotype in *ore1* and *ORE1*, it was not possible to assess the progression of stigma senescence. In addition, the lack of the stigma also resulted in very poor seed set in self-pollinated spikes, highlighting again their potential use as female sterile plants for hybrid seed production (Figure 4.20B).

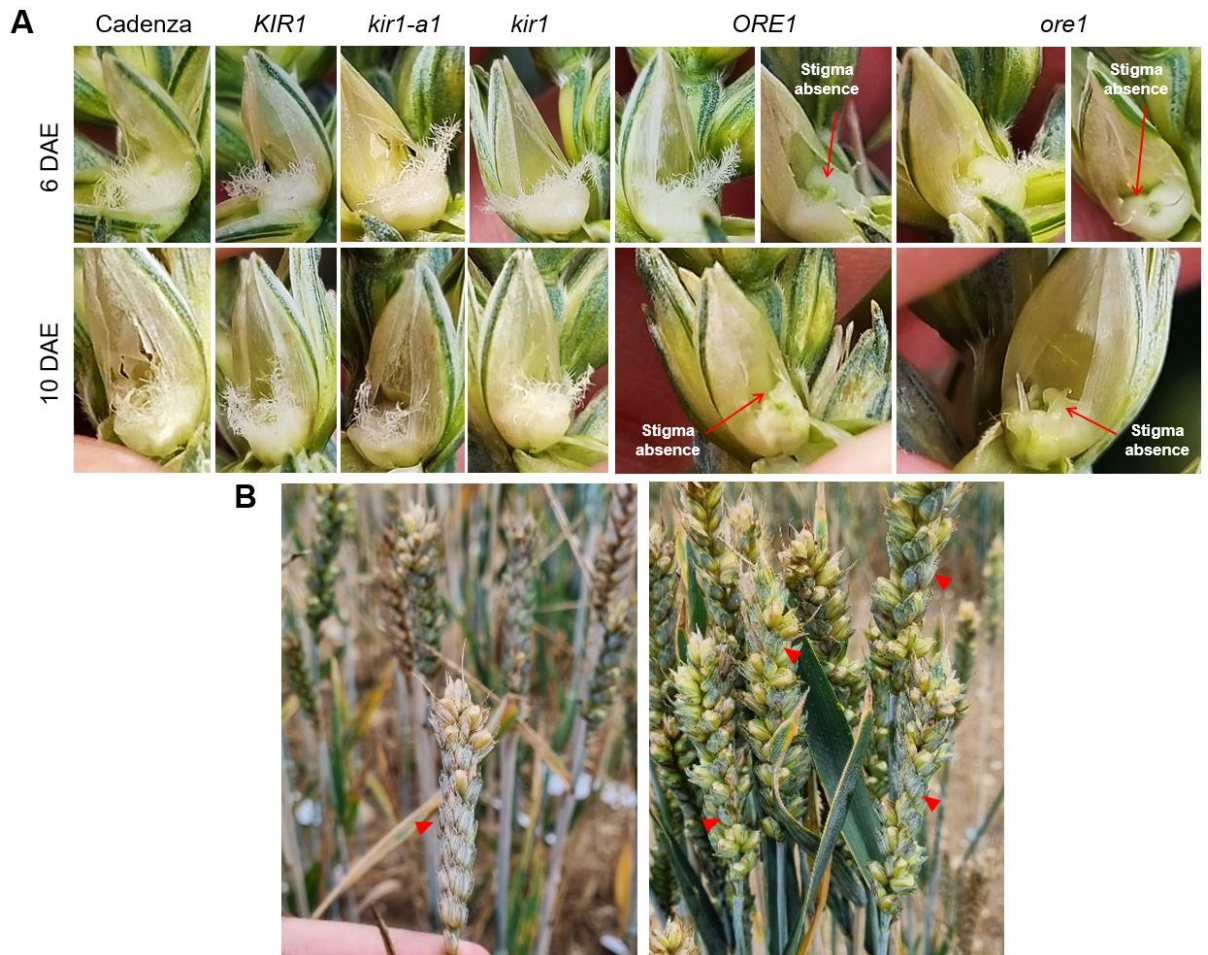


**Figure 4.20** Development of the unpollinated stigma under field conditions for mutant and cv. Cadenza populations and reduced grain set in *ORE1* and *ore1* populations.

(A) Representative images illustrating the physical appearance of the unpollinated carpels at 6 and 10 days after emasculating (DAE) in wild type Cadenza, *KIR1*, *kir1-a1*, *kir1*, *ORE1* and *ore1*. Red arrows indicate the ‘absence of stigma’ phenotype in both *ORE1* and *ore1* plants. (B) Wheat spikes with floret sterility (red arrowheads) in *ore1* (left) and *ORE1* (right) genotypes.



#### 4.4.5.3.2. Flag leaf senescence

Given the important role of NAC TFs in promoting overall plant senescence, I measured chlorophyll content of the flag leaf at 13, 24, 33 and 38 days after anthesis (Figure 4.21). Again, I saw no significant difference between the rate of senescence in Cadenza, *KIR1*, *kir1-a1* and *kir1*, suggesting the presence of *KIR1* paralogs could potentially mask the effect of the mutations on group 2 chromosomes (addressed in the Discussion). Although not significant, *ORE1* and *ore1* mutant plants showed a slight delay in the yellowing of the leaf when compared to Cadenza, but the sibling lines contrasting at *ORE1* were not significantly different.

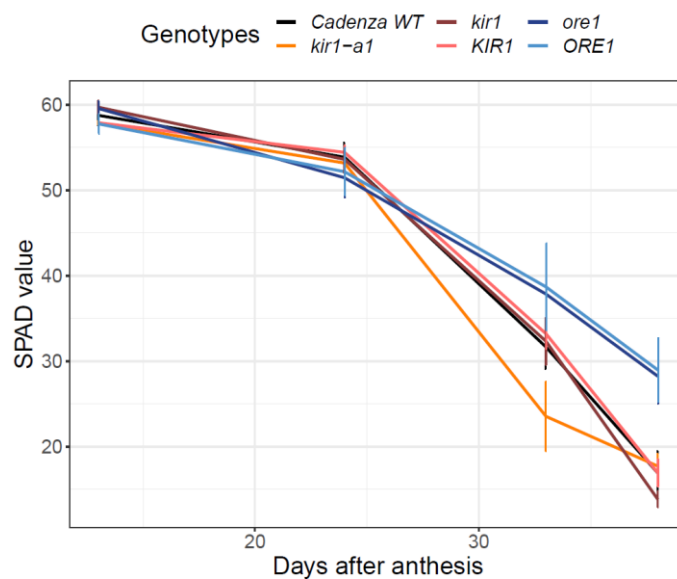


**Figure 4.21 Flag leaf senescence in *KIR1* and *ORE1* mutant and Cadenza populations.**

SPAD chlorophyll meter readings to quantify flag leaf senescence from 13 to 38 days after anthesis. Eight flag leaves were measured for each time point and plot. Data represent the average and s.e.m. of three biological replicates.

## 4.5. Discussion

In this chapter, we explored genetic mechanisms underlying stigma development in the absence of pollination via transcriptome profiling and reverse genetics. We focussed on the identification of genes that may regulate processes relevant to stigmatic longevity, as they hold the potential to facilitate successful cross-pollination in a broad set of male-female hybrid combinations.

### 4.5.1. The development of the unpollinated stigma is under tight genetic control

The strong association observed between transcript profiles and physiological processes in the different wheat cultivars analysed, indicate that stigma development and senescence in the absence of pollination are indeed the result of a tightly regulated transcriptional process. Notably, more than half of the high confidence genes (Appels et al., 2018) were expressed at some point during stigma life cycle, and 44 % of genes encoding TF (Evans et al., 2022) were expressed differentially. Moreover, correlation analysis of the WGCNA co-expression modules revealed three major temporal waves of gene expression, corresponding to the growth, peak, and deterioration phases of stigma development (Figure 4.7 and 4.7). This classification facilitates the dissection and identification of genes that potentially govern these age-related stages.

### 4.5.2. Differential expression analysis provides insights into the genetic regulation underlying the growth and peak phases

Examination of the transcriptional changes observed during the first half of our time course analysis has shed light into the biological processes and potential genetic regulation that underlie the growth and peak phases of stigma development in wheat. For instance, I found that most of the DEGs that were upregulated during the early stages of stigma development (i.e., W9 and W9.5 in the growth phase meta-module) were significantly enriched for processes such as cell growth and differentiation, nucleic acid metabolism, cell cycle or cellular component organisation (Figure 4.9), which is consistent with stigmas undergoing a period of rapid growth and cellularisation during early developmental stages (Waddington et al., 1983). During these phases, our analysis also revealed a concurrent significant upregulation of TF families with well-established roles in flower development and reproduction such as the MIKC-type MADS-box TFs

(Figure 4.10). Within this set of regulatory genes, I identified the wheat orthologs of *APETALA-1* (*AP-1*) and *SEPALLATA-3*, whose interaction has been shown to promote normal flower development in *Arabidopsis* (Pelaz et al., 2001). Furthermore, in wheat, the orthologs of *AP-1*, including *VRN1*, *FUL2* and *FUL3*, have been shown to act with *AGL6-like* genes to play critical roles in spikelet and spike meristem development (Kong et al., 2022; Li et al., 2019), indicating that *AP-1* like genes might also play a role during stigma formation and development in wheat.

In addition, stigma development and function have been shown to be strongly linked to the plant hormone, auxin. For instance, disruption of the protein kinase PID, involved in polar auxin transport results in the elimination of stigma formation, while its overexpression leads to the over proliferation of stigmas (Bennett et al., 1995; He et al., 2019). Consistent with these observations, I identified that auxin signalling-related genes were significantly enriched during the growth stage of stigma development (Figure 4.12). Following on this, I noted an overrepresentation of TFs B3 and B3-ARF, known for their pivotal roles in auxin transport and distribution during morphogenesis (Figure 4.10; Ballester et al., 2021). In *Arabidopsis*, the B3-domain *NGA* genes have been described as key regulators of style and stigma development (Ballester et al., 2021; Gaillochet et al., 2018). Their expression in the developing wheat stigma suggests a functional conservation of these genes in the determination and development of floral structures. Furthermore, several other B3-ARF TFs, including wheat orthologs of *OsARF6*, *OsARF12*, *OsARF17*, and *OsARF25*, were also found to be upregulated during early stages of development. Interestingly, in rice, combinations of double knock-out mutants involving these TFs results in larger stigmas (Zhao et al., 2022). Collectively, these findings enhance our understanding of the regulatory networks that govern stigmatic growth in wheat. Moreover, the conservation of some of these regulatory genes across eudicot and monocot species (Ciaffi et al., 2011) suggests that research in other species may offer valuable insights into the molecular events underlying wheat stigma development.

Shifting now our focus to the peak phase, I identified DEGs significantly enriched for processes related to transport, response to extracellular stimuli, cell communication and signal transduction (Figure 4.9). This aligns with the characteristics of a mature stigma preparing for its encounter with the pollen grain, which represents one of the most important plant cell-cell interactions in crop production. However, our current understanding of the molecular players involved in wheat reproduction remains highly

limited (Robinson et al., 2023). During this reproductive stage, the stigma equips itself with the necessary proteins to facilitate pollen adhesion, pollen grain recognition, and hydration, all of which are essential for promoting pollen tube growth into the style and ovary tissues. Previous proteomic analyses conducted in triticale (*x Triticosecale* Wittmack *ssp.*) and brassica (*Brassica carinata*) stigmas have revealed a decline in the levels of multiple enzymes involved in pollen adhesion as the stigma ages. These patterns parallel the gene expression profiles observed in certain modules within the peak phase (e.g., ME10, ME5, ME27, ME8; Figure 4.6). Within these modules, I have identified genes that may be associated with various stages of the pollen-stigma interaction, such as the *CIPK* genes involved in pollen germination and pollen tube growth (Mähs et al., 2013). However, other genes previously detected in the proteome of triticale stigmas and transcriptome of rice stigmas (Li et al., 2007; Robinson et al., 2023), such as those involved in vesicular trafficking to the stigma surface, peroxidases and catalases implicated in the breakdown of pollen coat exines, or ROS-associated factors are yet to be uncovered in the wheat stigma. A more in-depth examination of this data holds the potential to provide valuable insights into the processes occurring within the mature, yet unpollinated, stigma.

#### 4.5.3. Comparative transcriptomics as a method to identify candidate genes involved in stigma deterioration

One of the aims of this chapter was to identify TFs regulating stigma senescence, a process likely akin to leaf and floral senescence. In plants, senescence is primarily controlled by factors such as age and external and internal stimuli, including hormones and TFs. Previous studies have highlighted the role of TF in the regulation of senescence across a wide range of plant species, with the upregulation of specific TFs coinciding with the onset of cell death processes (Bengoa Luoni et al., 2019; van Doorn & Woltering, 2008). Examination of the expression patterns of TFs present in wheat stigmas revealed that, among the 67 TF families currently annotated in wheat, six exhibited significant overrepresentations in genes belonging to senescence related co-expression modules (Figure 4.10). These included the NAC, WRKY, MYB, and AP2-ERF TF families, which have been recognised as integral components of the senescence regulatory network in wheat (Sultana et al., 2021). Members of the MYB family have diverse roles in plant development, but they are also involved in the regulation of senescence, like the positive regulator of leaf senescence *MYBH* (Huang et al., 2015). In

rice and Arabidopsis, functional analyses of WRKY family genes, including, for instance, *WRKY53*, *WRKY75*, and *WRKY6*, have revealed a participation in senescence related processes (reviewed in Chen et al., 2017). Additionally, the NAC family draws significant interest due to the demonstrated roles of several NAC TFs in regulating leaf senescence in Arabidopsis (Balazadeh et al., 2010; Kim et al., 2009) and in wheat (Borrill et al., 2019). Moreover, these NAC TFs have recently emerged as pivotal regulators of age-dependent stigma senescence (Gao et al., 2018; Šimášková et al., 2022) and petal senescence (Shibuya et al., 2014). Additionally, *ERF4/8* and *ERF34* genes from the AP2/ERF family have been identified as promoters of leaf senescence in Arabidopsis (Koyama, 2014; Park et al., 2022); and in the context of senescent petals, a gene encoding an AP2 protein was found to be substantially up regulated in daffodils (*Narcissus pseudonarcissus*; van Doorn & Woltering, 2008).

To further investigate this question, I adopted a comparative transcriptomic approach, leveraging two independent publicly available expression datasets spanning multiple tissues and growth stages as well as additional stigma developmental time courses (Figure 4.11 and 4.14). On one hand, this analysis revealed interesting parallelisms between the transcriptomes of senescing leaves and stigmas, suggesting shared genetic mechanisms in wheat. This genetic redundancy between analogous developmental processes was particularly evident in early stigma development as well, which highlighted the complexity of stigma life cycle and its notable resemblance to various aspects of the plant's life cycle, albeit on a compressed timescale. On the other hand, I identified a subset of 66 genes that were specifically expressed in senescent stigmas and their expression patterns were shared across all four MS cultivars. Within this set I identified the well-established stigma senescence regulators *KIR1* and *ORE1* alongside other co-regulated TFs such as *ERF-1*, *MYB116*, *NAC080* and *WRKY11*. Briefly, *ERF-1* has been implicated in the regulatory network of the floral senescence related gene *FOREVER YOUNG FLOWER (FYF)*; Chen et al., 2022). *MYB116* was found to be able to bind to NAC TFs in senescent leaves in Arabidopsis and was also found to be highly upregulated in aged flowers of *Camellia lutchuensis* (Hickman et al., 2013; Liu et al., 2022). *WRKY11*, acting as a part of WRKY-OBE complexes, is responsible for repressing the transcription of a wide range of biotic and abiotic stress-responsive genes (Du et al., 2023) and *NAC080* has shown an important role in regulating the response to various cold conditions in tea tree (*Camellia sinensis*; Hao et al., 2018). While there is no direct information about the role of *WRKY11* and *NAC080* in developmental

senescence processes, it is worth noting that stress-responsive genes are also closely linked to environmentally induced senescence (Woo et al., 2013). Although it is still too early to speculate on the precise functions of these genes in the regulation of stigma senescence, our findings provide valuable insights into the biological mechanisms of senescence and sets the stage for further research. It also offers an example of how combining publicly available expression transcriptomes can aid the discovery of candidate genes for various biological processes.

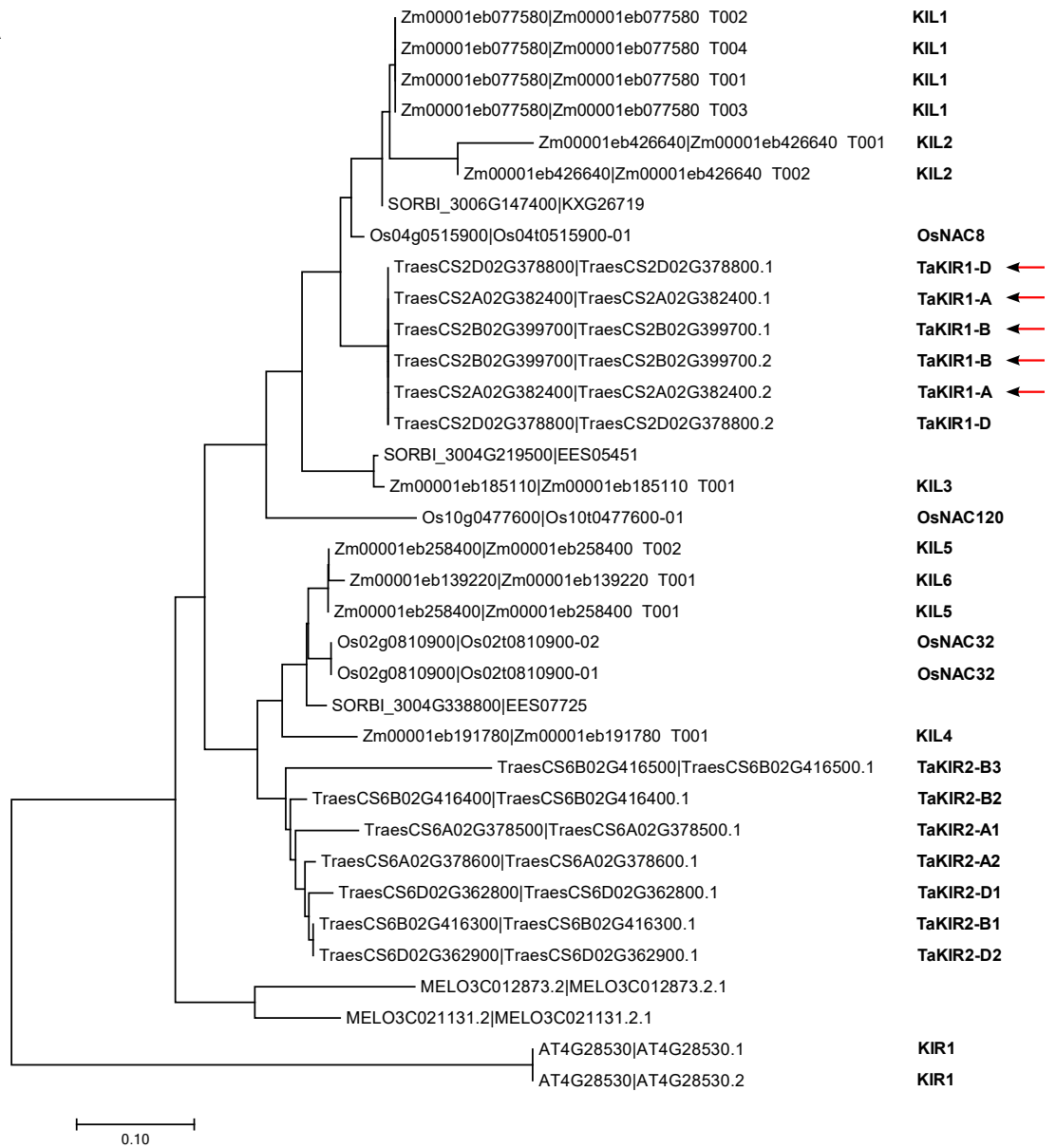
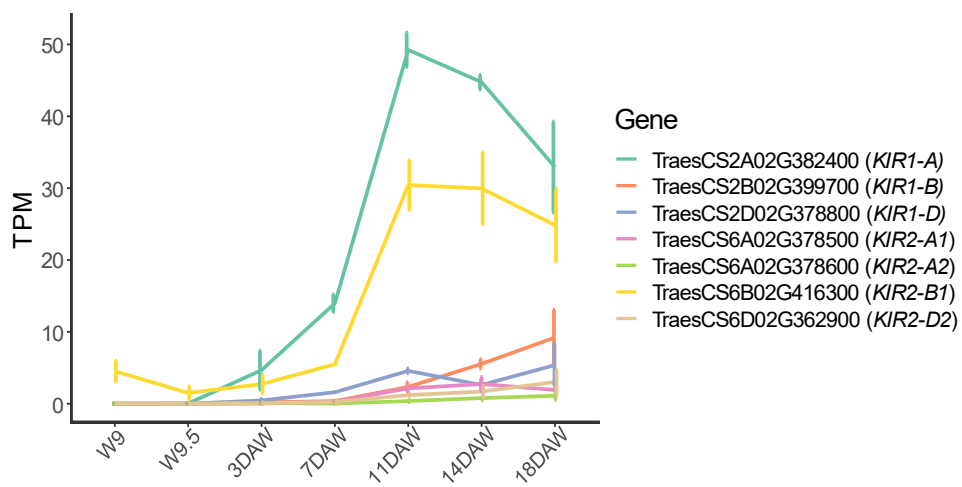
#### 4.5.4. Lessons from studying *kir1* and *ore1* loss of function mutants

To better understand the biological processes taking place in the aged wheat stigma, I focused on the NAC TFs *KIR1* and *ORE1*, which have been previously characterised for their roles in triggering stigma senescence in *Arabidopsis* (Gao et al., 2018). Phenotypic characterisation of *kir1* and *ore1* TILLING mutants uncovered previously unknown mechanisms of cellular senescence in wheat stigmas. Among these mechanisms, I observed an increment of plasma membrane permeability as indicated by the entry of PI into the cell (Figure 4.18A), ultimately resulting in membrane rupture. In addition to plasma membrane degeneration, I also found weaker or no PI signal in highly senesced stigmas that resulted in a set of samples that did not qualify for cell death quantification analysis (refer to materials and methods). This weakened signal is indicative of nuclear disintegration due to the absence of discernible nuclear content, a hallmark of advanced cell corpse clearance. Interestingly, I also found papilla cells undergoing cell death in clusters (Figure 4.18A) suggesting a coordinated response likely mediated through cell-cell signalling as supported by the overrepresentation of genes related to cell communication (GO: 0007154) and cell-cell signalling (GO: 0007267) processes in senescence related co-expression modules (Figure 4.9). These patterns of stigma deterioration align with canonical programmed cell death events, consistent with findings reported by Gao et al. (2018) for aged *Arabidopsis* stigmas.

Interestingly, the rate at which these cell death processes occurred in the unpollinated stigmas differed between the wild-type and the loss of function *ore1* mutants (Figure 4.18B) implicating *ORE1* in the regulation of stigma senescence onset in wheat. In contrast, I found no significant differences in the rate of stigmatic death in *KIR1* deficient mutants compared to wild-type stigmas under controlled and field conditions (Figure 4.18B). Three potential factors may account for the absence of a mutant phenotype in *kir1* plants. Firstly, the TILLING mutation aimed at disrupting KIR1-D1

function sits within an alternative splicing region (Figure 4.15A and Appendix 4.1). This region, however, is excluded in the predominantly expressed gene variant likely resulting in the production of a functional protein. This suggests a potential functional redundancy of *KIR1*, as mutations in A and B homoeologs lead to a phenotype that is indistinguishable from wild-type plants with three functional copies. Future analyses including the use of missense mutants may provide clarification. Nonetheless, it is also important to note that, during the selection of the stop codon mutation, there was insufficient evidence to definitively assess its impact due to the then recently annotation of wheat gene models (Appels et al., 2018) and the lack of senescing stigma-specific expression data. Secondly, it is also plausible that the lack of a mutant phenotype in *kir1* plants may be due to the presence of potentially functional *KIR1* paralogs (Figure 4.22A), which may mask the effects of the mutations in the other gene copies. Examination of the expression data revealed that among the six additional *KIR1* copies located on chromosomes 6A, 6B and 6D (referred to as *KIR2* in Figure 4.22B), *KIR2-B1* shows the highest expression in senescing stigmas, making it an interesting candidate for mutagenesis. Further exploration could entail simultaneous targeting of A, B, and D gene copies using CRISPR-Cas, significantly reducing the time needed to generate triple mutants compared to conventional crossing schemes (where obtaining BC<sub>1</sub> triple mutants takes approximately 3.5 years, Figure 4.15C). Lastly, the intricate nature of phenotyping dynamic processes, coupled with the high variability observed across biological replicates, may hinder the identification of subtle differences between the genotypes.

Finally, the observed extension of stigma receptivity in *ORE1*- and *KIR1*-deficient mutants (Figure 4.19B) raised an interesting question regarding the possibility of a corresponding extension in seed set. However, the failure to effectively extend seed set suggests that factors beyond stigma receptivity, such as the viability of the unfertilised ovule, are lost during floral senescence (Van Durme et al., 2023; Williams, 1965). The effects of ovule longevity and the period of stigma receptivity in limiting the period in which pollination and fertilisation can occur are further discussed in Chapter 5 section 5.2.

**A****B**



**Figure 4.22 Gene duplication of *KIR1* in hexaploid wheat.**

(A) Phylogenetic tree of the closest *KIR1* homologs in different dicot (*Arabidopsis* (AT) and melon (*Cucumis melo*; MELO)) and monocot species (wheat (Traes), maize (Zm), rice (Os) and sorghum (*Sorghum bicolor*; SORBI)). Peptide sequences were used to construct a rooted neighbor-joining tree including splice variants when present. These are indicated by either .1, -01 or T001 at the end of the label. Peptide sequences were obtained from Ensembl and evolutionary analyses were conducted in MEGA7 (Kumar et al., 2016). Gene names are listed on the right-hand side, with the exception of MELO and SORBI, for which names have not yet been assigned. Arrows indicate genes for which mutant lines have been generated and phenotyped in this chapter. (B) Expression profile for *KIR1* paralogs. Data obtained from stigma development time course (section 4.4.1). Values are the average TPM (transcripts per million)  $\pm$  s.e.m. of three biological replicates. Note that some genes were excluded as they showed no expression during the time course.

In conclusion, this research highlights the complexity of studying floral longevity and emphasises the importance of the new resources generated from this preliminary study to advance in the understanding of female reproductive biology in wheat. Furthermore, these data pave the way for future genetic modulation to fine tune different aspects of stigma biology (e.g., stigma growth) with a view to ultimately improve seed set efficiency, which remains a prominent challenge in the establishment of hybrid wheat.

## 4.6. Appendices

### CLUSTAL O (1.2.4) multiple sequence alignment

```

KIR1-A1.2      MGLREIESTLPPGFRFYPSDQELVCHYLCKKVTNERASQGTLEVDLHAREPWELPDVAKLTASEWYFFSFRDRKYATGSRTNRATKTGYWKATGKDREVRSPATRAVVGMRKTLVIFYQG      120
KIR1-A1.1      MGLREIESTLPPGFRFYPSDQELVCHYLCKKVTNERASQGTLEVDLHAREPWELPDVAKLTASEWYFFSFRDRKYATGSRTNRATKTGYWKATGKDREVRSPATRAVVGMRKTLVIFYQG      120
KIR1-B1.1      MGLREIESTLPPGFRFYPSDQELVCHYLKVKVTNERASQGTLEVDLHAREPWELPDVAKLTASEWYFFSFRDRKYATGSRTNRATKTGYWKATGKDREVRSPATRAVVGMRKTLVIFYQG      120
KIR1-B1.2      MGLREIESTLPPGFRFYPSDQELVCHYLKVKVTNERASQGTLEVDLHAREPWELPDVAKLTASEWYFFSFRDRKYATGSRTNRATKTGYWKATGKDREVRSPATRAVVGMRKTLVIFYQG      120
KIR1-D1.2      MGLREIESTLPPGFRFYPSDQELVCHYLKVKVTNERASQGTLEVDLHAREPWELPDVAKLTASEWYFFSFRDRKYATGSRTNRATKTGYWKATGKDREVRSPATRAVVGMRKTLVIFYQG      120
KIR1-D1.1      MGLREIESTLPPGFRFYPSDQELVCHYLKVKVTNERASQGTLEVDLHAREPWELPDVAKLTASEWYFFSFRDRKYATGSRTNRATKTGYWKATGKDREVRSPATRAVVGMRKTLVIFYQG      120
*****

KIR1-A1.2      RAPNGSKTSWVMHEFRLDSPHLPPR-----EDVLCRVFQKQKVDGEQDNARSSSPTFAGSSQAAQELPVM DASSDQMMGSGSAGFAP      203
KIR1-A1.1      RAPNGSKTSWVMHEFRLDSPHLPPRVRTNYMSHVLLR-----LAPLRS AFLIDLDAIQEDVLCRVFQKQKVDGEQDNARSSSPTFAGSSQAAQELPVM DASSDQMMGSGSAGFAP      232
KIR1-B1.1      RAPNGSKTSWVMHEFRLDSPHLPPRVRTNCTRL-----QVYLLFAIASAGVSNLDAIQEDVLCRVFQKQKLDGEQDNARSSSPTFARSSQVAQELPVM DASSDQMMGSGAAGFVA      232
KIR1-B1.2      RAPNGSKTSWVMHEFRLDSPHLPPR-----EDWVLCRVFQKQKLDGEQDNARSSSPTFARSSQVAQELPVM DASSDQMMGSGAAGFVA      203
KIR1-D1.2      RAPNGSKTSWVMHEFRLDSPHLPPR-----EDWVLCRVFQKQKLDGEQDNARSSSPTFAGSSQAAQELPVM DASSDQMMGSGSAGFAA      203
KIR1-D1.1      RAPNGSKTSWVMHEFRLDSPHLPPRVRTHQLLLYVTCIPLFGLAPLFAIAVGVANLDAIQEDWVLCRVFQKQKLDGEQDNARSSSPTFAGSSQAAQELPVM DASSDQMMGSGSAGFAA      240
*****

KIR1-A1.2      PRQEEIFCGPSPLMNAAMWQQYNSLLLDQYPQEETASVSPTMGIGARGGAGDECGFFFN SGFEDMATLGAMRFPQGWS*      281
KIR1-A1.1      PRQEEIFCGPSPLMNAAMWQQYNSLLLDQYPQEETASVSPTMGIGARGGAGDECGFFFN SGFEDMATLGAMRFPQGWS*      310
KIR1-B1.1      PRQEELICGNPLMNAAMWQQYNSLLLDQYPQEEMAGSSPMMA---TGGAGDECGFFFN SGFEDTATLGTMRFPQAWS*      307
KIR1-B1.2      PRQEELICGNPLMNAAMWQQYNSLLLDQYPQEEMAGSSPMMA---TGGAGDECGFFFN SGFEDTATLGTMRFPQAWS*      278
KIR1-D1.2      SRQEEMICGNPLMNAAMWQQYNSLLLGQYPQEEMAGSSPMMA---TGGAGDECGFFFN SGFEDTASLGAMRFPQAWS*      278
KIR1-D1.1      SRQEEMICGNPLMNAAMWQQYNSLLLGQYPQEEMAGSSPMMA---TGGAGDECGFFFN SGFEDTASLGAMRFPQAWS*      315
*****

```

#### Appendix 4.1 ClustalW alignment of KIR1 protein variants 1 and 2 in all three A, B and D homoeologs.

NAC subdomains are highlighted in grey. Selected stop codon mutations are highlighted in red and missense mutations in light blue.

**Appendix 4.2 Analysis of variance for stigma area in *ore1* and *kir1* mutant populations at 8, 12, 14 and 16 DAE.**

Tukey HSD (honest significant differences) test was used to perform multiple pairwise-comparisons between group means. Diff: difference between means of the groups lower  $\pm$  the upper end point of the confidence interval at 95%.

	<b>8 vs 12 DAE</b>		<b>8 vs 14 DAE</b>		<b>8 vs 16 DAE</b>		<b>12 vs 14 DAE</b>		<b>12 vs 16 DAE</b>		<b>14 vs 16 DAE</b>	
	diff	<i>P</i> value	diff	<i>P</i> value	diff	<i>P</i> value	diff	<i>P</i> value	diff	<i>P</i> value	diff	<i>P</i> value
<b><i>ORE1</i></b>	-1.35 $\pm$ 3.53	0.889	-4.38 $\pm$ 3.53	0.016	-4.89 $\pm$ 3.53	0.003	-3.03 $\pm$ 3.53	0.125	-3.55 $\pm$ 3.27	0.027	-0.52 $\pm$ 3.53	1.000
<b><i>ore1</i></b>	-2.72 $\pm$ 3.53	0.211	-3.09 $\pm$ 3.77	0.158	-3.82 $\pm$ 3.77	0.045	-0.37 $\pm$ 3.53	0.999	-1.11 $\pm$ 3.53	0.956	-0.73 $\pm$ 3.77	0.997
<b><i>KIR1</i></b>	-5.04 $\pm$ 3.68	0.003	-4.65 $\pm$ 3.94	0.013	-7.63 $\pm$ 3.68	0.000	0.39 $\pm$ 3.68	1.000	-2.59 $\pm$ 3.41	0.233	-2.97 $\pm$ 3.68	0.176
<b><i>kir1</i></b>	-1.67 $\pm$ 3.68	0.793	-4.88 $\pm$ 3.68	0.004	-5.37 $\pm$ 3.52	0.001	-3.22 $\pm$ 3.41	0.074	-3.70 $\pm$ 3.24	0.018	-0.48 $\pm$ 3.24	0.999

**Appendix 4.3 Analysis of variance for the percentage of green pixels in *ore1* and *kir1* mutant populations at 8, 12, 14 and 16 DAE.**

Tukey HSD (honest significant differences) test was used to perform multiple pairwise-comparisons between group means. Diff: difference between means of the groups lower  $\pm$  the upper end point of the confidence interval at 95%.

	<b>8 vs 12 DAE</b>		<b>8 vs 14 DAE</b>		<b>8 vs 16 DAE</b>		<b>12 vs 14 DAE</b>		<b>12 vs 16 DAE</b>		<b>14 vs 16 DAE</b>	
	diff	<i>P</i> value	diff	<i>P</i> value	diff	<i>P</i> value	diff	<i>P</i> value	diff	<i>P</i> value	diff	<i>P</i> value
<b><i>ORE1</i></b>	-19.46 $\pm$ 39.67	0.709	-61.45 $\pm$ 42.41	0.002	-56.38 $\pm$ 39.67	0.002	-41.99 $\pm$ 39.67	0.033	-36.92 $\pm$ 36.73	0.048	-5.06 $\pm$ 39.67	0.999
<b><i>ore1</i></b>	-38.28 $\pm$ 39.67	0.063	-26.36 $\pm$ 42.41	0.445	-71.20 $\pm$ 42.41	0.0003	-11.92 $\pm$ 39.67	0.966	-32.92 $\pm$ 39.67	0.149	-44.84 $\pm$ 42.41	0.034
<b><i>KIR1</i></b>	-15.31 $\pm$ 61.61	0.987	-74.05 $\pm$ 61.61	0.012	-86.23 $\pm$ 61.61	0.003	-58.73 $\pm$ 61.61	0.068	-70.92 $\pm$ 61.61	0.017	-12.18 $\pm$ 61.61	0.997
<b><i>kir1</i></b>	0.12 $\pm$ 61.61	1.000	-57.46 $\pm$ 57.63	0.051	-60.01 $\pm$ 57.63	0.037	-57.58 $\pm$ 57.63	0.050	-60.14 $\pm$ 57.63	0.037	-2.55 $\pm$ 53.35	1.000

**Appendix 4.4 Analysis of variance for the percentage of green pixels between *ore1* and *ORE1* and *kir1* and *KIR1* mutant populations at 8, 12, 14 and 16 DAE.**

Tukey HSD (honest significant differences) test was used to perform multiple pairwise-comparisons between group means. Diff: difference between means of the groups lower  $\pm$  the upper end point of the confidence interval at 95%.

	<i>ORE1 vs ore1</i>		<i>KIR1 vs kir1</i>	
	diff	<i>P</i> value	diff	<i>P</i> value
<b>8 DAE</b>	20.37 $\pm$ 42.41	0.729	-15.47 $\pm$ 61.61	0.986
<b>12 DAE</b>	-1.55 $\pm$ 36.73	1.000	0.03 $\pm$ 61.61	1.000
<b>14 DAE</b>	55.46 $\pm$ 42.41	0.005	1.12 $\pm$ 57.63	1.000
<b>16 DAE</b>	5.56 $\pm$ 39.67	0.999	10.75 $\pm$ 57.63	0.998

## 5. General discussion

While hybrids have proven enormously successful in allogamous crops like maize, the adoption of hybrid wheat has been partly hindered by its self-fertilising nature and the absence of an efficient system for hybrid seed production. Despite the clear definition of male and female ideotypes for efficient wheat hybrid seed production (see Chapter 1, section 1.3.2.2), efforts to improve crucial female traits, such as stigma receptivity, have been slow. To address this research gap, this thesis used several approaches to evaluate the life cycle of the unpollinated stigma and explored its role in enhancing pollination capacity for improved hybrid seed production and its genetic regulation.

Briefly, in Chapter 2, we developed a phenotyping approach for the quantification of female floral traits of field-grown plants by combining light microscopy and machine learning. The application of this approach revealed the presence of distinct stigma growth patterns among male sterile cultivars, characterised by three key phases: growth, peak and deterioration. Additionally, these observations suggested the existence of a common underlying developmental programme regulated by changes in expression of transcription factors. Chapter 3 examined the temporal and spatial distribution of hybrid seed set in six male sterile cultivars, each varying in the onset of stigma deterioration. The findings unveiled consistent grain production within a 10 to 15-day pollination window. Finally, in Chapter 4, RNA-sequencing provided new insights into the genetic regulation of the different phases of stigma development, pinpointing potential regulators such as NAC TFs *KIRI* and *OREI*. However, additional examination of loss-of-function mutants revealed that extension of stigma longevity and pollen receptivity did not translate into higher seed set, suggesting the involvement of additional processes in the control of female fertility.

### 5.1. The longevity of the unpollinated stigma does not represent a major barrier for hybrid seed production

For years, researchers have delved into the challenges of hybrid seed production, with a focus on understanding the factors contributing to low seed set rates (reviewed by De Vries, 1971). Among these factors, the duration of stigma receptivity in the male sterile line emerged as a notable concern as it potentially limits the timing of pollination and fertilisation (Heslop-Harrison, 2000; Williams, 1965). In the 1960s, the fertility of female reproductive organs were evaluated under various conditions, revealing a wide

range of receptivity periods, from 2 to 13 days, with the peak receptivity typically occurring within 2 to 5 days after anthesis (De Vries, 1971). The reported variations in stigma receptivity were often attributed to the diversity of experimental approaches used to assess female receptivity and differences in environmental conditions – with dry and warm weather shortening the receptive period (Imrie, 1966; Pickett, 1993). These early findings sparked the notion that female performance, closely linked to the duration of stigma receptivity, does diminish after a relatively short timeframe. This concept persisted in the hybrid wheat breeding community, with contemporary reviews highlighting stigma receptivity as a potential barrier to achieving efficient hybrid seed set (Selva et al., 2020; Whitford et al., 2013). However, the duration of stigma receptivity has been generally assessed by quantifying seed set on the male sterile line at different pollination times, neglecting the developmental processes the stigma itself undergoes in the absence of pollination.

In Chapters 2 and 3, a detailed examination of stigma maturation and senescence in the male sterile line revealed that, without pollination, stigmas begin to exhibit signs of aging (such as tissue shrinkage indicative of tissue deterioration) around 9 and 14 days after W9.5, depending on the cultivar. Despite slight variations across the three years tested, the patterns of stigma development remained notably consistent, with MS cultivars 24522, 24485, and 24516 typically deteriorating between 2 and 5 days earlier than 24512, BSS1, and GSS1 (Figure 2.10 and 3.10). Contrary to the prevailing notion that environmental conditions outweigh genetic effects in determining the duration of stigma receptivity (De Vries, 1971; Khan et al., 1973), the consistency of these findings hinted towards a strong genetic contribution. Subsequent gene expression analyses revealed the presence of a developmentally controlled programme that indeed regulates the life span of the unpollinated stigma, which is in line with recent analysis using *Arabidopsis* and maize (Gao et al., 2018; Šimášková et al., 2022). This was evident through the robust upregulation of senescence-associated genes during the late peak and deterioration phases across all MS cultivars tested (24485, 24522, 24512, and BSS1 in Figure 2.10, 4.10 and 4.14). Additionally, MS cultivar 24522 exhibited a premature upregulation of these genes, signifying a more advanced onset of senescence compared to the other MS cultivars which further aligned with the observed phenotypic aspect of the stigma.

While the observed onset of stigma deterioration, falling within a 9 to 14 DAW9.5 window, coincides with previously reported receptive periods, this range extends

beyond the recorded 2 to 5 day optimum pollination window (De Vries, 1971). To further investigate whether this 5-day difference in the onset of stigma deterioration effectively led to variations in cross-pollination rates among the various MS cultivars, we measured hybrid seed set at different pollination times during two consecutive field seasons. Contrary to initial expectations, hybrid seed set remained remarkably stable during the 15-day pollination window across all tested MS cultivars, demonstrating sustained receptivity to pollen throughout the entire time course (Figure 3.12 and Table 3.3). Based on this data, we refute the widely held notion within the breeding community that the short life span of the female stigma poses a hindrance to the efficacy of hybrid seed production.

An additional factor supporting this conclusion is the asynchronous nature of floret development and maturation at different sites along the wheat spike, which extends the period available for seed set. In this project, stigma longevity was assessed exclusively within florets produced by central spikelets of main tillers. However, mirroring the progression of anthesis, stigma development initiates in the central third of the spike and continues towards the top and the bottom (Figure 3.13). Though it requires further investigation, this implies that the female longevity at the spike level might surpass the documented 9 to 14 DAW9.5 life span, thereby increasing the time window in which cross-fertilisation can occur. Similarly, at the plot level (e.g., 1 m<sup>2</sup> plots), which are of greater relevance for hybrid seed production, the emergence of secondary tillers (initiated later in plant's life cycle) further contributes to extending the female receptive period. This reasoning echoes the experimental approach followed by Langer et al. (2014) to evaluate the duration of flowering in a set of 51 winter wheat lines used as pollen donors. The recorded flowering duration, calculated as the difference between the initiation and cessation of flowering at the plot level, varied from 9 to 18 days. This range notably exceeds the 2 to 6 day period documented previously for the completion of anthesis in a single spike (Waines & Hegde, 2003). Consequently, while the individual stigmas may have a relatively short life span, this is substantially extended at the spike and plot level. Section 5.3 explores other strategies to improve hybrid seed production in a more effective way.



## 5.2. Challenges in assessing stigma receptivity

In wheat, the duration of stigma receptivity has typically been measured by examining seed set on the male sterile line upon pollination, and in Chapter 3, we adhered to this established approach for studying female performance. However, it is important to recognise that this estimation does not directly measure stigma receptivity *per se* (i.e., its ability to support pollen germination). Various factors, such as environmental conditions, pollen viability, accessibility of pollen to the female flower, or ovule longevity, come into play during the seed production process (Van Durme et al., 2023; Williams, 1965). Consequently, variations in seed set could be attributed to any of these factors, and the absence of seed would not necessarily indicate the non-functionality of the stigma. To examine stigma receptivity exclusively, two main methods have been commonly employed: (1) semi *in situ* determination, also known as stigmatic germination, and (2) *in vitro* determination. Acetocarmine and aniline blue staining can be used to assess pollen germination on the stigma surface as illustrated in Figure 4.19 for aniline blue. Although these methods offer simple visualisation, their scalability to field-based experiments remain challenging due to the necessity for hand pollinations and the availability of sufficient viable pollen during analysis. On the other hand, *in vitro* determination methods have demonstrated the capability to instantly assess the receptivity of various types of stigmas and locate the receptive area, making some of them well-suited for large scale breeding experiments. These methods rely on the detection of high enzymatic activity on the stigmatic surface at reproductive maturity and have been extensively used to evaluate the reproductive capacity of the unpollinated stigma in diverse array of plant species of Bromeliaceae (e.g., *Ananas parguazensis*), Balsaminaceae (e.g., *Impatiens flaccida*), Brassicaceae (e.g., *Brassica napus*), and Iridaceae (e.g., *Crocus vernus*), among others (Dafni, 1992; Dafni & Maués, 1998; Galen & Plowright, 1987; Heslop-Harrison, 1977; Kulloli et al., 2010; Souza et al., 2016). During the initial years of the Ph.D., I attempted to implement various of these enzymatic tests on wheat with the aim of extending this approach to field experiments. However, different challenges like inconsistent reproducibility between experiments, confounding factors such as wounding after carpel dissection, or the hydrophobicity of the wheat stigma made the implementation of these tests quite intricate. Nevertheless, there is potential for optimisation, and they remain a rapid and cost-effective avenue for exclusively assessing stigma receptivity.

### **5.3. Future directions in breeding female ideotypes for hybrid seed production**

As demonstrated in Chapter 3 and detailed in section 5.1, my findings suggest that extending the duration of stigma receptivity is unlikely to resolve the challenge of low hybrid seed production in wheat. Nonetheless, it is worth considering a plausible scenario wherein two heterotic groups have such extreme flowering phenology that they surpass the 15-day pollination window, potentially requiring further improvement in the duration of stigma receptivity. While the answer to this question is still unclear, it prompts a shift in focus toward enhancing other traits that, as of yet, remain an unexploited source of variation in wheat and could contribute to improved pollen reception capabilities in the male sterile line. For example, recent studies have delved into the phenotypic variations within elite wheat germplasm, exploring factors such as the opening angle of the floret (gapping), level of stigma exertion, and stigma size (El Hanafi et al., 2020; Leahy, 2008; Sade, 2019; Tadlock, 2015). Advancements in understanding the genetic mechanisms governing these traits hold the potential to open new avenues for the improvement of the female parent.

#### **5.3.1. Ovary expansion**

In 2017, Okada et al. shed light on the mechanism behind floret opening, highlighting the role of the unfertilised ovary in reopening the wheat flower after anthesis. A process achieved by the swelling of the ovary as a result of starch accumulation in the mesocarp cells and repression of cell death (Okada et al., 2017). In Chapter 2 and 3, we showed that male sterile cultivars display distinct patterns of ovary expansion, with maximum width typically reached towards the end of the peak phase (between 9 and 14 DAW9.5; Figure 3.10 and 3.11). Importantly, these variations persist consistently across field seasons, emphasising the suitability of this trait for breeding initiatives. Further exploration of this trait across a broader spectrum of wheat varieties at a specific time point (e.g., at the end of the peak phase) and subsequent QTL mapping could enhance our understanding of the genetic control of this trait in cereals. Additionally, the methodologies outlined in Chapter 2 could be effectively employed for conducting such studies. Overall, this exploration could open the door to the development of novel genetic markers for use in hybrid breeding programmes.

### 5.3.2. Stigma exertion and stigma size

Stigma exertion and stigma size contribute greatly to foreign pollen interception and have been exploited extensively in hybrid rice seed production. Early studies showed that spikelets with exerted stigmas were the main contributor to hybrid seed set, accounting for 70–80% of the generated seeds (Li, 1995). To date, hundreds of QTLs controlling stigma exertion and size have been detected and used in QTL pyramiding to enhance hybrid seed production in rice (summarised in (Jiang et al., 2021; Qi & Wu, 2022)).

In wheat, initial efforts to develop a pool of female parents with favourable floral traits explored the phenotypic variation in elite germplasm for stigma exertion and size under field conditions, revealing a significant positive correlation between these two traits (Tadlock, 2015). Additional genome wide association studies revealed two markers associated with stigma length on chromosomes 1D and 2A in tetraploid wheat (El Hanafi et al., 2020) and four markers linked to chromosomes 2D, 5A, 7A and 7B in hexaploid wheat (Leahy, 2008). Despite these insightful studies, the genetic basis of these traits in wheat and their contribution to improving cross-pollination rates remain unknown. The transcriptomics experiment conducted in Chapter 4 yielded a substantial dataset, offering numerous avenues for further investigation, particularly in understanding how changes in gene expression can influence stigmatic growth. For example, an interesting comparison lies between MS cultivars 24512 and 24522 as they showed the most significant variations in stigma size (Figure 4.13A). Together, this information could provide valuable tools for future use in breeding female ideotypes for hybrid seed production.

### 5.3.3. Additional strategies

As briefly outlined in Chapter 1, additional strategies to increase the chances of successful cross-pollination and hybrid seed production could come from redesigning the floral and spike architecture of the male sterile line. This could be achieved by using floral mutants from wheat and related cereals. For instance, a recent study by Selva et al. (2023) identified *HvSL1* and *HvMADS16* as the causative genes for the presence of functional supernumerary carpels, leading to multiple grains per floret in barley. Another example is paired spikelets in wheat, influenced by the relative expression levels of *Ppd-1*, *FT1*, *TB1* and *HB2* genes (Boden et al., 2015; Dixon et al., 2018; Dixon et al., 2022). Additionally, mutants affecting inflorescence branching, as observed in

tetraploid 'Miracle wheat' (Poursarebani et al., 2015), where spikelets are replaced by lateral branch-like structures, have the potential to further enhance successful cross-pollination leading to a higher spike yield. Conversely, as proposed by Selva et al. (2020), encouraging the formation of less compact spikes could enhance pollen reception by creating additional space for wider floret opening. However, modifying floral organ identity in female ideotypes should only occur if reversibility in F<sub>1</sub> plants is ensured, as it may impact overall performance and final yield in the hybrids.

Establishing a robust hybrid seed production system is likely to necessitate both molecular engineering and the incorporation of desirable traits from wheat and its relatives. To achieve this, a comprehensive exploration is crucial, not only into the genetic and phenotypic variations within wheat's elite germplasm, as discussed in the previous section, but also within its ancestral lineage. For example, comparing grass species with contrasting mating systems, such as between *Aegilops* and *Triticum* genus – a group distinguished by varied mating systems ranging from obligate out-crossing to high selfing (Burgarella et al., 2023) – provides a valuable approach to unravel the distinct drivers of the selfing syndrome in grasses (Escobar et al., 2010) and understand their impact on female fertility attributes. Similarly, the processes controlling apomixis are worthy of further investigation, as apomixis represents an alternate approach for producing and maintaining hybrid genotypes that is not restricted by the challenges of low pollen production and a poor seed multiplication ratio (Barcaccia & Albertini, 2013).

#### **5.4. Advancing our understanding of female fertility in wheat**

While this thesis has primarily focused on elucidating the role of stigma longevity in enhancing hybrid seed production, the fundamental aspects of stigma development and function should not be ignored, as they lay the groundwork for further investigation. This thesis represents a pioneering effort in establishing a comprehensive and integrated understanding of the maturation and senescence processes of the stigma in the absence of pollination, addressing a poorly understood aspect of floral biology in self-pollinating crops.

In Chapter 2, the quantitative monitoring of morphological changes during carpel development unveiled a well-defined pattern of growth and senescence for stigma and

ovaries. Equivalent patterns for the post-anthesis development of the unpollinated stigma have also been reported in maize, peas, and *Arabidopsis* (Bassetti & Westgate, 1993; Carbonell-Bejerano et al., 2010; Vercher et al., 1984), suggesting a conserved developmental programme that ensues in the absence of pollination. In this context, the sustained growth of stigma and ovary expansion emerges as a crucial survival strategy that female reproductive organs have developed to secure seed set by increasing the likelihood of cross-pollination from nearby male fertile plants. Understanding these mechanisms is crucial for addressing climate change challenges that significantly impact plant reproduction, particularly in self-pollinating crops. For instance, in cereals, high temperatures during the flowering period can induce pollen dysfunction and impeded pollen shedding by blocking anther dehiscence, resulting in male sterility and subsequent yield losses (Resentini et al., 2023). In rice, a recent review investigates whether exerted stigmas can mitigate the effects of heat stress on spikelet fertility by enhancing pollen receptivity (Qi & Wu, 2022). In summary, elucidating the molecular basis of plant adaptation is essential for advancing plant breeding towards developing varieties resilient to climate change, and this work provides a framework to investigate genetic variation for female reproductive fitness under diverse environments.

Through a detailed dissection of the conserved developmental process of the wheat stigma, our research has identified distinct phases guided by morphological cues and transcriptional changes. These phases serve as a visual reference for researchers and breeders, enabling rapid identification of flowers at specific developmental stages. This resource is valuable not only in wheat but also applies to other cereals, facilitating the testing of new hypotheses. In addition, the implementation of this scale played a crucial role in interpreting the transcriptional analyses carried out in Chapter 4. While our primary focus was to identify transcription factors related to stigmatic senescence, this analysis also revealed a complex network of differentially expressed genes across the entire life cycle of the wheat stigma. Specifically, as detailed in section 4.5.2, our examination of transcriptional changes during early stages of stigma development provided insights into the biological processes and potential genetic regulation governing the growth and functional maturity of the wheat stigma. This research sets the stage for promising avenues in wheat reproductive biology.

## 5.5. Concluding statement

Overall, this thesis represents an important step forward in understanding the molecular processes regulating female fertility in wheat, as it addresses a previously overlooked aspect of the floral biology of self-pollinating crops: the development of the unpollinated stigma. Through the implementation of a high-throughput phenotyping approach, we have uncovered well-defined phases of stigma development, providing valuable insights applicable to the classification of male sterile cultivars according to the onset of stigma deterioration. Additionally, this scalable phenotyping approach, shared and successfully implemented by breeders and researchers internationally, not only facilitates the study of stigma size and ovary diameter in large-scale breeding experiments but also lays the foundation for future hypothesis generation in wheat and other cereals.

Furthermore, this work has demonstrated that the three phases of a wheat stigma's life cycle are associated with unique transcriptional landscapes and the generated data opens new avenues for exploring mechanisms that govern different aspects of stigma biology in grasses. The identification of key genes and pathways involved in these processes will allow breeders and researchers to manipulate and fine-tune plant reproduction by exploring novel genetic variation.

In summary, our work challenges the notion that stigma longevity limits hybrid wheat seed production efficiencies. Instead, our data suggests that breeding efforts should shift their focus to other female traits such as stigma and ovary growth and expansion, and this research provides a solid framework to perform such investigations. Importantly, this thesis demonstrates the benefit of developing precise phenotyping techniques and genetic resources to investigate reproductive traits underlying hybrid seed production, and the knowledge gained will advance the pursuit to improve breeding programs that aim to exploit heterosis in wheat.

## Bibliographical references

- Adamski, N. M., Borrill, P., Brinton, J., Harrington, S. A., Marchal, C., Bentley, A. R., Bovill, W. D., Cattivelli, L., Cockram, J., & Contreras-Moreira, B. (2020). A roadmap for gene functional characterisation in crops with large genomes: lessons from polyploid wheat. *Elife*, *9*, e55646.
- Akel, W., Rapp, M., Thorwarth, P., Würschum, T., & Longin, C. F. H. (2019). Hybrid durum wheat: heterosis of grain yield and quality traits and genetic architecture of anther extrusion. *Theoretical and applied genetics*, *132*(4), 921-932. <https://doi.org/10.1007/s00122-018-3248-6>
- Appels, R., Eversole, K., Stein, N., Feuillet, C., Keller, B., Rogers, J., Pozniak, C. J., Choulet, F., Distelfeld, A., & Consortium, I. W. G. S. (2018). Shifting the limits in wheat research and breeding using a fully annotated reference genome. *Science*, *361*(6403), eaar7191.
- Ashman, T.-L., & Schoen, D. J. (1994). How long should flowers live? *Nature*, *371*(6500), 788-791.
- Balazadeh, S., Siddiqui, H., Allu, A. D., Matallana-Ramirez, L. P., Caldana, C., Mehrnia, M., Zanon, M. I., Köhler, B., & Mueller-Roeber, B. (2010). A gene regulatory network controlled by the NAC transcription factor ANAC092/AtNAC2/ORE1 during salt-promoted senescence. *The Plant Journal*, *62*(2), 250-264.
- Ballester, P., Martínez-Godoy, M. A., Ezquerro, M., Navarrete-Gómez, M., Trigueros, M., Rodríguez-Concepción, M., & Ferrándiz, C. (2021). A transcriptional complex of NGATHA and bHLH transcription factors directs stigma development in Arabidopsis. *Plant Cell*, *33*(12), 3645-3657. <https://doi.org/10.1093/plcell/koab236>
- Barcaccia, G., & Albertini, E. (2013). Apomixis in plant reproduction: a novel perspective on an old dilemma. *Plant Reproduction*, *26*(3), 159-179. <https://doi.org/10.1007/s00497-013-0222-y>
- Bassetti, P., & Westgate, M. E. (1993). Emergence, Elongation, and Senescence of Maize Silks. *Crop Science*, *33*(2), crops1993.0011183X003300020011x. <https://doi.org/https://doi.org/10.2135/cropsci1993.0011183X003300020011x>
- Bates, D., Mächler, M., Bolker, B., & Walker, S. (2015). Fitting Linear Mixed-Effects Models Using lme4. *Journal of statistical software*, *67*(1), 1 - 48. <https://doi.org/10.18637/jss.v067.i01>
- Beddington, J. (2010). Food security: contributions from science to a new and greener revolution. *Philosophical Transactions of the Royal Society B: Biological Sciences*, *365*(1537), 61-71. <https://doi.org/10.1098/rstb.2009.0201>
- Bengoa Luoni, S., Astigueta, F. H., Nicosia, S., Moschen, S., Fernandez, P., & Heinz, R. (2019). Transcription Factors Associated with Leaf Senescence in Crops. *Plants (Basel)*, *8*(10). <https://doi.org/10.3390/plants8100411>

- Bennett, S. R., Alvarez, J., Bossinger, G., & Smyth, D. R. (1995). Morphogenesis in pinoid mutants of *Arabidopsis thaliana*. *The Plant Journal*, 8(4), 505-520.
- Bing-Hua, L., & Jing-Yang, D. (1986). A Dominant Gene for Male Sterility in Wheat. *Plant Breeding*, 97(3), 204-209. <https://doi.org/https://doi.org/10.1111/j.1439-0523.1986.tb01054.x>
- Boden, S. A., Cavanagh, C., Cullis, B. R., Ramm, K., Greenwood, J., Jean Finnegan, E., Trevaskis, B., & Swain, S. M. (2015). Ppd-1 is a key regulator of inflorescence architecture and paired spikelet development in wheat. *Nature plants*, 1(2), 1-6.
- Boeven, P. H. G., Würschum, T., Rudloff, J., Ebmeyer, E., & Longin, C. F. H. (2018). Hybrid seed set in wheat is a complex trait but can be improved indirectly by selection for male floral traits. *Euphytica*, 214(7), 110. <https://doi.org/10.1007/s10681-018-2188-1>
- Bohra, A., Jha, U. C., Adhimoolam, P., Bisht, D., & Singh, N. P. (2016). Cytoplasmic male sterility (CMS) in hybrid breeding in field crops. *Plant Cell Reports*, 35(5), 967-993. <https://doi.org/10.1007/s00299-016-1949-3>
- Bolser, D. M., Kerhornou, A., Walts, B., & Kersey, P. (2015). Triticeae resources in ensembl plants. *Plant and Cell Physiology*, 56(1), e3-e3.
- Borrill, P., Adamski, N., & Uauy, C. (2015). Genomics as the key to unlocking the polyploid potential of wheat. *New Phytologist*, 208(4), 1008-1022.
- Borrill, P., Harrington, S. A., Simmonds, J., & Uauy, C. (2019). Identification of transcription factors regulating senescence in wheat through gene regulatory network modelling. *Plant Physiology*, 180(3), 1740-1755.
- Borrill, P., Ramirez-Gonzalez, R., & Uauy, C. (2016). expVIP: a customizable RNA-seq data analysis and visualization platform. *Plant Physiology*, 170(4), 2172-2186.
- Bray, N. L., Pimentel, H., Melsted, P., & Pachter, L. (2016). Near-optimal probabilistic RNA-seq quantification. *Nature biotechnology*, 34(5), 525-527.
- Burgarella, C., Bremaud, M.-F., Von Hirschheydt, G., Viader, V., Ardisson, M., Santoni, S., Ranwez, V., David, J., & Glemin, S. (2023). Mating systems and recombination landscape strongly shape genetic diversity and selection in wheat relatives. *bioRxiv*, 2023.2003.2016.532584.
- Carbonell-Bejerano, P., Urbez, C., Carbonell, J., Granell, A., & Perez-Amador, M. A. (2010). A fertilization-independent developmental program triggers partial fruit development and senescence processes in pistils of *Arabidopsis*. *Plant Physiology*, 154(1), 163-172.
- Chen, F., Hu, Y., Vannozzi, A., Wu, K., Cai, H., Qin, Y., Mullis, A., Lin, Z., & Zhang, L. (2017). The WRKY Transcription Factor Family in Model Plants and Crops. *Critical Reviews in Plant Sciences*, 36(5-6), 311-335. <https://doi.org/10.1080/07352689.2018.1441103>



- Chen, L., & Liu, Y.-G. (2014). Male Sterility and Fertility Restoration in Crops. *Annual Review of Plant Biology*, 65(1), 579-606. <https://doi.org/10.1146/annurev-arplant-050213-040119>
- Chen, Q.-F., & Wehling, P. (2003). Improving male fertility restoration of common wheat for *Triticum timopheevii* cytoplasm. *Plant Breeding*, 122(5), 401-404. <https://doi.org/https://doi.org/10.1046/j.1439-0523.2003.00875.x>
- Chen, W.-H., Lin, P.-T., Hsu, W.-H., Hsu, H.-F., Li, Y.-C., Tsao, C.-W., Hsu, M.-C., Mao, W.-T., & Yang, C.-H. (2022). Regulatory network for FOREVER YOUNG FLOWER-like genes in regulating *Arabidopsis* flower senescence and abscission. *Communications Biology*, 5(1), 662.
- Ciaffi, M., Paolacci, A. R., Tanzarella, O. A., & Porceddu, E. (2011). Molecular aspects of flower development in grasses. *Sexual Plant Reproduction*, 24(4), 247-282. <https://doi.org/10.1007/s00497-011-0175-y>
- Crow, J. F. (1998). 90 years ago: the beginning of hybrid maize. *Genetics*, 148(3), 923-928.
- Cseh, A., Poczai, P., Kiss, T., Balla, K., Berki, Z., Horváth, Á., Kuti, C., & Karsai, I. (2021). Exploring the legacy of Central European historical winter wheat landraces. *Scientific Reports*, 11(1), 23915. <https://doi.org/10.1038/s41598-021-03261-4>
- D'Souza, L. (1970). Studies on the suitability of wheat as pollen donor for cross pollination, compared with rye, Triticale and Secalotricum. *Zeitschrift fur Pflanzenzuchtung*, 63, 246-269.
- Dafni, A. (1992). *Pollination ecology: a practical approach*. Oxford University Press.
- Dafni, A., & Maués, M. M. (1998). A rapid and simple procedure to determine stigma receptivity. *Sexual Plant Reproduction*, 11, 177-180.
- Darvey, N., Zhang, P., Trethowan, R., Dong, C. M., Jacob, L., Nicholas, B., Tapsell, C., & Hummel, A. (2020). Improved blue aleurone and other segregation systems. In: Google Patents.
- De Vries, A. P. (1971). Flowering biology of wheat, particularly in view of hybrid seed production — A review. *Euphytica*, 20(2), 152-170. <https://doi.org/10.1007/BF00056076>
- Dice, L. R. (1945). Measures of the amount of ecologic association between species. *Ecology*, 26(3), 297-302.
- Dixon, L. E., Greenwood, J. R., Bencivenga, S., Zhang, P., Cockram, J., Mellers, G., Ramm, K., Cavanagh, C., Swain, S. M., & Boden, S. A. (2018). TEOSINTE BRANCHED1 Regulates Inflorescence Architecture and Development in Bread Wheat (*Triticum aestivum*). *The Plant Cell*, 30(3), 563-581. <https://doi.org/10.1105/tpc.17.00961>
- Dixon, L. E., Pasquariello, M., Badgami, R., Levin, K. A., Poschet, G., Ng, P. Q., Orford, S., Chayut, N., Adamski, N. M., Brinton, J., Simmonds, J., Steuernagel, B., Searle, I. R., Uauy, C., & Boden, S. A. (2022). MicroRNA-resistant alleles

of HOMEBOX DOMAIN-2 modify inflorescence branching and increase grain protein content of wheat. *Science Advances*, 8(19), eabn5907. <https://doi.org/doi:10.1126/sciadv.abn5907>

- Du, P., Wang, Q., Yuan, D. Y., Chen, S. S., Su, Y. N., Li, L., Chen, S., & He, X. J. (2023). WRKY transcription factors and OBERON histone-binding proteins form complexes to balance plant growth and stress tolerance. *The EMBO Journal*, 42(19), e113639.
- Du, Y. Y., Wang, P. C., Chen, J., & Song, C. P. (2008). Comprehensive functional analysis of the catalase gene family in *Arabidopsis thaliana*. *Journal of Integrative Plant Biology*, 50(10), 1318-1326.
- Easterly, A. C., Stroup, W. W., Garst, N., Belamkar, V., Sarazin, J. B., Moittié, T., Ibrahim, A. M. H., Rudd, J. C., Souza, E., & Baenziger, P. S. (2019). Determining the Efficacy of a Hybridizing Agent in Wheat (*Triticum aestivum* L.). *Scientific Reports*, 9(1), 20173. <https://doi.org/10.1038/s41598-019-56664-9>
- Edlund, A. F., Swanson, R., & Preuss, D. (2004). Pollen and stigma structure and function: the role of diversity in pollination. *The Plant Cell*, 16(suppl\_1), S84-S97.
- Edwards, I. B. (2001). Hybrid Wheat. In W. J. A. Alain P. Bonjean (Ed.), *The World Wheat Book. A History of Wheat Breeding* (pp. 1019-1045). Lavoisier Publishing.
- El Hanafi, S., Bendaou, N., Kehel, Z., Sanchez-Garcia, M., & Tadesse, W. (2020). Phenotypic evaluation of elite spring bread wheat genotypes for hybrid potential traits. *Euphytica*, 216(11), 168. <https://doi.org/10.1007/s10681-020-02695-7>
- Escobar, J. S., Cenci, A., Bolognini, J., Haudry, A., Laurent, S., David, J., & Glémin, S. (2010). AN INTEGRATIVE TEST OF THE DEAD-END HYPOTHESIS OF SELFING EVOLUTION IN TRITICEAE (POACEAE). *Evolution*, 64(10), 2855-2872. <https://doi.org/10.1111/j.1558-5646.2010.01045.x>
- Evans, C. E., Arunkumar, R., & Borrill, P. (2022). Transcription factor retention through multiple polyploidization steps in wheat. *G3*, 12(8), jkac147.
- Fábián, A., Sáfrán, E., Szabó-Eitel, G., Barnabás, B., & Jäger, K. (2019). Stigma functionality and fertility are reduced by heat and drought co-stress in wheat. *Frontiers in Plant Science*, 10, 244.
- Falk, T., Mai, D., Bensch, R., Çiçek, Ö., Abdulkadir, A., Marrakchi, Y., Böhm, A., Deubner, J., Jäckel, Z., & Seiwald, K. (2019). U-Net: deep learning for cell counting, detection, and morphometry. *Nature Methods*, 16(1), 67-70.
- FAO. (2022). *World food and agriculture statistical yearbook 2022*. FAO.
- Fischer, D. S., Theis, F. J., & Yosef, N. (2018). Impulse model-based differential expression analysis of time course sequencing data. *Nucleic Acids Research*, 46(20), e119-e119. <https://doi.org/10.1093/nar/gky675>

- Forlani, S., Masiero, S., & Mizzotti, C. (2019). Fruit ripening: the role of hormones, cell wall modifications, and their relationship with pathogens. *Journal of Experimental Botany*, 70(11), 2993-3006.
- Furbank, R. T., & Tester, M. (2011). Phenomics—technologies to relieve the phenotyping bottleneck. *Trends in plant science*, 16(12), 635-644.
- Gaillochet, C., Jamge, S., van der Wal, F., Angenent, G., Immink, R., & Lohmann, J. U. (2018). A molecular network for functional versatility of HECATE transcription factors. *The Plant Journal*, 95(1), 57-70.
- Galen, C., & Plowright, R. (1987). Testing the accuracy of using peroxidase activity to indicate stigma receptivity. *Canadian Journal of Botany*, 65(1), 107-111.
- Gao, Z., Daneva, A., Salanenka, Y., Van Durme, M., Huysmans, M., Lin, Z., De Winter, F., Vanneste, S., Karimi, M., & Van de Velde, J. (2018). KIRA1 and ORESARA1 terminate flower receptivity by promoting cell death in the stigma of Arabidopsis. *Nature plants*, 4(6), 365-375.
- Garapati, P., Xue, G.-P., Munné-Bosch, S., & Balazadeh, S. (2015). Transcription factor ATAF1 in Arabidopsis promotes senescence by direct regulation of key chloroplast maintenance and senescence transcriptional cascades. *Plant Physiology*, 168(3), 1122-1139.
- Goldman, M., Goldberg, R., & Mariani, C. (1994). Female sterile tobacco plants are produced by stigma-specific cell ablation. *The EMBO Journal*, 13(13), 2976-2984.
- González, M. V., Coque, M., & Herrero, M. (1995). Papillar integrity as an indicator of stigmatic receptivity in kiwifruit (*Actinidia deliciosa*). *Journal of Experimental Botany*, 46(2), 263-269.
- Gupta, P. K., Balyan, H. S., Gahlaut, V., Saripalli, G., Pal, B., Basnet, B. R., & Joshi, A. K. (2019). Hybrid wheat: past, present and future. *Theor Appl Genet*, 132(9), 2463-2483. <https://doi.org/10.1007/s00122-019-03397-y>
- Hanson, M. R., & Bentolila, S. (2004). Interactions of mitochondrial and nuclear genes that affect male gametophyte development. *Plant Cell*, 16 Suppl(Suppl), S154-169. <https://doi.org/10.1105/tpc.015966>
- Hao, X., Wang, B., Wang, L., Zeng, J., Yang, Y., & Wang, X. (2018). Comprehensive transcriptome analysis reveals common and specific genes and pathways involved in cold acclimation and cold stress in tea plant leaves. *Scientia Horticulturae*, 240, 354-368.
- Hartley, M., & Olsson, T. S. (2020). dtolai: Reproducibility for deep learning. *Patterns*, 1(5).
- He, Y., Yan, L., Ge, C., Yao, X.-F., Han, X., Wang, R., Xiong, L., Jiang, L., Liu, C.-M., & Zhao, Y. (2019). PINOID is required for formation of the stigma and style in rice. *Plant Physiology*, 180(2), 926-936.
- Heizmann, P., Luu, D., & Dumas, C. (2000). Pollen-stigma adhesion in the Brassicaceae. *Annals of Botany*, 85(suppl\_1), 23-27.

- Heslop-Harrison, J. (1979). Pollen-stigma interaction in grasses: a brief review. *New Zealand Journal of Botany*, 17(4), 537-546.
- Heslop-Harrison, Y. (1977). The pollen-stigma interaction: pollen-tube penetration in *Crocus*. *Annals of Botany*, 41(5), 913-922.
- Heslop-Harrison, Y. (2000). Control gates and micro-ecology: the pollen-stigma interaction in perspective. *Annals of Botany*, 85(suppl\_1), 5-13.
- Heslop-Harrison, Y., & Shivanna, K. (1977). The receptive surface of the angiosperm stigma. *Annals of Botany*, 41(6), 1233-1258.
- Heslop-Harrison, J., & Heslop-Harrison, Y. (1980). The pollen-stigma interaction in the grasses. I. Fine-structure and cytochemistry of the stigmas of *Hordeum* and *Secale*. *Acta botanica neerlandica*, 29(4), 261-276.
- Hickman, R., Hill, C., Penfold, C. A., Breeze, E., Bowden, L., Moore, J. D., Zhang, P., Jackson, A., Cooke, E., & Bewicke-Copley, F. (2013). A local regulatory network around three NAC transcription factors in stress responses and senescence in *A. rabidopsis* leaves. *The Plant Journal*, 75(1), 26-39.
- Howe, K. L., Contreras-Moreira, B., De Silva, N., Maslen, G., Akanni, W., Allen, J., Alvarez-Jarreta, J., Barba, M., Bolser, D. M., & Cambell, L. (2020). Ensembl Genomes 2020—enabling non-vertebrate genomic research. *Nucleic Acids Research*, 48(D1), D689-D695.
- Huang, C.-K., Lo, P.-C., Huang, L.-F., Wu, S.-J., Yeh, C.-H., & Lu, C.-A. (2015). A single-repeat MYB transcription repressor, MYBH, participates in regulation of leaf senescence in *Arabidopsis*. *Plant molecular biology*, 88, 269-286.
- Hucl, P. (1996). Out-crossing rates for 10 Canadian spring wheat cultivars. *Canadian Journal of Plant Science*, 76(3), 423-427. <https://doi.org/10.4141/cjps96-075>
- Imrie, B. (1966). Stigma receptivity in cytoplasmic male sterile wheat. *Australian Journal of Experimental Agriculture*, 6(21), 175-178.
- Jiang, J., Xu, L., Xiao, M., Hu, C., Zhang, Y., Wang, D., & Dang, X. (2021). Genetic analysis and QTLs identification of stigma traits in japonica rice (*Oryza sativa* L.). *Euphytica*, 217(5), 82. <https://doi.org/10.1007/s10681-021-02813-z>
- Jibrán, R., A Hunter, D., & P Dijkwel, P. (2013). Hormonal regulation of leaf senescence through integration of developmental and stress signals. *Plant molecular biology*, 82, 547-561.
- Jones, M. R. W., Long, K., Phillips, A., & Uauy, C. (2022). *Collation and orthology-based identification of hormone-related genes in bread wheat*. <https://doi.org/10.5281/zenodo.7082848>
- Kempe, K., & Gils, M. (2011). Pollination control technologies for hybrid breeding. *Molecular Breeding*, 27(4), 417-437. <https://doi.org/10.1007/s11032-011-9555-0>
- Kersey, P. J., Allen, J. E., Allot, A., Barba, M., Boddu, S., Bolt, B. J., Carvalho-Silva, D., Christensen, M., Davis, P., & Grabmueller, C. (2018). Ensembl Genomes

2018: an integrated omics infrastructure for non-vertebrate species. *Nucleic Acids Research*, 46(D1), D802-D808.

- Keydel, F., Münzer, W., & Fischer, K. (1979). Interactions between cytoplasmatic male sterile wheat lines and restoration lines. *Cereal Research Communications*, 19-25.
- Khan, M. N., Heyne, E., & Arp, A. L. (1973). Pollen Distribution and the Seedset on *Triticum aestivum* L. 1. *Crop Science*, 13(2), 223-226.
- Kim, H. J., Hong, S. H., Kim, Y. W., Lee, I. H., Jun, J. H., Phee, B. K., Rupak, T., Jeong, H., Lee, Y., Hong, B. S., Nam, H. G., Woo, H. R., & Lim, P. O. (2014). Gene regulatory cascade of senescence-associated NAC transcription factors activated by ETHYLENE-INSENSITIVE2-mediated leaf senescence signalling in *Arabidopsis*. *Journal of Experimental Botany*, 65(14), 4023-4036. <https://doi.org/10.1093/jxb/eru112>
- Kim, J. H., Woo, H. R., Kim, J., Lim, P. O., Lee, I. C., Choi, S. H., Hwang, D., & Nam, H. G. (2009). Trifurcate feed-forward regulation of age-dependent cell death involving miR164 in *Arabidopsis*. *Science*, 323(5917), 1053-1057.
- Kimura, S., Kawarazaki, T., Nibori, H., Michikawa, M., Imai, A., Kaya, H., & Kuchitsu, K. (2013). The CBL-interacting protein kinase CIPK26 is a novel interactor of *Arabidopsis* NADPH oxidase AtRbohF that negatively modulates its ROS-producing activity in a heterologous expression system. *The journal of biochemistry*, 153(2), 191-195.
- Kingma, D. P., & Ba, J. (2014). Adam: A method for stochastic optimization. *arXiv preprint arXiv:1412.6980*.
- Kingsbury, N. (2011). *Hybrid: the history and science of plant breeding*. University of Chicago Press.
- Kirby, E. (2002). Botany of the wheat plant. *Bread Wheat. Improvement and Production. Food and Agriculture Organization of the United Nation. Rome*, 19-37.
- Koenig, W. D. (2002). Global patterns of environmental synchrony and the Moran effect. *Ecography*, 25(3), 283-288.
- Kong, X., Wang, F., Geng, S., Guan, J., Tao, S., Jia, M., Sun, G., Wang, Z., Wang, K., & Ye, X. (2022). The wheat AGL6-like MADS-box gene is a master regulator for floral organ identity and a target for spikelet meristem development manipulation. *Plant Biotechnology Journal*, 20(1), 75-88.
- Koyama, T. (2014). The roles of ethylene and transcription factors in the regulation of onset of leaf senescence. *Frontiers in Plant Science*, 5, 650.
- Krasileva, K. V., Vasquez-Gross, H. A., Howell, T., Bailey, P., Paraiso, F., Clissold, L., Simmonds, J., Ramirez-Gonzalez, R. H., Wang, X., & Borrill, P. (2017). Uncovering hidden variation in polyploid wheat. *Proceedings of the National Academy of Sciences*, 114(6), E913-E921.

- Krishnaswamy, S., Verma, S., Rahman, M. H., & Kav, N. N. (2011). Functional characterization of four APETALA2-family genes (RAP2. 6, RAP2. 6L, DREB19 and DREB26) in Arabidopsis. *Plant molecular biology*, 75, 107-127.
- Kulloli, S. K., Ramasubbu, R., Sreekala, A., & Pandurangan, A. (2010). Cytochemical localization of stigma-surface esterases in three species of Impatiens (Balsaminaceae) of Western Ghats. *Asian Journal of Experimental Biological Sciences*, 1, 106-111.
- Kumar, S., Stecher, G., & Tamura, K. (2016). MEGA7: molecular evolutionary genetics analysis version 7.0 for bigger datasets. *Molecular biology and evolution*, 33(7), 1870-1874.
- Kuznetsova, A., Brockhoff, P. B., & Christensen, R. H. B. (2017). lmerTest Package: Tests in Linear Mixed Effects Models. *Journal of statistical software*, 82(13), 1 - 26. <https://doi.org/10.18637/jss.v082.i13>
- Langer, S. M., Longin, C. F. H., & Würschum, T. (2014). Phenotypic evaluation of floral and flowering traits with relevance for hybrid breeding in wheat (*Triticum aestivum* L.). *Plant Breeding*, 133(4), 433-441.
- Langfelder, P., & Horvath, S. (2008). WGCNA: an R package for weighted correlation network analysis. *BMC Bioinformatics*, 9(1), 1-13.
- Langfelder, P., & Horvath, S. (2012). Fast R functions for robust correlations and hierarchical clustering. *Journal of statistical software*, 46(11).
- Leahy, F. (2008). *Inflorescence characteristics which enhance hybrid wheat production* [University of East Anglia].
- Lee, M.-O., Cho, K., Kim, S.-H., Jeong, S.-H., Kim, J.-A., Jung, Y.-H., Shim, J., Shibato, J., Rakwal, R., & Tamogami, S. (2008). Novel rice OsSIPK is a multiple stress responsive MAPK family member showing rhythmic expression at mRNA level. *Planta*, 227, 981-990.
- Lesaffre, T., & Billiard, S. (2020). The joint evolution of lifespan and self-fertilization. *Journal of Evolutionary Biology*, 33(1), 41-56.
- Levy, A. A., & Feldman, M. (2022). Evolution and origin of bread wheat. *The Plant Cell*, 34(7), 2549-2567. <https://doi.org/10.1093/plcell/koac130>
- Li, C., Lin, H., Chen, A., Lau, M., Jernstedt, J., & Dubcovsky, J. (2019). Wheat VRN1, FUL2 and FUL3 play critical and redundant roles in spikelet development and spike determinacy. *Development*, 146(14), dev175398.
- Li, M., Xu, W., Yang, W., Kong, Z., & Xue, Y. (2007). Genome-wide gene expression profiling reveals conserved and novel molecular functions of the stigma in rice. *Plant Physiology*, 144(4), 1797-1812.
- Li, Q. (1995). Environmental variation of stigma exposure rate and its effect on the differentiation and fruiting of stigma. *Seed Science and Technology*, 2, 32-33.
- Licausi, F. (2011). Regulation of the molecular response to oxygen limitations in plants. *New Phytologist*, 190(3), 550-555.

- Liu, C., Shen, L., Xiao, Y., Vyshedsky, D., Peng, C., Sun, X., Liu, Z., Cheng, L., Zhang, H., & Han, Z. (2021). Pollen PCP-B peptides unlock a stigma peptide–receptor kinase gating mechanism for pollination. *Science*, 372(6538), 171-175.
- Liu, W., Yin, H., Feng, Y., Yu, S., Fan, Z., Li, X., & Li, J. (2022). Comparative Transcriptome Analysis of Flower Senescence of *Camellia lutchuensis*. *Current Genomics*, 23(1), 66.
- Longin, C. F., Mi, X., & Würschum, T. (2015). Genomic selection in wheat: optimum allocation of test resources and comparison of breeding strategies for line and hybrid breeding. *Theoretical and applied genetics*, 128(7), 1297-1306. <https://doi.org/10.1007/s00122-015-2505-1>
- Longin, C. F. H., Gowda, M., Mühleisen, J., Ebmeyer, E., Kazman, E., Schachschneider, R., Schacht, J., Kirchhoff, M., Zhao, Y., & Reif, J. C. (2013). Hybrid wheat: quantitative genetic parameters and consequences for the design of breeding programs. *Theoretical and applied genetics*, 126, 2791-2801.
- Longin, C. F. H., Mühleisen, J., Maurer, H. P., Zhang, H., Gowda, M., & Reif, J. C. (2012). Hybrid breeding in autogamous cereals. *Theoretical and applied genetics*, 125, 1087-1096.
- Longin, C. F. H., & Reif, J. C. (2014). Redesigning the exploitation of wheat genetic resources. *Trends in plant science*, 19(10), 631-636.
- Love, M. I., Huber, W., & Anders, S. (2014). Moderated estimation of fold change and dispersion for RNA-seq data with DESeq2. *Genome Biology*, 15(12), 1-21.
- Lukac, M., Gooding, M. J., Griffiths, S., & Jones, H. E. (2012). Asynchronous flowering and within-plant flowering diversity in wheat and the implications for crop resilience to heat. *Annals of Botany*, 109(4), 843-850.
- Ma, N., Ma, C., Liu, Y., Shahid, M. O., Wang, C., & Gao, J. (2018). Petal senescence: a hormone view. *Journal of Experimental Botany*, 69(4), 719-732.
- Mähs, A., Steinhorst, L., Han, J.-P., Shen, L.-K., Wang, Y., & Kudla, J. (2013). The calcineurin B-like Ca<sup>2+</sup> sensors CBL1 and CBL9 function in pollen germination and pollen tube growth in *Arabidopsis*. *Molecular Plant*, 6(4), 1149-1162.
- Martín-Trillo, M., & Cubas, P. (2010). TCP genes: a family snapshot ten years later. *Trends in plant science*, 15(1), 31-39.
- Martín, A., Atienza, S., Ramírez, M., Barro, F., & Martín, A. (2008). Male fertility restoration of wheat in *Hordeum chilense* cytoplasm is associated with 6HchS chromosome addition. *Australian Journal of Agricultural Research*, 59(3), 206-213.
- McInnis, S. M., Desikan, R., Hancock, J. T., & Hiscock, S. J. (2006). Production of reactive oxygen species and reactive nitrogen species by angiosperm stigmas and pollen: potential signalling crosstalk? *New Phytologist*, 172(2), 221-228.
- Miller, P., Lanier, W., & Brandt, S. (2001). Using growing degree days to predict plant stages. *Ag/Extension Communications Coordinator, Communications Services, Montana State University-Bozeman, Bozeman, MO, 59717(406)*, 994-2721.

- Mitchell, J., & Petolino, J. (1988). Heat stress effects on isolated reproductive organs of maize. *Journal of plant physiology*, 133(5), 625-628.
- Molnár-Láng, M., Barnabas, B., & Rajki, E. (1980). Changes in the shape, volume, weight and tissue structure of the pistil in the flowers of male sterile wheats during flowering. *Cereal Research Communications*, 371-379.
- Mueller-Roeber, B., & Balazadeh, S. (2014). Auxin and its role in plant senescence. *Journal of Plant Growth Regulation*, 33, 21-33.
- Ng, P. C., & Henikoff, S. (2003). SIFT: Predicting amino acid changes that affect protein function. *Nucleic Acids Res*, 31(13), 3812-3814.  
<https://doi.org/10.1093/nar/gkg509>
- Okada, T., Jayasinghe, J. E. A. R. M., Nansamba, M., Baes, M., Warner, P., Kouidri, A., Correia, D., Nguyen, V., Whitford, R., & Baumann, U. (2017). Unfertilized ovary pushes wheat flower open for cross-pollination. *Journal of Experimental Botany*, 69(3), 399-412. <https://doi.org/10.1093/jxb/erx410>
- Onyemaobi, I., Liu, H., Siddique, K. H., & Yan, G. (2017). Both male and female malfunction contributes to yield reduction under water stress during meiosis in bread wheat. *Frontiers in Plant Science*, 7, 2071.
- Park, S. J., Park, S., Kim, Y., Hyeon, D. Y., Park, H., Jeong, J., Jeong, U., Yoon, Y. S., You, D., & Kwak, J. (2022). Ethylene responsive factor34 mediates stress-induced leaf senescence by regulating salt stress-responsive genes. *Plant, Cell & Environment*, 45(6), 1719-1733.
- Paszke, A., Gross, S., Massa, F., Lerer, A., Bradbury, J., Chanan, G., Killeen, T., Lin, Z., Gimelshein, N., & Antiga, L. (2019). Pytorch: An imperative style, high-performance deep learning library. *Advances in neural information processing systems*, 32.
- Paux, E., Lafarge, S., Balfourier, F., Derory, J., Charmet, G., Alaux, M., Perchet, G., Bondoux, M., Baret, F., Barillot, R., Ravel, C., Sourdille, P., Le Gouis, J., & Consortium, o. b. o. t. B. (2022). Breeding for Economically and Environmentally Sustainable Wheat Varieties: An Integrated Approach from Genomics to Selection. *Biology*, 11(1), 149. <https://www.mdpi.com/2079-7737/11/1/149>
- Pelaz, S., Gustafson-Brown, C., Kohalmi, S. E., Crosby, W. L., & Yanofsky, M. F. (2001). APETALA1 and SEPALLATA3 interact to promote flower development. *The Plant Journal*, 26(4), 385-394.
- Pequeno, D. N. L., Hernández-Ochoa, I. M., Reynolds, M., Sonder, K., Moleromilan, A., Robertson, R. D., Lopes, M. S., Xiong, W., Kropff, M., & Asseng, S. (2021). Climate impact and adaptation to heat and drought stress of regional and global wheat production. *Environmental Research Letters*, 16(5), 054070.  
<https://doi.org/10.1088/1748-9326/abd970>
- Percival, J. (1921). *The wheat plant*. Bloomsbury Academic.



- Philipp, N., Weichert, H., Bohra, U., Weschke, W., Schulthess, A. W., & Weber, H. (2018). Grain number and grain yield distribution along the spike remain stable despite breeding for high yield in winter wheat. *PLoS One*, *13*(10), e0205452.
- Pickett, A. A. (1993). *Hybrid wheat: results and problems* (Vol. 15 ). Paul Parey Scientific Publishers.
- Pieruschka, R., & Schurr, U. (2019). Plant phenotyping: past, present, and future. *Plant Phenomics*, *2019*, 7507131.  
<https://doi.org/https://doi.org/10.34133/2019/7507131>
- Pound, M. P., Atkinson, J. A., Townsend, A. J., Wilson, M. H., Griffiths, M., Jackson, A. S., Bulat, A., Tzimiropoulos, G., Wells, D. M., & Murchie, E. H. (2017). Deep machine learning provides state-of-the-art performance in image-based plant phenotyping. *Gigascience*, *6*(10), gix083.
- Poursarebani, N., Seidensticker, T., Koppolu, R., Trautewig, C., Gawroński, P., Bini, F., Govind, G., Rutten, T., Sakuma, S., Tagiri, A., Wolde, G. M., Youssef, H. M., Battal, A., Ciannamea, S., Fusca, T., Nussbaumer, T., Pozzi, C., Börner, A., Lundqvist, U., . . . Schnurbusch, T. (2015). The Genetic Basis of Composite Spike Form in Barley and ‘Miracle-Wheat’. *Genetics*, *201*(1), 155-165.  
<https://doi.org/10.1534/genetics.115.176628>
- Poutanen, K. S., Kårlund, A. O., Gómez-Gallego, C., Johansson, D. P., Scheers, N. M., Marklinder, I. M., Eriksen, A. K., Silventoinen, P. C., Nordlund, E., Sozer, N., Hanhineva, K. J., Kolehmainen, M., & Landberg, R. (2022). Grains – a major source of sustainable protein for health. *Nutrition Reviews*, *80*(6), 1648-1663.  
<https://doi.org/10.1093/nutrit/nuab084>
- Primack, R. B. (1985). Longevity of individual flowers. *Annual review of ecology and systematics*, *16*(1), 15-37.
- Qi, B., & Wu, C. (2022). Potential roles of stigma exertion on spikelet fertility in rice (*Oryza sativa* L.) under heat stress. *Frontiers in Plant Science*, *13*, 983070.  
<https://doi.org/10.3389/fpls.2022.983070>
- Ramírez-González, R. H., Borrill, P., Lang, D., Harrington, S. A., Brinton, J., Venturini, L., Davey, M., Jacobs, J., van Ex, F., Pasha, A., Khedikar, Y., Robinson, S. J., Cory, A. T., Florio, T., Concia, L., Juery, C., Schoonbeek, H., Steuernagel, B., Xiang, D., . . . Tan, Y. (2018). The transcriptional landscape of polyploid wheat. *Science*, *361*(6403), eaar6089. <https://doi.org/doi:10.1126/science.aar6089>
- Ramirez-Gonzalez, R. H., Uauy, C., & Caccamo, M. (2015). PolyMarker: A fast polyploid primer design pipeline. *Bioinformatics*, *31*(12), 2038-2039.  
<https://doi.org/10.1093/bioinformatics/btv069>
- Ray, D. K., Mueller, N. D., West, P. C., & Foley, J. A. (2013). Yield trends are insufficient to double global crop production by 2050. *PLoS One*, *8*(6), e66428.
- Resentini, F., Orozco-Arroyo, G., Cucinotta, M., & Mendes, M. A. (2023). The impact of heat stress in plant reproduction [Review]. *Frontiers in Plant Science*, *14*.  
<https://doi.org/10.3389/fpls.2023.1271644>

- Robinson, R., Sprott, D., Couroux, P., Routly, E., Labbé, N., Xing, T., & Robert, L. S. (2023). The triticale mature pollen and stigma proteomes—assembling the proteins for a productive encounter. *Journal of Proteomics*, 278, 104867.
- Sade, F. B. (2019). *Genotype-by-Floral Characteristics Interaction for Hybrid Wheat (Triticum aestivum L.) Production in Texas* [Texas A&M University].
- Schindelin, J., Arganda-Carreras, I., Frise, E., Kaynig, V., Longair, M., Pietzsch, T., Preibisch, S., Rueden, C., Saalfeld, S., Schmid, B., Tinevez, J.-Y., White, D. J., Hartenstein, V., Eliceiri, K., Tomancak, P., & Cardona, A. (2012). Fiji: an open-source platform for biological-image analysis. *Nature Methods*, 9(7), 676-682. <https://doi.org/10.1038/nmeth.2019>
- Schneider, J., Berkner, M. O., Philipp, N., Schulthess, A. W., & Reif, J. C. (2021). Assessing the Suitability of Elite Lines for Hybrid Seed Production and as Testers in Wide Crosses With Wheat Genetic Resources. *Frontiers in Plant Science*, 12, 689825. <https://doi.org/10.3389/fpls.2021.689825>
- Selva, C., Riboni, M., Baumann, U., Würschum, T., Whitford, R., & Tucker, M. R. (2020). Hybrid breeding in wheat: how shaping floral biology can offer new perspectives. *Functional Plant Biology*, 47(8), 675-694.
- Selva, C., Yang, X., Shirley, N. J., Whitford, R., Baumann, U., & Tucker, M. R. (2023). HvSL1 and HvMADS16 promote stamen identity to restrict multiple ovary formation in barley. *Journal of Experimental Botany*, 74(17), 5039-5056. <https://doi.org/10.1093/jxb/erad218>
- Shahri, W., & Tahir, I. (2014). Flower senescence: some molecular aspects. *Planta*, 239, 277-297.
- Shaikhali, J., Heiber, I., Seidel, T., Ströher, E., Hiltcher, H., Birkmann, S., Dietz, K.-J., & Baier, M. (2008). The redox-sensitive transcription factor Rap2. 4a controls nuclear expression of 2-Cys peroxiredoxin A and other chloroplast antioxidant enzymes. *BMC plant biology*, 8(1), 1-14.
- Shibuya, K., Shimizu, K., Niki, T., & Ichimura, K. (2014). Identification of a NAC transcription factor, EPHEMERAL 1, that controls petal senescence in Japanese morning glory. *The Plant Journal*, 79(6), 1044-1051.
- Šimášková, M., Daneva, A., Doll, N., Schilling, N., Cubría-Radio, M., Zhou, L., De Winter, F., Aesaert, S., De Rycke, R., & Pauwels, L. (2022). KIL1 terminates fertility in maize by controlling silk senescence. *The Plant Cell*, 34(8), 2852-2870. <https://doi.org/https://doi.org/10.1093/plcell/koac151>
- Singh, S. P., Srivastava, R., & Kumar, J. (2014). Male sterility systems in wheat and opportunities for hybrid wheat development. *Acta Physiologiae Plantarum*, 37(1), 1713. <https://doi.org/10.1007/s11738-014-1713-7>
- Smyth, D. R., Bowman, J. L., & Meyerowitz, E. M. (1990). Early flower development in Arabidopsis. *The Plant Cell*, 2(8), 755-767. <https://doi.org/https://doi.org/10.1105/tpc.2.8.755>

- Souza, E. H., Carmello-Guerreiro, S. M., Souza, F. V. D., Rossi, M. L., & Martinelli, A. P. (2016). Stigma structure and receptivity in Bromeliaceae. *Scientia Horticulturae*, *203*, 118-125.  
<https://doi.org/https://doi.org/10.1016/j.scienta.2016.03.022>
- Su, P., Yan, J., Li, W., Wang, L., Zhao, J., Ma, X., Li, A., Wang, H., & Kong, L. (2020). A member of wheat class III peroxidase gene family, TaPRX-2A, enhanced the tolerance of salt stress. *BMC plant biology*, *20*, 1-15.
- Sultana, N., Islam, S., Juhasz, A., & Ma, W. (2021). Wheat leaf senescence and its regulatory gene network. *The Crop Journal*, *9*(4), 703-717.  
<https://doi.org/https://doi.org/10.1016/j.cj.2021.01.004>
- Tadlock, J. K. (2015). *Floral characteristics and hybrid performance of potential candidates of a hybrid wheat (Triticum aestivum L.) program in Texas* [Texas A&M University].
- Tan, Q., Chen, S., Gan, Z., Lu, Q., Yan, Z., Chen, G., Lin, S., Yang, W., Zhao, J., & Ba, Y. (2023). Grain shape is a factor affecting the stigma exertion rate in rice. *Frontiers in Plant Science*, *14*, 1087285.
- Tang, Y., Li, M., Chen, Y., Wu, P., Wu, G., & Jiang, H. (2011). Knockdown of OsPAO and OsRCCR1 cause different plant death phenotypes in rice. *Journal of plant physiology*, *168*(16), 1952-1959.
- Tester, M., & Langridge, P. (2010). Breeding technologies to increase crop production in a changing world. *Science*, *327*(5967), 818-822.  
<https://doi.org/10.1126/science.1183700>
- Uauy, C., Paraiso, F., Colasuonno, P., Tran, R. K., Tsai, H., Berardi, S., Comai, L., & Dubcovsky, J. (2009). A modified TILLING approach to detect induced mutations in tetraploid and hexaploid wheat. *BMC plant biology*, *9*, 1-14.
- Underwood, C. J., & Mercier, R. (2022). Engineering Apomixis: Clonal Seeds Approaching the Fields. *Annual Review of Plant Biology*, *73*(1), 201-225.  
<https://doi.org/10.1146/annurev-arplant-102720-013958>
- Van der Walt, S., Schönberger, J. L., Nunez-Iglesias, J., Boulogne, F., Warner, J. D., Yager, N., Gouillart, E., & Yu, T. (2014). scikit-image: image processing in Python. *PeerJ*, *2*, e453.
- van Doorn, W. G., & Woltering, E. J. (2008). Physiology and molecular biology of petal senescence. *Journal of Experimental Botany*, *59*(3), 453-480.
- Van Durme, M., Olvera-Carrillo, Y., Pfeiffer, M. L., Doll, N. M., De Winter, F., Lin, Z., & Nowack, M. K. (2023). Fertility loss in senescing Arabidopsis ovules is controlled by the maternal sporophyte via a NAC transcription factor triad. *Proceedings of the National Academy of Sciences*, *120*(25), e2219868120.
- Vercher, Y., Molowny, A., Lopez, C., García-Martínez, J.-L., & Carbonell, J. (1984). Structural changes in the ovary of *Pisum sativum* L. induced by pollination and gibberellic acid. *Plant science letters*, *36*(2), 87-91.

- Vogler, A., Bertossa, M., Aulinger-Leipner, I., & Stamp, P. (2010). Weather Effects on Cross-Pollination in Maize. *Crop Science*, *50*(2), 713-717.  
<https://doi.org/https://doi.org/10.2135/cropsci2009.04.0213>
- Waddington, S., Cartwright, P., & Wall, P. (1983). A quantitative scale of spike initial and pistil development in barley and wheat. *Annals of Botany*, *51*(1), 119-130.
- Waines, J., & Hegde, S. (2003). Intraspecific gene flow in bread wheat as affected by reproductive biology and pollination ecology of wheat flowers. *Crop Science*, *43*(2), 451-463.
- Walker, E. R. (1906). *On the structure of the pistils of some grasses* (Vol. 6). University of Nebraska.
- Walkowiak, S., Gao, L., Monat, C., Haberer, G., Kassa, M. T., Brinton, J., Ramirez-Gonzalez, R. H., Kolodziej, M. C., Delorean, E., & Thambugala, D. (2020). Multiple wheat genomes reveal global variation in modern breeding. *Nature*, *588*(7837), 277-283.
- Whitford, R., Fleury, D., Reif, J. C., Garcia, M., Okada, T., Korzun, V., & Langridge, P. (2013). Hybrid breeding in wheat: technologies to improve hybrid wheat seed production. *Journal of Experimental Botany*, *64*(18), 5411-5428.  
<https://doi.org/10.1093/jxb/ert333>
- Williams, R. (1965). The effect of summer nitrogen applications on the quality of apple blossom. *Journal of Horticultural Science*, *40*(1), 31-41.
- Wils, C. R., & Kaufmann, K. (2017). Gene-regulatory networks controlling inflorescence and flower development in *Arabidopsis thaliana*. *Biochimica et Biophysica Acta (BBA)-Gene Regulatory Mechanisms*, *1860*(1), 95-105.
- Wingen, L. U., Orford, S., Goram, R., Leverington-Waite, M., Bilham, L., Patsiou, T. S., Ambrose, M., Dicks, J., & Griffiths, S. (2014). Establishing the AE Watkins landrace cultivar collection as a resource for systematic gene discovery in bread wheat. *Theoretical and applied genetics*, *127*, 1831-1842.
- Woo, H. R., Kim, H. J., Nam, H. G., & Lim, P. O. (2013). Plant leaf senescence and death—regulation by multiple layers of control and implications for aging in general. *Journal of cell science*, *126*(21), 4823-4833.
- Worthen, J. M., Yamburenko, M. V., Lim, J., Nimchuk, Z. L., Kieber, J. J., & Schaller, G. E. (2019). Type-B response regulators of rice play key roles in growth, development and cytokinin signaling. *Development*, *146*(13), dev174870.
- Würschum, T., Liu, G., Boeven, P. H. G., Longin, C. F. H., Mirdita, V., Kazman, E., Zhao, Y., & Reif, J. C. (2018). Exploiting the Rht portfolio for hybrid wheat breeding. *Theoretical and applied genetics*, *131*(7), 1433-1442.  
<https://doi.org/10.1007/s00122-018-3088-4>
- Xie, Z., Nolan, T. M., Jiang, H., & Yin, Y. (2019). AP2/ERF transcription factor regulatory networks in hormone and abiotic stress responses in *Arabidopsis*. *Frontiers in Plant Science*, *10*, 228.

- Yamaguchi, T., Lee, D. Y., Miyao, A., Hirochika, H., An, G., & Hirano, H.-Y. (2006). Functional diversification of the two C-class MADS box genes OSMADS3 and OSMADS58 in *Oryza sativa*. *The Plant Cell*, *18*(1), 15-28.  
<https://doi.org/https://doi.org/10.1105/tpc.105.037200>
- Yoo, S. J., Kim, S.-H., Kim, M.-J., Ryu, C.-M., Kim, Y. C., Cho, B. H., & Yang, K.-Y. (2014). Involvement of the OsMKK4-OsMPK1 cascade and its downstream transcription factor OsWRKY53 in the wounding response in rice. *The plant pathology journal*, *30*(2), 168.
- Yoshida, S. (2003). Molecular regulation of leaf senescence. *Current Opinion in Plant Biology*, *6*(1), 79-84.  
<https://doi.org/https://doi.org/10.1016/S1369526602000092>
- Young, M. D., Wakefield, M. J., Smyth, G. K., & Oshlack, A. (2010). Gene ontology analysis for RNA-seq: accounting for selection bias. *Genome Biology*, *11*(2), R14. <https://doi.org/10.1186/gb-2010-11-2-r14>
- Zadoks, J. C., Chang, T. T., & Konzak, C. F. (1974). A decimal code for the growth stages of cereals. *Weed research*, *14*(6), 415-421.
- Zeven, A. (1968). Cross pollination and sources of restorer genes in wheat and a semi-hybrid variety. *Euphytica*, 75-&.
- Zhang, S., Ma, M., Zhang, H., Zhang, S., Qian, M., Zhang, Z., Luo, W., Fan, J., Liu, Z., & Wang, L. (2019). Genome-wide analysis of polygalacturonase gene family from pear genome and identification of the member involved in pear softening. *BMC plant biology*, *19*(1), 1-12.
- Zhao, Z.-X., Yin, X.-X., Li, S., Peng, Y.-T., Yan, X.-L., Chen, C., Hassan, B., Zhou, S.-X., Pu, M., Zhao, J.-H., Hu, X.-H., Li, G.-B., Wang, H., Zhang, J.-W., Huang, Y.-Y., Fan, J., Li, Y., & Wang, W.-M. (2022). miR167d-ARFs Module Regulates Flower Opening and Stigma Size in Rice. *Rice*, *15*(1), 40.  
<https://doi.org/10.1186/s12284-022-00587-z>
- Zhu, T., Wang, L., Rimbart, H., Rodriguez, J. C., Deal, K. R., De Oliveira, R., Choulet, F., Keeble-Gagnère, G., Tibbits, J., & Rogers, J. (2021). Optical maps refine the bread wheat *Triticum aestivum* cv. Chinese Spring genome assembly. *The Plant Journal*, *107*(1), 303-314.

## **Appendix A**

**Millan-Blauquez, M., Hartley, M., Bird, N., Manes, Y., Uauy, C., & Boden, S. A. (2022).** A scalable phenotyping approach for female floral organ development and senescence in the absence of pollination in wheat. *Development*, 149(18), dev200889.

# A scalable phenotyping approach for female floral organ development and senescence in the absence of pollination in wheat

Marina Millan-Blanquez<sup>1</sup>, Matthew Hartley<sup>1,2</sup>, Nicholas Bird<sup>3</sup>, Yann Manes<sup>4</sup>, Cristobal Uauy<sup>1,\*</sup> and Scott A. Boden<sup>1,5,\*</sup>

## ABSTRACT

In the absence of pollination, female reproductive organs senesce, leading to an irrevocable loss in the reproductive potential of the flower, which directly affects seed set. In self-pollinating crops like wheat (*Triticum aestivum*), the post-anthesis viability of unpollinated carpels has been overlooked, despite its importance for hybrid seed production systems. To advance our knowledge of carpel development in the absence of pollination, we created a high-throughput phenotyping approach to quantify stigma and ovary morphology. We demonstrate the suitability of the approach, which uses light-microscopy imaging and machine learning, for the analysis of floral organ traits in field-grown plants using fresh and fixed samples. We show that the unpollinated carpel undergoes a well-defined initial growth phase, followed by a peak phase in which stigma area reaches its maximum and the radial expansion of the ovary slows, and a final deterioration phase. These developmental dynamics were consistent across years and could be used to classify male-sterile cultivars. This phenotyping approach provides a new tool for examining carpel development, which we hope will advance research into female fertility of wheat.

**KEY WORDS:** Carpel development, Machine learning, Stigma, Ovary, Wheat, Hybrid breeding

## INTRODUCTION


The fertilisation of the pistil by a pollen grain is a vital event in the life cycle of a flowering plant as it contributes to the reproductive fitness of a species. In grasses, the pistil (or carpel) typically consists of an ovary bearing two styles densely covered by a feathery and dry-type stigma (Walker, 1906; Heslop-Harrison and Shivanna,

1977). The stigmatic tissue plays a key role in successful fertilisation as it facilitates the interception and hydration of the pollen grain and mediates pollen tube growth into the stylodium branches towards the ovary containing the ovule (Heslop-Harrison, 1979; Edlund et al., 2004). After successful fertilisation, the ovary undergoes growth and differentiation to develop into a grain. Under favourable growing conditions, the duration of carpel receptivity (or functionality) does not present a serious limitation to seed formation in self-pollinating species, such as wheat (*Triticum aestivum*) or rice (*Oryza sativa*). However, environmental stresses such as heat and drought (Fábíán et al., 2019; Onyemaobi et al., 2016; Mitchell and Petolino, 1988) or the absence of viable pollen [e.g. male sterile cultivars used in hybrid breeding (Kempe and Gils, 2011)] can affect normal seed set.

Female floral organs have developed a series of survival mechanisms to secure seed set in the absence of self-pollination by increasing the likelihood of receiving pollen from neighbouring male fertile plants. Indeed, this process (directly or indirectly) has been harnessed by breeders to produce hybrid seeds in crops like maize (*Zea mays*), rice, barley (*Hordeum vulgare*) and wheat. In maize, one of the survival strategies described to increase pollen capture is silk (i.e. stigma) emergence and elongation from the husk (Bassetti and Westgate, 1993), whereas in wheat, the radial expansion of the unfertilised ovary pushes the floret open, facilitating access to airborne pollen, a phenomenon known as the ‘second opening’ (Molnár-Láng et al., 1980; Okada et al., 2018). However, if pollination still does not occur after a specific duration of time, which varies between species (Primack, 1985; Ashman and Schoen, 1994), a series of developmental processes leads to the senescence of the floral organs and the irreversible loss of reproductive potential (Carbonell-Bejerano et al., 2010). For example, in several plants, the loss of papilla integrity has been regarded as one of the primary symptoms indicating the end of the floral receptive period and stigma senescence, which is often manifested by the shrunken appearance of the stigma (Gao et al., 2018; Okada et al., 2018; González et al., 1995). These senescence processes are coordinated by transcription factors, including *KIRAI* (*KIR1*) and *ORESAR1* (*ORE1*) in *Arabidopsis* (Gao et al., 2018). Similarly, the unfertilised ovary undergoes a series of morphological changes that converge in the lignification of the epidermal cells and eventual collapse of the ovary walls (Carbonell-Bejerano et al., 2010; Okada et al., 2018). In many of these studies, the phenotypic characterisation of these processes is time consuming and labour intensive, and is, therefore, usually performed only under controlled growing conditions and on a small number of plants. These phenotyping approaches, although extremely informative, are often not conducive for translation into breeding targets, for which the screening of large germplasm sets is required.

<sup>1</sup>John Innes Centre, Norwich Research Park, Norwich NR4 7UH, UK. <sup>2</sup>European Molecular Biology Laboratory, European Bioinformatics Institute (EMBL-EBI), Wellcome Genome Campus, Hinxton, Cambridge CB10 1SD, UK. <sup>3</sup>KWS UK Ltd, Thriplow, Hertfordshire SG8 7RE, UK. <sup>4</sup>Syngenta France S.A.S., Le Jardin des Entreprises, 28 000 Chartres, France. <sup>5</sup>School of Agriculture, Food and Wine, Waite Research Institute, University of Adelaide, Glen Osmond 5064, South Australia, Australia.

\*Authors for correspondence (scott.boden@adelaide.edu.au; cristobal.uauy@jic.ac.uk)

 M.M.B., 0000-0003-1238-3179; M.H., 0000-0001-6178-2884; N.B., 0000-0002-2476-9020; Y.M., 0000-0001-8453-7320; C.U., 0000-0002-9814-1770; S.A.B., 0000-0001-5297-4067

This is an Open Access article distributed under the terms of the Creative Commons Attribution License (<https://creativecommons.org/licenses/by/4.0>), which permits unrestricted use, distribution and reproduction in any medium provided that the original work is properly attributed.

Handling Editor: Ykä Helariutta  
Received 26 April 2022; Accepted 15 August 2022

In recent years, high-throughput phenotyping technologies have provided new opportunities to phenotype a diverse range of plant species at various scales, ranging from cellular to tissue and organ levels (Pieruschka and Schurr, 2019; Furbank and Tester, 2011). For instance, machine-learning-based algorithms, like neural networks, have become an essential tool for reliably extracting morphological information and providing visual quantitative parameters of microscopy images. These approaches can be used in large-scale experiments, like those of crop breeding programmes, and provide a way to quantify the morphological changes of the developing carpel in the absence of pollination.

To advance our knowledge of carpel development in the absence of pollination, we developed a phenotyping approach for the quantification of stigma area and ovary diameter of field-grown plants by combining light microscopy and machine learning. We focused on bread wheat carpels due to the current need to improve outcrossing rates in hybrid breeding programmes (Selva et al., 2020) and the lack of knowledge on the dynamics of stigma and ovary development among male sterile (MS) wheat cultivars under production conditions in the field. We applied our phenotyping approach to three MS cultivars during two consecutive field seasons to gain insights into genetic and environmental variation for these two floral traits, and show that it is scalable to produce practical advances in breeding programmes.

## RESULTS

### Defining quantifiable parameters of late carpel development and senescence

To investigate the development of wheat carpels in the absence of pollination and determine the parameters that correlate with key phases of their life cycle, we used nuclear and cytoplasmic male sterile (NMS and CMS, respectively) plants. We imaged the unpollinated carpels of field-grown plants starting from Waddington stage 9.5 (W9.5, normally shortly after ear emergence; Fig. 1A), which corresponds with the most advanced

developmental stage for an unpollinated carpel. W9.5 is shortly before the stage at which male fertile plants reach anthesis (W10) and release viable pollen on the receptive stigma surface. At W9.5, stigma branches are well elongated and spread outwards to generate the plumose architecture, whereas the unfertilised ovary shows a round shape (Fig. 1A). In subsequent timepoints after W9.5, the unfertilised ovary gradually expands horizontally leading to the second opening of the floret (as previously described by Okada et al., 2018 and Molnár-Láng et al., 1980). During this period of ovary growth, stigma branches continue to grow and quickly curve away from each other, increasing the stigma surface area and contributing to the extrusion of the unpollinated stigma outside the floret for the capture of airborne pollen. Towards the end of the time course, papilla cells of the stigma hairs start to lose turgor and become atrophied as the stigma degenerates (Fig. 1A, red arrowheads). Finally, the onset of stigma degeneration is followed by a slight and gradual decline in ovary radial size, causing the floret to close again (Molnár-Láng et al., 1980).

To quantify the observed morphological changes in these parameters, we imaged unpollinated carpels and manually delineated the area covered by the stigma hairs and the diameter of the ovary using Fiji (Fig. 1B). We distinguished a developmental pattern for stigma area characterised by an initial bell curve followed by a gradual reduction in area indicative of tissue deterioration. The ovary diameter gradually increased and reached a plateau with little changes in the diameter thereafter (Fig. 1C). More importantly, these patterns appear to be quite consistent across different cultivars and replicates (Fig. 5). Taken together, these findings suggest that stigma area and ovary diameter are promising parameters to quantitatively track the life cycle of the unpollinated carpel.

### Overview of the approach

The rapid and accurate phenotyping of large numbers of field-grown plants represents a challenge for plant researchers. Here, to

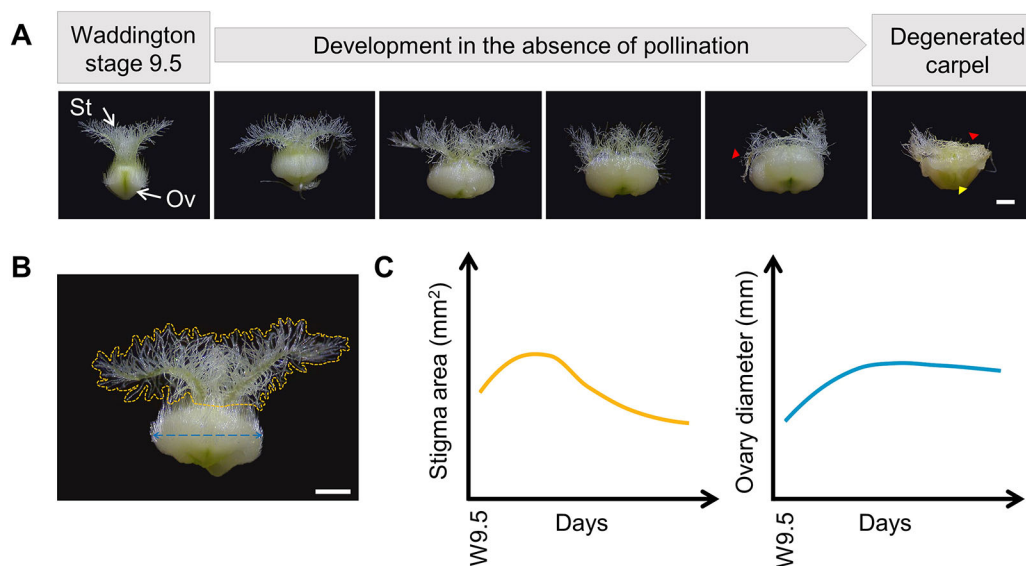


**Fig. 1. Representative stages of late carpel development in the absence of pollination.** (A) Morphological changes observed in the stigma (St) and ovary (Ov) from Waddington stage 9.5 (approximate timing of ear emergence) until complete degeneration of the carpel (from left to right). Arrowheads indicate regions of the stigma (red) and ovary (yellow) where symptoms of cell degeneration are visible. (B) Diagram illustrating the morphological traits of interest. The yellow line delimits the area covered by the stigmatic hairs, the blue line depicts the diameter of the ovary. (C) Representative growth trends observed for the stigma hair area (yellow) and ovary diameter (blue) in the absence of pollination for field-grown plants. For the regression curves, we used a single exemplar MS cultivar ( $n=10-30$  carpels sampled from six plants per timepoint, from a total of 8 timepoints). Scale bars: 1 mm.



accelerate research into female floral traits, we propose a phenotyping approach that can be implemented in the screening of large populations, such as those of pre-breeding programmes (Fig. 2). This approach provides a visualisation and quantification toolbox for morphometric information of stigma area and ovary diameter. A summary of each step is provided below, and detailed descriptions can be found in the Materials and Methods.

**Experimental design, sample collection and image acquisition**

As our main aim was to study carpels in the absence of pollination, the first step is to prevent cross-pollination of MS plants in the field. To achieve this, different strategies can be used. For example, in this

study, we grew sterile rye surrounding the experimental plots to create an effective pollen barrier from surrounding fertile plants (Fig. 2A; Fig. S1). When anthers from the outer florets of the central spikelets started to turn yellow and stigmatic branches started to spread outwards (W9.5), we tagged spikes to indicate the beginning of the time course. Depending on the location and scale of the experiment, logistical issues such as transport and preservation methods were also considered at the time of sampling. For sample collection, we carefully dissected wheat carpels from central spikelets in the field, which can be performed by eye as they are relatively large (Fig. 2B). Alternatively, we cut individual tillers between the uppermost and penultimate internode and transported

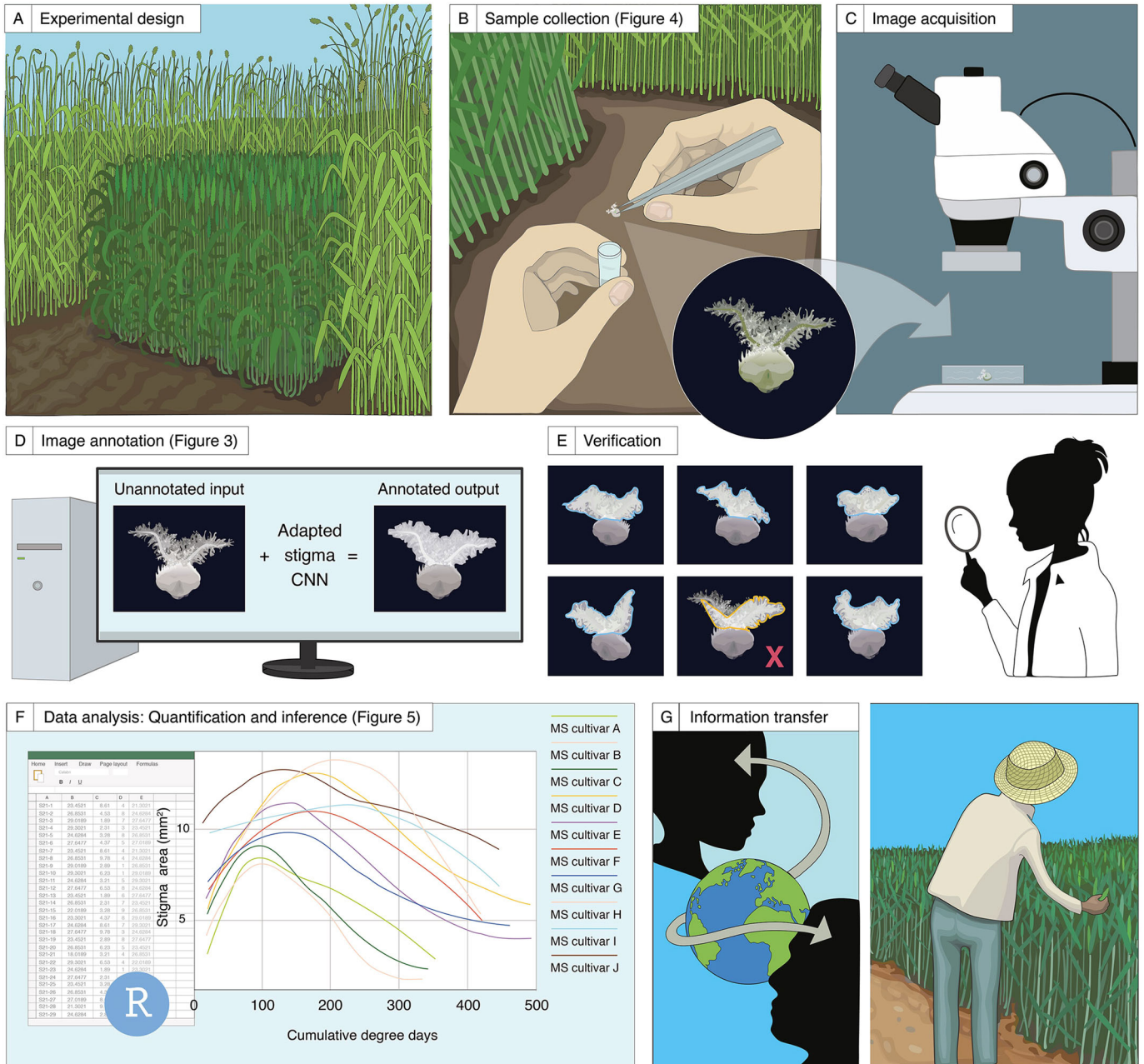


**Fig. 2. Schematic representation of the proposed phenotyping approach for the study of carpel development in the absence of pollination under field conditions.** (A-C) Experimental design, sample collection and image acquisition. (D,E) Annotation of microscopy images and quantification of the stigma area (an example shown in D) and verification of the CNN outputs (E). (F,G) The applicability of the phenotyping approach to enhance our understanding of the post-anthesis behaviour of unpollinated carpels.

them in water to the laboratory for carpel dissection. Once dissected, we stored the carpels in 95% ethanol and acetic acid (75% v/v) for image acquisition at a later timepoint, or fresh (non-fixed) specimens were imaged directly if tillers had been transported to the laboratory. We used a stereo microscope with an integrated camera to acquire the two-dimensional RGB image of the carpel against a black background (Fig. 2C). We used different magnifications and fields of view to capture the best representative plane of the carpel (Fig. S3). In the case of the fixed samples, we placed carpels in Petri dishes with 70% ethanol to preserve the feathery appearance of the stigma. Only one image per sampled carpel is required for subsequent steps.

#### Annotation of microscopy images and quantification of carpel traits

To process and perform quantitative analyses of the microscopy images, we trained a machine-learning (ML)-based algorithm to automatically and rapidly annotate and measure stigma area and ovary diameter (Fig. 2D). The trained networks return a set of annotated images alongside their shape descriptors, together with a CSV file containing the measurements of the analysed images in an output folder (see supplementary Materials and Methods for a step-by-step guide on how to use the trained networks). This step requires some manual curation wherein the user inspects, detects and corrects annotation errors, or removes corrupted images (Fig. 2E).

#### Data modelling and knowledge transfer

We developed code to model growth dynamics of stigma area and ovary diameter (Fig. 2F). The open-access customisable R scripts (see supplementary Materials and Methods) can produce a range of outputs to compare genotypes, environmental conditions or specific developmental stages, thereby helping to generate new hypotheses. Additionally, the exploitation of the knowledge generated could be key in the progress towards establishing successful hybrid breeding programmes, as the selection of MS cultivars can now be based on previously unreported phenotypic information (Fig. 2G).

#### Development and validation of the stigma and ovary convolutional neural networks

Our aim was to develop an automated phenotyping method to detect and annotate the perimeter covered by the stigma hairs and the ovary to determine stigma area and ovary diameter across the life cycle of wheat carpels. To carry out automated image annotation and measurement, we trained a convolutional neural network (CNN) on a set of representative carpel images with manual annotations of the stigma perimeter ( $n=86$  images) and ovary perimeter ( $n=121$  images) using the UNet design (Falk et al., 2019) (Fig. 3A). The training dataset spanned a random sample of seven genotypes, ranging from early carpel development (W9.5 and earlier) to fully degenerated carpels (Fig. 1A), and included both fixed and non-

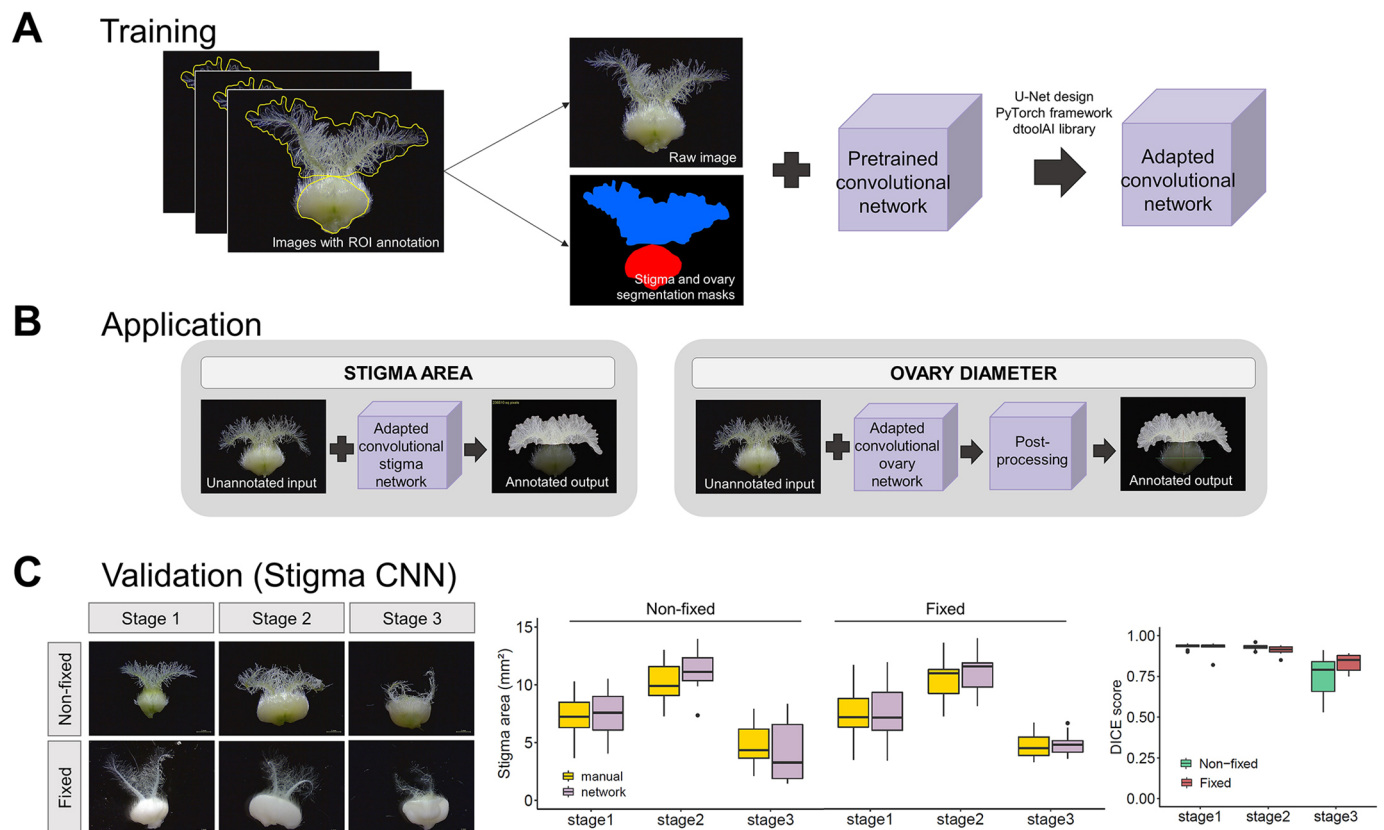


**Fig. 3. Development and validation of a CNN for stigma and ovary annotation.** (A) Pipeline for the development of the stigma and ovary networks. Region of interest, ROI. (B) Application of the adapted network for stigma area annotation to new data. (C) Cross-validation of ground-truth measurements and network values extracted from 60 randomly chosen images divided into six classes according to floral age (stage) and sampling method. The first box plot (middle) shows the distribution of the stigma areas in mm<sup>2</sup> per cross-validation class ( $n=10$  images per stage×method combination) determined by manual (yellow) and network (pink) annotation. There were no significant differences for any of the six classes (stage×sampling method combination). The second box plot (right) indicates DICE scores of stigma area in non-fixed (green) and fixed (red) samples. A DICE score of 0 indicates no spatial overlap between the two sets of annotation results, 1 indicates complete overlap. The box plots show the middle 50% of the data with the median represented by the horizontal line. Whiskers represent datapoints within 1.5 times the interquartile range with outliers highlighted as individual points. Scale bars: 1 mm.

fixed carpels. After successfully training the networks, we obtained an adapted stigma CNN that is able to quantify the area covered by stigmatic hairs and an adapted ovary CNN that, after some post-processing of the network output, quantifies the diameter of the ovary (Fig. 3B).

To evaluate the performance of the resulting adapted CNNs, we applied the network to an unseen set of 60 microscopy images without manual annotations (Fig. 3C). Subsequently, we manually annotated this new dataset using Fiji to provide a ground-truth reference with which to compare the CNN annotated outputs. We divided the cross-validation process according to the developmental stage of the carpels, sampling method (fixed or non-fixed), and the tissue of interest (Fig. 3C; Fig. S4 for ovary CNN validation). We observed a high overlap in stigma areas and ovary diameters of fixed and non-fixed samples between the manual and automated annotations across all three developmental stages. There were no significant differences between the manual and automated annotations, apart for ovary diameter of the non-fixed samples at stage 3 ( $P=0.03$ , one-way ANOVA with Tukey's post hoc test; Table S2). Additionally, we calculated the Dice similarity coefficient (DSC) for each group of images that allowed quantitative evaluation of the performance of the adapted networks (Fig. 3C; Fig. S4). Overall, we found very uniform DSC values between the ground-truth and CNN annotation across floral traits, sampling methods and developmental stages (with the exception of the stigma CNN at the last developmental stage), with DSC averages of 0.89 and 0.95 for the stigma and ovary CNNs, respectively. Taken

together, these results show that our machine-learning approach quantifies key parameters of the carpel life cycle in wheat, which are in agreement with the more time-consuming manual measurements.

#### Variation in stigma and ovary growth patterns can be studied on fixed carpels

Chemical fixation is commonly used to prevent tissue autolysis and degradation, while preserving morphology and cellular details for subsequent macroscopic or microscopic evaluations. Fixatives, however, can lead to changes in the volume and shape of the treated specimens due to cell shrinkage or swelling. Thus, artefacts of the technique could potentially lead to erroneous conclusions when measuring morphological traits of fixed samples.

To assess the effect of the fixative solution (ethanol and acetic acid) on stigma area and ovary diameter, we used four MS cultivars and sampled carpels at five timepoints over an 18-day period. Analysis of variance (three-way ANOVA) indicated that the fixative significantly reduces stigma area ( $P<0.001$ ), whereas ovary diameter remained unchanged after applying the fixative ( $P=0.25$ ) (Fig. 4A-C; Fig. S5). For stigma area, the fixative $\times$ timepoint interaction was borderline non-significant ( $P=0.09$ ) (Table S3), suggesting that the response to the fixative might change with floral age. By analysing individual timepoints, we observed that at 3 and 7 days after W9.5, at the peak of the stigma area, there were no significant differences between fixed and non-fixed samples, whereas at 0 and 13 days ( $P<0.05$ ), and at 18 days ( $P<0.001$ ) after W9.5 (Fig. 4A), the fixed samples show a reduced stigma area.

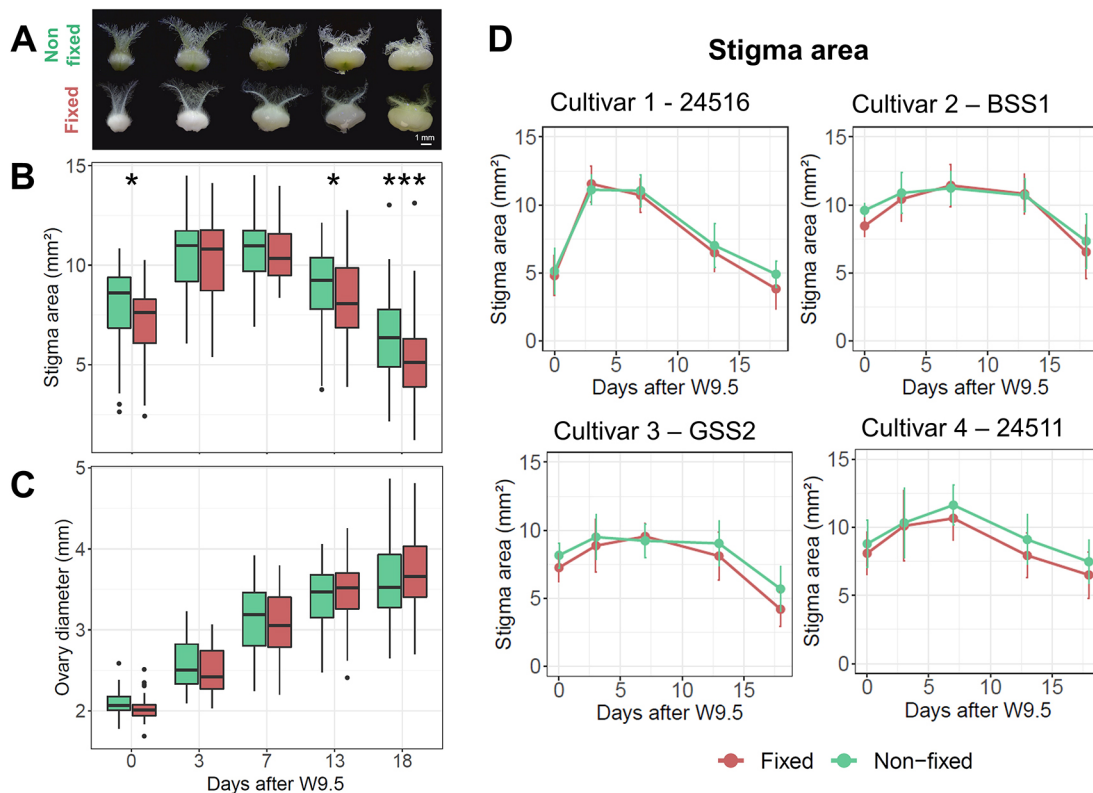


**Fig. 4. Effects of the fixative on carpel morphology across time and cultivars.** (A) Representative images of carpels before (non-fixed) and after (fixed) applying the fixative. (B,C) Box plots showing the comparison between non-fixed (green) and fixed (red) samples for stigma area (B) and ovary diameter (C) at different sampling points. Data are the average of the four cultivars shown in panel D, and represent 10-20 carpels from a total of four plants per timepoint and cultivar.  $*P<0.05$ ;  $***P<0.001$  (Tukey's test). The box plots show the middle 50% of the data with the median represented by the horizontal line. Whiskers represent datapoints within 1.5 times the interquartile range with outliers highlighted as individual points. (D) Developmental dynamics of stigma area of four MS cultivars, comparing non-fixed (green) and fixed (red) carpel samples (between 10 and 20 carpels from a total of four plants per timepoint). Error bars denote the s.e.m.

Importantly, the absence of a significant fixative×cultivar interaction ( $P>0.52$ ) suggests that all four cultivars react to the fixative in a similar manner (Fig. 4D). Taken together, we saw that fixing the carpels in ethanol and acetic acid reduced stigma area, even though the developmental dynamics of stigma area were conserved in the four cultivars across the 18 days (Fig. 4D). We therefore conclude that the use of the ethanol and acetic acid fixative allows us to accurately capture the growth dynamics of stigma area and ovary diameter, and to investigate phenotypic variation among diverse genotypes. Nonetheless, caution must be taken to compare absolute stigma areas across development, given the significant reduction at early and late timepoints.

### Application of the phenotyping approach provides insight into the developmental behaviour of the unpollinated wheat carpel

Having established the method to quantitatively measure the progression of carpel development in the absence of pollination,

we next sought to employ this approach to gain insights into genetic and environmental variation for these two floral traits. To accomplish this, we applied our phenotyping approach to three MS cultivars grown during two consecutive field seasons (2020 and 2021), for which we performed a developmental time course starting from W9.5 until the stage at which the carpel had visually deteriorated. We selected MS cultivars BSS1, 24522 and 24512 as they captured a large part of the variation observed in a broader panel phenotyped in 2020 (M.M.B., unpublished). To accommodate for season-specific differences in temperature between the two seasons (Fig. S2), we incorporated daily temperatures in our model to normalise developmental stages by cumulative degree days.

We found that all three MS cultivars exhibited contrasting developmental patterns for stigma area and ovary diameter, and that these differences among cultivars were largely maintained across field seasons (Fig. 5A,B). Phenotypic differences, particularly in stigma area, were observed in both the growth (positive slope) and deterioration (negative slope) phases of carpel development, which

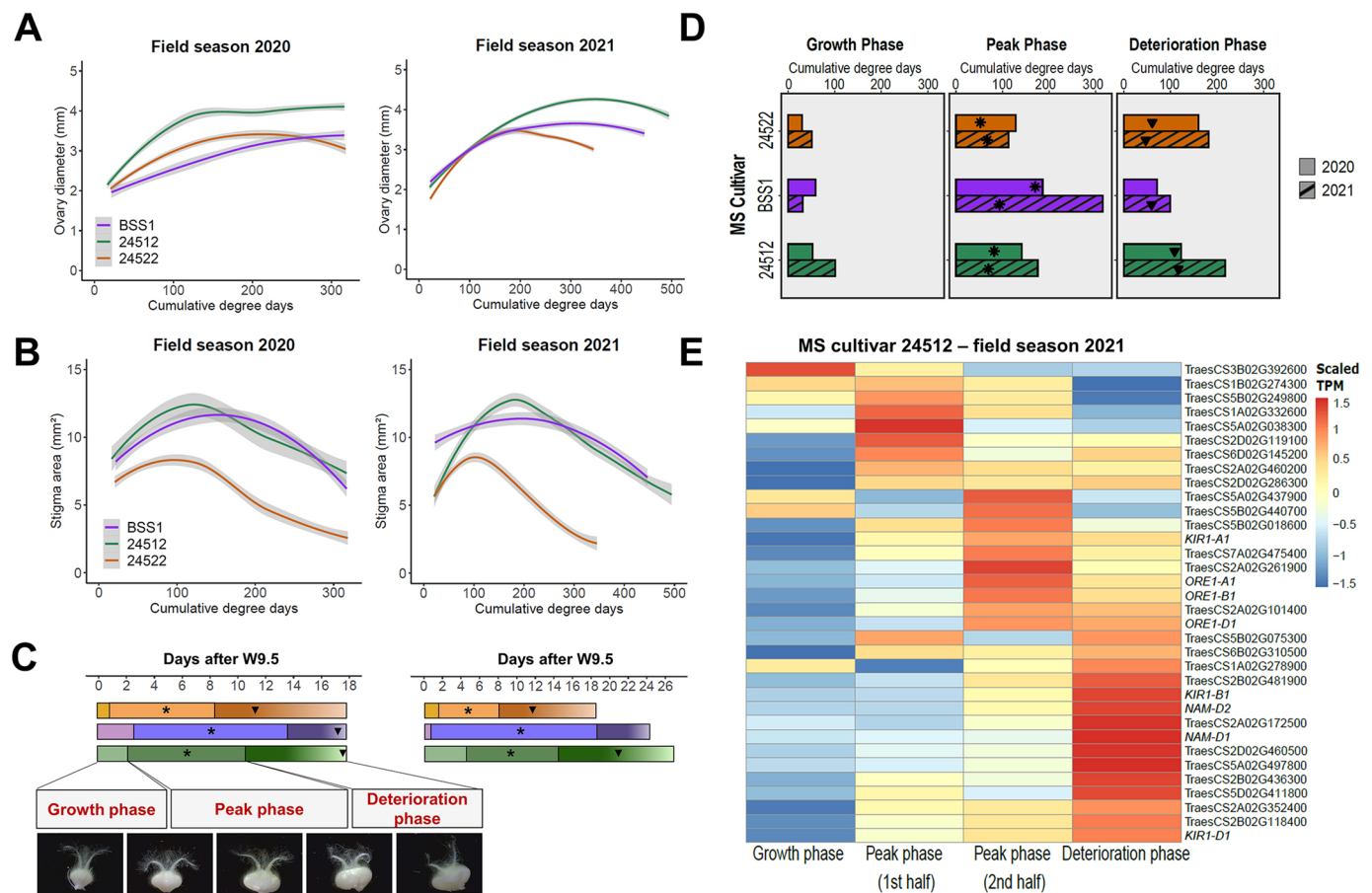


**Fig. 5. Phenotypic quantification of carpel development in three distinct MS cultivars under field conditions.** (A) Temporal trends of ovary diameter (mm) in 2020 and 2021. (B) Temporal trends of stigma area (mm<sup>2</sup>) for 2020 and 2021 field seasons. (C) Growth, peak and deterioration phases represented in days after W9.5 for 24522 (orange), BSS1 (purple) and 24512 (green). The temporal units are directly comparable with cumulative degree days shown in panel A. Representative images illustrating carpel appearance at the beginning and end of each phase are shown (the third picture represents a carpel with 100% stigma area). Scale bar: 2 mm. (D) Bar charts show the duration (in degree days) of each of the phases across cultivars and field seasons. The end of the deterioration phase is marked by the last sampling point. In A and B, polynomial regression models at a 95% confidence interval (Loess smooth line) are shown. Grey shading represents the s.e.m. Five carpels from four and six plants were sampled at each timepoint in 2020 and 2021, respectively. In C and D, asterisks indicate maximum stigma area; black triangles indicate a 40% drop in stigma area with respect to the maximum area. Before plotting, outliers were filtered out following the interquartile range criterion. (E) Heatmap illustrating the relative expression of *KIR1*, *ORE1* and genes associated with leaf senescence (Borrill et al., 2019) in stigma samples from MS cultivar 24512. Samples were collected in the growth, peak (first and second half) and deterioration phases during the 2021 field season. Expression levels are normalised within each gene across the four timepoints and rows are sorted according to the similarity of expression and waves of expression in each phase of stigma development. For absolute expression values, see Table S4.

inevitably impacted on the overall duration of the life cycle. For instance, we could distinguish the fast development of carpels from cultivar 24522 from the slow progression of carpels from cultivar BSS1 (Fig. 5B). Despite these differences, all three patterns seem to underline a common developmental trend for the dynamics of stigma and ovary traits that is characterised by an initial growth phase, followed by a peak phase in which the stigma reaches its maximum and the radial expansion of the ovary slows down, and a final deterioration phase. This conceptual framework for quantifying and classifying the development of the unpollinated carpel is presented in Fig. 5C,D. The results obtained from breaking down late carpel development into more descriptive phases are detailed below.

### Growth phase

The stigma and ovaries experienced rapid and exponential growth during the first phase. The growth phase was underway at W9.5 (around ear emergence) and extended for 1 to 4 days until the stigma was well developed and potentially receptive for pollination. The end of the phase coincided with a developmental stage parallel to W10 (anthesis) in male fertile plants. We found that for all three cultivars, the end of this phase could be described by the stigma showing an area of approximately 85% of its maximum area measured. The criteria for us to select the 85% cut-off for stigma area as the end of the growth phase was based on 85% being the percentage that was present in all three cultivars across both field seasons and happened shortly after W9.5, thus mimicking anthesis (Fig. S6).

### Peak phase

This second phase is denoted by the stigmatic tissue reaching its maximum size (asterisks in Fig. 5C) at around 5 to 10 days after W9.5 (depending on the cultivar and year). After reaching this peak, a gradual and irreversible decline in stigma area was accompanied by a notable arrest of the ovary radial expansion. To mirror the behaviour of stigma area at the beginning of this phase, we selected a 15% drop in stigma area to mark the end of the peak phase. Using this classification, we observed that this phase extended until 8 to 14 days after W9.5 in 2020, and 8 to 18 days in 2021 (Fig. 5C). Considering previous studies on female receptivity in wheat in which the hybrid seed set was maintained from 7 to 13 days (Pickett, 1993; Kirby, 2002; De Vries, 1971), we hypothesise that the peak phase of wheat stigma development coincides with the maximum reproductive potential of the carpel under free pollination conditions. Nonetheless, further analyses of pollen germination and seed setting rates during each of the three phases are needed to prove this hypothesis. Ideally these experiments would be conducted both under free-pollinating conditions (i.e. field trials mimicking hybrid production blocks) and using controlled hand pollinations, as results will most likely differ between experiments owing to the fact that other aspects of the female flower (e.g. opening angle of glumes) play a part in the reproductive potential of the floret (Selva et al., 2020).

### Deterioration phase

During this phase, symptoms of stigma deterioration started to become obvious and clusters of stigma hairs collapsed in response to a loss in turgor pressure (inverted triangles in Fig. 5C indicate a 40% drop in stigma area). The collapse of the remaining stigma hairs continued for several days, resulting in a completely deteriorated stigma at 18 and 27 days after W9.5 in 2020 and 2021, respectively (Fig. 5C,D). By the end of this phase, the ovary

walls also showed an irregular surface due to tissue deterioration. Based on these observations, we speculate that the onset of this phase marks the irrevocable loss of the reproductive potential of the floret.

Dissecting carpel development into growth, peak and deterioration phases allowed us to assign the cultivars BSS1, 24512 and 24522 into slow-, moderate- and fast-developing carpels, respectively, according to when they reached the beginning of the deterioration phase. For example, cultivar BSS1 reached the onset of the deterioration phase at 14 and 18 days after W9.5 in 2020 and 2021, respectively. This was approximately 4 days after the onset of the deterioration phase for cultivar 24512, and 6 and 10 days after the onset of the deterioration phase for cultivar 24522 in 2020 and 2021, respectively (Fig. 5C). The developmental pattern classification also allowed comparisons across field seasons, for which the relative ranking of cultivars was well conserved between years. Although we adjusted for cumulative degree days, the colder and damper weather conditions of 2021 (Fig. S2) were reflected in an extension in the duration of most phases in some but not all cultivars (Fig. 5D). For example, the durations of the three phases were largely unaffected in cultivar 24522, whereas in cultivar BSS1, the duration of the peak phase in 2021 (315 degree days) was almost twice that of the previous year (186 degree days). These initial analyses suggest that although the developmental dynamics of stigma area and ovary diameter were largely consistent across years, there were cultivars in which the duration of the developmental phases could be sensitive to other environmental changes that remain to be tested.

To provide further support for the proposed stages of the stigma life cycle, we investigated the expression of genes encoding senescence-related transcriptional regulators that we expect to be upregulated during the late peak and deterioration phases. Stigmas were sampled across the different phases of development using field-grown MS cultivar 24512, and the extracted RNA from these samples was used for an RNA-sequencing transcriptome experiment. We focused on the expression of wheat homologues of the *KIR1* and *ORE1* transcription factors (TFs) (Fig. S7), shown previously to promote stigma senescence in *Arabidopsis* (Gao et al., 2018), and the 36 top-ranked genes proposed to coordinate leaf senescence in wheat (Borrill et al., 2019), which included genes belonging to the GRAS, HSF and RWP-RK TF families. All six *KIR1* and *ORE1* wheat homologs were expressed, and 28 of the 36 TFs associated with leaf senescence were also expressed in the stigma, suggesting a large overlap between leaf and stigma senescence processes (Fig. 5E). Of the 34 TFs expressed in the stigma, we identified distinct waves of expression in their transcript profiles across the four sampling timepoints. Although eight TFs had the highest expression in the growth and early peak phase, over 70% of the expressed senescence-related TFs (including wheat *KIR1* and *ORE1*) were upregulated towards the end of the peak phase (ten genes) or at the deterioration phase (15 genes) (Fig. 5E). These results highlight that the proposed phases of late carpel development, determined using microscopy, associate with expected transcriptional changes based on the biological processes that occur during these later stages (Fig. 5E).

## DISCUSSION

### High-throughput phenotyping for the quantification of floral traits in unpollinated wheat carpels

Our understanding of floral developmental processes has been assisted by the establishment of scales that describe changes in the shape, size and surface features of floral organs leading up to

anthesis (Waddington et al., 1983; Smyth et al., 1990). These scales often divide a continuous developmental process into defined stages, which are characterised by landmark events, such as the appearance of stigmatic branches. These scales have facilitated the interpretation of genetic studies and have contributed towards our understanding of the mechanisms that underlie the transitions leading to a given landmark event. During post-pollination stages, the focus shifts towards the developing fruit. Previous work, however, has also illustrated the importance of the quantitative monitoring of morphological changes associated with late carpel development (i.e. in the absence of pollination), such as silk elongation in maize (Bassetti and Westgate, 1993) or ovary radial expansion in wheat (Okada et al., 2018), as they represent survival mechanisms to ensure seed set by cross-pollination. So far, the few studies investigating the progression of the unpollinated female carpel after anthesis have focused in giving detailed descriptions of flowers from one or two different genotypes grown in controlled environment conditions. These types of meticulous approaches are arduous and expensive not only to implement in large-scale experiments but also to execute under field conditions, in which equipment is often limited. Consequently, studies investigating detailed phenotypes in the field are lacking.

To enhance our understanding of the biological processes that occur in the unpollinated carpel under breeding-relevant conditions, we created a machine-learning-based approach to phenotype field-grown MS wheat cultivars. Given the sequence of morphological changes that we observed in the unpollinated wheat carpel (Fig. 1A), we quantified changes in stigma area and ovary diameter to describe carpel development. Our findings are twofold: (1) we demonstrate the suitability of our approach for the detailed study of floral organ traits in field screenings, and (2) we show that the unpollinated carpel undergoes a well-defined pattern of growth and senescence characterised by gradual changes in stigma and ovary sizes (Fig. 5A, B). Based on these findings, we propose developmental phases that are relative to the maximum stigma area and ovary size (Fig. 1C, Fig. 5C), and with which to build the foundations of future research of floral organ development and senescence in the absence of pollination.

### Considerations on the use of the stigma- and ovary-adapted CNNs

The quantification of stigma area and ovary diameter cannot be easily determined from surface observations of wheat spikes and requires the dissection and microscopy of individual carpels. The manual annotation and quantification of microscopy images is cumbersome and often delays scientific discoveries. Deep-learning-based approaches, such as the use of CNNs, have emerged as a solution to perform image quantification in an automated, rapid, and less biased manner, lifting the burden of image analysis from researchers. In this work, we developed two CNNs (both publicly available at [https://github.com/Uauy-Lab/ML-carpel\\_traits](https://github.com/Uauy-Lab/ML-carpel_traits)) that enable non-machine-learning experts to quantify stigma area and ovary diameter on their local computer in a matter of hours (Fig. 3). Evaluation metrics on the performance of the adapted networks (Fig. 3C; Table S2) demonstrate their capability to satisfactorily measure both floral traits by condensing each RGB image to a single value (i.e. pixels). Measurements between manual and CNN annotation were largely indistinguishable (Table S1), with the network being less capable at later stages (Fig. 3C; Fig. S1). We believe that one of the reasons for the poorer performance could be due to the difficulty in distinguishing the stigma and ovary from each other when the stigma is severely deteriorated and resting on

top of the ovary (Fig. S8). Also, it is worth noting that the ovary CNN relies on the performance of the stigma CNN to correctly predict the diameter of the ovary (see Materials and Methods for the detailed description of the algorithm), such that a bad prediction of the stigma area will likely affect ovary annotation. Poor-quality images (i.e. out-of-focus or poor-resolution images) and certain carpel orientations (Fig. S3) also hinder the identification of the ovary and/or stigma, impairing the normal performance of the CNNs. In the case of blurry images, using post-processing tools (e.g. Photoshop or other image-sharpening techniques) to adjust the sharpness of the image might reduce the likelihood of incorrect annotations. However, there will still be certain cases for which there may not be an immediate reason for the failure of the CNN. We therefore suggest including an additional output-verification step (Fig. 2E) to identify potential errors before continuing with the downstream analyses.

### The implementation of the phenotyping approach opens new research paths on the biology of late carpel development

To gain a more comprehensive overview of the developmental dynamics of the unpollinated carpel, we used our phenotyping approach (Fig. 2) to examine the sequential progression of changes in stigma and ovary morphology in three MS cultivars over two field seasons (Fig. 5). Across cultivars and seasons, we were able to identify an initial stigma and ovary growth phase, followed by a peak phase describing carpel developmental maturity, and a subsequent deterioration phase characterised by the eventual collapse of the female reproductive tissues and expression of multiple senescence-associated genes (Fig. 5C,E). Equivalent patterns for the post-anthesis development of the unpollinated stigma have also been reported in maize, peas (*Pisum sativum*) and *Arabidopsis* (Bassetti and Westgate, 1993; Vercher et al., 1984; Carbonell-Bejerano et al., 2010), suggesting a conserved developmental programme that ensues in the absence of pollination.

Despite the conserved overall patterns, we identified differences in the duration of the growth, peak and deterioration phases in the three wheat MS cultivars used here. Gene expression studies of unpollinated carpels and stigma in *Arabidopsis* and maize (Carbonell-Bejerano et al., 2010; Gao et al., 2018; Šimášková et al., 2022) have demonstrated that the lifespans of these floral structures are controlled by transcription factors that regulate developmental programmed cell death in these tissues. Here, we also identified distinct waves of expression of genes encoding senescence-associated TFs across late stigma development in a single wheat MS cultivar. Our results, along with previous evidence from *Arabidopsis* and maize, raise the prospect that the phenotypic variation observed among the three wheat MS cultivars could be due to differential gene expression patterns across cultivars that alter the onset of stigma senescence (Fig. 5B,C). Thus, new transcriptomic studies investigating the developmental transitions observed among the different field-grown cultivars would contribute to our understanding of the mechanisms governing these phases. We also observed that MS cultivars 24512 and 24522 had largely equivalent peak phase durations across years, whereas the duration of the peak phase in the CMS cultivar BSS1 varied almost twofold between field seasons (Fig. 5D). This suggests that, despite accounting for temperature in our analyses (by using cumulative degree days), the duration of the stigma peak phase is sensitive to additional environmental factors. The response to these additional environmental factors could depend on the genotype, sterility system used and/or the developmental phase in which the environmental stimuli are encountered. Consistent with this,

several studies in wheat have attributed differential seed set rates of out-crossing MS plants (i.e. an indicator for the duration of stigma receptivity) to environmental factors such as temperature, relative humidity and soil water availability (Fábíán et al., 2019; De Vries, 1971; Imrie, 1966). Therefore, additional studies under field and controlled environment conditions will shed light on the causalities for the variation observed in ovary and stigma development across field seasons. Our phenotyping approach now improves the accessibility of the wheat carpel to detailed phenotypic analyses of the size of populations that are used in breeding programmes. This facilitates the identification of mutations that underpin genetic variation in carpel development, thus contributing to understanding gene function on a genome-wide scale. All in all, we provide a framework in which to conduct these new studies targeting diverse environments and genotypes, which will facilitate future hypothesis generation not only in wheat but also in other cereal crops.

### First steps towards an integrated developmental scale of the unpollinated wheat flower

The ultimate role of the carpel is the production of a viable seed. Thus, increasing the functional lifespan of carpels and stigmas (i.e. floral receptivity) are desirable agronomic traits that have the potential to increase the effective pollination period and seed set (Williams, 1965). Yet, detailed evaluations of carpel and stigma development and how they relate to female floral receptivity and seed set are still lacking, especially in cereals. It is reasonable to think that the functional lifespan of stigma receptivity would coincide with stigma cell integrity, as illustrated in early studies of kiwifruit (*Actinidia deliciosa*) and maize (González et al., 1995; Bassetti and Westgate, 1993). According to these studies, we could, for example, speculate (1) that seed set rates will be higher if pollination occurs during the peak phase compared with the deterioration phase, or (2) that cultivars with a prolonged peak phase (such as BSS1) will be receptive to pollination for longer than cultivars with a shorter peak phase (such as 24512 or 24522) (Fig. 5C). However, as recently demonstrated in *Arabidopsis*, a delay in stigma senescence caused by the disruption of two transcription factors promoting programmed cell death was only accompanied by a minor extension in floral receptivity, suggesting that additional processes must be involved in controlling the duration of floral receptivity, for instance, ovule viability (Gao et al., 2018). New studies, therefore, need to be conducted to investigate stigma receptivity under defined phases of carpel development to clarify the relationship between stigma morphology and viability, pollen germination, and seed set. Additionally, such information will allow a greater understanding of how genetic and environmental factors affect various aspects of the stigma life cycle (e.g. loss of stigma receptivity, onset of stigma cell death). The next steps towards understanding the cross-pollination process in the field will also require integrating the changes in carpel morphology with those of the overall spike. For instance, as reviewed by Selva et al. (2020), certain wheat spike architectures, like the openness of the floret, facilitate airborne pollen access, which would additionally contribute to increasing out-crossing rates in hybrid production.

Our approach for phenotyping carpel development provides a new tool for examining a fertility trait that is poorly understood and hitherto time consuming to analyse. Taken together with recent advances in genetic resources (Krasileva et al., 2017; Wingen et al., 2014; Sansaloni et al., 2020) and genome sequence data (Walkowiak et al., 2020; International Wheat Genome Sequencing et al., 2018), this approach provides a new opportunity to unlock

genetic variation for stigma and ovary traits that associate with floret fertility, which is vital given that improved fertilisation will help in addressing the increasing demands to enhance global food production.

## MATERIALS AND METHODS

### Germplasm

We used both spring and winter MS hexaploid wheat (*Triticum aestivum*) cultivars derived from commercial inbred lines. CMS and NMS systems were used for the generation of the male sterile cultivars. BSS1 and GSS2 correspond to winter CMS cultivars, whereas the winter cultivars 24511, 24512, 24516 and 24522, and the spring cultivars Jetstream, Alderon, BLA1, Mairra, Cadenza, Chamsin and BLA2 are NMS cultivars. CMS and NMS cultivars were provided by KWS (Thriplow, UK) and Syngenta (Whittlesford, UK), respectively.

We used MS cultivar 24516 as an example to illustrate the developmental dynamics of the unpollinated wheat stigma and ovary in Fig. 1. To train the CNN for the quantification of carpel traits, we used a random sample of plants extracted from a set of the seven spring NMS cultivars. The selection criteria for the generation of the training set, however, were based on the diversity of carpel images rather than being based on individual cultivars.

We used four winter MS cultivars (24511, 24516, BSS1 and GSS2) to characterise the effects of the fixative on stigma area and ovary diameter during the 2020 field season. Finally, for the multi-year field experiment performed to investigate the developmental patterns of the unpollinated carpel, we grew three winter MS cultivars (BSS1, 24512 and 24522) during two consecutive years. We selected these three cultivars as they represent a large part of the variation observed for carpel development in the absence of pollination from an original pool of 31 MS cultivars phenotyped in 2020 under field conditions (M.M.B., unpublished). Table S1 provides a summary of all cultivars used in the experiments.

### Glasshouse and field experiments

For the development of the stigma and ovary CNNs, we grew between ten and 20 plants per MS cultivar (Jetstream, Alderon, BLA1, Mairra, Cadenza, Chamsin and BLA2) in the glasshouse in 1 l pots under long day conditions (16 h light: 8 h dark) and hand dissected carpels from either the first, second or third tiller at various timepoints that were representative of the different carpel morphologies. We stored a random selection of the dissected carpels in a fixative solution of 95% ethanol and absolute acetic acid (75% v/v), and kept them at 4°C until image acquisition (approximately 1 month after fixation). The cultivars selected are representative of carpel morphology diversity in wheat germplasm.

For the carpel development time course experiments, we grew plants at John Innes Centre Church Farm (Bawburgh, UK; 52°37'50.7"N 1°10'39.7"E) in a randomised complete block design with two replicates (1 m plots) per MS cultivar in 2020, and three replicates in 2021 (Fig. S1). The number of replicates were chosen according to traditional use in field experiments and seed availability. To avoid unwanted cross-pollination, sterile rye barriers were grown surrounding the MS plots. To record environmental data, we placed data loggers (EasyLog USB, Lascar Electronics) next to the experimental plots at a 50 cm height. Average temperature and relative humidity were measured every hour for the duration of the experiment (Fig. S2).

In both field seasons, we tagged main spikes when carpels in the outer florets (floret 1 and 2) of central spikelets reached W9.5 (Waddington et al., 1983). This is shortly after full ear emergence (Zadoks growth stage 59; Zadoks et al., 1974). At the time of sampling, we cut individual tillers between the uppermost and penultimate internode and transported them in water to the laboratory for carpel dissection. We harvested four to seven carpels from the outer florets of central spikelets from two spikes per plot and timepoint. These timepoints were W9.5 and 3, 7, 13 and 18 days after W9.5 (DAW9.5), with the only exception that the 2021 time course was extended for nine more days (i.e. 27 DAW9.5) in cases in which the carpel was not completely senesced at 18 DAW9.5. Owing to the limited availability of spikes tagged at W9.5, sample sizes for the extended timepoints varied from two to six spikes per timepoint. Carpels that needed

fixation were placed in 2 ml Eppendorf tubes containing fresh fixative solution, as described above.

### Image acquisition and manual annotations

To generate the training set, we used two different stereo microscopes equipped with an integrated camera for image capture (ZEISS Stemi 305 with a 1.2 Megapixel integrated colour camera; Leica MZ16 coupled with a Leica CLS100x white light source; and a Leica DFC420 5 Megapixel colour camera). For the downstream experiments using the adapted CNNs, we only used the ZEISS Stemi 305, as it is easier to operate and to transport to the field. Depending on the size of the carpel, we used different magnifications (from 1× to 4×) to ensure that the complete carpel was captured in the image (Fig. S3). We adapted the illumination and time of exposure for each image to ensure high contrast between the carpel and the black background. To maintain the feathery structure of the stigma in fixed samples, we imaged the carpels submerged in a 70% ethanol solution using a Petri dish (one carpel per image). Images were saved as RGB JPEG files.

To evaluate the effect of the fixative on carpel morphology traits, we first imaged the carpels as non-fixed samples and then placed them in the fixative solution (as described previously) for image acquisition at a later time. For manual annotations of stigma and ovary perimeters, we analysed the resulting images using the open-source image-processing package Fiji.

### Development of stigma and ovary CNNs

To carry out automated image annotation and measurement, we trained a CNN using the U-Net design, which can be easily adapted to new tasks with only few annotated images (Falk et al., 2019). The network was implemented in the PyTorch framework (Paszke et al., 2019), using the dtolAI library (Hartley and Olsson, 2020). The networks were trained on carpel JPEG images with manual annotations of the stigma perimeter ( $n=86$  images) and ovary perimeters ( $n=121$  images). These 207 images were randomly selected from a total of 1601 dissected carpels. The Dice coefficient (Dice, 1945) was used as a loss function, and weight updates were applied using the Adam optimizer (Kingma and Ba, 2015).

The trained stigma network predicted a mask corresponding to the stigma location for each RGB input image. The stigma mask was used to calculate the stigma area directly by extracting the number of pixels. The trained ovary network predicted two masks for each RGB input image: one corresponding to the ovary location and the other to the stigma location. To determine the ovary diameter, the following algorithm was applied: (1) determination of the centroid of the predicted stigma mask; (2) determination of the centroid of the predicted ovary mask; (3) taking the perpendicular to the line drawn through the centroids; (4) determination of the two points where this line crosses the border of the predicted ovary mask; and (5) measurement of the length of this line, converting to physical units from the original input image scale.

We converted pixels (CNN output) to stigma area (mm<sup>2</sup>), and ovary diameter (mm) according to the scale bar used in each image. Implementation scripts and training data are available at [https://github.com/Uauy-Lab/ML-carpel\\_traits](https://github.com/Uauy-Lab/ML-carpel_traits) and [https://opendata.earlham.ac.uk/wheat/under\\_license/toronto/Millan-Blanquez\\_et\\_al\\_2022\\_machine-learning-carpel-traits/](https://opendata.earlham.ac.uk/wheat/under_license/toronto/Millan-Blanquez_et_al_2022_machine-learning-carpel-traits/), respectively.

### Statistical analyses and data visualisation

#### Evaluation of CNN performance

To evaluate differences in stigma area and ovary diameter between the manual and CNN annotations, we selected a random set of 60 microscopy images that were not used to train the networks (30 images of fixed carpels and 30 of non-fixed carpels). We divided the images into three different developmental stages based on the appearance of the carpel to account for all the possible carpel morphologies to which the algorithm could be exposed. Stage 1 represents a young carpel (stigma and ovary still developing), stage 2 represents a fully developed carpel (widely spread stigma and enlarged ovary) and stage 3 includes visibly deteriorated carpels. We performed one-way ANOVA using Tukey's post hoc test for each trait and sampling method, including 'floral age' as the single factor (Table S2). To measure the

spatial overlap between the manual and CNN annotation, we calculated Dice similarity coefficients on the same set of images.

### Carpel development time courses

For the quantification of stigma area and ovary diameter of fixed and non-fixed samples, a total of 666 and 634 images were annotated by the stigma CNN and ovary CNN, respectively, and used for subsequent analyses. We conducted three-way ANOVAs (fixative, timepoint and cultivar) to test the effect of the fixative on stigma area and ovary diameter, and their interaction with floral age (timepoint) and cultivar (Table S3). We included block and spike information in the model as random effects to account for the nested nature of the experimental design. Tukey's multiple comparison method was used to adjust for multiple comparisons.

To generate the patterns describing stigma and ovary development for MS cultivars 24512, 24522 and BSS1, 294 images were annotated by the stigma and ovary CNNs in 2020, and 520 images in 2021, and used for downstream analyses. Next, we filtered outliers following the interquartile range criterion and used Loess smooth lines with a span value of 0.9 (i.e. width of the moving window when smoothing the data) and a 95% confidence interval. To have an estimate of the amount of growth the plants achieved during the different field seasons, we calculated cumulative degree days using 0°C as base temperature (according to Miller et al., 2001) and average daily temperatures as follows:

$$\text{cumulative degree days} = \sum_{i=0}^j (\text{mean temperature}) - \text{base temperature},$$

where  $i$  is the beginning of the temporal window considered (e.g. the W9.5 date) and  $j$  is the end of the temporal window considered (e.g. sampling date at 7 days after W9.5).

Codes to model carpel and ovary development were executed in RStudio version 4.0.3 and are available at [https://github.com/Uauy-Lab/ML-carpel\\_traits](https://github.com/Uauy-Lab/ML-carpel_traits). Image data used for the statistical analyses (i.e. one-way and three-way ANOVAs provided in Tables S2 and S3, respectively) are also available at [https://opendata.earlham.ac.uk/wheat/under\\_license/toronto/Millan-Blanquez\\_et\\_al\\_2022\\_machine-learning-carpel-traits/](https://opendata.earlham.ac.uk/wheat/under_license/toronto/Millan-Blanquez_et_al_2022_machine-learning-carpel-traits/).

Detailed step-by-step instructions are provided in the supplementary Materials and Methods.

### Stigma transcriptome analysis by RNA sequencing

During the 2021 field season, we used MS cultivar 24512 to investigate the expression patterns of senescence-related genes in the stigmatic tissues. We collected stigma samples at four developmental timepoints spanning the proposed growth, peak and deterioration phases (3, 7, 13 and 18 DAW9.5). We sampled plants between 11.00 h and 15.00 h and dissected five to eight stigmas (size dependent) from the primary and secondary florets of the central four spikelets. We stored stigmas in DNA/RNA Shield solution (Zymo Research, R1100-50) at -20°C. The stigma samples included both the stigma and style, as these structures are intimately linked in wheat.

We extracted RNA from three independent biological replicates using TRIzol/Chloroform (TRI Reagent, Sigma-Aldrich; Chloroform, ≥99.8%, Thermo Fisher Scientific) and purified using the RNA Clean and Concentrator kit (Zymo Research, R1013) as specified in the protocol for RNA extraction from wheat stigmas stored in DNA/RNA shield (<https://dx.doi.org/10.17504/protocols.io.36wgg7kj3vk5/v1>). RNA quantity and quality were assessed by spectrophotometric analysis (NanoDrop One/OneC; Thermo Fisher Scientific) and by agarose gel electrophoresis. Total RNA samples with a quality value greater than an RNA integrity number of 6 were used for Illumina HiSeq 150-bp paired-end sequencing (Novogene).

RNA sequencing data were pseudoaligned to the wheat RefSeqv1.1 transcriptome (International Wheat Genome Sequencing et al., 2018) using kallisto (Bray et al., 2016). We filtered for genes that expressed on average >0.5 transcripts per million (TPM) in at least one of the timepoints to exclude genes with low expression (consistent with Ramírez-González et al., 2018). TPM values were normalised across the four timepoints for each gene, and the individual TPM values are presented in Table S4.



### Acknowledgements

We thank the John Innes Centre (JIC) Field Trials and Horticultural Services teams for technical support in field and glasshouse experiments, the JIC Bioimaging facility and staff for their contribution to this publication, and Prof. Lars Østergaard (JIC) and Dr Azahara Martín for feedback on the work. We also thank James Simmonds and Tobin Florio for their assistance during the field trials and Flozbox studio (<https://flozbox-science.com/>) for designing Fig. 2. Finally, we thank Dr Simon Tyrrell and Dr Robert Davey for making the image data publicly available.

### Competing interests

N.B. is employed by KWS UK and Y.M. is employed by Syngenta, France. The remaining authors declare that they have no conflict of interest.

### Author contributions

Conceptualization: M.M.B., C.U., S.A.B.; Methodology: M.M.B.; Software: M.H.; Formal analysis: M.M.B.; Investigation: M.M.B.; Data curation: M.M.B.; Writing - original draft: M.M.B., M.H., C.U., S.A.B.; Writing - review & editing: M.M.B., N.B., Y.M., C.U., S.A.B.; Visualization: M.M.B.; Supervision: N.B., C.U., S.A.B.; Funding acquisition: C.U., S.A.B.

### Funding

This work was supported by the Biotechnology and Biological Sciences Research Council, UK through the Designing Future Wheat (BB/P016855/1) and Genes in the Environment (BB/P013511/1) Institute Strategic Programmes. Additional funding was provided by the European Research Council (ERC-2019-COG-866328) and the Royal Society (UF150081). M.M.B. was supported by a Biotechnology and Biological Sciences Research Council (BBSRC) Norwich Research Park Biosciences Doctoral Training Grant (BB/M011216/1). Open Access funding provided by University of Adelaide. Deposited in PMC for immediate release.

### Data availability

Training codes used for the development of the CNNs, adapted stigma and ovary CNNs, and R scripts used for data curation and visualisation can be found at [https://github.com/Uauy-Lab/ML-carpel\\_traits](https://github.com/Uauy-Lab/ML-carpel_traits). Datasets for the training and validation of the models and raw images used for the different experimental analyses are freely available at [https://opendata.earlham.ac.uk/wheat/under\\_license/toronto/Millan-Blanquez\\_et\\_al\\_2022\\_machine-learning-carpel-traits/](https://opendata.earlham.ac.uk/wheat/under_license/toronto/Millan-Blanquez_et_al_2022_machine-learning-carpel-traits/).

### Peer review history

The peer review history is available online at <https://journals.biologists.com/dev/lookup/doi/10.1242/dev.200889.reviewer-comments.pdf>.

### References

- Ashman, T.-L. and Schoen, D. J. (1994). How long should flowers live? *Nature* **371**, 788-791. doi:10.1038/371788a0
- Bassetti, P. and Westgate, M. E. (1993). Emergence, elongation, and senescence of maize silks. *Crop Sci.* **33**, 271-275. doi:10.2135/cropsci1993.0011183X003300020011x
- Borrill, P., Harrington, S. A., Simmonds, J. and Uauy, C. (2019). Identification of transcription factors regulating senescence in wheat through gene regulatory network modelling. *Plant Physiol.* **180**, 1740-1755. doi:10.1104/pp.19.00380
- Bray, N. L., Pimentel, H., Melsted, P. and Pachter, L. (2016). Near-optimal probabilistic RNA-seq quantification. *Nat. Biotechnol.* **34**, 525-527. doi:10.1038/nbt.3519
- Carbonell-Bejerano, P., Urbez, C., Carbonell, J., Granell, A. and Perez-Amador, M. A. (2010). A fertilization-independent developmental program triggers partial fruit development and senescence processes in pistils of Arabidopsis. *Plant Physiol.* **154**, 163-172. doi:10.1104/pp.110.160044
- De Vries, A. P. (1971). Flowering biology of wheat, particularly in view of hybrid seed production—a review. *Euphytica* **20**, 152-170. doi:10.1007/BF00056076
- Dice, L. R. (1945). Measures of the amount of ecologic association between species. *Ecology* **26**, 297-302. doi:10.2307/1932409
- Edlund, A. F., Swanson, R. and Preuss, D. (2004). Pollen and stigma structure and function: the role of diversity in pollination. *Plant Cell* **16**, S84-S97. doi:10.1105/tpc.015800
- Fábián, A., Sáfrán, E., Szabó-Eitel, G., Barnabás, B. and Jäger, K. (2019). Stigma functionality and fertility are reduced by heat and drought co-stress in wheat. *Front. Plant Sci.* **10**, 244. doi:10.3389/fpls.2019.00244
- Falk, T., Mai, D., Bensch, R., Çiçek, Ö., Abdulkadir, A., Marrakchi, Y., Böhm, A., Deubner, J., Jäckel, Z., Seiwald, K., et al. (2019). U-Net: deep learning for cell counting, detection, and morphometry. *Nat. Methods* **16**, 67-70. doi:10.1038/s41592-018-0261-2
- Furbank, R. T. and Tester, M. (2011). Phenomics – technologies to relieve the phenotyping bottleneck. *Trends Plant Sci.* **16**, 635-644. doi:10.1016/j.tplants.2011.09.005
- Gao, Z., Daneva, A., Salanenka, Y., Van Durme, M., Huysmans, M., Lin, Z., De Winter, F., Vanneste, S., Karimi, M., Van de Velde, J. et al. (2018). KIRA1 and ORESARA1 terminate flower receptivity by promoting cell death in the stigma of Arabidopsis. *Nat. Plants* **4**, 365-375. doi:10.1038/s41477-018-0160-7
- González, M. V., Coque, M. and Herrero, M. (1995). Papillar integrity as an indicator of stigmatic receptivity in kiwifruit (*Actinidia deliciosa*). *J. Exp. Bot.* **46**, 263-269. doi:10.1093/jxb/46.2.263
- Hartley, M. and Olsson, T. S. G. (2020). dtoolAI: reproducibility for deep learning. *Patterns* **1**, 100073. doi:10.1016/j.patter.2020.100073
- Heslop-Harrison, J. (1979). Pollen-stigma interaction in grasses: a brief review. *N. Z. J. Bot.* **17**, 537-546. doi:10.1080/0028825X.1979.10432570
- Heslop-Harrison, Y. and Shivanna, K. (1977). The receptive surface of the angiosperm stigma. *Ann. Bot.* **41**, 1233-1258. doi:10.1093/oxfordjournals.aob.a085414
- Imrie, B. (1966). Stigma receptivity in cytoplasmic male sterile wheat. *Aust. J. Exp. Agric.* **6**, 175-178. doi:10.1071/EA9660175
- International Wheat Genome Sequencing, C., Investigators, I. R. P., Appels, R., Eversole, K., Feuillet, C., Keller, B., Rogers, J., Pozniak, C. J., Choulet, F., Distelfeld, A., et al. (2018). Shifting the limits in wheat research and breeding using a fully annotated reference genome. *Science* **361**, eaar7191. doi:10.1126/science.aar7191
- Kempe, K. and Gils, M. (2011). Pollination control technologies for hybrid breeding. *Mol. Breed.* **27**, 417-437. doi:10.1007/s11032-011-9555-0
- Kingma, D. P. and Ba, J. (2015). ADAM: a method for stochastic optimization. In: *3rd International Conference for Learning Representations*. San Diego. doi:10.48550/arXiv.1412.698
- Kirby, E. (2002). Botany of the wheat plant. In *Bread Wheat. Improvement and Production* (ed. B. C. Curtis, S. Rajaram and H. Gómez Macpherson), pp. 19-37. Rome: Food and Agriculture Organization of the United Nation.
- Krasileva, K. V., Vasquez-Gross, H. A., Howell, T., Bailey, P., Paraiso, F., Clissold, L., Simmonds, J., Ramirez-Gonzalez, R. H., Wang, X., Borrill, P. et al. (2017). Uncovering hidden variation in polyploid wheat. *Proc. Natl. Acad. Sci. USA* **114**, E913-E921. doi:10.1073/pnas.1619268114
- Miller, P., Lanier, W. and Brandt, S. (2001). Using growing degree days to predict plant stages. *Montguide* MT200103 AG 7/2001.
- Mitchell, J. C. and Petolino, J. F. (1988). Heat stress effects on isolated reproductive organs of maize. *J. Plant Physiol.* **133**, 625-628. doi:10.1016/S0176-1617(88)80019-1
- Molnár-Láng, M., Barnabas, B. and Rajki, E. (1980). Changes in the shape, volume, weight and tissue structure of the pistil in the flowers of male sterile wheats during flowering. *Cereal Res. Commun.* **8**, 371-379.
- Okada, T., Jayasinghe, J., Nansamba, M., Baes, M., Warner, P., Koudiri, A., Correia, D., Nguyen, V., Whitford, R. and Baumann, U. (2018). Unfertilized ovary pushes wheat flower open for cross-pollination. *J. Exp. Bot.* **69**, 399-412. doi:10.1093/jxb/erx410
- Onyemaobi, I., Liu, H., Siddique, K. H. and Yan, G. (2016). Both male and female malfunction contributes to yield reduction under water stress during meiosis in bread wheat. *Front. Plant Sci.* **7**, 2071. doi:10.3389/fpls.2016.02071
- Paszke, A., Gross, S., Massa, F., Lerer, A., Bradbury, J., Chanan, G., Killeen, T., Lin, Z., Gimelshein, N., Antiga, L. et al. (2019). PyTorch: an imperative style, high-performance deep learning library. In: *33rd Conference on Neural Information Processing Systems*. Vancouver: NeurIPS Proceedings. doi:10.5555/3454287.3455008
- Pickett, A. A. (1993). Hybrid wheat-results and problems. *Fortschr. Pflanzenzücht.* **15**.
- Pieruschka, R. and Schurr, U. (2019). Plant phenotyping: past, present, and future. *Plant Phenomics* **2019**, 1-6. doi:10.34133/2019/7507131
- Primack, R. B. (1985). Longevity of individual flowers. *Annu. Rev. Ecol. Syst.* **16**, 15-37. doi:10.1146/annurev.es.16.110185.000311
- Ramírez-González, R., Borrill, P., Lang, D., Harrington, S., Brinton, J., Venturini, L., Davey, M., Jacobs, J., van Ex, F., Pasha, A. et al. (2018). The transcriptional landscape of polyploid wheat. *Science* **361**, eaar6089. doi:10.1126/science.aar6089
- Sansaloni, C., Franco, J., Santos, B., Percival-Alwyn, L., Singh, S., Petroli, C., Campos, J., Dreher, K., Payne, T., Marshall, D. et al. (2020). Diversity analysis of 80,000 wheat accessions reveals consequences and opportunities of selection footprints. *Nat. Commun.* **11**, 4572. doi:10.1038/s41467-020-18404-w
- Selva, C., Riboni, M., Baumann, U., Würschum, T., Whitford, R. and Tucker, M. R. (2020). Hybrid breeding in wheat: how shaping floral biology can offer new perspectives. *Funct. Plant Biol.* **47**, 675-694. doi:10.1071/FP19372
- Šimásková, M., Daneva, A., Doll, N., Schilling, N., Cubría-Radio, M., Zhou, L., De Winter, F., Aesaert, S., De Rycke, R., Pauwels, L. et al. (2022). KIL1 terminates fertility in maize by controlling silk senescence. *Plant Cell* **34**, 2852-2870. doi:10.1093/plcell/koac151
- Smyth, D. R., Bowman, J. L. and Meyerowitz, E. M. (1990). Early flower development in Arabidopsis. *Plant Cell* **2**, 755-767. doi:10.1105/tpc.2.8.755
- Vercher, Y., Molowny, A., López, C., García-Martínez, J. L. and Carbonell, J. (1984). Structural changes in the ovary of *Pisum sativum* L. induced by pollination and gibberellic acid. *Plant Sci. Lett.* **36**, 87-91. doi:10.1016/0304-4211(84)90240-2

- Waddington, S., Cartwright, P. and Wall, P.** (1983). A quantitative scale of spike initial and pistil development in barley and wheat. *Ann. Bot.* **51**, 119-130. doi:10.1093/oxfordjournals.aob.a086434
- Walker, E. R.** (1906). *On the Structure of the Pistils of Some Grasses*, Vol. VI. University studies from University of Nebraska.
- Walkowiak, S., Gao, L., Monat, C., Haberer, G., Kassa, M. T., Brinton, J., Ramirez-Gonzalez, R. H., Kolodziej, M. C., Delorean, E., Thambugala, D. et al.** (2020). Multiple wheat genomes reveal global variation in modern breeding. *Nature* **588**, 277-283. doi:10.1038/s41586-020-2961-x
- Williams, R.** (1965). The effect of summer nitrogen applications on the quality of apple blossom. *J. Hortic. Sci.* **40**, 31-41. doi:10.1080/00221589.1965.11514118
- Wingen, L. U., Orford, S., Goram, R., Leverington-Waite, M., Bilham, L., Patsiou, T., Ambrose, M., Dicks, J. and Griffiths, S.** (2014). Establishing the A. E. Watkins landrace cultivar collection as a resource for systematic gene discovery in bread wheat. *Theor. Appl. Genet.* **127**, 1831-1842. doi:10.1007/s00122-014-2344-5
- Zadoks, J. C., Chang, T. T. and Konzak, C. F.** (1974). A decimal code for the growth stages of cereals. *Weed Res.* **14**, 415-421. doi:10.1111/j.1365-3180.1974.tb01084.x